Aerospace Engineering Sciences Graduate Theses & Dissertations

Aerospace Engineering Sciences

Spring 1-1-2015

Understanding Enhancements in Outer Radiation Belt Electrons through Measurement and Modeling

Quintin George Schiller
University of Colorado Boulder, quintin.schiller@colorado.edu

Understanding Enhancements in Outer Radiation Belt Electrons through Measurements and Modeling

BY

QUINTIN GEORGE SCHILLER

B.S., UNIVERSITY OF WISCONSIN, 2007

M.S., UNIVERSITY OF COLORADO, 2012

A THESIS SUBMITTED TO THE

FACULTY OF THE GRADUATE SCHOOL OF THE

UNIVERSITY OF COLORADO IN PARTIAL FULFULLMENT OF THE

REQUIREMENT FOR THE DEGREE OF

DOCTOR OF PHILOSOPHY

DEPARTMENT OF AEROSPACE ENGINEERING SCIENCES

2015

THIS THESIS ENTITLED:
UNDERSTANDING ENHANCEMENTS IN OUTER RADIATION BELT ELECTRONS THROUGH MEASUREMENTS AND MODELING
WRITTEN BY QUINTIN GEORGE SCHILLER
HAS BEEN APPROVED FOR THE DEPARTMENT OF AEROSPACE ENGINEERING SCIENCES

_____

PROFFESSOR XINLIN LI

_____

PROFFESSOR DAN BAKER

_____

PROFFESSOR HUMBERTO GODINEZ

_____

PROFFESSOR DELORES KNIPP

_____

PROFFESSOR SCOTT PALO

DATE: AUGUST 19TH, 2015

THE FINAL COPY OF THIS THESIS HAS BEEN EXAMINED BY THE SIGNATORIES AND WE FIND

THAT BOTH THE CONTENT AND THE FORM MEET ACCEPTABLE PRESENTATION STANDARDS OF

SCHOLARLY WORK IN THE ABOVE MENTIONED DISCIPLINE

SCHILLER, QUINTIN GEORGE (PH.D., AEROSPACE ENGINEERING SCIENCES)

UNDERSTANDING ENHANCEMENTS IN OUTER RADIATION BELT

ELECTRONS THROUGH MEASUREMENTS AND MODELING

THESIS DIRECTED BY PROFESSOR XINLIN LI

Electrons in Earth's magnetosphere typically originate with energies below ten kiloelectron volts (keV). Electrons trapped in the radiation belts can have energies that exceed 10 MeV and must be naturally accelerated within Earth's magnetosphere. Still, the processes that govern this highly dynamic region are not fully understood. The outer radiation belt is not only a scientific puzzle but understanding it is an operational necessity, as these high energy electrons are capable of damaging spacecraft and can even result in spacecraft failure. In this work, we investigate our ability to observe these particles and understand the natural acceleration processes that generate them. We approach the problem on three fronts: (i) from an instrumentation perspective we develop a first-of-its-kind miniaturized particle telescope flown on a CubeSat platform, (ii) from an observational perspective we investigate in detail an outer belt enhancement case-study, and (iii) from a modeling perspective we develop a data assimilation model to better understand the mechanisms causing the acceleration. Finally, we construct an event-specific method to estimate electron lifetimes for diffusion models using CubeSat data, and use it to fully investigate the case study using the assimilative model, ultimately combining the three approaches. The ensuing results substantiate CubeSats as scientific observatories, demonstrate new data assimilation applications to the radiation belts, and strengthen our understanding of magnetospheric dynamics and the role of acceleration mechanisms.

FOR MOM AND DAD

WHOM, WITH UNCONDITIONAL LOVE AND SUPPORT,

ENSURE EVERY DOOR I STUMBLE ACROSS IS UNLOCKED

Finally, and most importantly, Georgia is a friend, a wife, a mother, and inspires me to be as exemplary as she is.

TABLE OF CONTENTS

CHAPTER 6: New Event-Specific Electron Lifetimes for Radial Diffusion
Models   229

CHAPTER 7: Summary, Conclusions, and Future Work   251

TABLES

CHAPTER 1: Introduction

NONE

CHAPTER 2: Relevant Background

NONE

CHAPTER 3: Measuring Relativistic Particles

CHAPTER 4: Observing a Non-Storm Enhancement

NONE

CHAPTER 5: Using Data Assimilation to Investigate Source Parameters

CHAPTER 6: New Event-Specific Electron Lifetimes for Radial Diffusion Models

NONE

CHAPTER 7: Summary, Conclusions, and Future Work

NONE

FIGURES

CHAPTER 4: Observing a Non-Storm Enhancement

CHAPTER 5: Using Data Assimilation to Understand Source Parameters

CHAPTER 6: New Event-Specific Electron Lifetimes for Radial Diffusion Models

CHAPTER 7: Summary, Conclusions, and Future Work

NONE

CHAPTER 1

INTRODUCTION

The region dominated by Earth's internally generated magnetic field, known as the magnetosphere, is an extraordinarily complex system. The spatial and temporal regimes alone extend over many orders of magnitude. Additionally, there exist several distinct plasma populations that interact with each other, and Earth's magnetic field, to create an intricate and fascinating system.

As society becomes increasingly more reliant on space-based technology, the need to understand the environment inside Earth's magnetosphere becomes pressing. Conditions in the geospace system, or space weather, can be compared to terrestrial weather. Just as terrestrial weather must be understood and predicted to mitigate the risk to aircraft and pilots, space weather must be as well to protect spacecraft and astronauts. The necessity to understand and forecast the complex system echoes our reliance on the assets it contains.

A population of particles that are especially damaging to spacecraft are the electrons that comprise Earth's Van Allen radiation belts. Of particular interest is the outer radiation belt, which is comprised of high-energy electrons (~100 keV to several MeV) whose fluxes can fluctuate by many orders of magnitude. The heart of the belt resides roughly between 3-7 Earth radii at the equator and overlaps with a number of spacecraft orbits; most notably GPS and

geosynchronous orbits. The outer belt electrons can pose a significant threat to spacecraft electronics systems via surface or deep-dielectric charging.

High energy particles in the radiation belts are a scientific conundrum. They originate either from the sun in the form of the solar wind (at most 10 keV), or from the Earth in the form of atmospheric escape (~ 1 eV). Physical processes in the magnetosphere are capable of acceleration, thus enhancing the fluxes of, the radiation belts on timescales from minutes to days. Thus, understanding Earth's natural particle accelerator is both a scientific puzzle and an operational necessity.

Despite decades of research, the physical processes controlling the flux of outer belt electrons are not well understood. There is a number of competing processing that determine the net flux. These processes can be broadly grouped into acceleration, loss, or transport mechanisms. Furthermore, due to the random quantum mechanical nature of electron-matter interactions, the ability to accurately observe the particles is a challenge. Scientists and engineers continue to strive towards better instrumentation, ultimately searching for the perfect particle telescope, which may not even exist.

The work in this thesis addresses electron dynamics in the outer belt from three different approaches. The first approach regards observing the particles from a novel instrument platform, the second uses particle data to analyze in detail an acceleration event, and the third uses a data assimilation technique to extract information about the acceleration mechanisms.

First, in Chapter 2 I present a brief introduction to the terrestrial magnetospheric system, including particle and wave populations that comprise it, and mechanics that are believed to control the dynamics of the outer radiation

belt. In particular, I focus on the processes that transport particles throughout the system, cause particles to be lost, and accelerate electrons to relativistic energies. I then present a brief discussion of the importance and difficulty of accurately observing energetic particles, and various platforms that have been used to do so. I finalize the chapter with an overview of modeling the radiation belts using the Fokker-Planck equation, including models that incorporate data assimilation. This overview serves to provide the general context for the outer Van Allen radiation belt, the dynamic electron populations that comprise it, and situations that affect the flux of relativistic electrons, the latter of which are the focus of this thesis.

Measuring energetic particles is extremely challenging. Despite decades of experience, there remain difficulties yet to overcome. One approach to improve measurements is to augment existing technology, sometimes making it more massive and power hungry. An alternative to this approach is to make smaller, more specialized detectors, with the hope that they require less mass, power, and financial resources, but at the cost of losing some functionality. In Chapter 3 I introduce the Relativistic Electron and Proton Telescope integrated little experiment (REPTile), a miniaturized version of the Relativistic Electron-Proton Telescope (REPT). REPTile was developed at the University of Colorado (CU) with mentorship from the CU Aerospace Engineering Sciences Department (AES) and the Laboratory for Atmospheric and Space Physics (LASP). REPTile is a unique instrument in that was designed to fly onboard the Colorado Student Space Weather Experiment (CSSWE) CubeSat. It has been modeled and tested with unprecedented detail to verify the instrument's performance despite the stringent resource limitations inherent in a CubeSat platform. I step through my

role on the project, which bridges the entire lifecycle of the instrument, from conceptual design to scientific results, to show that REPTile is a novel telescope design that produces publication-quality science.

Chapter 4 is dedicated to using REPTile observations, as well as measurements from two additional spacecraft (Time History of Events and Macroscale Interactions during Substorms [THEMIS] and the Van Allen Probes), to perform a detailed analysis of a particularly interesting outer belt electron enhancement event. The findings are unexpected, as the associated geomagnetic activity was negligible and typical enhancements are associated with geomagnetic storms. The results of the analysis demonstrate an exception to the traditional view that geomagnetic storm conditions are necessary to result in large outer belt enhancements. Furthermore, the results substantiate theories that distinguish between the relative importance of geomagnetic storms and substorms for acceleration processes.

Chapter 5 discusses various approaches of using data assimilation to understand acceleration events. In particular, the data assimilation combines a physical model, which describes radiation belt dynamics, with in-situ observations of the electron population, to provide an estimate of the system that is superior to either the model or the observations independently. Moreover, I present in detail a new approach to extract additional information about the physical processes that cause the electron enhancements; in particular the intensity, location, and radial extent of the source region.

In Chapter 6 I present a new technique to estimate electron lifetimes using CSSWE observations. As the event-specific estimates presented are obtained from REPTile measurements, they are more accurate than, for example,

commonly used statistically-derived timescales. Furthermore, Van Allen Probe wave measurements are used to derive transport coefficients for the particles. The electron lifetimes and diffusion rates can be applied to radial diffusion models, and are done so in an improved version of the data assimilation algorithm presented in the previous chapter. The data assimilation is performed on the non-storm time enhancement event presented in Chapter 4 to estimate the intensity, location, and radial extent of the particle acceleration. With the best possible estimates of loss and transport timescales, our confidence in the acceleration parameters is high. This work produces simultaneous, quantitative estimates of loss, transport, and acceleration mechanisms and the relative contribution from each.

Finally, I conclude the thesis by summarizing the work completed, and subsequent conclusions drawn, in Chapter 7. Additionally, I note that work is still required to complete current outstanding studies. I also present ideas for potential extensions to the core studies that constitute this thesis. As a whole, the core work advances our understanding of radiation belt electron dynamics and, in particular, the outer belt source region for storm and non-storm time events.

CHAPTER 2

RELEVANT BACKGROUND AND THEORY

2.1 The Earth's Inner Magnetosphere

The sun spits forth an omnidirecitonal slew of charged particles called the solar wind. They carry with them a magnetic field called the interplanetary magnetic field (IMF). These particles flow outward, like a stream downhill, until they encounter an object that obstructs them. In the case of the Earth, this object is the magnetic field generated deep inside the Earth's core. Like the stream around a boulder, the solar wind is diverted around the Earth. The resulting cavity, inside of which Earth's magnetic field dominates rather than the solar wind and IMF, is known as Earth's magnetosphere. At the subsolar point the balance of solar wind flow pressure and Earth's magnetic field pressure determines the location of the boundary, known as the magnetopause. While typically the force balance places the magnetopause at ~10 Earth radii (R_E = 6371 km), its exact location is highly variable. During periods of increased solar wind velocity and/or density the magnetopause can be compressed inside of geosynchronous orbit (~6.6 R_E), although such strong events are uncommon. While the solar pressure compresses Earth's intrinsic dipole field on the dayside, the magnetopause stretches for hundreds of R_E down the tail.

The solar wind and IMF interact with Earth's magnetosphere and produce a highly dynamic system. The result is a number of distinct particle populations

that overlap each other in space and energy, but each has unique dynamical characteristics. Starting from lowest energy, the particle populations in the inner magnetosphere that I cover here are the ionosphere, the plasmasphere, the ring current, and the radiation belts.

2.2 Particle Populations

The ionosphere is very low energy, with particles temperatures in the few hundreds of Kelvin. It begins near 90 km in altitude above the surface of the Earth and extents to ~500 km. The electron densities in the ionosphere range in magnitude, but peak roughly around 10^5 [$\#/cm^3$]. Despite the nomenclature, the ionosphere is only ~1% ionized, and the plasma here is dominated by the neutral population. The height profile of ionospheric constituents is diagrammed in Figure 1. The ionosphere is relevant for radiation belt studies from both the electric fields perspective, because many of the magnetospheric current systems close through the ionosphere, and also from the particle perspective, as the ionosphere can populate the inner magnetosphere via ionospheric outflow and the magnetosphere can deposit large amounts of energy into the polar regions via particle precipitation.
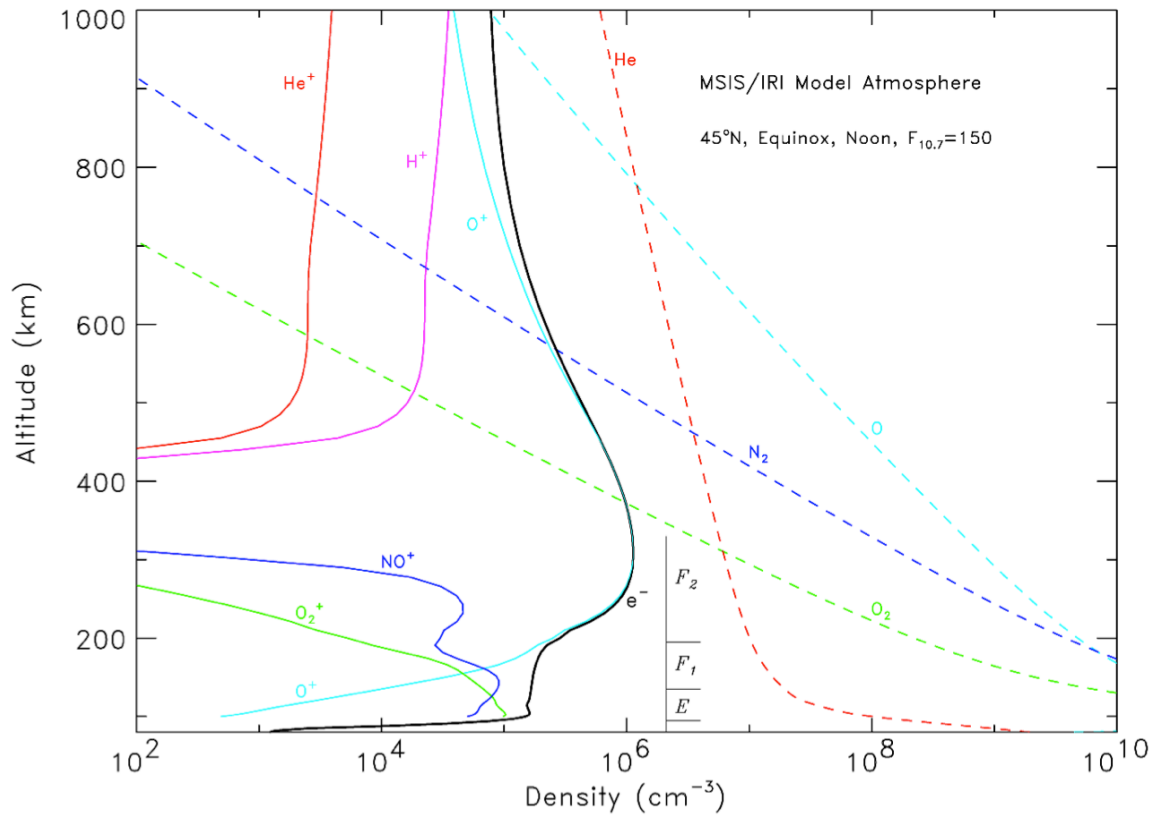
Figure 1: The ionosphere constituents as a function of height from the MSIS/IRI atmospheric model.
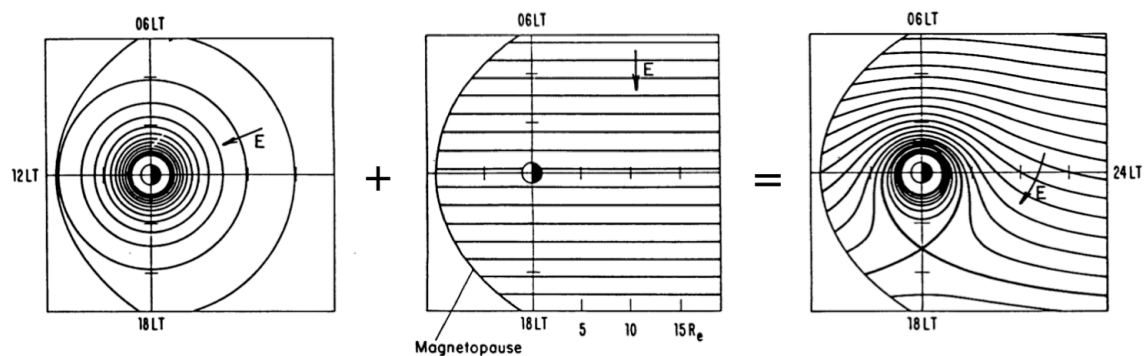
Figure 2: Corotational (left), convective (middle), and net (right) electric fields. Adapted from *Lyons and Williams* [1984].

Slightly higher in energy than the ionosphere is the plasmasphere, which is a region consisting of cold (~ 1 electron Volt [eV]), dense (~10^3 [#/cm^3]) plasma. Interestingly, even though the plasmasphere is only ~10% iononized, the dynamics in the plasmasphere are dominated by the plasma. The plasmasphere is roughly symmetric about the Earth, and extends to distances of ~6 R_E during geomagnetically quiet conditions. During geomagntically active conditions, the plasmasphere loses its symmetry and can be compressed within ~2 R_E. It is comprised mostly of hydrogen ions, but He$^+$, N$^+$, N^{2+}, O$^+$, and O^{2+} have also been observed. Earth's corotational electric field (Figure 2, left panel) dominates close to the Earth, where the plasmasphere tends to corotate about the Earth. However, the corotational field strength decreases with radial distance. At further distances from the Earth the convective electric field (Figure 2 middle panel) dominates, which causes particles to flow sunward. Somewhere inbetween, a boundary exists where the corotational field is equal to the convective field. This seperatrix is diagrammed in the right panel of Figure 2. Inside this separatrix plasma tends to co-rotate about the Earth and outside particles convect sunward and are ultimately lost through the magnetopause.

During geomagntically quiet conditions, this separatrix is the boundary between trapped and lost populations. A steep density gradient at the boundary between the trapped and lost populations represents the outer limit of the plasmasphere and is called the plasmapause. During geomagnetically active times, convection can be enhanced, and the separatrix moves radially inward. During these conditions, part of the plasmasphere can be transferred from a co-rotational state to a convective state, and a drainage plume is formed on the
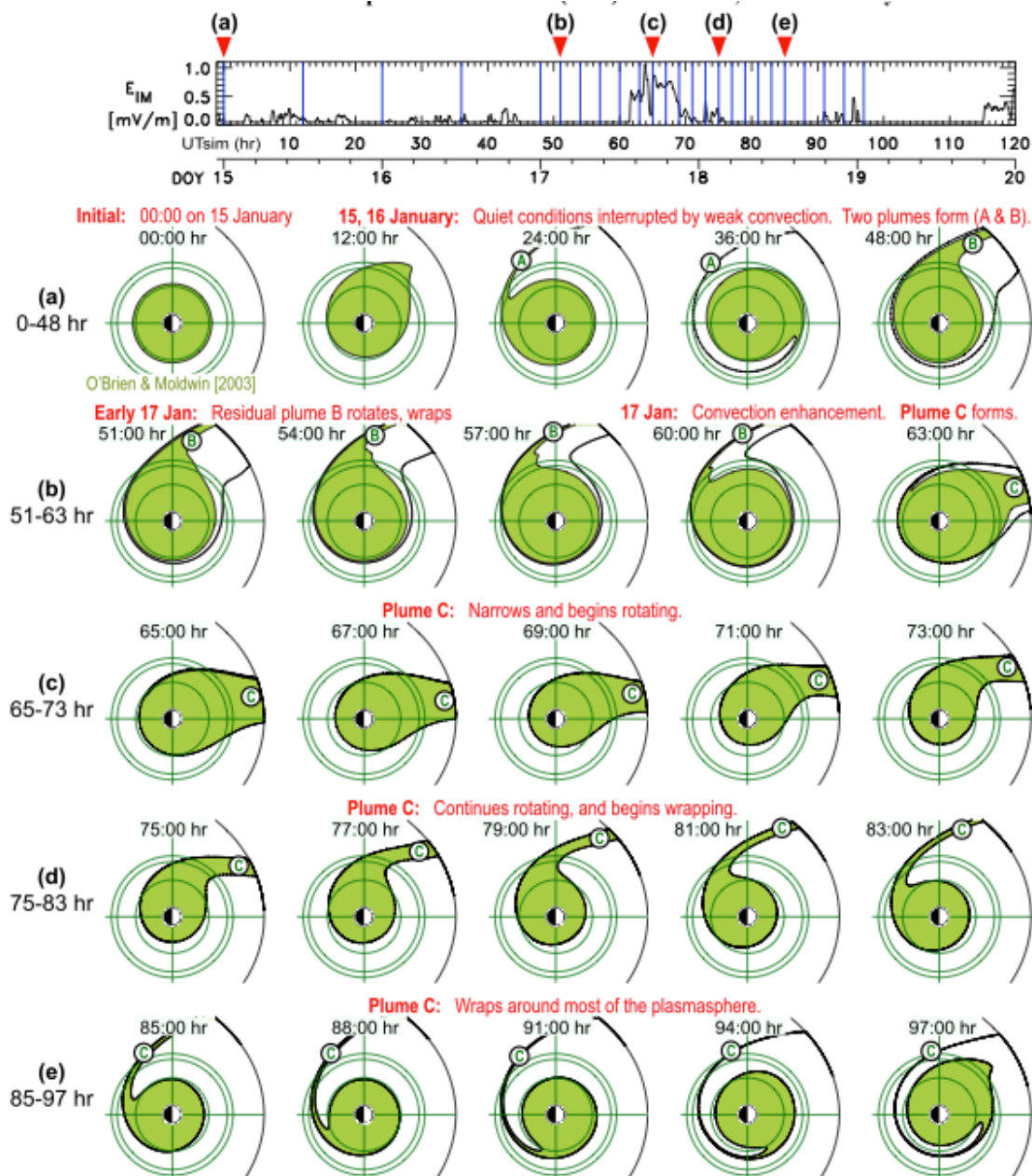
Figure 3: Overview of plasmapause evolution from Jan 15-20, 2013, using test particle simulations. Image from *Goldstein et al.* [2014].

dusk-side as plasma convects sunward. *Goldstein et al.* [2014] simulate the evolution of the plasmapause from Jan. 15-20, 2013 in Figure 3. Strong plume structures can be seen in rows a), c), and d), but the overall morphology of the plasmasphere is as complex as the solar wind and IMF conditions that drive it.

The plasmasphere is relevant to the radiation belts as large temperature anisotropies in the presence of cool plasmaspheric plasma can provide the free energy needed to dampen or enhance wave growth. The waves, in turn, can cause enhancements or depletions in the radiation belts. Thus, the plasmapause can represent a boundary between wave regimes.

Often overlapping in physical space with the plasmasphere is the ring current. The ring current consists of electrons and ions from 10 to 100s keV in energy. The ring current is more tenuous than the plasmasphere, with densities of 10-1000 [#/cm^3]; however, the density of ring current is highly dependent on geomagnetic conditions, since the particles stem from inward transport of particles that originate in the tail. During periods of geomagnetic activity, particles are transported in sudden bursts, called substorms, as the tailward field depolarizes and injects tail plasma into the inner magnetosphere. During this process, the particles undergo a charge-dependent drift around the Earth; electrons drifting eastward and ions westward. With the separation of charges a current is created, which is called the ring current. The ring current can create an inductive magnetic field that opposes Earth's internal field. In fact a measurement of this - the variation of Earth's equatorial surface field to infer the presence of ring current particles - is used as a proxy for geomagnetic activity.

Ring current particles contain the bulk of the energy density in the inner magnetosphere (see *Zhao et al.* [submitted] and references therein). They also provide a particle population that waves can interact with to accelerate to radiation belt energies. In this respect, the ring current particles can be known as the 'seed' population, as they are the particles that can grow to ultrarelativistic energies that population the outer belt.

Finally, the most energetic particles in the inner magnetosphere are those that comprise the Van Allen radiation belts. The radiation belts are torodial regions of space that are dominated by either relativistic protons (the inner belt – 1-2 R_E), or energetic electrons (the outer belt[s] – 3-7 R_E). The author would like to note that the inner belt, while typically viewed as a dominated by protons, does have a significant energetic electron population of energies <0.5 MeV [*Li et al.*, 2015; *Fennel et al.*, 2015]. While the traditional view suggests only one outer electron belt is present, recent findings spearheaded by *Baker et al.* [2013] show that a two, or even three [*Kellerman et al.*, 2014], outer belt structures are observed. A slot region separates the inner and outer belts. While the location and the extent of the slot depends on particle energy, the slot typically is seen between 2-4 R_E where particle fluxes are extremely low. The work in this thesis is in regards to the energetic and relativistic electrons that populate the outer belt, which have energies ranging from 100 keV to >15 MeV.

The outer belt is of particular interest because of its high variability. The fluxes can increase or decrease many orders of magnitude over the course of hours. Typically, enhancements are associated with strong geomagnetic storms. One of many examples is a study by *Reeves et al.* [2013], who showed a 2.5 MeV electron increase of over two orders of magnitude in 12 hours associated with a strong geomagnetic storm signature (-110 nT Dst). However, recent studies reemphasize the significance of enhancements without a strong storm signature; such as *Schiller et al.* [2014], who showed a similar increase across multiple energy channels (0.6 – 1.3 MeV) during a period with no storm signature (-29 nT Dst), or *Su et al.* [2014], who showed a less intense enhancement also associated
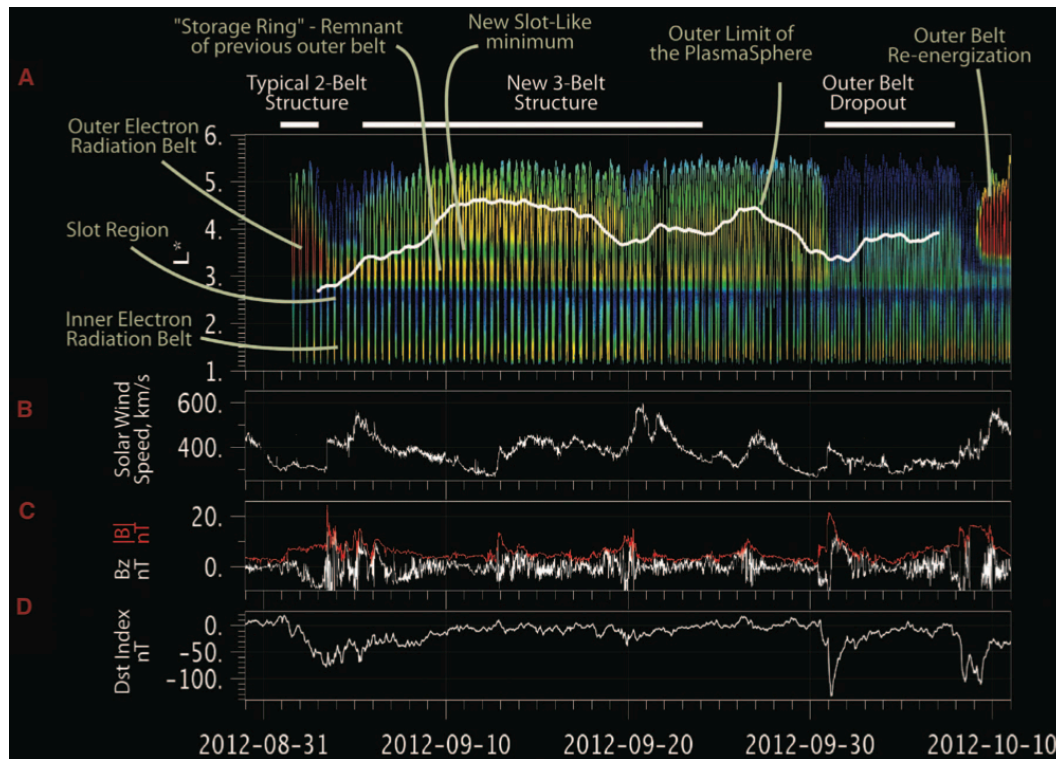
Figure 4: Radiation belt dynamics for a ~1 month period exhibiting typical complexity. Panel a) shows the log of 4.5 MeV electron fluxes, covering 3.5 orders of magnitude, with the plasmapause overplotted in white. *Baker et al.* **[2013].**

with a very small storm signature (-35 nt Dst). The causes of these large enhancements and the conditions required for them are not well understood.

The outer belt's inconsistent response to geomagnetic storms is exemplified in *Baker et al.* [2013] and shown in Figure 4. During this ~40 day period in the Fall of 2013, the Van Allen Probes measured three geomagnetic storms on September 1, September 30, and October 9. All three storms had drastically different effects on the outer radiation belt. The September 1 storm removed the outer half of the belt and created an interesting double outer belt feature. The September 30 event completely depleted the outer belt, and the October 9 double-dipped storm enhanced the radiation belt fluxes to levels
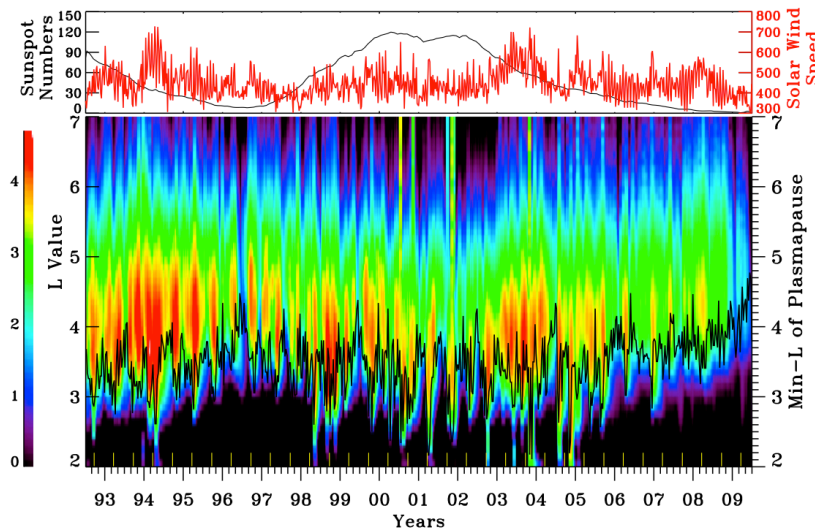
Figure 5: Radiation belt variability over the course of a solar cycle. The top panel displays yearly averaged sunspot number (black) and weekly averaged solar wind speed in km/s (red). The bottom panel shows monthly averaged electron log flux of 2 - 6 MeV electrons [#/cm2/s/sr] as measured by the SAMPEX spacecraft. The y-axis corresponds to the radial distance of equatorial crossings of the field line occupied by SAMPEX. The black curve is the 10-day minimum plasmapause location. Image from *Li et al.* [2011].

higher than when the period began. Why seemingly similar storms have such different effects on the belts is not well understood.

The radiation belts are highly dynamic on decade timescales as well. Figure 5 shows the highly relativistic electron population (2-6 MeV) as measured by the SAMPEX [*Baker et al.*, 1993] spacecraft for the first 18 years of its 20-year mission [*Baker et al.*, 2012]. During this time, it is clear that the heart of the electron population regularly fluctuates over four orders of magnitude during this period, with the lowest fluxes occurring during solar minimum (1995 – 1997 and 2007 onward) and largest fluxes during the maximum (1993 and 2000 – 2002) and declining phase of the solar cycle (1993-1995 and 2002 – 2007).

These decade-level variations are caused by the solar events that drive the system. Two prominent solar disturbances are coronal mass ejections (CMEs),

which are more common during solar max, and corotating interaction regions (CIRs), which are prevalent during the declining phase. Each has a different affect on the magnetosphere (see *Borovsky and Denton* [2006]*)*, in part contributing to the solar cycle dependence of the radiation belts. While significant progress has been made in this area, the community still lacks an ability to consistently predict the response of the radiation belts for individual solar drivers.

This idea – to predict and forecast radiation belt response for unique and real-time solar wind conditions – is the ultimate operational goal. Progress has been made, for example, by *Li* [2004], *Turner and Li* [2008]*, Turner et al.* [2011], *Kellerman et al.* [2013], and *Hartley et al.* [2014], who use solar wind velocity (V_{sw}), the north-south component of the IMF (IMF B_z), or solar wind density to significantly outperform persistence models to predict GEO fluxes out to 24 and 48 hours. However, each of these techniques perform better or worse during different solar phases, implying a gap in our understanding of the solar-terrestrial coupling.

As previously stated, the radiation belt response to individual drivers is highly variable. A well-cited study by *Reeves et al.* [2003] demonstrates that, using only a storm-time signature of Dst < -50 nT, half of the 276 storms between 1989 and 2000 produced an electron enhancement at geosynchronous orbit. One quarter resulted in no change, and the remaining quarter resulted in a net depletion. The complex response of the radiation belts is a delicate balance between effects that add, remove, or transport particles throughout the system. The resulting flux observed in the radiation belts is dictated by which of these processes dominate for a given event. Before we discuss these ideas (source, loss,

and transport mechanisms) in detail in Section 2.4, we must first present how charged particles move in the presence of a magnetic field.

2.3 Charged Particle Motion

The fundamental nature of plasma is that it can obey the laws of electrodynamics in addition to Newtonian forces. That is, it has a very complex interaction with itself, other nearby plasmas, and background magnetic and electric fields. The relativistic Lorentz force law describes a particle's motion:

Equation 1: Lorentz force law

$$\frac{dp}{dt} = q\gamma \left(E + v \times B \right)$$

where p is the relativistic momentum, q is the charge of the particle, E is the local electric field, B is the local magnetic field, v is the particle velocity, and γ is the relativistic correction and is equal to $\left(1 - \frac{v^2}{c^2} \right)^{-\frac{1}{2}}$, with c being the speed of light.

When in the presence of a uniform magnetic field the particle will undergo two motions. If it has a velocity parallel to the magnetic field vector, the particle will travel along the magnetic field line. If there is some component of the velocity perpendicular to the magnetic field direction, the particle will also gyrate around the magnetic field line. This fundamental motion is the first of three, and is termed the gyromotion.

If the background magnetic field is non-uniform, the particle will exchange energy between the parallel and perpendicular (to the magnetic field vector) directions to conserve its magnetic moment, μ, where

Equation 2: 1st adiabatic invariant

$$\mu = \frac{mv_\perp}{2B}$$

such that m is the mass of the particle and $v_\perp$ is the velocity component that is perpendicular to the magnetic field vector. μ will be conserved so long as the changes to the system occurs on timescales significantly longer than the gyroperiod itself. Thus, μ is also known as the first adiabatic invariant because of this conservation. Furthermore, as the background magnetic field changes, the conservation of μ describes how the particle will exchange momentum in the perpendicular and parallel directions. For reference, the gyroperiod of a typical outer belt particle in a dipole field is on the order of 10^{-3} seconds: a 1 MeV electron with 90 degree pitch angle at L = 5 has a gyroperiod of 0.0004s [*Roederer, 1970*].

For every particle, there is a background magnetic field magnitude sufficient to convert entirety of the particles momentum into the perpendicular direction. Based on the configuration of the background field and the centripetal component of the force acting on the particle, the particle can reverse its direction and travel in the opposite direction on the field line. This point, where the particle motion changes from parallel to anti-parallel (or vice-versa), is known as the mirror point, and has strength defined as

Equation 3: Magnetic mirror

$$B_m = \frac{B_{eq}}{\sin^2 \alpha_{eq}}$$

Here, B_m is the magnetic field strength of the mirror point, B_{eq} is the minimum magnetic field strength the particle encounters in the magnetic trap (in the magnetosphere, this typically occurs near the magnetic equator), and α_{eq} is the pitch angle of the particle at the minimum magnetic field strength, and is defined as $\tan^{-1}\left(\frac{v_\perp}{v_\parallel}\right)$.

In a dipolar field, such as that exists in the magnetosphere, the particles can be trapped between two magnetic mirror points, which occur over the north and south poles. If the particles are trapped, they can bounce between the two mirror points. (It is of note that if a mirror point is too close to the Earth's surface, the particle has a very high chance of colliding with neutrals in the atmosphere, which results in the particle being lost from the system. The likelihood of a collision becomes significant near altitudes of ~100km, but varies depending on the neutral atmospheric density profile.) This bounce motion is associated with the second adiabatic invariant, K, which is defined as

Equation 4: 2ⁿᵈ adiabatic invariant

$$K = \int_{s_m'}^{s_m} [B_m - B(s)]^{1/2} \, ds$$

where s_m is the point in physical space where the mirror occurs, and s'_m is the point in the conjugate hemisphere. This invariant will also be conserved if the changes to the background magnetic field are much slower than that of the bounce motion. For reference, the bounce period of a typical outer belt particle in a dipole field is on the order of 10^0 seconds: a 1 MeV electron with 60 degree pitch angle at L = 5 has a bounce period of 0.37s [*Roederer*, 1970].

The final motion associated with an adiabatic invariant is the drift motion, which is caused by two different mechanisms that have compounding results. The first is the gradient-$B_\perp$ drift (whereas the gradient-$B_{||}$ contributes to the bounce motion). The magnetic field strength is inversely proportional to the cube of distance, so a particle gyrating around a field line will feel a different magnetic field as its gyration carries it closer and further from the dipole. As the background magnetic field strength changes throughout at gyroperiod, so does the particle's gyroradius. This results in a drift perpendicular to the gradient in the magnetic field – or in an east-west direction.

The second contributor is the curvature drift, which is caused by the curved nature of a dipolar magnetic field line. Similar to the gradient-$B_{||}$ drift, the particle feels a centripetal force perpendicular to the curve as it travels along a field line. The particle reacts to this force by making the perpendicular component of the electric field go to zero in the particle's frame, which results in a drift perpendicular to the field curvature – or in an east-west direction. The two drifts combined are known as the gradient-curvature drift.

The invariant associated with this drift ensures that the magnetic flux enclosed by the particle's drift path remains constant, and similar to the other

invariants, is conserved so long as the changes to the field are on a longer timescale than the invariants themselves. The third invariant is defined as

Equation 5: 3rd adiabatic invariant

$$\Phi = \oint A_\phi \, dl$$

where A is Earth's magnetic vector potential and dl is the curve along which the particle's guiding center drift shell lies. This invariant can be written more intuitively as

Equation 6: L*

$$L^* = \frac{2\pi M}{\Phi R_E}$$

where M is the magnetic moment of Earth's dipole field. The L* parameter is the radial distance at the equator the particle would be found if in a purely dipole field, as defined by *Roederer* [1970]. For reference, the drift period of a typical outer belt particle in a dipole field is on the order of 10^3 seconds: a 1 MeV electron with 90 degree pitch angle at L = 5 has a drift period of 788s [*Roederer, 1970*]. An excellent review of adiabatic invariants can be found in *Green and Kivelson* [2004].

Instead of traditional coordinates to describe a particle's position and velocity (x, y, z, v_x, v_y, v_z), one can also use phase space coordinates (PSC). In this case, a particle is assigned their associated adiabatic invariants (μ, K, L*) and the phase of each motion they are in (Φ_μ, Φ_K, Φ_{L^*}). It is common to average over the

phase of each motion and reduce the six-dimensional space to three-dimensions, simply µ, K, and L*. One can also convert electron flux into phase space density (PSD) by the equation

Equation 7: Phase space density

$$f = \frac{j}{p^2}$$

where f is the electron phase space density, j is electron flux, and p is the momentum of the electron. The resulting PSD is a function of µ, K, and L*, and is written as f(µ, K, L*) [*Schulz and Lanzerotti,* 1974].
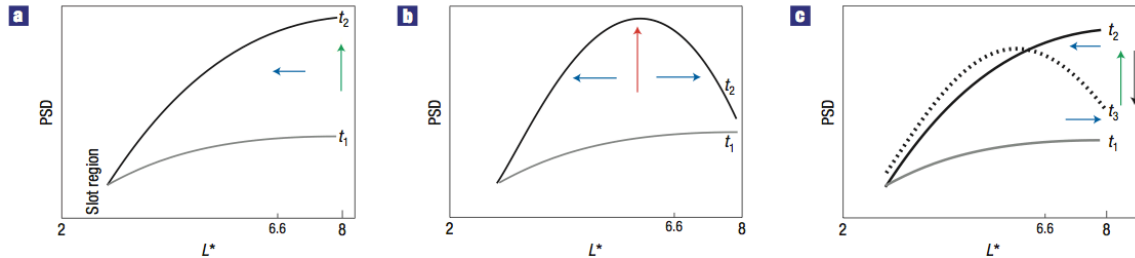
Figure 6: Schematic comparing an increase in PSD from inward radial diffusion (a) to local acceleration (b). A variable outer boundary, however, can also explain a local peak in PSD (c). Image from *Chen et al.* [2007].

Electron PSD can often be a more useful quantity than flux. Whereas flux measurements are for fixed energy, there can be flux increases or decreases that do not correspond to real losses or enhancements; the particles can simply be changing energy (or pitch angle or radial distance) to conserve their adiabatic invariants.   Thus, increases and decreases in flux measurements do not

necessarily correspond to real losses or gains of particles. Phase space densities can distinguish between processes that conserve the invariants and processes that break the invariants and result in real losses or accelerations, that is, separating adiabatic from non-adiabatic motion. One purely adiabatic affect that can be disguised with flux losses is known as the Dst effect [*Kim and Chan*, 1997], where compressions and expansions of the magnetosphere result in fully adiabatic changes in flux profiles that appear to match the changes in the Dst index. PSD profiles are often used not only to identify real sources or losses, but also to identify the cause of the enhancement (e.g. local accelerations vs. radial transport, see Figure 8) or loss (magnetopause shadowing or wave-particle interactions) as discussed in Section 2.4.

Without dynamic changes to the background magnetic field, all particles would conserve these three invariants. However, the magnetosphere is a variable place and driven by processes that occur on very short timescales, sufficient to violate all three invariants simultaneously. The results make the magnetosphere a spectacularly interesting scientific puzzle, and at the core are wave-particle interactions – a key mechanism for violating the invariants.

2.4 Wave-Particle Interactions

The net flux of relativistic electrons observed by a spacecraft is a result of the delicate balance between transport, loss, and source mechanisms that simultaneously influence the particles in the magnetosphere. Although the relative causes and contributions of each process not fully understood, here we will briefly provide an overview of the different mechanisms that are associated with each process.

2.4.1 Radial Transport

Radiation belt particles ultimately originate from either the solar wind or from the Earth. Transport processes are required to move the particles inward from the tail (originating from the solar wind) or outward from the ionosphere to populate the inner magnetosphere. Particles can be accelerated or decelerated during this process. As inward radial transport is recognized as the most significant source of magnetospheric particles [*Friedel et al.,* 2002], we will focus on transport from the tailward plasma sheet to the inner magnetosphere.

Radial transport requires an electron source population at high L, such as the plasma sheet in the tail of the magnetosphere [e.g., *Ingraham et al.,* 2001]. The plasma sheet represents a source of PSD for the inner magnetosphere for at least a low energy population (~1-100s keV, although the upper energy limit of particle injections continues to be debated [e.g. *Falthammer,* 1965; *Dai et al.,* 2015]). Radial diffusion always acts to smooth the PSD profile. With an outwardly positive PSD gradient, these particles can violate the third invariant and diffuse radially inward, as in Panels a) and b) of Figure 6. Radial transport by diffusion in the third adiabatic invariant is a result of incoherent scattering by the stochastic fluctuating fields at electron drift frequencies and harmonics, such as ULF waves in the Pc4–5 band [e.g., *Falthammer,* 1965; *Fei et al.,* 2006; *Tu et al.,* 2012]. Despite maintaining constant μ, electrons that have their third invariant broken will gain energy as they diffuse radially inwards to regions of increased magnetic field strength.

Another form of transport in the magnetosphere, which can also break particle invariants, is a sudden injection. A sudden injection, which is nondiffusive, can occur from a strong interplanetary shock, for example. Both diffusion and sudden injections are well associated with geomagnetic activity [e.g., *Elkington et al.*, 1999; *Li et al.*, 1993, 2003]. Both also result in a smoothing of the phase space density (PSD) radial profile and thus cannot by themselves create local peaks in PSD.

2.4.2 Loss

Adiabatic effects can cause a decrease in observed electron flux; particles remain in the system but only appear to have been lost. There are a number of ways in which electrons can truly be lost from the inner magnetosphere. The primary processes are magnetopause shadowing, outward radial diffusion, and atmospheric precipitation.

Magnetopause shadowing occurs when an electron encounters the magnetopause and, due to strong local magnetic field gradients, is lost at the outer boundary. As relativistic electrons' drift period is on the order of minutes, a change in location of the magnetopause can very quickly affect the entire radiation belt population. This mechanism has been suggested as a mechanism for flux dropouts, particularly during the main phase of geomagnetic storms [e.g. *Li et al.,* 1997a; *Kim and Chan*, 1997; *Millan and Thorne,* 2007]. Shadowing has recently been shown to have a significant role in magnetospheric dynamics [*Turner et al.,* 2012a], and can occur upon the sudden inward motion of the magnetopause that is typically associated with solar wind pressure pulses (e.g. Figure 6 panel c)).

A second cause of magnetopause shadowing is outward radial diffusion. As mentioned before, radial diffusion transports particles away from the peak in PSD (e.g. Figure 6 panel b)). If some of the PSD gradient is radially negative (that is, the PSD peak is inward of the particles' location), a particle can be transported outward. Particles can be radial transported outward until their drift paths intersect with the magnetopause where they are lost. Outward radial diffusion is also a cause of de-energization of the electrons; since as the particles diffuse outward they experience decreasing magnetic field strength. In order to conserve the first invariant in a region of low magnetic field strength, they must also decrease their momentum and can be 'lost' from the energetic population.

Finally, particles can be lost due to collisions with neutrals in Earth's atmosphere, known as precipitation loss. This happens when an electron's equatorial pitch angle is sufficiently small that its mirror point is below ~100km in altitude, where the likelihood of a collision and ensuing charge exchange with the dense neutral population is high, and it is then considered to be in the bounce loss cone. A number of processes are capable of sending radiation belt electrons into the loss cone. Here we will focus on pitch angle scattering from wave-particle interactions; namely electromagnetic ion cyclotron (EMIC), hiss, whistler mode chorus waves. These waves, and the typical generation regions, are illustrated in Figure 7.

EMIC waves occur in the dusk sector and are much more common during geomagnetic activity [*Erlandson and Ukhorskiy*, 2001]. They are believed to be generated by a ring current temperature anisotropy ($T_\perp > T_\parallel$) associated with proton injections from the tail. Dense, cool plasma, as found in the

plasmasphere, can enhance EMIC wave growth. The waves are typically found near the plasmapause in the dusk sector and the plasma plume in the post-noon sector, or other places where westward drifting protons encounter the plasmapause. They resonate with electrons above a few 100keV, cause pitch angle scattering, and can scatter MeV electrons into the loss cone [*Thorne et al.*, *2005*]. The waves appear at frequencies at or below the local proton gyrofrequency (~0.1 - 5 Hz), and typically are found with stopbands at the O^+, He^+, and H^+ gyrofrequencies. EMIC waves are associated with 'precipitation bands' (following *Blake et al.* [1996]; see *Thorne and Kennel, 1971*), which are longer duration (5-30 s) relativistic electron loss events as observed by LEO satellites, and hypothesized to be an significant contributor to relativistic electron precipitation [e.g. *Blum et al., 2013*].
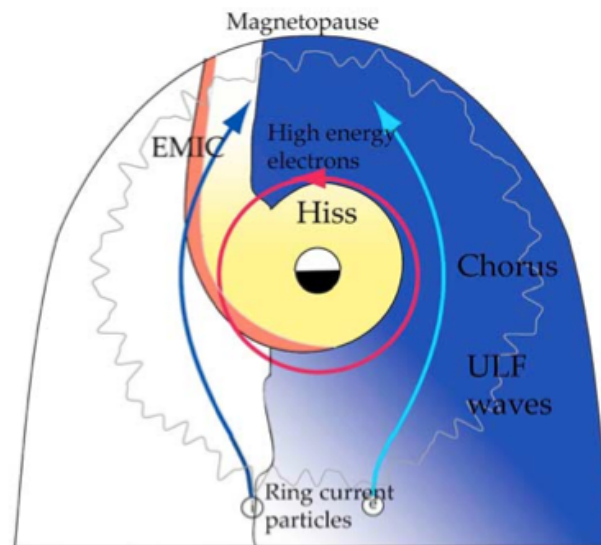
Figure 7: A simplified cartoon showing the basic regions inside the magnetosphere where plasma waves are capable of resonant interactions with relativistic electrons. Whistler mode chorus (blue) and hiss (yellow) waves, as well as EMIC waves (red) and ULF waves (wavy gray) are diagrammed. Image reproduced from *Shprits et al.* [2006b].

Whistler mode hiss is a broadband wave type found inside the plasmapause at all local times (LTs), but is often more intense in the dayside sector. Hiss covers a frequency range from 100 Hz to a few kHz, with maximum power typically in the 100-300 Hz range. Hiss amplitudes are also associated with increased geomagnetic activity [*Meredith et al.*, 2004]. The generation mechanism for hiss is not well understood, but there is evidence from ray-tracing simulations that hiss is an evolution of chorus waves that propagate inside the plasmasphere [*Bortnik et al*, 2008]. Plasmaspheric hiss can scatter with MeV electrons found inside the plasmasphere and cause electron loss timescales from a few to hundreds of days [*Ni et al.*, 2013]. There is good correlation between the plasmapause and the inner edge of the outer radiation belt [*Li et al.*, 2006], confirming hiss is a relevant loss mechanism to relativistic electrons.

Whistler mode chorus waves are unique because they have a dual role; they can cause both loss and enhancements of MeV electrons. They are found outside the plasmasphere, most prominently in the dawn and dayside sectors, and are also highly correlated with geomagnetic activity [e.g. *Bunch et al.*, 2012]. They are believed to be generated by an electron-cyclotron instability associated with plasma sheet electron injections, and are thus most strongly associated with substorm activity [e.g. *Meredith et al.*, 2001]. They occur at or below a harmonic of the local electron gyrofrequency in the range of 100 Hz – 5 kHz. Relativistic electron losses are strongly associated with microburst activity [*O'Brien et al.*, 2004], theorized to be generated by whistlers, but a one-to-one direct correlation between the waves and the precipitation events has yet to be observed.
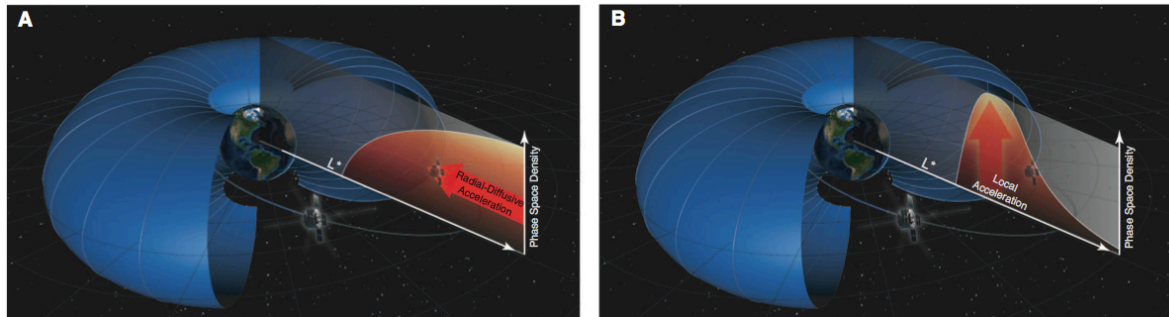
Figure 8: A cartoon from *Reeves et al.* **[2013] that illustrates the two different mechanisms for creating an increase in phase space density: inward radial transport (left panel) or local acceleration (right panel).**

Microbursts are sudden and brief (< 1 s) isotropic scattering events and have been to shown contribute a significant amount to relativistic electron losses [e.g. *O'Brien et al.*, 2004; *Thorne et al.*, 2005 and references therein].

2.4.3 Acceleration

Acceleration mechanisms, which replenish the relativistic electron content, can be classified into two broad categories: inward radial transport and internal acceleration. These mechanisms are illustrated in Figure 8. Radial transport mechanisms can again be broadly classified into two subcategories: radial diffusion and sudden injection, both of which violate the third adiabatic invariant. Radial transport, as previously described, results in a smoothing of the phase space density (PSD) radial profile and thus cannot by itself create local peaks in PSD (see Figure 6).

Local acceleration, on the other hand, is a result of the violation of electrons' first or second adiabatic invariant. Wave activity is the most promising explanation [e.g. *Summers et al.*, 1998; *Millan and Baker*, 2012] for MeV

electron enhancements, with chorus [*Meredith et al.*, 2003; *Thorne et al.*, 2013] and magnetosonic [*Horne et al.*, 2007] waves both likely candidates for acceleration. Unlike radial transport, these mechanisms produce a peak in PSD where the scattering is occurring [e.g., *Chen et al.*, 2007; *Reeves et al.*, 2013]. Both theory and modeling results show that these waves are particularly efficient at accelerating electrons to MeV energies, as discussed below.

Whistler mode chorus, as previously described, is most prominent in the dawn and noon sectors between 0.1 – 1 f_{ce}, where f_{ce} is the local electron gyrofrequency. Chorus waves are theorized to interact with energetic electrons to accelerate them to MeV energies [*Horne and Thorne*, 1998], as long as the resonance condition is met:

Equation 8: Cyclotron resonance

$$\omega - k_\parallel v_\parallel = \frac{m \omega_{ce}}{\gamma}$$

where ω is the chorus wave frequency, $k_\parallel$ and $v_\parallel$ are the components of the wave number and electron velocity parallel to B, respectively, m is the resonance harmonic number, and γ is the relativistic correction factor. A resonant interaction violates the first and second adiabatic invariants and allows for a change in both energy and pitch angle [*Bortnik and Thorne*, 2007].

Magnetosonic waves are found predominantly on the dayside both inside and outside the plasmasphere [*Horne et al.*, 2000] below 0.1 f_{ce} but above the local proton gyrofrequency [*Horne et al.*, 2007]. Magnetosonic wave types can also resonate with the electrons' gyration period to accelerate them to relativistic

energies. Furthermore, both wave types can be excited by anisotropies in a 'source' population (10-100 keV electrons injected from the plasmasheet on the nightside), and can resonate with a 'seed' population (>100 keV electrons, such as ring current particles) to accelerate them to multi-MeV energies [e.g. *Summers et al.*, 1998]. Gyroresonant wave-particle interactions are theorized to be a significant contributor to accelerating electrons to relativistic energies [e.g., *Horne and Thorne*, 1998]. These processes are also well associated with geomagnetic activity [e.g. *Dessler and Karplus*, 1961; *Reeves*, 1998; *Li et al.*, 2001].

Peaks in PSD are often used to diagnose that local acceleration has occurred [e.g. *Turner and Li*, 2008; Reeves *et al.*, 2013; *Schiller et al.*, 2014]. However, care has to be used when using PSD peaks as a diagnostic feature as a dynamic outer boundary can also cause peaks in PSD (see Panel c) of Figure 7) [e.g. *Green and Kivelson*, 2006; *Chen et al.*, 2007; *Turner et al.*, 2012]. Furthermore, relativistic electron enhancements are often the result of multiple simultaneous acceleration and transport processes; one cannot simply assume that only acceleration is occurring, or that only one type of acceleration mechanism is taking place. For example, modeling is often most successful when all the processes are included [e.g. *Li et al.*, 2007; *Tu et al.*, 2009; 2013; 2014; *Shprits et al.*, 2013].

2.5 Observing Charged Particles

Taking in-situ measurements of the radiation belt environment is challenging for a number of reasons. The most obvious drawback is the sheer amount of resources required to put an observatory in orbit. Furthermore, a single observatory takes a very sparse sample of the magnetospheric

populations. The number of spacecraft needed to take global observations, compounded with the cost of developing and launching them, is formidable.

Not only do magnetospheric dynamics cover such a large regime of physical space (~1 - 10^7 m), but particle measurements must be taken over an enormous range in energy (~1 – 10^7 eV), direction (4π sr), and time (10^{-3} – 10^9 s). Recently, with NASA's Magnetospheric Multiscale mission (MMS) joining the ranks of space-based observatories like the five Time History of Events and Macroscale Interactions during Substorms (THEMIS) spacecraft, the two Van Allen Probes, the four CLUSTER spacecraft, POLAR, a slew of geosynchronous satellites, and low-orbit spacecraft like POES and CubeSats, the magnetosphere is finally being observed with resolutions required to definitively answer fundamental questions about the roles of source, transport, and loss.

However, a subtler drawback for taking in-situ measurements of energetic electrons is how the particles behave when interacting with the telescopes themselves; they behave in a quantum-mechanical nature when interacting with matter. That is, each individual interaction is indescribable, but many interactions are describable statistically. The possible outcomes of electron-matter interactions are numerous and include atomic excitation and ionization, bremsstrahlung radiation (where the particle loses energy into the generation of high-energy, such as X-ray photons), dissociation of molecules, and excitation of molecules in the incident material [*Vampola*, 1998]. Any of these processes can result in a large deviation to the particle's incident trajectories, causing them to potentially evade the detecting material all together [*Vampola*, 1998].

There are a number of telescope designs to address the random nature of
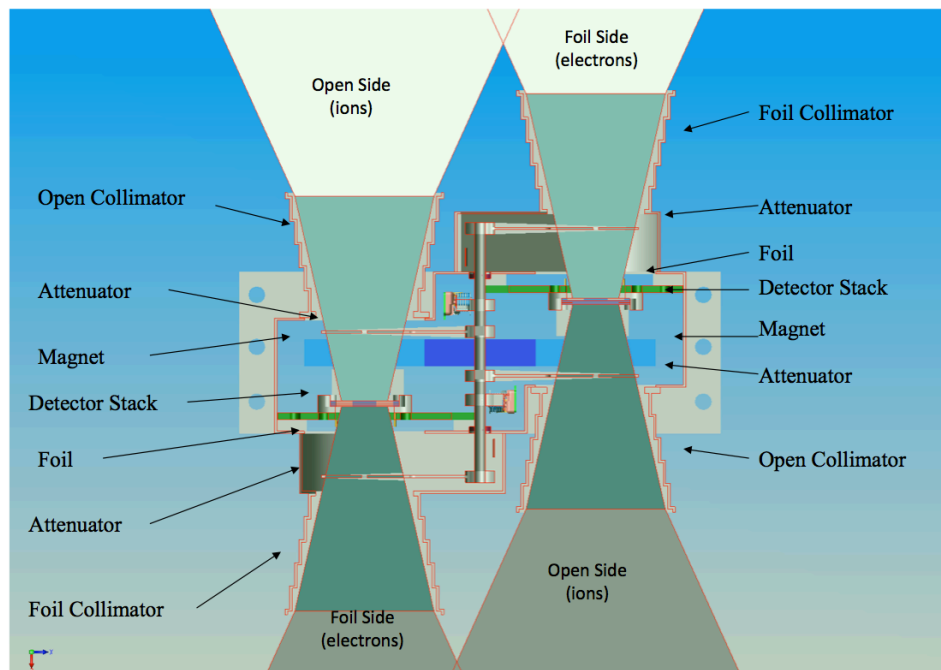
Figure 9: Schematic for the design of the Solid State Telescope onboard THEMIS.
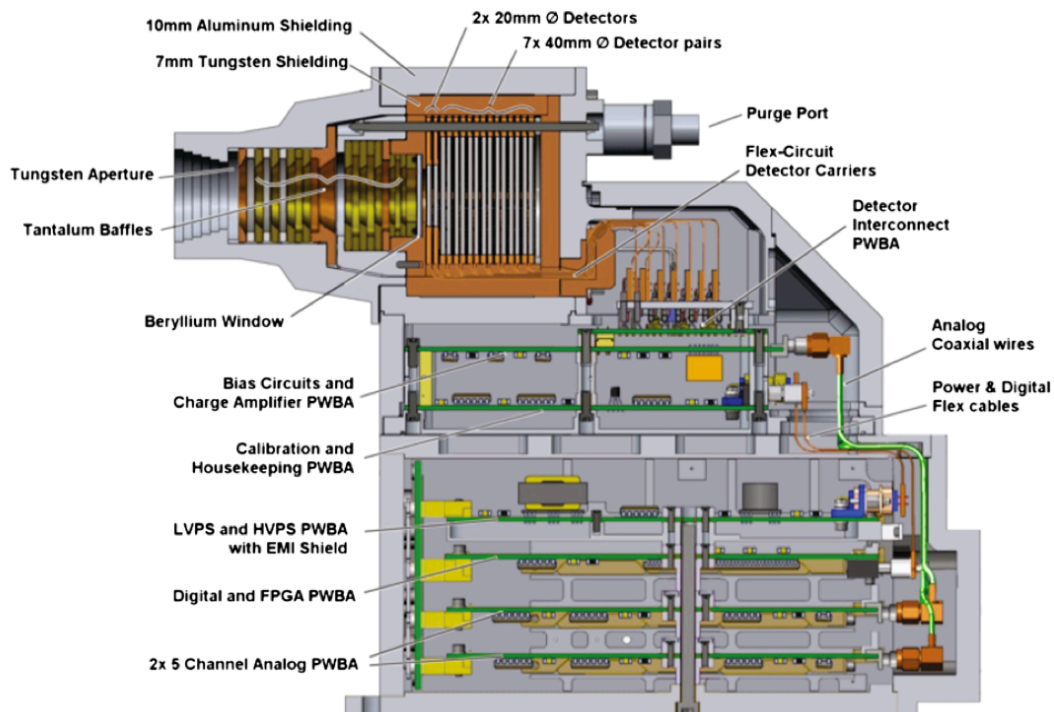
Figure 10: Schematic for the REPT instrument and associated electronics on board the Van Allen Probes
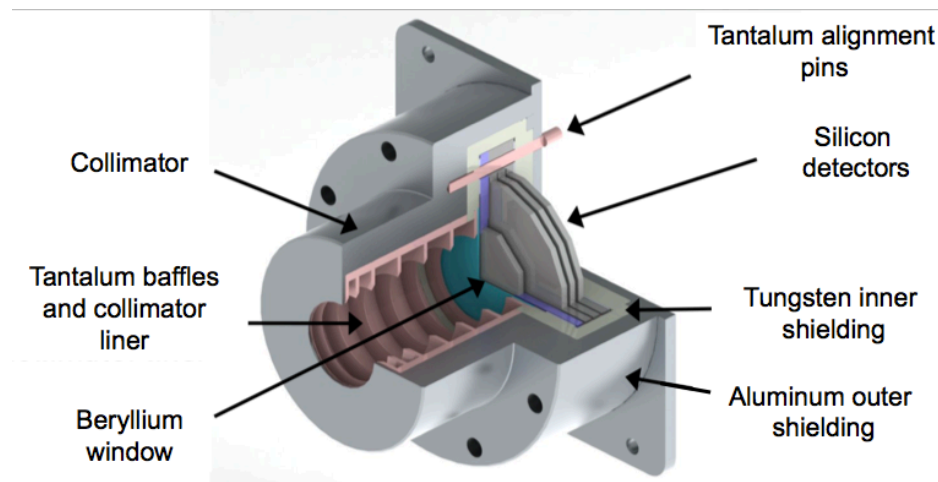
Figure 11: Schematic of the REPTile instrument onboard CSSWE.

electron-matter interactions; such as electro-static analyzers (ESAs), spectrometers, and solid state telescopes. For this work, we will focus on solid state telescopes, as they have been shown to be reliable when observing MeV electrons [*Baker et al.*, 2013]. Notable solid state telescopes are the Solid State Telescope (SST) onboard the THEMIS mission (Figure 9) [*Angelopoulos*, 2008], the Relatvistic Electron-Proton Telescope onboard the Van Allen Probes (Figure 10) [*Baker et al.*, 2013], and the Relativistic Electron and Proton Telescope integrated little experiment (REPTile) onboard the Colorado Student Space Weather Experiment (CSSWE) CubeSat (Figure 11) [*Schiller et al.*, 2010].

For solid state telescopes in particular, it is critical to understand how the instrument responds to the on-orbit energetic electron environment. This is most often done using a combination of modeling, solid-state radiation tests, and particle accelerator beam tests. Modeling is often done using software packages such as Geant4, which was developed by physicists at the European Organization for Nuclear Research (CERN) [*Agostinelli et al.*, 2003]. Geant4 is

used to simulate the performance of high-energy particle/photon/matter interactions, and has been used by the Large Hadron Collider (LHC) at CERN, the Tevatron at FermiLab, and the Gamma Ray Large Area Space Telescope (GLAST) [geant4.web.cern.ch]. The simulation code uses Monte Carlo methods to model the passage of particles through matter, and is ideal for simulating an instrument's response to the relativistic electrons and protons found in Earth's magnetosphere. REPT [*Baker et al.,* 2013], REPTile [*Schiller and Mahendrakumar,* 2010], and the SST [*Turner et al.,* 2012b] have all used Geant4 to properly understand the instrument response. Geant4 has been shown to agree with beam tests, and is considered a reliable alternative to particle accelerator testing if a project is resource constrained [*Baker et al.,* 2013].

2.6 Modeling Particle Motion

Radiation belt models are used to describe particle motion in the inner magnetosphere. Their goal is to reproduce physical processes to best describe the state of the system. Differences between observations and model results can provide insight into physical processes that are poorly understood or not included in the model. Additionally, the models aim to distinguish between the relative contributions of diffusion, acceleration, and loss in the radiation belts.

As introduced in Section 2.3, particle PSD is a comprehensive approach to radiation belt electron motion. If the adiabatic invariants are broken without bias, the electrons can diffuse over the broken invariants. An approach that uses PSC to model this diffusion process uses the general Fokker-Planck equation

Equation 9: General Fokker-Planck

$$\frac{\partial f}{\partial t} + \sum_i \frac{\partial}{\partial J_i}\left[\left(\frac{dJ_i}{dt}\right)_v f\right] = \sum_{ij} \frac{\partial}{\partial J_j}\left[D_{ij}\frac{\partial f}{\partial J_i}\right] - \frac{f}{\tau} + S$$

where f is PSD, J_i (i=1, 2, 3) are the three adiabatic invariants, the subscript v refers to non-stochastic processes, D_{ij} is the tensorial diffusion coefficient, τ the particle's lifetimes and S the source rate. Here, f/τ is the loss term and S is the source term [*Schulz and Lanzerotti*, 1974].

Equation 9 can reduce when describing collisionless plasmas be removing the non-stochastic term to reduce to:

$$\frac{\partial f}{\partial t} = \sum_{ij} \frac{\partial}{\partial J_j}\left[D_{ij}\frac{\partial f}{\partial J_i}\right] - \frac{f}{\tau} + S$$

The equation can simplify again if one is only concerned with diffusion in the L* parameter, and not in energy, pitch angle, or cross-term diffusion:

Equation 10: Simplified Fokker-Planck

$$\frac{\partial f}{\partial t} = L^2 \frac{\partial}{\partial L}\left(\frac{D_{LL}}{L^2}\frac{\partial f}{\partial L}\right) - \frac{f}{\tau} + S$$

where L is the invariant L* parameter and D_{LL} is the radial diffusion coefficient [*Schulz and Lanzerotti*, 1974]. Equation 10 is used when modeling particles with fixed first and second adiabatic invariants so that they may diffuse in L*.

1D Fokker-Planck modeling has been performed for some time now. Some notable examples use data from DEMETER [*Zhao and Li*, 2013]; LANL-

GEO, GPS, and Polar [*Tu et al.*, 2009]; and CRRES [*Brautigham and Albert*, 2000; *Shprits et al.*, 2005, 2007].

2.7 Data Assimilation

Data assimilation is a technique that blends a physical model, such as the Fokker-Planck equation, with observations to produce an estimate of the state of the system that is superior to either the model or the observations alone. Data assimilation techniques have been used extensively where sparse data is typical, such as in terrestrial weather applications [*Kalnay*, 2003], satellite orbit determination [*Tapley et al.* 2004], unmanned aerial vehicle control [*Stachura and Frew*, 2011], and oceanography [*Evensen*, 1994]. The sparse and restricted measurements of the energetic electron environment in Earth's radiation belts make data assimilation a natural approach to form a global picture of electron dynamics.

There are different flavors of data assimilation, some of which are outlined here ranging from simple to complex: simple linear interpolation, direct observational injection, Kalman filters, and 4DVAR methods. More advanced techniques, such as direct injection methods, have been proven successful at reconstructing aspects of the electron environment in the outer radiation belt. Direct insertion runs a physics-based model while substituting the in situ observations as they become available. The model then propagates the measurements into regions of interest that lack observations. Work by *Maget et al.* [2007] and *Bourdarie et al.* [2005, 2009] used the Salammbô code, developed at the Office National d'Etudes et de Recherche Aérospatiales in Toulouse, France [*Beutier and Boscher*, 1995], to directly insert PSD data in a 3D Fokker-Planck

equation. The three dimensions for this model are L, pitch angle, and energy.

Another method of data assimilation is the Kalman filter [*Kalman*, 1960]. Kalman filters have been used more commonly than other methods to express radiation belt dynamics and recently 3D Kalman filters have been used. *Tu et al.* [2014] use the Dynamic Radiation Environment Assimilation Model (DREAM, see *Reeves et al.* [2012]) in three dimensions, known as the DREAM3D model. They assimilated individual storm events and show that event-specific loss and acceleration parameters are necessary to best describe the outer belt. *Kellerman et al.* [2014] use the Versatile Electron Radiation Belt (VERB, see *Subbotin and Shprits* [2009]) to assimilate a CRRES dataset and show that, for a specific event in March-April, 1991, the model shows a unique 4-belt structure. While 3D models more accurately describe the physical dynamics of the environment, they also introduce additional challenges, such as requiring conjunctions between satellites to determine pitch angle distributions. On storm timescales, this limitation hinders the 3D code from reproducing the full dynamics of the environment and thus 1D diffusion can be a reasonable approach despite the inherent limitations on describing full-system dynamics.

An early study by *Naehr and Toffoletto* [2005] showed that, for a simple one dimensional radial diffusion model, an extended Kalman filter (EKF) [*Jazwinski*, 1970] outperforms direct insertion for a highly idealized case. Furthermore, using an identical twin experiment (a method of assimilating a synthesized radiation belt environment to measure the performance of the filter), *Naehr and Toffoletto* [2005], as well as others [e.g., *Koller et al.*, 2007; *Shprits et al.*, 2007; *Kondrashov et al.*, 2007; *Daae et al.,* 2011; *Schiller and Godinez,* 2013] show that the Kalman filter technique accurately reproduces the synthesized electron phase

space density (PSD) environment. These studies are generally performed for simplified cases with clearly specified dynamics, but they verify the robustness and functionality of Kalman filters to reproduce 1D radial diffusion.

One study performed by *Ni et al.* [2009a] demonstrated that the Kalman filter is able to reproduce the location and magnitude of PSD peaks and dropouts using two independent data sets. Another example verifying the Kalman filter's practicality was completed by *Daae et al.* [2011], who examined the Kalman filter's robustness to initial conditions, boundary conditions, and loss timescales. This study in particular explicitly demonstrates that the Kalman filter technique can reproduce radiation belt dynamics regardless of choice of initial conditions, boundary conditions, or loss timescales. Additionally, *Daae et al.* [2011] showed that the difference in PSD between drastically different initial conditions is reduced to 15% after one day, and slowly decays to zero on the order of 14 days, quantifying the memory span of the filter. These studies, as well as others [e.g., *Ni et al.,* 2009b], indicate that the Kalman filter is robust to various data, input, and model parameters.

More recent studies have attempted to reduce the uncertainties associated with the radiation belt state estimation. State estimates can be unreliable due to the unknown, and thus potentially large, errors in both the model and the observations. A study by *Godinez and Koller* [2012] use an ensemble Kalman filter to attempt to improve errors associated with state estimates. They use a localized adaptive covariance inflation technique to account for the ambiguous model uncertainty. *Podladchikova et al.* [2014a] attempt to specify the errors and biases associated with the model, and suggest methods to reducing the errors on the state estimate using smoothing techniques [*Podladchikova et al.*, 2014b].

Kondrashov et al. [2011] show that, in the case where model errors are significantly smaller than observational errors, conversion of PSD to a base 10 logarithm PSD significantly improve the analysis and prediction skill.

Another data assimilation tool is the observation residual vector, or the innovation vector, which is a measure of the processes that exist in the measurements but are not present in the physical model. *Koller et al.* [2007], *Shprits et al.* [2007], *Daae et al.* [2011], and *Schiller et al.* [2012] used the innovation vector to infer enhancements in local acceleration and/or loss. *Shprits et al.* [2012] used the innovation vector to perform a statistical analysis and found a strong correlation between the plasmapause and the location of an inferred source region.

Physical processes can also be estimated directly by including model parameters in the Kalman filter's state vector. This allows for an estimate of, for example, source rate or loss timescale. *Kondrashov et al.* [2007] included loss parameters in the state vector of an EKF. They used an electron PSD data set to estimate the loss timescale inside and outside the plasmasphere for a radial diffusion model with loss. *Reeves et al.* [2012] demonstrated the ability to estimate the time-dependent amplitude parameter of a Gaussian shaped source term for a single storm. *Schiller et al.* [2012] expanded this idea to estimate the intensity, location, and radial extent for five storm periods in 2002 to find that the local source typically occurs inside of GEO and is sufficient to repopulate the outer belt.

2.8 Open Questions and Motivation

In the following work, we improve measurement techniques of radiation belt electrons and use those measurements to investigate the role of relativistic electron enhancements in radiation belt dynamics. Specifically, we attempt to answer the following engineering and science questions.

2.8.1 Engineering Questions

From an operational perspective, I have briefly examined the limitations of acquiring a global picture of radiation belt dynamics. I have also discussed the challenges inherent with measuring energetic particles in near-Earth space. In this thesis, I attempt to answer these questions: **1) Can reliable, publication-quality measurements of energetic particles be made from a less resource intensive platform? 2) What scientific contributions could such observations make?** I will answer these questions in Chapter 3.

2.8.2 Science Questions

From a scientific prospective, I have briefly discussed the extreme and unpredictable variability of outer radiation belt electrons. I have overviewed the principal processes that affect relativistic electrons from a solar driving perspective and from a magnetospheric perspective, and portrayed the puzzling nature of radiation belt dynamics. From within the magnetosphere, I have outlined the processes associated with depletions, enhancements, and transport. Decades of research have gone into understanding the radiation belts, but there is still much to learn about the physical processes that control them. In this work, I investigate the following questions: **1) When, where, and over what**

radial extent do radiation belt enhancements occur? 2) What is the magnitude of the source rate? 3) Are storm signatures required to observe large enhancements? 4) What is the individual contribution of source, loss, and transport mechanisms? I address questions 1) - 3) in Chapters 4 and 5, and outline a method to answer question 4) in Chapter 6.

CHAPTER 3

MEASURING RELATIVISTIC PARTICLES

3.1 Introduction

The following chapter presents the Relativistic Electron and Proton Telescope integrated little experiment (REPTile), which is a novel design to measure energetic particles from nanosatellite platforms.   REPTile is a miniaturized version of the REPT instrument, currently flying onboard the Van Allen Probes mission.   REPTile is the science payload flown onboard the Colorado Student Space Weather Experiment (CSSWE) CubeSat, which was funded by the National Science Foundation (NSF) and launched in September of 2012.   This timely launch allowed for conjunctive observations with other magnetospheric missions, including SAMPEX, the Van Allen Probes, and the BARREL balloon campaigns.

The CSSWE mission was run mainly by students in the Aerospace Engineering Sciences Department (AES), but had significant student contributions from the Mechanical Engineering and Computer Sciences Departments. The project had mentorship from faculty and staff in AES and from the Laboratory for Atmospheric and Space Physics (LASP), as well as from Xinlin Li, the principal investigator (PI); Scott Palo, a co-PI; and Shri Kanekal, also a co-PI. CSSWE completed its massively successful mission in December, 2014, after more than two years on orbit. The cause of the end of mission was

battery failure, after which CSSWE was no longer able to power on. Data from the mission have been used in 15 peer-reviewed journal publications and there are more papers in preparation that use the data. The mission timeline is depicted below. Notable items in the figure are initial concepts for the mission, spacecraft delivery (January 2012), launch (September 2012), and mission end (December 2014).
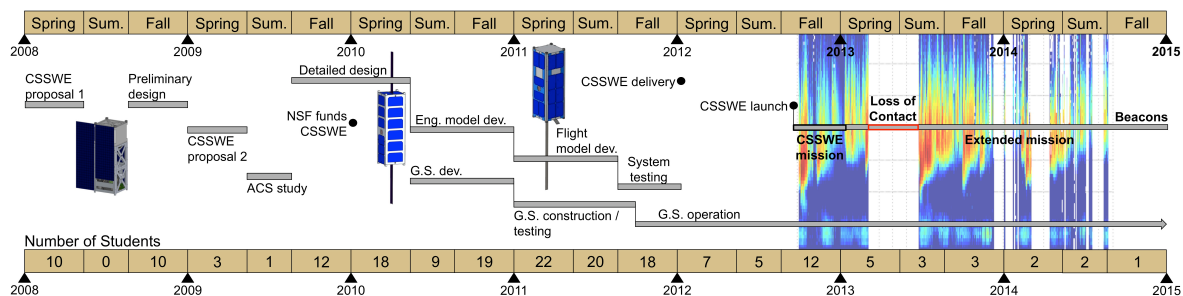
Figure 12: CSSWE mission timeline

This chapter presents innovative new work that spearheads the design and verification of miniaturized particles telescopes. Furthermore, it represents the pinnacle of space-based particle telescope modeling. Significant detail is presented on understanding the instrument and electronics response, since formal performance testing, such as particle accelerator beam tests, were beyond the resources of the project.

Section 3.2, titled Understanding Instrument Response, is based on work published in *Schiller and Mahendrakumar* [2010], a paper that won the Frank J. Redd third place award for best student paper in the competitive student scholarship competition at Utah State University's (USU) American Institute of

Aeronautics and Astronautics (AIAA) conference in 2010. This paper was published during the detailed design phase of the project, before full system integration had begun. In addition to presenting the instrument, this section briefly illustrates the challenges of making in-situ space-based measurements of energetic particles. It also discusses the science motivations and the ensuing instrument design. Most importantly, this chapter presents performance simulations that are unprecedented in detail. The modeling demonstrates that, with sufficient knowledge of an instrument's response, reliable measurements can be made from resource restrictive instrumentation.

Section 3.3, titled REPTile Development and Testing, is based on the work published in *Blum and Schiller* ([2012], a paper that won third place in the student scholarship competition at the USU/AIAA conference in 2012. This paper was published after full system and subsystem testing, but before launch. This section presents engineering work performed to prepare the instrument for launch. Specifically, it presents efforts to characterize and validate the performance of the instrument, from the component level to the full system. Only through such detailed characterization tests can science platforms like REPTile be reliable.

Section 3.4, titled Science Operations and Initial Results, is based on *Schiller et al.* [2014b], a peer-reviewed paper published by the Institute of Electrical and Electronics Engineers. This section briefly summarizes the on-orbit results and scientific contributions of the spacecraft. Additionally, it briefly addresses modeling and operational steps taken to correct for an on-orbit detector failure. Finally, Section 3.5 presents additional details on the scientific

contributions of the mission, as well as presents works completed since the publication of *Schiller et al.* [2014b].

These chapters focus on my contributions to the CSSWE mission and the REPTile instrument. However, work is included that was conducted by several colleagues, including David Gerhardt, Drew Turner, Abhishek Mahendrakumar, Jianbao Tao, and Lauren Blum. Additional acknowledgements are presented at the beginning of each section, but I would also like to recognize all the students who helped with every aspect that made CSSWE a success. Specifically, I would like to acknowledge the past project managers, Tyler Redick and Lauren Blum, and especially the systems engineer, David Gerhardt. I would also like to acknowledge contributions from faculty and staff from the AES Department and from LASP, particularly Karl Hubbell, Vaughn Hoxie, Chris Belting, Gail Tate, and Rick Kohnert, who provided guidance, mentorship, and patience when working with the student team.

3.2 Understanding Instrument Response:

REPTile: A Miniaturized Detector for a CubeSat Mission to Measure Relativistic Particles in Near-Earth Space

by Q. Schiller and A. Mahendrakumar, published in *Proceedings of the 24th Annual AIAA/USU Conference on Small Satellites*, 2010.

Winner: Frank J. Redd Award for Best Student Paper: Third Place

We would like to begin this section with a most gracious acknowledgement to Drew Turner, without whom this paper would not have been written. The authors would also like to thank the CSSWE team, current and

Abstract

The Relativistic Electron and Proton Telescope integrated little experiment (REPTile) is a solid-state particle detector designed to measure solar energetic protons and relativistic electrons in Earth's outer radiation belt. These particles pose a radiation threat to both spacecraft and astronauts in space, and developing a better understanding of these particles has been identified as a critical area of research by NASA's Living With a Star program. REPTile has been designed specifically to meet the requirements for a CubeSat mission, namely the Colorado Student Space Weather Experiment, which is an example of how CubeSats can be employed to provide important scientific measurements for very low cost. This paper focuses on the REPTile design and functionality. The particular difficulties of energetic particle detection are introduced to provide a full understanding of the REPTile design, and then the design itself is covered in detail, including both mechanical and electronic aspects. The paper finishes with a detailed discussion of the various simulations that have been conducted to develop accurate estimates of the detector performance followed by a discussion of the instrument test plan.

3.2.1 Introduction

The Sun acts as the ultimate driver of space weather, the study of the dynamics of particles and fields that make up space plasmas, which can have serious implications for manmade systems both in space and on the ground. The Sun is continually spewing forth a turbulent stream of magnetic field tied with mostly low-energy ions and electrons called the solar wind. This solar wind serves to tie the solar system together since through it energy can be transported from events on the solar surface to every planet and body in the solar system. Near the Earth, the space environment is a vast and highly dynamic region consisting of a plethora of different plasmas primarily split into two categories: those in the solar wind and those in the magnetosphere. Earth's magnetosphere, the region of plasmas and energetic particles whose dynamics are governed by the magnetic fields generated within the Earth, is home to the processes that cause such spectacles as the aurora. Anyone lucky enough to catch a glimpse of these spectacular light shows in the night sky is witness to the fascination of space weather.

In recent decades, scientists and engineers have realized that space weather is extremely important to understand and forecast as society becomes more and more dependent on space-based technology. They have found that events on the Sun, such as solar flares or coronal mass ejections, can have serious effects on Earth's magnetosphere, atmosphere, and even on ground-currents within the Earth itself. For example, a high magnitude solar flare on the Sun can send a blast of highly energetic photons (X-rays) and relativistic protons and electrons moving nearly the speed of light (solar energetic particles, SEPs) at the

Earth. SEPs arrive at the Earth less than ten minutes after the flare is generated on the Sun, almost simultaneously with the light that warns us that there has been a flare at all. They are guided by Earth's magnetosphere to the poles, where they interact with the atmosphere and result in reduced transmission of radio signals from spacecraft and increased levels of radiation for any person at high latitudes at the time. Events also associated with a solar flare are coronal mass ejections (CMEs), which are the explosive releases of a massive amount of solar material into the solar wind. When Earth's magnetosphere is impacted by a CME, the result is often a magnetospheric storm that can have further negative effects on manmade systems. During such a storm, spacecraft are at risk from an enhancement of the intensity and fluxes of the outer radiation belt, which is composed primarily of relativistic electrons that have been known to embed themselves in sensitive electronic components and fatally disable spacecraft in the region. Also, an enhanced ring current associated with geomagnetic storms can induce intense ground-currents on Earth, overloading power grid systems to cause power outages on a continental scale [*Kappenman*, 2001}.

Currently, there are still several outstanding questions concerning some of the physical processes that can result in negative space weather effects on manmade systems; such as, the source, loss, and transport processes of Earth's outer radiation belt electrons. Earth's outer radiation belt is a system of relativistic electrons that are trapped within Earth's magnetosphere and form a torus shaped region with variable equatorial plane boundaries from 3 to 7 Earth Radii R_E with peak intensities around 4 to 5 R_E, as seen in Figure 13. These electrons can be potentially fatal to spacecraft and astronauts in the region since they carry enough energy to penetrate into electronics boxes and through

spacesuits. Energetic electrons can bury themselves in electronic components, and when fluxes are high enough, they can build up enough charge to result in dielectric breakdown and discharge through the material, which can be critically fatal to spacecraft systems [*Baker*, 2002]. With a better understanding of the source, loss, and transport of energetic electrons, it will be possible to improve the forecast and provide a warning system for spaceflight operations in the region.

Another outstanding question concerning the serious implications of space weather is: how do solar flare location, magnitude, and frequency relate to the timing, duration, and energy spectrum of SEPs reaching Earth? Developing a better understanding of the answer to this question is critical for mitigating the risks of airline flight crews and passengers, loss of navigation capabilities due to increased error in GPS, and loss or degradation of radio communications. Solar flares can occur anywhere on the solar surface during any time in the solar cycle. However, they occur most frequently in mid to low solar latitudes around solar maximum, that is, when solar activity is high. Despite their significance, there is no existing model to determine how powerful an SEP event will be based on the type and location of the accompanying flare.

To address these critical space weather questions, it is necessary to make in-situ measurements of the energetic particles, namely relativistic electrons from Earth's outer radiation belt and the energetic particles associated with solar flares. This work serves as a detailed description of an instrument that has been developed specifically to make these measurements for very low cost from a low-
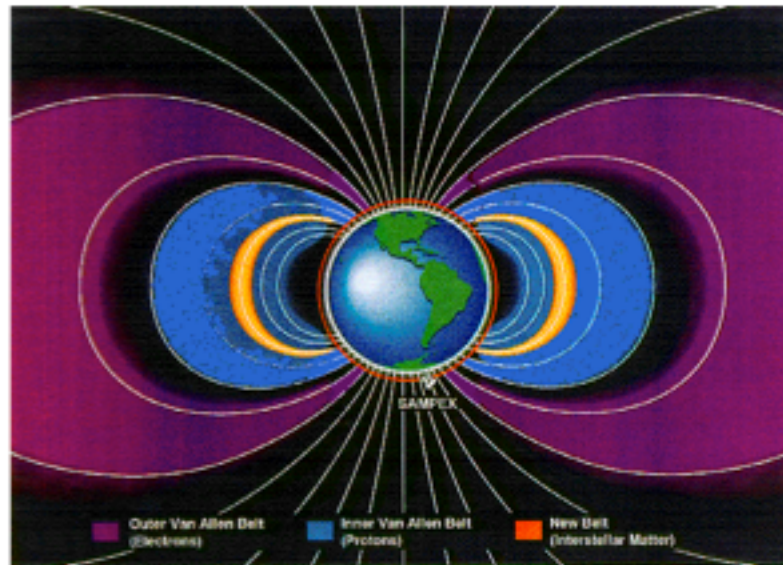
Figure 13: An artistic representation of the inner and outer radiation belts [*Mewaldt et al.*, 1994].
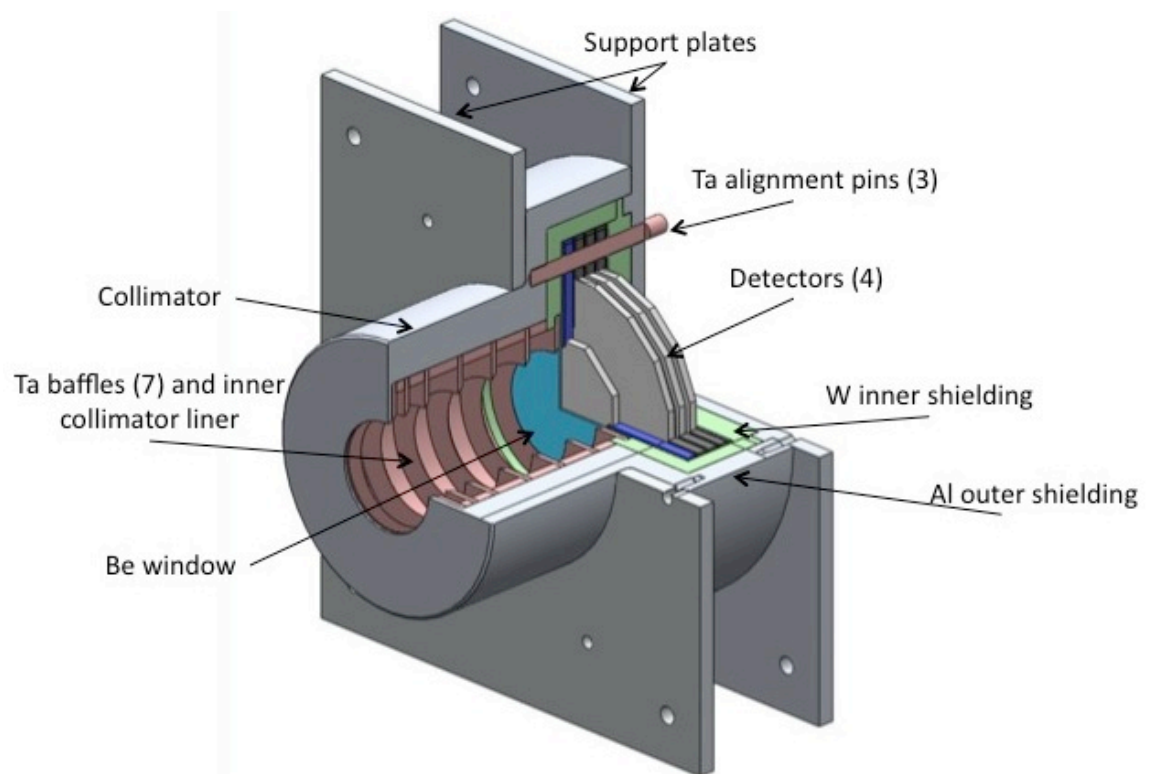
Figure 14: Cross-sectional view of REPTile.

Earth orbit (LEO) CubeSat mission [cubesat.calpoly.edu/index.php/about-us].

In the following sections, a general background of energetic particle detection is provided, followed by a detailed discussion of the University of Colorado's Relativistic Electron and Proton Telescope integrated little experiment (REPTile) instrument. REPTile has been designed primarily by engineering graduate students to measure outer belt electrons with energies ranging from 500 keV to >3 MeV and SEP protons from 10-40 MeV, and will be incorporated as the principle science instrument on the NSF-funded Colorado Student Space Weather Experiment (CSSWE). The following sections are initiated with a discussion on the difficulties in designing an instrument to measure energetic particles. Despite the inherent challenges, a review of the unique mitigation techniques incorporated in the design of the REPTile instrument is presented. Details on simulations of the performance of the instrument follows the design section, and the work is concluded by discussing the importance of taking important scientific measurements from small, low-cost spacecraft in conjunction with larger, more expensive missions.

3.2.2 Measuring Energetic Particles

As discussed thoroughly by *Vampola* [1998], measuring energetic particles of particular incident energies accurately is no trivial task. Due to the complex behavior of individual particles interacting in matter, energetic electrons and protons behave quite differently as they pass through a material. Being relatively massive, protons are well behaved with respect to electrons. Protons pass through solid matter with trajectories that are not greatly diverted and their deposited energy is inversely proportional to their velocity. However, very high-

energy protons are able to penetrate through any reasonable amounts of instrument shielding and will appear as noise in a particle detector's signal.

Electrons, on the other hand, behave in practically the opposite way. Electrons up to ~10 MeV in energy are easily stopped by properly designed shielding. Statistically, their trajectories scatter to the point that a beam of electrons incident on any material will result in some significant percentage of fully backscattered electrons (i.e. reflected by the material itself). For example, up to 25% of electrons incident on aluminum will be diffusely backscattered upon encountering its surface [*Vampola*, 1998]. This phenomena is caused by a wide range of electron interactions with matter including atomic excitation and ionization, bremsstrahlung radiation (i.e. the generation of high-energy photons caused by an electron accelerated in a curved trajectory), dissociation of molecules, and material lattice excitation. Any of these processes can result in a large deviation to electrons' incident trajectories and, due to this significant scattering in matter, energetic electrons do not deposit consistent amounts of measurable energy. A statistical understanding of an instrument's response to incident electrons at various energies is critical to developing an accurate electron-detecting instrument.

The design of a relativistic particle telescope must consider both the scattering properties of electrons as well as the shield-penetrating capabilities of energetic protons. As *Vampola* [1998] states:

> Few investigators who have flown energetic electron spectrometers have really understood the behavior of their instruments" primarily due to a lack of understanding or proper simulations of the instrument's response to electron scattering and shield penetrating particles.

Vampola [1998] and *Leo* [1987] discuss different types of instruments and the strengths and shortcomings of each. Of these, collimated and shielded solid-state detector stacks are the most common type of energetic particle instruments used for indirect energy measurement. However, instrument designers often overlook, disregard, or simply misunderstand the response of their design to electron scattering and shield-penetrating particles.

Poor instrument design allows for electron scattering in a collimating chamber where shielding paths are thin, while electron reflection occurs in the collimating chamber where incidence occurs at oblique angles. An instrument is most susceptible to noise from shield-penetrating particles through large areas of shielding, which become transparent to certain energies of protons and electrons. The instrument is most sensitive to this source of noise in the shielding around the detector stack. Large thicknesses of shield surrounding the detector stack will minimize shield-penetrating particles. However, due to mass restrictions, a balance between shield thickness and noise must be accommodated and accounted for in the resulting data. The generation of secondary particles in shield alloys must also be taken into account. High-Z materials, when bombarded by incident radiation, produce larger amounts of energetic secondary particles when compared to low-Z materials. However, dense materials, which serve as the best shields for blocking high-energy particles, tend to also be high-Z materials. Thus, an adequate shield design must take thickness, mass, density, and nuclear charge into account, but also the noise from any secondary particles generated in the shields.

The most common types of detectors used to measure energetic particles are made of a semiconducting material, such as doped silicon [*Leo*, 1987]. When

an incoming energetic particle hits such a detector, it results in an electron-hole pair generation in the doped silicon. A bias voltage must be applied across the detector to accelerate these loose electrons to an anode on which they can be measured and amplified by sensitive electronics. This amplified electronic signal can then be analyzed further to determine particle type and approximate incident energy in incremental counting bins, which are the raw data produced by an instrument.

In the following section, an innovative new instrument design, which accounts for all of the above-mentioned difficulties, yet is small enough to be incorporated onto a CubeSat, is introduced. In addition, it's mechanical assembly and electronic signal chain are described in detail.

3.2.3 REPTile Design

The following sections demonstrate the design of the REPTile instrument, specifics regarding it's assembly, and details on the electronic system used to process data.

Instrument Geometry

The geometry of the REPTile instrument, shown in Figure 14, is designed to meet a required signal to noise ratio of at least 2 when the complications mentioned above are taken into account. To do so, REPTile is a loaded-disc collimated telescope design incorporating layered shielding and a beryllium
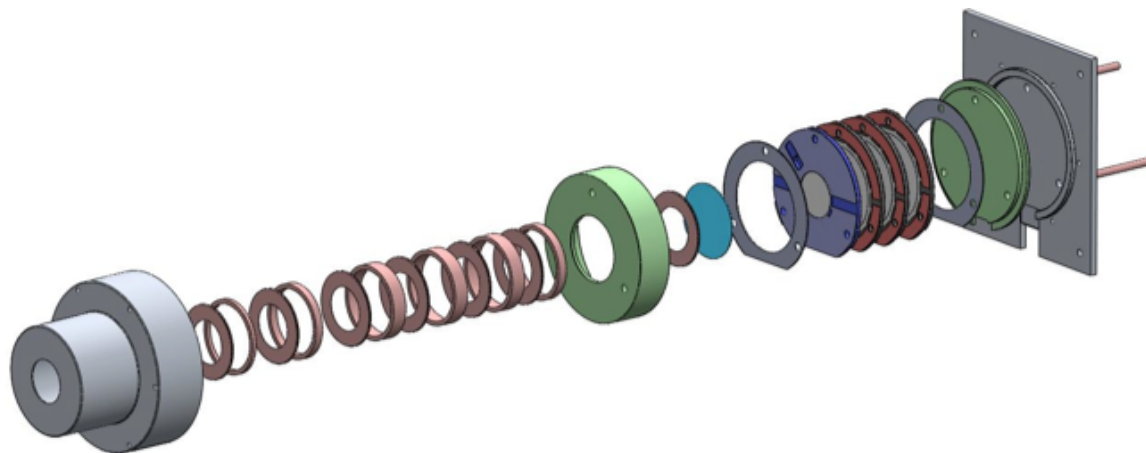
Figure 15: Exploded view of the REPTile assembly.
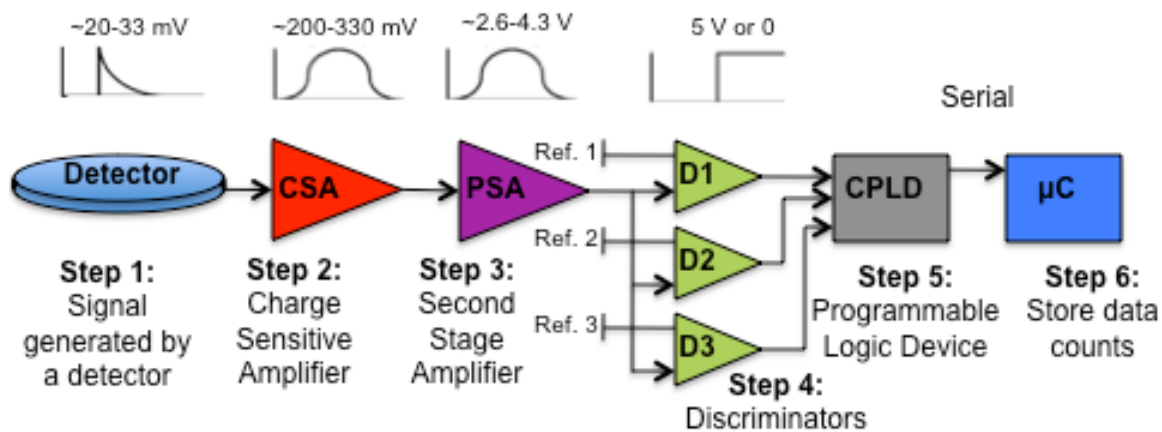
Figure 16: REPTile electronics block diagram.
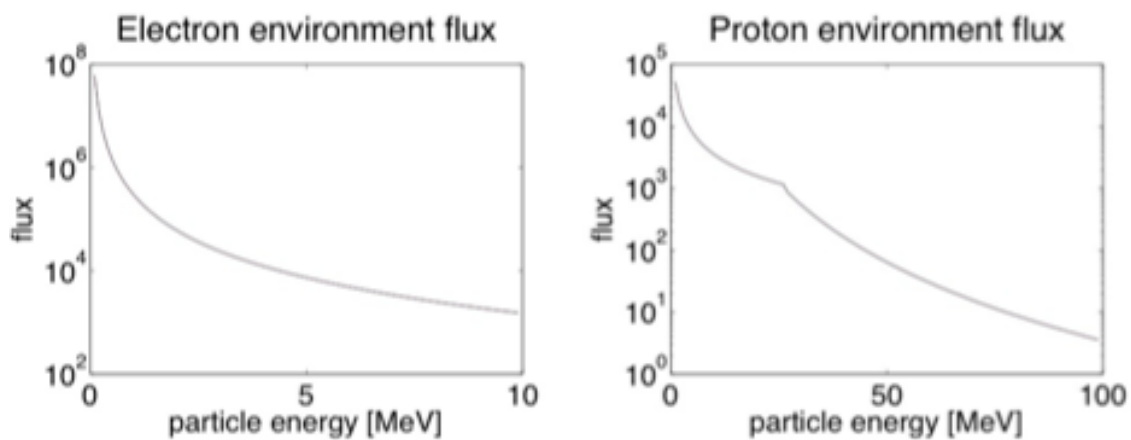
Figure 17: The spectral power laws used for protons and electrons. The units of flux are [# / s / MeV / Sr / cm²].

window to block lower-energy particles from entering the detector stack. In the collimator, tantalum baffles prevent electrons from scattering off of the collimator walls and into the detector stack. This affect is demonstrated superbly in panel d) of Figure 19, where a beam of 2 MeV electrons are fired into the collimator but out of the instrument's field of view. The baffles effectively cause the particles to back-scatter, thus preventing them from entering the detector stack. The spacing of the baffles is designed to maintain a 50° field of view such that an out-of-field electron cannot directly enter the detector stack without impacting at least one baffle after its initial scattering. Additionally, the baffles also incorporate knife-edges to decrease the number of particles reflecting off the baffle edge and into the detectors. Tantalum is used for the collimator lining and baffle material due to its high density but reasonably low secondary particle generation

As can also be seen in Figure 14, the main shielding of the instrument consists of an outer aluminum shell with a smaller chamber of heavy tungsten shielding within it. Due to the large area of the instrument's end cap, additional heavy shielding is applied to further reduce the noise from particles penetrating the rear of the instrument. Tungsten is used for the inner shielding due to it's high density; however, tungsten behaves poorly in regards to secondary particles. The layered shield design accommodates this with an aluminum outer layer, which serves to soften incoming particles before they encounter the tungsten. This layered shielding configuration stops all electrons with energy (E) less than 10 MeV and all protons with E < 85 MeV.

The beryllium window at the front of the detector stack acts as a high-pass filter for incoming field of view particles. Despite a thickness of 0.5 mm, the

beryllium foil effectively stops electrons up to 400 keV and protons up to 8 MeV. This window sets the lower limit for the instrument energy range. It also limits the count rate the electronics handle since there are increasingly more particles at lower energies, as seen in Figure 17.

For the detector stack, Micron Semiconductor solid-state doped silicon detectors are employed. The front detector in the stack (i.e. immediately behind the Be-window) has an effective area with a 20mm diameter, while detectors 2 through 4 have effective areas of 40mm in diameter. The design uses the same detectors used on the Relativistic Electron and Proton Telescope (REPT) instrument, which is being designed for NASA's Radiation Belt Storm Probes mission. This is no coincidence; the REPTile and REPT design teams have worked closely together on the REPTile design, it is quite advantageous to use the same detectors given the strict time and monetary budgets for REPTile. The final REPTile design results in a total instrument mass of 1.25 kg (including structural supports) with a cylindrical envelope of 7.6 cm (diameter) × 6.0 cm (length).

Mechanical Assembly

Figure 15 shows an exploded view of REPTile's components. To assemble the instrument, the outer aluminum shielding serves as the base for the assembly stack. The collimator discs are loaded into the collimator and are press fit by the inner tungsten shielding. These discs are free to rotate, though since they are held under compression, any rotation will be minimal and they will not rattle. The last collimator baffle has the Be-window adhered to its inner face. It is press fit between the tungsten shield and the PCB-casing on the first (20mm) detector.

A spacer is included between the Be-window and the first detector. The thickness of this spacer (as well as that of the one behind the fourth detector) is dependent on the measured thicknesses of the actual manufactured parts to conform to the design requirements. Detectors 2 through 4 (40mm) are installed after the first detector. The PCB casings ensure that the sensitive material is isolated from other parts. Finally, the tungsten and aluminum end caps are used to close and seal the detector chamber. Fasteners and alignment pins hold the entire assembly together. Three threaded tantalum pins insert through the holes in the end caps, spacers, detectors, and tungsten shields. These align the detector stack and restrict rotation, which could shear the detector electronic cables. The alignment pins screw into the inside of the outer aluminum shield and will be held in place with nuts on the outside of the aluminum end cap.

The cables from the detectors are flex-circuits with a built-in ground plane ending in 10-pin connectors that interface with the instrument electronics board residing behind the instrument in the spacecraft. Housing and breakout points for these cables have been incorporated in the design of each detector and in the bottoms of the tungsten and aluminum end caps through a system of slots and notches. The wire breakouts have been designed in such a way that there is no line-of-sight directly into the sensitive areas on the detectors, and thus, noise through this weak part of the shielding is highly reduced.

Electronics Design

REPTile electronics have three major roles to play in the mission, namely: 1) to identify particles that hit the detectors; 2) to find the approximate energy of these particles; 3) convert the analog data to digital data for transmission to

Command and Data Handling (C&DH). The signal chain block diagram is shown in Figure 16.

When a particle hits a silicon detector the response is a very small voltage spike on the order of 20 to 33mV. These signals are highly sensitive to noise since the amplitude of the signal is very low. There are two stages of amplification in the circuit. In the first stage, the voltage spikes are converted to a pulse which is amplified to a similar pulse of approximately ten times higher amplitude. This amplifier is called a charge sensitive amplifier (CSA). An IC A225 from Amptek Inc. is used as the CSA in the design. The A225 is a space graded IC and very sensitive to noise. Due to this sensitivity, the A225 is placed very close to the detectors reducing the effect of noise.

The second stage amplification is thirteen times amplification of the output of the CSA. The purpose of this stage of amplification is to have clearly distinguishable voltage bands for electrons and protons. Amplification is performed by a generic OpAmp and the approximate voltage level for electrons and protons would be from 2.6V to 4.3V.

The stage where the analog signal is converted to digital is at a three level discriminator chain. An analog to digital converter (ADC) can be used in place of the discriminators; however, the rate at which the particles hit the detector exceeds the ADC operational margins. The discriminators used are simply OpAmp comparators and they compare a predefined reference voltage with the output of the second stage amplification. The reference voltages for the discriminators represent deposited energy of 0.25, 1.5, and 4.5 MeV and are provided by digital to analog converters (DACs) from C&DH. The first discriminator returns a 1 if the voltage exceeds the equivalent of 0.25 MeV

deposited on the detector. The second discriminator in the chain returns a 1 if the input voltage exceeds the equivalent of 1.5 MeV deposited in the detector. The final discriminator outputs 0 unless the input voltage exceeds the equivalent of 4.5 MeV deposited. Thus, a return of 100 signifies energy deposited between 0.25 and 1.5 MeV, 110 signifies energy deposited between 1.5 and 4.5 MeV, and 111 signifies energy deposited greater than 4.5 MeV. The reference energies are determined by detailed simulations discussed in the next section.

A discriminator chain output of 100 indicates a particle has deposited 0.25 < E < 1.5 MeV in an individual detector. The binning logic incorporated in the Complex Programmable Logic Device (CPLD), the next stage in the signal chain, classifies this type of incident particle as an electron. A discriminator chain output of 110 indicates a particle deposited 1.5 < E < 4.5. These particles' data are discarded. Finally, a discriminator chain output of 111 indicates deposited E > 4.5 MeV and classifies the hit as a proton. Depending on the number of detectors a particle hits, the incident energy of the particle can be estimated, and the incident energy ranges are described in Table 1.

Particle	D1	D2	D3	D4
Electrons	0.5 – 1.5	1.5 – 2.2	2.2 – 2.9	> 2.9
Protons	10 – 18	18 – 25	25 – 30	30 – 40

Table 1: Energy Range

The reference voltages can be varied by software in the C&DH module. This design provides the versatility to adjust the reference voltages of each discriminator throughout the mission, in case; for example, of a detector

malfunction. The exact reference voltage values will be found through testing as described later.

The final stage in the electronics chain, the CPLD, filters the data received by the discriminators to send the valid data to C&DH and discards the invalid data. The CPLD and DACs are connected to the C&DH subsystem through an I2C bus, in which the CPLD and DAC are slaves. Additionally, there are housekeeping sensors on the electronic board which keeps the track of temperature, voltage and, current of the whole system. All the sensors communicate with the master using an I2C bus.

3.2.4 Performance Simulations

To test the performance of the instrument, the REPTile team uses the Geant4 software tool. Geant4, developed by physicists at the European Organization for Nuclear Research (CERN), is used to simulate the performance of the Large Hadron Collider (LHC), the Tevatron at FermiLab, and the Gamma Ray Large Area Space Telescope (GLAST). The simulation code uses Monte Carlo methods to model the passage of particles through matter, and it is ideal for simulating an instrument's response to the relativistic electrons and protons found in Low Earth Orbit (LEO) [geant4.web.cern.ch].
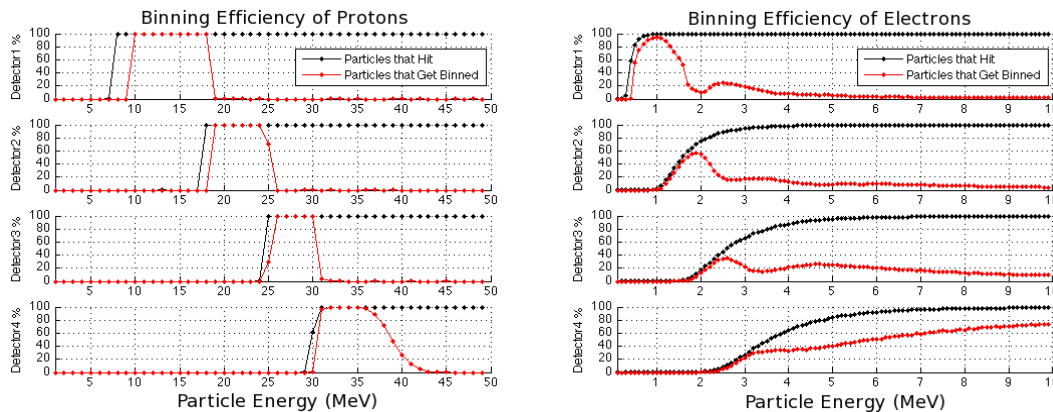
Figure 18: REPTile binning efficiencies for signal particles through the instrument's field of view.
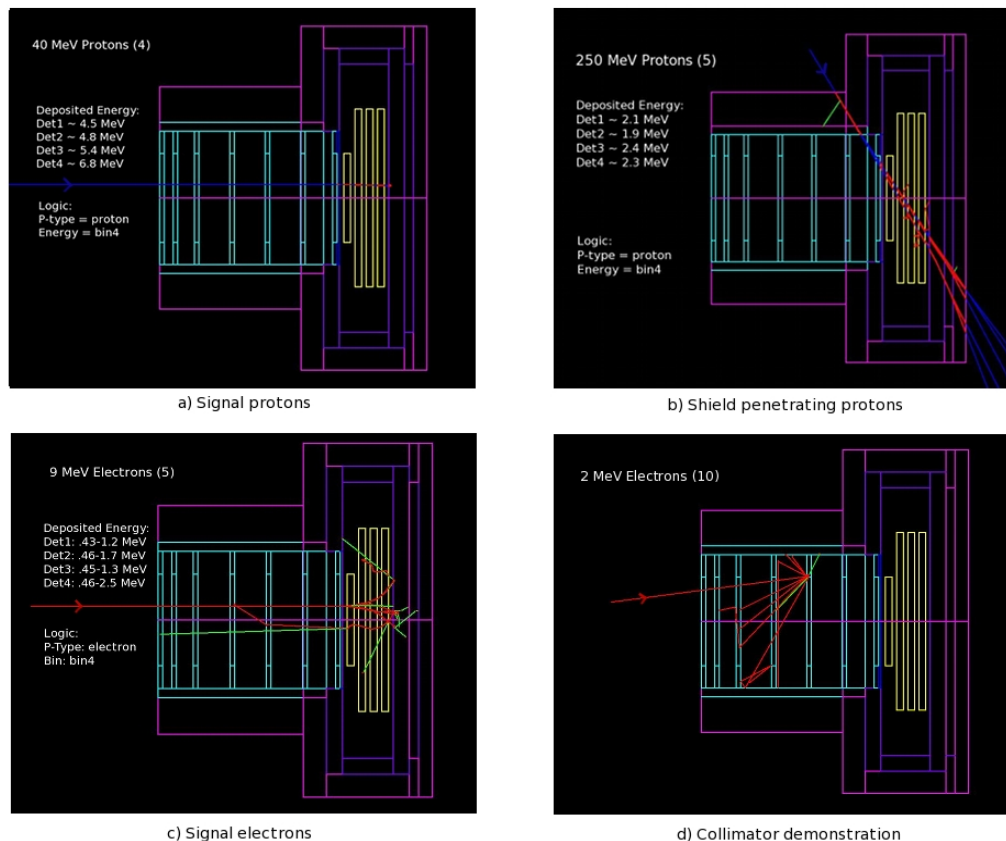
Figure 19: Geant4 simulations of the reptile instrument. Protons can be seen in blue, electrson in red, and high energy photons in green. Protons inside of ta material are hidden due to the cascade of electrons caused by their interaction wit the substance, resulting in a red path. The incident energy, type, and number of each particle can be seen in the upper left of each panel. On the left of panels a-c is displayed the average particle energy deposited in each detector, as well as the binning logic for the particles as would be sent to C&DH.

Geant4 Modeling

Geant4 creates a software environment in which the instrument is assembled and bombarded with particles. The simulation results are analyzed to determine specific design constraints of REPTile geometric features. For example, the collimator and heavy shielding chambers went through multiple design iterations to confirm the required performance efficiency.

The analyzed Geant4 output is a series of numbers corresponding to the energy deposited by individual particles in each of the four detectors. The particles are then logically binned based on the energy deposited as described in previous sections. To determine the binning efficiency, each detector is integrated over energy for particles incident on the instrument:

Equation 11: Count rate

$$C_i = \int_0^\infty I(E)\gamma\alpha_i(E)dE$$

where C is the count rate [#/s], i is the index (1 - 4) of the detector, I is the environmental flux of the particle, γ is the geometric factor for the incident particles, α is the binning efficiency of the detector, and E is the energy of the particle. These quantities are described below.

The incident electron spectral flux is determined to be $3.003 \times 10^5 \times E^{-2.3028}$ using solar max AE8 for L=4 and B/B_0 = 27.1 [modelweb.gsfc.nasa.gov/models/trap.html]. This incidence is used for all simulations as it represents higher-than-average fluxes. Similarly, we determine the incident proton spectral flux using GOES-11 storm condition data analyzed

in *Mewaldt et al.* [2005]. The result is a spectral power law with a knee such that I(E)= 5.2008 × 10^4 × E$^{-1.1682}$ for 0.1 < E < 26 MeV and 9.6489 × 10^8 × E$^{-4.2261}$ for 26 < E < 1000. These power laws can be seen in Figure 17.

The geometric factor ϒ describes the number of particles incident at one surface that will penetrate a second. Configuration factor algebra is used to find ϒ through summing infinite nonoverlapping surfaces both completely covering a surface as well as enclosing the surface. The geometric factors for various REPTile surfaces are found in the Howell Catalog [me.utexas.edu/~howell/index.html], which provides geometric factors for a series of different surface shapes and configurations. For example, the geometric factor for the instrument field of view is

Equation 12: Field of view

$$\gamma_{FOV} = \frac{1}{2}\left(X - \left[X^2 - 4\left(\frac{R_2}{R_1}\right)^2 \right] \right)^{\frac{1}{2}}$$

where a is the distance in cm from the front of the instrument to the first detector, r_1 is the radius of the boresight, r_2 is the radius of the first detector, $R_1 = r_1/a$, $R_2 = r_2/a$, and $X = 1 + (1 + R_2{}^2) / (R_1{}^2)$.

Statistical analyses of Geant4 simulations are done using MATLAB codes created by Quintin Schiller and Jainbao Tao. The result, α, ascertains the binning efficiency for each detector and every energy step for protons (1 < E < 350 MeV) and electrons (0.1 < E < 9.9 MeV). The field of view binning efficiencies are shown in Figure 18, where the panels, from top to bottom, represent detectors 1

through 4 respectively. In each panel, the y-axis represents the percentage of particles and the x-axis represents the specified particle energy. The black line corresponds to particles depositing energy into the detector and the red line signifies particles depositing the required energies to bin the particle as either electrons or protons. These plots aid in determining the energy binning ranges of the detectors as described in Table 1.

In total, ten particle beams are shot from various incidence angles at the instrument in the Geant4 environment. The data from each beam are classified into signal (particles depositing energy after entering from the instrument's field of view) and noise (particles depositing energy without entering from the instrument's field of view). Particles that entered from the instrument's field of view are classified as signal particles, such as panels a) and c) in Figure 19. Signal particles are represented with a single particle beam through the center of the collimator. All particles that contacted shielding prior to entering the detector stack are classified as noise, such as panel b) in Figure 19.

Figure 19 panel a) provides an example of 40 MeV protons fired down the instrument's field of view. These protons are of high enough energy to pass through all four detectors and embed themselves in the rear of the instrument. Observe how, even after impacting the Be window and all four Si detectors, the protons' deviations from their path are extremely small. Another note-worthy component of Figure 19 can be seen in panel c), where a beam of 9 MeV electrons are fired down the instrument's boresight. Upon impact with the first detector, the electrons immediately begin to diverge into a scatter-cone, where they interact with the remaining detectors and the rear of the shielding, releasing additional particles and electromagnetic radiation. Note the back-scattering

which occurs in addition to the scatter-cone. In particular, one particle rebounds off the rear of the chamber, travels backward through the detectors and Be foil, and embeds itself in a collimator baffle. The chaotic nature of relativistic electrons interacting with matter is an excellent example of the importance of performing this type of analysis on high-energy particle detectors.

In addition to the field of view particles, nine particle beams are chosen to represent the most basic noise estimates. Panel b) in Figure 19, an example of simulated noise, displays 250 MeV protons fired through the shielding. These particles pass through the entire instrument and exit the rear shielding with little trajectory deviation, yet they deposit enough energy in all four detectors to be logically binned as bin 4 protons. Analysis of noise particles such as these is critical to understand how the REPTile will interact with the ambient environment in LEO, and how those interactions affect the data.

To determine the geometric factor of this particular shot, or any particle vector, the instrument is broken up into a variety of surfaces. The geometric factor γ is calculated for each surface and a single beam directed toward the detector stack is fired through each surface, similar to the examples seen in Figure 19. The resulting nine beams represent all particles penetrating the instrument classified as noise, and the sum of the nine geometric factors total to the entire surface of the instrument shielding. The geometric factors of all ten beams combined result in the geometric factor of the instrument as a whole.

A large geometric factor indicates that a large number of incident particles may penetrate the surface and impact the detector stack. To reduce noise from surfaces with large geometric factors, such as the rear of the instrument,

additional shielding is implemented. In this way, a balance is created between different aspects of Equation 11. That is, if a large geometric factor, γ, indicates a high particle countrate through an aspect of shielding, additional shielding is applied to decrease the binning efficiency, α. This analysis allows shielding to be applied to only necessary areas of the instrument where significant noise originates from. Thus, for small spacecraft under a strict mass budget, superfluous shielding can be avoided.

The resulting signal to noise ratios are outlined in Table 2. As per defined by the mission requirements, the signal to noise ratio for each detector and particle type is confirmed to be > 2. The modeled signal to noise ratio is lower than expected to observe in orbit due to a variety of factors not included in the Geant4 simulation. For example, in the REPTile flight structure, the collimator baffles are knife-edged to reduce particle reflectance, an aspect not included in the model. Additionally, the incident particle flux used in the simulations is a spectral power law estimated during periods of storm or sub-storm activity. It is likely that the majority of the mission will observe a particle flux at non-storm levels. Finally, in addition to the instrument shielding included in the simulations, there will be supplemental shielding from other components of the spacecraft; such as the spacecraft chassis and batteries. These components are not included in the Geant4 simulations.

Particle	D1	D2	D3	D4
Electron	87.9	42.2	28.9	23.8
Proton	13.6	8.5	6.4	2.2

Table 2: Simulated signal to noise ratio
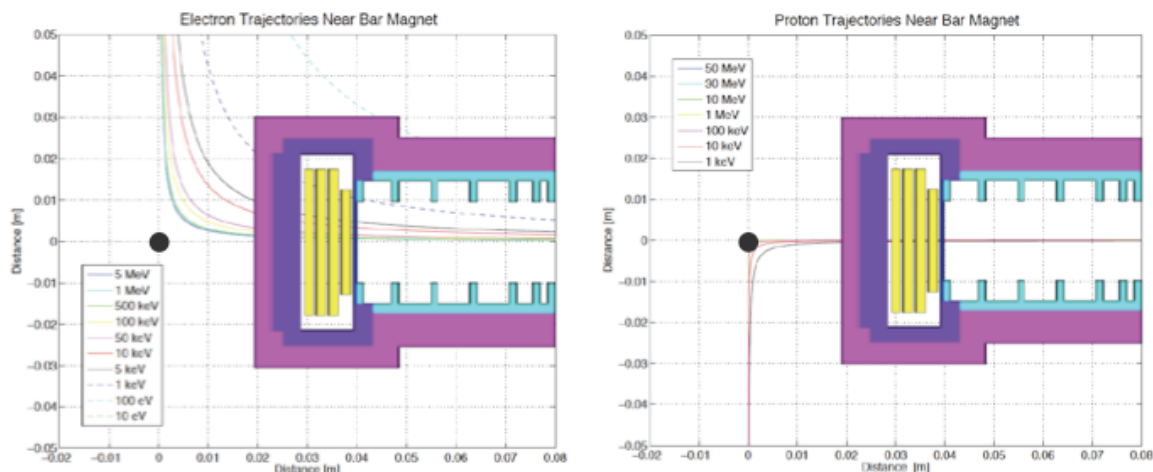
Figure 20: Particle deflection distances due to the instrument proximity to the permanent magnet of ACS.

Passive Attitude Control Interaction

The attitude control system (ACS) used in this mission is, like many previous small spacecraft missions, passive magnetic. A permanent bar magnet will be used to orient the structure so the instrument's field of view is nearly perpendicular to the local magnetic field lines. A series of hysteresis rods will damp angular oscillations and torques caused by the magnet and Earth's geomagnetic field. The result of the magnetic ACS system is permanent alignment with the local magnetic field to within ±10 degrees. (For further details see presentations by *David Gerhardt* [2010] and *Dr. Scott Palo* [2010].)

A permanent magnet aboard the spacecraft can potentially interfere with the science objectives of the mission. Simulations of energetic particle interactions with an appropriate constant magnetic field (from the magnetic ACS) are conducted to determine the effect of the permanent magnet on the

instrument's data. Relativistic test-particle simulations are run using a simple force model employing the magnetic component of the relativistic Lorentz force:

Equation 13: Lorentz force

$$\vec{F} = q\gamma\left(\vec{v}x\vec{B}\right)$$

where γ is the relativistic Lorentz factor, a is the particle's charge, v is the particle's velocity, and B is the local magnetic field vector. The local magnetic field at each point in the simulation space is calculated using a constant value for Earth's field at LEO and a dipole field using a magnetic moment identical to that which will be used for CSSWE. The initial position of the test-particle beam is one meter away from the magnet, which is small compared to an energetic particle's gyro-radius but large with respect to the strength of the permanent magnet on the spacecraft. The initial velocities are dependent on the incoming test-particle's energy and are directed down the instrument bore-sight. Particle trajectories of various energy and species are integrated to determine the effect of the passive magnetic ACS.

The result of this analysis, as seen in Figure 20, confirm that the use of a small onboard permanent magnet will affect the trajectories of the ambient relativistic particles, but not significantly for the energies REPTile is required to measure. The magnetic field from the onboard permanent magnet for the passive ACS is weak enough that it will not interfere with energetic particles' trajectories until after the particles have passed through the detector stack. Particles of high energy entering the detector chamber from the field of view do

not markedly change their trajectory until after they have left the rear of the instrument. Additionally, in the model, the magnetic dipole is placed at the nearest possible location to the instrument. Current design places the magnet further away than shown in this analysis, which results in even less affect on ambient particles. Thus, the passive magnetic ACS will not have a negative effect on CSSWE's science objectives.

Instrument Test Plan

Without access to a particle beam facility, the REPTile team must find alternative methods to test the performance of the detectors. The current test plan for the detectors involves two sources of radiation: atmospheric sources, resulting from galactic cosmic rays, and radioactive materials. Initially, atmospheric source tests will confirm the functionality of the detectors and their ability to respond to energies higher than those available in a laboratory environment. The atmospheric particles occur in a broad spectrum of energies and these tests will validate the detectors response to relativistic particles, though the incident energy values will be unknown.

Unlike cosmic rays, the radioactive sources will emit alpha or beta radiation at known discrete energy values. For example, a trinucleide source of Americium, Polonium, and Curium emit α and β decay at a variety of precise energies between 2 and 6 MeV. By confirming the detector's linear response to known particle energies, these tests will calibrate the detector's response to energetic radiation observed in space. Additionally, both the atmospheric and

radioactive tests can be simulated in Geant4 to confirm the behavior of the detectors.

In addition to the detectors, the electronics shall also undergo rigorous testing. Specific voltage pulses shall be injected into each stage of the signal chain to ensure that each component operates as specified, starting with the digital end of the signal chain. The digital inputs to the CPLD will verify the data stream through the CPLD and discriminators. An analog input into the discriminators will test their performance and aid in establishing reference voltages. Digital inputs into the pulse shaper and discriminators will simulate the output of the charge-sensitive amplifier and pulse shaper respectively. Analog inputs to the charge-sensitive amplifier designed to simulate the output from the detectors will be propagated through the circuit to test the signal chain.

3.2.5 Conjunctive Science

Small spacecraft, like CubeSats, have a variety of distinctive benefits; low cost, small mass, and ease of launch, to name a few. In addition to these conveniences, they are capable of magnifying their mission goals through conjunctive science; that is, taking measurements in parallel with instruments aboard other spacecraft. For example, REPTile's data could be enhanced through congruent measurements made by REPT. REPTile, which is on a highly inclined, low altitude orbit, is capable of measuring electrons whose equatorial crossing point is ~5 R_E: the heart of the outer radiation belt. Likewise, the REPT instrument aboard NASA's Radiation Belt Storm Probes (RBSP) mission, a pair of spacecraft on a highly elliptical, low inclination orbit, is also designed to measure outer belt electrons. From that orbit, REPT passes through the outer radiation

belt to R_E ~6 at 10° inclination to measure the same particles available to REPTile, but at lower latitudes and further from Earth [*Mauk et al.* 2009]. REPTile will measure the outer radiation belt electrons observed by REPT, but close to Earth at high latitudes. Additionally, REPTile measurements will be simultaneous with data from the GOES and SAMPEX spacecraft, potentially amplifying it's scientific significance further.

3.2.6 Summary

This paper has introduced the Relativistic Electron and Proton Telescope integrated little experiment, REPTile, which is currently being designed and manufactured by graduate students at the University of Colorado at Boulder. REPTile will serve as the primary instrument aboard the Colorado Student Space Weather Experiment, CSSWE, a CubeSat mission which has been fully funded through the NSF and will be launching late 2011 or early 2012, depending on the availability of a launch vehicle-of-opportunity.

REPTile will be studying Earth's outer radiation belt electrons and solar energetic protons associated with solar flares, both of which have outstanding questions concerning their nature and behavior in near-Earth space, from a platform that cost less than $1M to design and manufacture. By measuring 0.5 to >3 MeV electrons from its low-Earth orbit, REPTile will be able to address relativistic electron precipitation and loss from the outer radiation belt, which is a key part of the delicate balance between source, loss, and transport that governs the extreme variability in outer belt intensities. Also, by measuring protons with $10 < E < 40$, REPTile measurements during SEP events associated with solar

flares will be used to determine properties of the events, measured from Earth, based on the original flare location and magnitude at the Sun.

Analyses presented in this paper represent the vanguard for energetic particle detector designs. The Geant4 simulations are an exceptionally thorough approach to instrument design, and its applications to space radiation are only just beginning to become realized. Using Geant4 to constrain the instrument and electronics design, as well as to address the critical issues normally ingnored or overlooked in energetic particle instrument design (i.e. electron scattering and shield-penetrating particles), further establishes the CSSWE mission as a unique method of undertaking space radiation studies. Additionally, this mission and the REPTile instrument provide an opportunity to represent the massive potential of small spacecraft, like CubeSats, to perform important science for a fraction of the cost of larger missions.

If this mission is successful, it will exemplify how small satellite missions can be used to greatly complement larger, more expensive missions in addressing critical science questions. For example, NASA's Radiation Belt Storm Probes mission, scheduled to launch in 2012, is being developed for the sole purpose of measuring the particles and fields believed to be important to outer radiation belt electron dynamics. RBSP will be in a low-inclination, GEO-transfer orbit, which leaves it unable to measure precipitating electrons at high latitudes very close to Earth. CSSWE with REPTile, however, will have some overlap in mission operations with RBSP, and will be able to measure these electrons. This leads to the possibility of conjunctive science, where RBSP and CSSWE data are used from the same observation times to provide a better understanding of key outer belt loss processes, like enhanced precipitation of electrons to high-

latitudes near LEO. In general, CubeSats and small spacecraft missions can complement larger, vastly more expensive missions by providing additional simultaneous measurements at different yet critical locations, which allows for a more comprehensive snapshot of the system being observed.

3.3 REPTile Development and Testing:

Characterization and testing of an energetic particle telescope for a CubeSat platform

by L. W. Blum and Q. Schiller, published in *Proceedings of the 26th Annual AIAA/USU Conference on Small Satellites*, 2012.

Winner: Frank J. Redd Award for Best Student Paper : Third Place

Abstract

The Relativistic Electron and Proton Telescope integrated little experiment (REPTile) instrument has been designed, built, and tested by a team of students at the University of Colorado. It is scheduled to launch on a 3U CubeSat, the

Colorado Student Space Weather Experiment (CSSWE), this August, 2012. The instrument will take measurements of energetic particles in the near-Earth environment, which are vital to understand, predict, and mitigate hazardous space weather effects — an area identified as a critical area of research by NASA's Living With a Star program. However, the task of designing a payload to return accurate and reliable data is extremely challenging due to the resource limitations imposed by a CubeSat platform. REPTile has undergone rigorous testing and calibration to verify its functionality and certify the validity of its measurements. This paper focuses on characterizing the telescope detectors and individual electronic components, as well as the integrated space craft system. The response to environmental conditions is quantified, and the variability minimized through on-board data handling as well as post-processing during mission operations. Thorough testing and calibration validates the data as a valuable contribution to outstanding questions in the study of space weather. The ability to address these questions by making differential energy measurements of energetic particles with an affordable, robust, and simple instrument design is what sets this instrument apart from others.

3.3.1 Introduction

The near-Earth space environment is a highly dynamic region, composed of numerous particle populations and variable magnetic and electric fields. Understanding this environment is becoming increasingly critical as society becomes more dependent on space-based technologies. Large variations in the particle population around Earth, caused by solar activity and other space

weather events, can have deleterious effects on satellite subsystems and harmful effects on the bodies of astronauts [*Turner*, 2000].

A number of outstanding questions remain regarding the generation, transport, and effects of energetic particles in space. Various mechanisms can generate harmful particles, such as solar energetic particles (SEPs) or energetic electrons, which threaten space based assets. The relationship between solar flares and the production of SEPs must be further investigated in order to understand the timing, duration, and energy spectrum of the SEPs measured at Earth. Additionally, relativistic electrons in the Earth's outer radiation belt, a toroidal region of highly energetic electrons trapped between 3 and 7 Earth radii, overlap a variety of popular satellite orbits. Electrons in this region can penetrate through spacecraft shielding, causing dielectric breakdown and discharging within sensitive electronics [*Baker*, 2002]. A number of spacecraft anomalies (e.g. Galaxy 15 [*Allen*, 2010]) have been attributed to geomagnetic activity and sudden enhancements in energetic electron fluxes [*Allen*, 2010; *Love et al.*, 2000] Geomagnetic storms and substorms, often associated with activity on the sun, can cause large fluctuations in both the location and overall magnitude of the outer radiation belt. Better understanding of the acceleration, loss, and transport processes affecting these energetic electrons will enable more accurate predictive capabilities to better protect assets in space.

A student led, National Science Foundation (NSF) funded CubeSat has been designed and built at University of Colorado to address these critical space weather questions. The *R*elativisit*c E*lectron and *P*roton *i*ntegrated *l*ittle *e*xperiment (REPTile) instrument will measure SEP protons in the energy range of 8.5 - 40MeV, and radiation belt electrons from .5 - >3MeV from a high-

inclination, low-altitude orbit. Both species will be measured in differential energy bins, an improvement on currently available measurement from a small satellite. Designed and built primarily by students over the past four years, the Colorado Student Space Weather Experiment (CSSWE) CubeSat was delivered this past January (2012) for integration as a secondary payload onto an Atlas-V launch vehicle, and is scheduled to launch August 2, 2012. An identical satellite, without the structural components, has been fabricated for testing and calibrations while the spacecraft is integrated and on orbit.

Due to the power, mass, volume, and budgetary constraints of a CubeSat, the telescope and instrument electronics have been miniaturized and simplified. These constraints, combined with the inherent difficulties in measuring energetic particles, demand careful characterization of REPTile. The outcome of the analysis is an instrument capable of returning reliable in-situ measurements of energetic protons and electrons. Moreover, this mission will provide greatly needed differential flux measurements of high energy particles from low-Earth orbit, as well as demonstrate that accurate measurements can be made from a CubeSat platform.

In this paper, we briefly discuss the REPTile design (Section 2), then focus on the testing and calibration of both the detectors and electronics. Section 3 outlines detailed testing done on a component-level, Section 4 describes a mitigation technique applied to the on-board binning logic, and Section 5 illustrates tests performed as a fully integrated spacecraft.
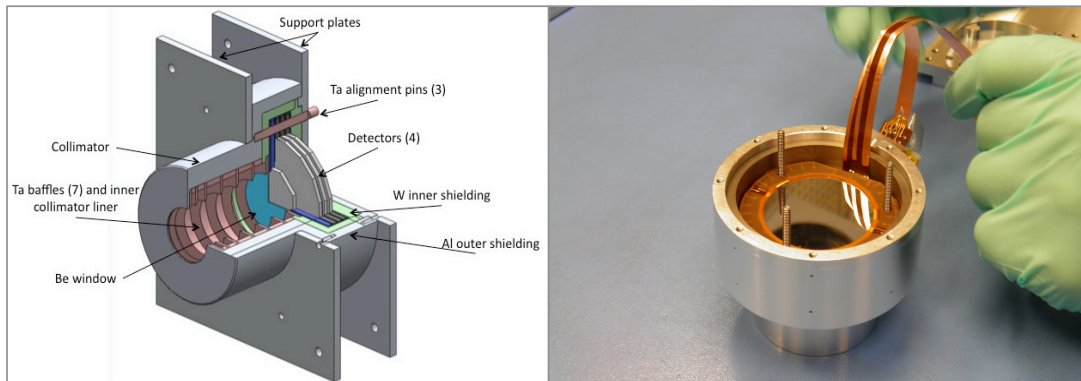
Figure 21: Left - Cross sectional view of the instrument geometry. Right - Flight instrument during integration. The collimator is facing down in the image, and the back plate not yet attached, so the fourth detector in the stack is visible.
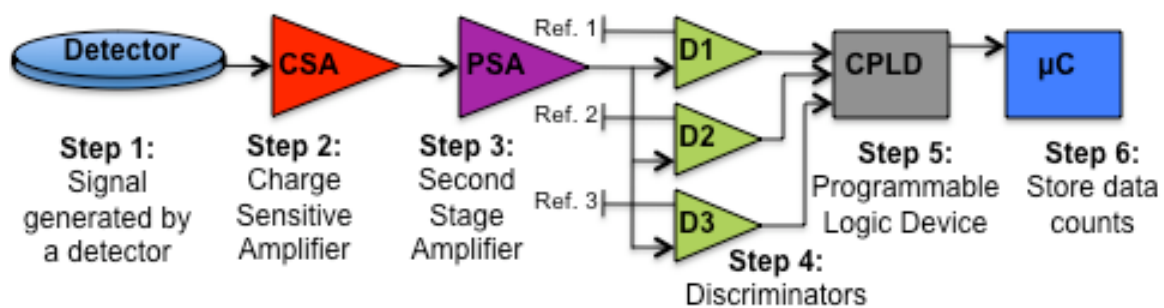
Figure 22: Instrument electronics block diagram.
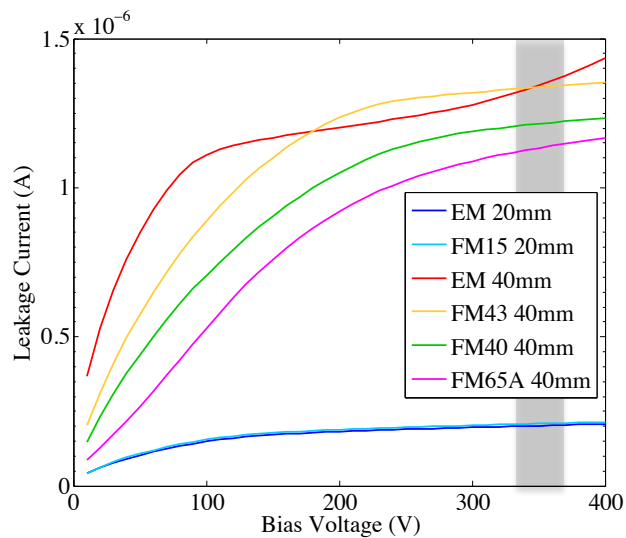
Figure 23: Detector leakage current versus bias voltage.

3.3.2 REPTile Design

The following section describes the general design of the REPTile instrument onboard the CSSWE CubeSat. The detector stack, instrument geometry, and data processing electronics are detailed below. The challenges of miniaturizing an instrument to fit within the constraints of a CubeSat dictate a number of the REPTile design features. Strict mass and volume budgets for CubeSats restrict REPTile's size, and the resulting space, power, and data transmission limitations play a large roll in the design of the electronics. Careful preflight testing and calibration is critical to understand and optimize instrument performance.

Design of the Energetic Particle Telescope

The REPTile instrument is a loaded-disc collimated telescope designed to measure energetic electrons and protons with a signal to noise ratio of two or greater. The instrument consists of a stack of four solid-state doped silicon detectors manufactured by Micron Semiconductor. The front detector has a diameter of 20mm, while the following three are 40mm across. Higher energy particles penetrate deeper into the detector stack and, as they do, they generate electron-hole pairs in the doped silicon [*Vampola*, 1998]. A bias voltage is applied across each detector to accelerate the loosened electrons to an anode, where they are collected and measured by instrument electronics. Using coincidence logic, the electronics determine which detectors the particle impacted, and thus the energy range of the particle.

Figure 21 illustrates the instrument geometry and various components. The detector stack is housed in a tungsten (atomic number Z=74) chamber, which is encased in an aluminum (Z=13) outer shield. The materials were chosen based

on a combination of their ability to shield energetic particles and minimize secondary electron generation within the housing. Tantalum (Z=73) baffles within the collimator prevent electrons from scattering into the detector stack from outside the instrument's 52° field-of-view, and give the instrument a geometric factor of 0.52 [Sr cm^2]. Tantalum is used because it strikes a balance between stopping power and relatively low secondary particle generation.

The instrument and its response to energetic particles have been modeled using Geant4, a software tool developed at the European Organization for Nuclear Research (CERN) to simulate the passage of particles through matter. As beam testing was not within the $840k budget of the CubeSat, detailed modeling of the instrument, as well as radioactive source testing, was conducted to characterize its performance. The current instrument shielding has been shown in Geant4 to stop all electrons with energies < 10MeV and protons up to 85MeV from penetrating through the outer casing and reaching the detectors from directions other than the collimator aperture. The 0.5mm thick beryllium foil at the front of the detector stack acts as a high-pass filter, stopping all electrons < 400keV and protons < 8MeV. This determines the cutoff energy on the lowest energy channel, and mitigates saturation of the detectors from the high count rates of lower energy particles.

The instrument will measure electrons in four energy bins: 0.5-1.5, 1.5-2.2, 2.2-2.9, and >2.9MeV. Protons will be measured and binned into four differential energy channels of 8.5-18.5, 18.5-25, 25-30.5, and 30.5-40MeV. More details on instrument design and simulations are available in Schiller and Mahendrakumar [2010]. The total instrument mass is 1.25kg, with a cylindrical envelope of 4.6cm (diameter) x 6.0cm (length).

Instrument Electronics Design

The REPTile electronics system acts to process and interpret the signals coming from the detectors and calculate electron and proton count rates in each of the four energy channels. A block diagram of the signal chain is depicted in Figure 22, showing the stages the signal passes through before count rates are calculated. The chain is duplicated for each of the four detectors.

When a particle hits a detector, it produces a shower of electrons in the silicon. This charge pulse is collected on the anode and passed to a charge sensitive amplifier (CSA), which acts to amplify the signal and convert it to a shaped voltage pulse. The CSA selected was the A225 from Amptek Inc., which is a space grade component but very sensitive to noise and other environmental factors. Due to this sensitivity, a number of measures were taken to remove background signals and noise from its signal. Details on the testing and correction methodologies are discussed in Section 3.2.

Following the CSA, a secondary amplification is performed by a pulse-shaping amplifier (PSA), which amplifies the signal by 3.4x and further shapes it. The output of this stage ranges from ~0-4V depending on the species and energy of the incident particle. These voltages are passed into a three-stage discriminator chain, which is used to identify whether the particle is an electron or proton based on the voltage measured. Each discriminator compares the output of the PSA to a predefined reference voltage. The reference voltages are set to 0.29, 1.35, and 3.88V, equivalent to energy deposition in the detectors of 0.25, 1.5, and 4.5MeV respectively, and are adjustable from the ground during operations. The first discriminator in the chain returns a 1 if the input voltage exceeds the equivalent of 0.25MeV deposited in the detector, and a 0 otherwise.

The second returns a 1 when the second voltage threshold is exceeded, and similarly for the final discriminator and third threshold. Thus a discriminator chain output of 100 indicates a particle has deposited 0.25-1.5MeV in a given detector.

In the final signal processing stage, the Complex Programmable Logic Device (CPLD) interprets the discriminator values and classifies the particle by species and energy. Particles depositing between 0.25 and 1.5MeV in a detector (a discriminator output of 100) are classified as electrons, and those depositing > 4.5MeV (discriminator output 111) as protons. Discriminator outputs of 110 are discarded as noise, as this energy range (1.5 to 4.5MeV) is contaminated by both electrons and protons. The number of detectors a particle hits determines the energy of the particle, as described by the binning logic applied by the CPLD (see Section 4). 6-second count rates are calculated for each energy channel for both electrons and protons, and these rates are passed on to the Command and Data Handling (C&DH) system to be stored and transmitted down to the ground.

The REPTile electronics board is also responsible for providing the 350V bias across each detector and for containing housekeeping sensors to track temperatures, voltages, and currents of the system. Housekeeping information includes the detector temperatures as well as the electronics board temperature, as the performance of these components is temperature sensitive. Due to the small sizes of the signals being measured, a number of the instrument and electronic components are very sensitive to noise. Careful testing and calibration of the system must be performed to ensure reliability in the data retrieved from the measurements.

3.3.3 Component-Level Testing

The first step in characterizing REPTile's performance was to test each component individually, followed by integrated testing of the system. Components were thoroughly tested to understand and quantify their behavior, and unacceptable performance warranted mitigation. The most sensitive components include the silicon detectors and the CSAs. The detectors were tested both with and without a radioactive source (Section 3.1), and the A225s were characterized over temperature, input signal amplitude, and input signal rate (Sections 3.2.1, 3.2.2, and 3.2.3 respectively).

Single Detector Testing

Each Micron detector was subject to a number of acceptability tests to characterize its performance and determine the limits of its operability. Testing results are shown below for six different detectors --- four flight model (FM) detectors and two engineering models (EMs).

First, the leakage current of each detector was measured. Leakage current is a measure of the performance and inherent noise of the detector, as simply biasing a detector can release electrons from the silicon. Large bias voltages release more electrons, producing larger leakage currents and thus more system noise. The background current produced by each detector was measured to determine how leakage current values vary. Leakage currents should be roughly constant over the operating range so that data processing does not need to incorporate any variations due to increased leakage current. Figure 23 shows the current measured on each flight and engineering model detector for varying voltage biases. The system is designed to operate with 350V across each detector,

with an assumed error in the high voltage supply of ±15V. Thus, in this voltage range, we look for the leakage current to remain relatively constant and below the system requirement of 2µA. Detector EM40 was selected as an engineering model rather than flight detector since the leakage current begins to rise again beyond a bias of 300V, rather than remaining flat. Leakage current is proportional to the area of the detector, so the two 20mm detectors produce ~1/4 the current of the 40mms.

A second test was performed to determine the depletion voltage of each detector. The depletion voltage is a measure of the voltage at which the silicon detector is fully biased. The bias voltage across the detector is intended to collect all electrons produced by incident particles, creating a charge pulse proportional in size to the magnitude of the energy deposited in the detector. If the bias voltage is too low, all of the electrons released by an incident particle will not be swept from the detector on a timescale readable by the electronics, and the complete charge may not be collected. The voltage at which all the loose charge is collected as one pulse, and at which the pulse magnitude no longer increases with increasing bias, is known as the depletion voltage. Detectors should be operated above this depletion voltage to ensure pulse magnitude is proportional to incident particle energy. A radioactive alpha source, americium 241 ([241]Am), was placed directly in front of single detectors, and the pulse magnitudes were measured by a multichannel analyzer (MCA), where channel number scales linearly with pulse size. [241]Am has a half-life of 432 years and releases 5.5MeV alpha particles. Figure 24 shows the magnitude of the charge pulses collected (as measured by MCA channel, plotted on the y-axis) versus detector bias voltage.

While ideally all four detectors would be biased at 350V, the output of the high voltage converters varies from component to component. Only three achieved a bias of 350V, with the fourth reaching a maximum of 300V. Based on the depletion voltage measurements shown above, as well as the leakage currents from Figure 23, flight model FM15 was selected to receive a bias of only 300V. This still allows for ±15V variation on each detector bias without affecting the noise or output pulse amplitude.

Testing the Charge Sensitive Amplifier

The function of the CSA is twofold: to 1) amplify the signal and 2) standardize the signal shape, as each particle-detector interaction is not uniform. Ideally, the CSA output signal amplitude is proportional to the input amplitude, which is determined by the amount of energy deposited into the detector from an incident particle.

The reality of measuring very small amounts of charge deposited by a single particle is extremely challenging, and due to the significant amplification required, the CSA output signal is very sensitive to noise. To mitigate board-level noise sources, a copper ground plane is included on the REPTile electronics board, and the plane is grounded to the spacecraft chassis multiple times. Additionally, the board layout is arranged in a way to minimize electro-magnetic interference (EMI) from wiring loops or noisy components. Filtering is applied to the high voltage converters, which bias the detectors at 350V, as they are especially noisy. However, despite the care taken to eliminate electronics noise, the A225 is still inherently sensitive to temperature, input signal rate, and input signal amplitude.
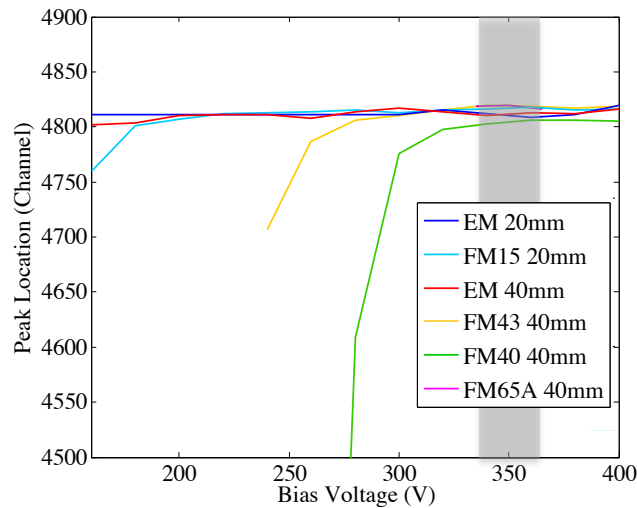
Figure 24: Detector pulse magnitude (as measured by a multichannel analyzer) versus bias voltage. Incident particles were generated by a ^{241}Am alpha source. Curves flatten out beyond the depletion voltage, and remain roughly constant in the operating range (shaded in grey).

With additional resources, the output of the CSA would be filtered so that variations in noise are removed from the signal in flight. However, due to the mass, volume, and power constraints intrinsic to CubeSat missions, there are not enough resources to address every level of noise. Instead, the performance of the CSA must be characterized in detail to understand which features must be actively corrected, and how the science is affected by those that are not. The following sections will describe the details of characterizing the CSA's performance under various conditions: temperature, input signal amplitude, and input signal rate.
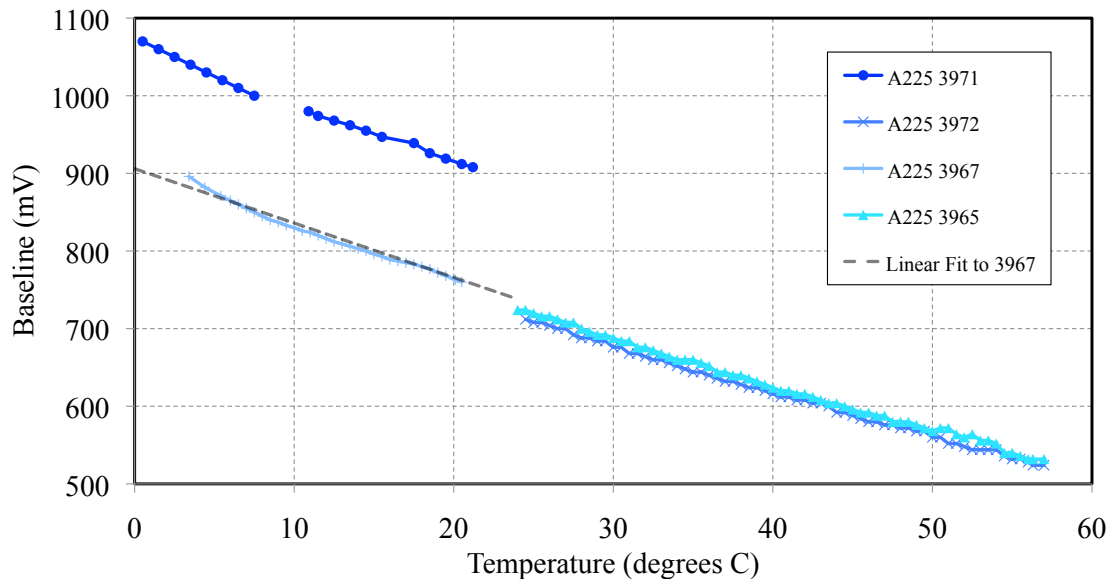
Figure 25: The response of the Amptek A225 CSA's baseline over temperature. The response is approximated as -7mV/C and removed from the output signal. The operational range of the satellite is ~-4 to 19° C.

A225 Temperature Sensitivity

As a result of mass and power restrictions, CSSWE implements a primarily passive thermal system. The satellite uses radiator windows covered in silver-coated Teflon tape, which possesses the desired emission properties, to maintain internal temperatures within the operational range of all components. Using Thermal Desktop, a design environment that creates thermal models, the expected range of the REPTile electronics board is modeled to be -4 to 19°C. All of the components onboard, including the Amptek A225 CSA, are rated to operate over this temperature range. However, the CSA's output is not consistent over this range, so its variations due to temperature are tested to be fully understood and accounted for.

The baseline output of the A225, that is, the steady-state output with no input signals, is inversely proportional to temperature, as shown in Figure 25. The A225 baseline varies significantly over the operational range, by ~200mV, which is a large enough fluctuation to significantly affect the science results without active removal. Thus, a simple subtraction circuit is developed to remove a linear approximation of the variation over temperature for each A225. Although the curve is exponential due to internal components of the A225, to first order between -4 and 19°C the response is linear. The baseline of each A225 is approximated to have a slope of -7mV/°C, with each component having a unique offset. However, over temperature extremes the linear approximation of the A225s' response breaks down. This fact is addressed in post processing of the science data.

A225 Dependence on Input Signal Amplitude

The A225's pile-up time is ~ 7μs; that is, the output signal pulse is ~7sμ wide, during which time the component cannot accurately respond to additional signals. However, the pile-up time is dependent on the amplitude of the input signals. In other words, if a particle deposits energy into a detector above a certain threshold, the A225 lag time is proportional to the deposition energy. An inconsistent lag time decreases the reliability of the data, as particles are not registered during the lag, so the response of the A225 pile-up time is critical to understand in order to determine if a mitigation scheme is necessary.
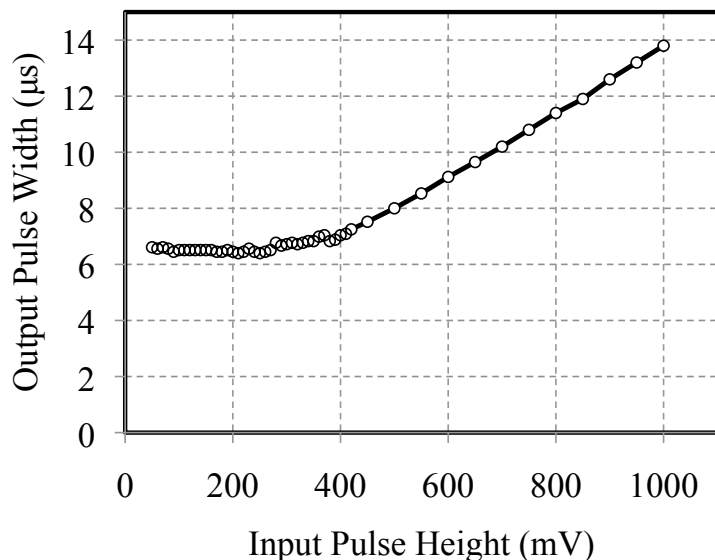
Figure 26: The effect of the amount of energy deposited in a detector on the A225 output pulse width. The pulse width is relatively constant at the ~ 7μs below 15 MeV deposition in the detector. A single particle depositing 15 MeV in a detector is an extremely rare event.
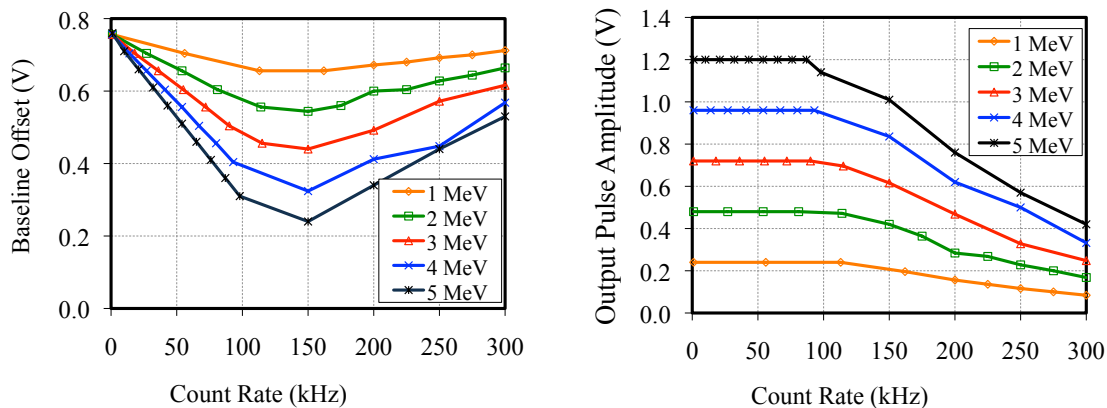
Figure 27: Response of the A225 to particle incident rate. The colored lines correspond to the energy deposited in the detector. The left panel depicts the variation in baseline and the right panel illustrates the decrease in signal amplitude.3

The relationship between the input pulse amplitude and the output pulse width (which defines pile-up time) is depicted in Figure 26. It shows that the output pulse width is relatively constant for deposited energies below 15MeV. Based on Geant4 analysis and a worst-case SEP particle spectrum [*Mewaldt et al.*, 2005], there is a sharp decrease in the number of particles depositing >15MeV in a detector. It is very rare for particles to deposit more than 15MeV in a single detector. Therefore, the A225 pile-up time can be treated as constant for all particle populations.

A225 Dependence on Particle Flux Rate

On orbit, CSSWE will encounter high signal rates (>400kHz) when passing through the outer radiation belts during geomagnetic storm times. Since the A225 also has features that depend on flux rate, characterizing how the component behaves over count rates is required to achieve accurate science data.

Detector	Maximum Expected Electron Count Rate [kHz]	Maximum Expected Proton Count Rate [kHz]
1	427	30
2	72	14
3	37	8
4	22	5

Table 3: Expected count rates for both species based on worst-case energy spectra.

As the signal rate increases, both the A225 baseline and the output signal amplitude are affected. The left panel of Figure 27 depicts the effect of count rate on the baseline. At low count rates (<10kHz), neither the baseline nor the output signal is affected. However, between 10kHz and 150kHz the baseline falls to

~30% of its nominal value (for particles depositing 5MeV). Above 150kHz, the baseline rises, recovering to ~70% of the nominal value at 300kHz (for particles depositing 5MeV). However, as seen in Table 3, only electrons exhibit high enough count rates to significantly affect the baseline. Electrons deposit between 0.25 and 1.5 MeV in a detector, so the baseline effect for electrons is negligible. The values in Table 3 are based on an electron storm-time energy spectrum derived from the AE8 Max model [http://modelweb.gsfc.nasa.gov/models/trap.html], an extremely large solar particle event of October-November 2003 [*Mewaldt et al.*, 2005], and the Geant4 software.

The right panel of Figure 27 shows the response of the output signal to count rate. For the output signal amplitude, there is no variation for count rates less than ~80kHz. However, above this value the amplitude begins to drop. For particles depositing 5MeV, the amplitude decreases quasi-linearly to ~70% of the nominal amplitude from 80kHz to 300kHz.

As demonstrated in Figure 27, the A225 does not produce consistently sized output pulses above ~80kHz, yet REPTile expects a count rate up to 460kHz on the first detector. Thus, an onboard processing technique is required to retain accurate science despite an overload of the first detector chain. We address the saturation by a modified coincidence binning scheme in the CPLD, as discussed in the next section.

Binning Logic in the Complex Programmable Logic Device

As described above, the A225 output signal amplitude is reduced significantly during periods of count rates greater than 100kHz. Particles

incident on a detector during these periods will not be properly measured. Only particles that deposit a large amount of energy in a detector (e.g. high energy protons) will be able to trip the first discriminator, and their amplitudes will inaccurately be reduced significantly. More often, the signal chain will constantly show that no particles are incident on the detector, as more abundant particles (e.g. lower energy electrons) will not deposit enough energy to compensate for the decrease in signal size. This error will only be encountered during high count rate events, such as geomagnetic storms in the outer radiation belt. Additionally, it will only affect the first detector, as higher energy particles are less abundant and the beryllium window and first detector shield the remaining detectors from the largest fluence of particles.

The binning logic in the CPLD takes the discriminator signal and increments the electron counter, proton counter, or discards the input as noise. A binning logic where the signal from the first detector, which is prone to saturation, will not affect the binning logic of the remaining detectors is used to mitigate the flux-dependent effect. The augmented binning logic can be seen in Figure 28, where the detectors are in order from left to right. D1, D2, and D3 represent the discriminators, which compare the particle signal to the adjustable reference voltages corresponding to 0.25, 1.5, and 4.5MeV respectively. The appropriate differential energy channels for both electrons and protons are outlined in the second column. Here a 0 represents that the particular discriminator for that detector was not tripped and the particle deposited less than the reference energy corresponding to that discriminator. A 1 represents the particular discriminator for that detector was tripped and the particle

		Detector											
		1			2			3			4		
Species	**Energy (MeV)**	D1	D2	D3	D1	D2	D3	D1	D2	D3	D1	D2	D3
Electron	0.5-1.5	1	0	0	0	0	0	0	0	0	0	0	0
Electron	1.5-2.2	X	0	0	1	0	0	0	0	0	0	0	0
Electron	2.2-2.9	X	0	0	1	0	0	1	0	0	0	0	0
Electron	>2.9	X	0	0	1	0	0	1	0	0	1	0	0
Proton	8.5-18.5	1	1	1	0	0	0	0	0	0	0	0	0
Proton	18.5-25	1	X	X	1	1	1	0	0	0	0	0	0
Proton	25-30.5	1	X	X	1	1	1	1	1	1	0	0	0
Proton	30.5-40	1	X	X	1	1	1	1	1	1	1	1	1

Figure 28: Coincidence logic for particle binning. D1, D2, and D3 represent the discriminators referencing 0.25, 1.5, and 4.5 MeV respectively. A 1 signifies the threshold must be achieved, a 0 signifies the threshold must not be achieved, and an X signifies that either a 1 or a 0 satisfies the logic in order to bin the particle in the corresponding energy and species.
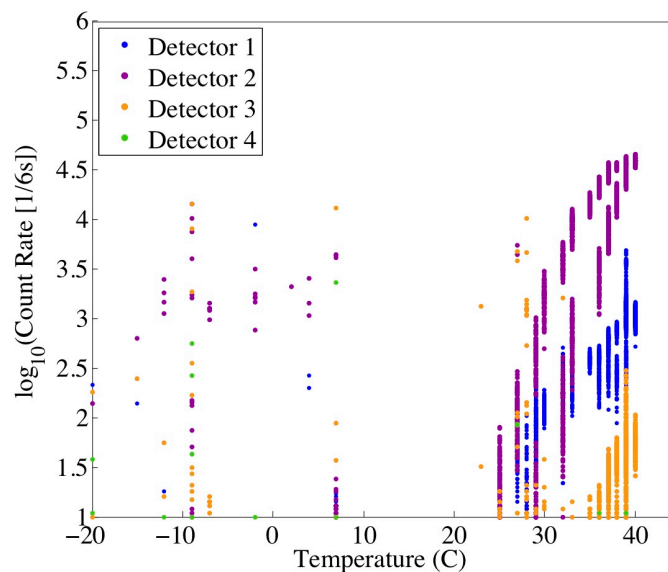
Figure 29: Measured singles count rate as a function of detector temperature for all four detectors. The maximum operational temperature is 25° C, at which point system noise potentially overwhelms science data.

deposited more than the reference energy. An X represents that either a 0 or 1 will satisfy the logic for the particle to be binned in the energy range. The X logic is present on only the first detector, where saturation-level count rates are expected. This scheme permits the binning logic to continue to operate even if the first detector becomes saturated and returns no signals.

3.3.4 Fully Integrated Spacecraft Testing

The previously described analyses were done at component-level or subsystem-level tests. Further testing was done with the fully integrated spacecraft to verify the functionality of the entire signal chain, including the interface between REPTile and Command and Data Handling (C&DH), as well as the ability of the spacecraft to store, access, and transmit data. The data from the following tests were received through radio communication with the satellite and post processed for analysis.

Cosmic Ray Muon Testing

The first fully integrated spacecraft test presented here involved measuring muon counts at the surface of the earth. When a very high-energy (>100MeV) galactic cosmic ray (GCR) interacts with the atmosphere, it produces a shower of particles that dissipate its energy in the atmosphere. The majority of the secondary particles are very short lived and quickly decay or collide with neutrals. Muons are one of the secondary particles, but they have a very low interaction cross-section so they are unlikely to interact with atmospheric particles. Furthermore, their mean lifetime is 2.2µs, long enough for the

relativistic particles to reach the Earth's surface. At the surface of the Earth they typically have energies of 4GeV, which is enough energy to pass through buildings and organic tissue, as well as all four of REPTile's detectors. 4GeV muons at the Earth's surface deposit ~0.6MeV in the silicon detectors when perpendicularly incident, which is enough energy to trip the first reference voltage and thus can be measured by the instrument.

Detector	Averaged Measured Muon Countrate [#/6s]	Averaged Measured Muon Flux [#/cm^2/s]
1 (20mm)	1.07	0.057
2 (40mm)	4.10	0.054
3 (40mm)	3.49	0.046
4 (40mm)	3.42	0.045

Table 4: Muon count rate and flux as measured by the CSSWE satellite.

To measure muon flux, the integrated spacecraft is positioned with the look direction of the instrument oriented vertically. The spacecraft is then commanded into science mode, in which the REPTile instrument is activated and begins to store count rate data. For this specific test, the CubeSat took muon data for 30 minutes, and then the data was requested and downloaded through the radio frequency (RF) link and analyzed. Since the muon flux is proportional to the receiving area of the detector, we expect to have 4x more counts on the 40mm detectors than the 20mm. As expected, outlined in Table 4, the larger detectors do see ~4x higher counts. This test confirms the basic functionality of all four detectors.

Thermal Vacuum Testing

A passive thermal control system is well suited to CubeSat missions as it is a simple, no power, and low mass approach to internal temperature control. However, these benefits are at the cost of performance, as the temperature of specific components cannot be precisely controlled. As presented in previous sections, the REPTile payload is extremely sensitive to various parameters, especially temperature. The detector signal becomes noisy with increased temperature, as valence electrons have a lower potential to overcome to be released from the silicon. As the noise rate becomes significant, it affects the A225 baseline and output signal. Clearly, there are many coupled factors that will affect the data quality as the temperature of the instrument varies. For this reason, it is critical to verify that the instrument, as well as the entire system, behaves acceptably over the operational temperature range.

To make this verification, the fully integrated CSSWE spacecraft is installed in a thermal vacuum chamber, with no particle beam or radiation source for the instrument to measure. The chamber evacuates the air to a pressure of $\sim2\times10^{-7}$torr $\sim2.6\times10^{-10}$atm and uses a chiller-controlled platen to cycle between -25 and 40°C approximately once a day, dwelling at the extremes for 4 hours. Housekeeping information and spacecraft vitals are monitored through the RF link established with the spacecraft inside of the chamber. When possible, the system enters science mode to best simulate on-orbit operations. The data is requested approximately once every 8 hours, as it will be on orbit.

The performance of the system over temperature determines two important items: 1) the temperature at which detector noise overwhelms the system and 2) the count rate that saturates the electronics. The first point,

diagnosing the maximum temperature for nominal operations, can be derived from Figure 29. The figure depicts the amount of system noise at a temperature range from -20 to 40°C. For this figure, no binning logic was applied; that is, the plot depicts individual hits on a detector large enough to trip any of the reference voltages. The individual hit data are also known as singles counts.

The singles count noise increases dramatically above ~25°C, at which point it could potentially overwhelm science data. Thus, 25°C represents the highest reliable operating temperature of the instrument. Although periods of temperature greater than 19°C are not expected, science data received above 25°C will be flagged with a warning and undergo additional processing to attempt to remove this component of system noise. Component and detector temperatures will be monitored on orbit to verify their operating temperatures.

The second point, to determine the count rate at which the combination of factors prevents signals from tripping the first reference voltage, is addressed in Figure 30. For this figure, the noise threshold limit (specifically, the reference voltage for the first discriminator) was reduced from 0.29V to 0.16V. As seen in the figure, the noise becomes significant at ~10°C due to the lower threshold. Additionally, the saturation becomes apparent at a count rate of 300kHz, when the count rate is expected to increase since the detector temperature is still rising, but there is an unexpected sharp decrease in counts. As previously discussed, this interesting saturation effect is due to the A225 output dependence on incident count rate. On orbit, since we expect for some saturation to occur in the outer radiation belt, especially during storm time activity, we will recognize this characteristic feature representing saturation and apply a warning flag to the data.
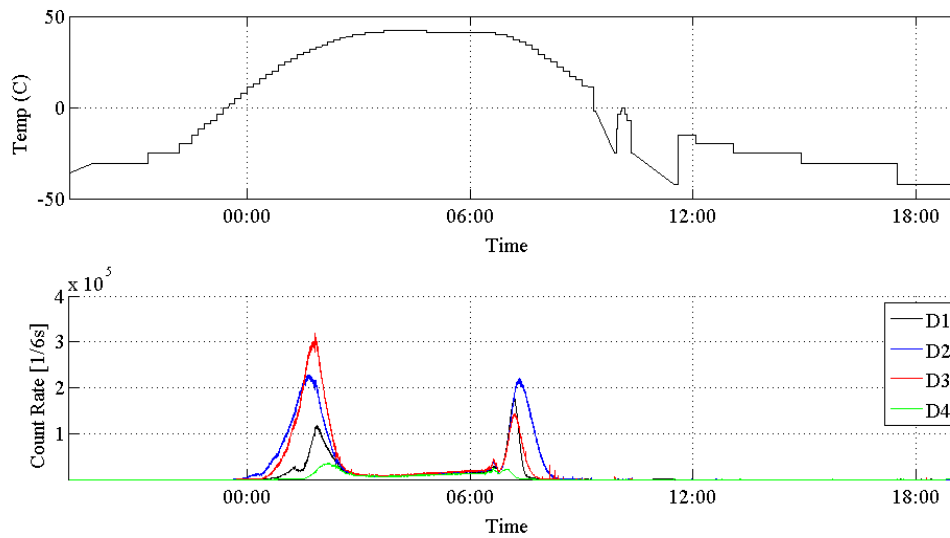
Figure 30: The top panel shows detector temperature over time. The noise threshold (reference voltage 1) was lowered from 0.29 to 0.16V. Data gaps between 09:00 and 12:00 are due to unrelated testing procedures. The bottom panel shows the measured noise singles counts in all four detectors. The nosie increases with temperature, but the electronics become saturated between ~02:00 and 07:00 and do not register counts.
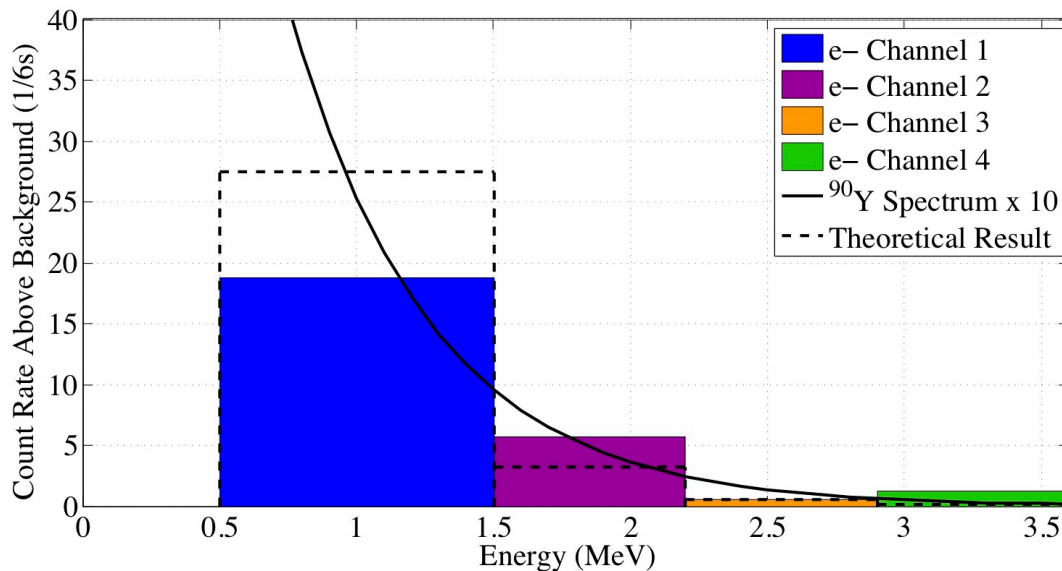
Figure 31: The 90Y spectrum (amplified by 10 for reference) plotted over the measured electrons from REPTile in the fully integrated CSSWE test. The theortecial result for each energy bin is plotted with dashed lines.

Radioactive Source (Strontium 90) Testing

As a NSF funded CubeSat mission, CSSWE has been designed, built, and tested for a budget well under that of other space weather projects. As a result, energetic particle beam tests are out of the scope of the REPTile budget. This fact motivates the extensive Geant4 simulation of the REPTile instrument discussed in detail in Schiller and Mahendrakumar [2010]. Without beam test capabilities, the most extensive system level test available is with a radioactive source. The source test is performed using a strontium 90 (^{90}Sr) source fitted close to the bore sight of the instrument to prevent attenuation in air. ^{90}Sr has a half-life of 28 years and decays into yttrium 90 (^{90}Y), emitting an electron with maximum energy of 0.546MeV. ^{90}Y has a half-life of 2.7 days and decays into Zirconium 90 (^{90}Zr), emitting an electron with maximum energy of 2.28MeV. Both isotopes emit electrons in a continuous kinetic energy spectrum from zero to the maximum.

Based on Geant4 simulations, very few of the electrons originating from the ^{90}Sr propagate through the beryllium window with enough energy remaining to deposit >0.25 MeV on the first detector. Thus, an assumption is made that all measured particles from the ^{90}Sr source originate from the ^{90}Y decay.

From independent measurements, the energy spectrum for the ^{90}Y source is derived and is equal to $798.3e^{-1.937E}$. Using the instrument response function, the ^{90}Y spectrum is integrated to determine the theoretical count rate in each energy bin. The results are shown in Figure 31, where the ^{90}Y spectrum has been amplified 10x to enhance its features on this scale. The background count rate is subtracted and instrument dead time is corrected for each differential energy bin. The measurements agree to theoretical results within expectation, despite the

challenges of designing such a sensitive payload with strict CubeSat requirements.

3.3.5. Summary

This paper describes the *R*elativistic *E*lectron and *P*roton *T*elescope *i*ntegrated *l*ittle *e*xperiment (REPTile) instrument onboard the Colorado Student Space Weather Experiment (CSSWE) CubeSat, which has been fully built and tested and is scheduled to launch in August, 2012. For a cost of less than \$1M, the CSSWE mission will provide valuable differential energetic electron and proton measurements from a simple and robust payload to help understand the dynamic near-Earth space environment.

Making such measurements from a CubeSat platform poses a number of challenges for both instrument design, as well as data calibration and analysis. Due to the simple, miniaturized design of the REPTile instrument and onboard data processing, the instrument must be thoroughly characterized to determine the quality of the measurements returned under a variety of conditions. Only through comprehensive testing and calibration are we able to understand the limitations of the instrument and correctly interpret the data received.

The REPTile instrument has undergone extensive testing to confirm detector operability and measure inherent system noise over temperature, energy deposition in the detectors, and incident particle flux. We have characterized REPTile's performance through instrument-level tests of the detectors and charge sensitive amplifiers, and have determined which aspects require correction from valuable onboard resources and which can be addressed in ground processing. This step is critical to ensure accurate data is retrieved

from the CSSWE CubeSat mission. As a result, adjustments have been made to the onboard data processing to account for issues like temperature variations, detector saturation, and increasing noise floors. We have also verified instrument functionality in completely integrated spacecraft tests, examining noise levels in a thermal vacuum chamber and count rates from cosmic ray muons and a radioactive source.

The successful comprehensive system tests fully validate REPTile's ability to provide reliable and accurate measurements. Such rigorous testing confirms that valuable scientific data will be returned from the CSSWE mission, and that legitimate and valuable science can be conducted as a CubeSat payload. Despite the restrictions inherent in CubeSats, REPTile --- an innovative, affordable, robust, and simple instrument --- will supply critical measurements which will enhance our ability to understand and predict the dangerous effects of energetic particles on space assets.

3.4 Science Operations and Initial Results:

Design and Scientific Return of a Miniaturized Particle Telescope onboard the Colorado Student Space Weather Experiment (CSSWE) CubeSat
by Q. Schiller, D. Gerhardt, L. Blum, X. Li, S. Palo, published in *35th IEEE Aerospace Conference*, 2014

Kohnert, Vaughn Hoxie, and Gail Tate. Finally, the authors acknowledge HAM radio operators around the world who have dedicated time and effort to communicating with CSSWE and other amateur spacecraft.

Abstract

The Relativistic Electron and Proton Telescope Integrated Little Experiment (REPTile) is a loaded-disc collimated solid-state particle telescope designed, built, tested, and operated by a team of students at the University of Colorado. It was launched onboard the Colorado Student Space Weather Experiment (CSSWE), a 3U CubeSat, from Vandenberg Air Force Base on September 13th, 2012, as part of NASA's Educational Launch of Nanosatellites (ELaNa) program.

REPTile takes measurements of energetic particles in the near-Earth environment. These measurements, by themselves and in conjunction with larger missions, are critical to understand, model, and predict hazardous space weather effects. However, miniaturizing a power- and mass-hungry particle telescope to return clean measurements from a CubeSat platform is extremely challenging. To overcome these challenges, REPTile underwent a rigorous design and testing phase. This paper highlights some of the design and testing which validates the data as a valuable contribution to the study of space weather.

CSSWE uses a keep-it-simple design approach to minimize risks associated with low budget and student built missions. A coherent testing plan confirmed that the spacecraft would remain healthy and take reliable measurements in orbit. This paper also highlights the system-level design and testing that verified spacecraft performance pre and post launch.

Despite the risks inherent CubeSat missions, REPTile to date has returned over 300 days of valuable science data, more than tripling its nominal mission lifetime of 90 days. Initial in-flight instrument results are presented, including engineering hurdles encountered in receiving and processing the data. Also, the preliminary scientific contributions of the mission are covered in this paper to demonstrate the capabilities of a low-budget CubeSat mission. As an affordable, robust, and simple instrument and mission design, CSSWE demonstrates that small satellites are a reliable platform to deliver quality science.

3.4.1 Introduction

In general, CubeSat missions are regarded as premature for performing high quality science on orbit. They have been thought of as either educational tools or simple proof-of-concept platforms to increase component technology readiness level (TRL). However, recent successes by science-targeted CubeSat missions, many of which are enabled by the National Science Foundation (NSF), prove that CubeSats can provide influential science on a limited budget. One such CubeSat is the Colorado Student Space Weather Experiment (CSSWE).

CSSWE is a 3U (10cm x 10cm x 30cm) CubeSat developed at the University of Colorado (CU) as a collaboration between the Laboratory for Atmospheric and Space Physics (LASP) and the Aerospace Engineering Sciences Department. A rendering of the spacecraft can be seen in Figure 32. Funding for CSSWE was received in January 2010 for $840k from the NSF. CSSWE's primary science objective is to study space weather in Earth's magnetosphere [*Li et al.*, 2013]. The science payload, the Relativistic Electron and Proton Telescope
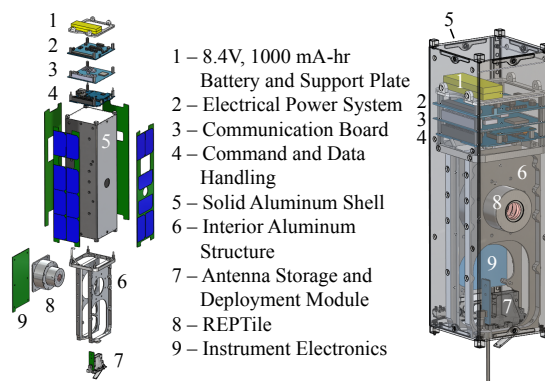
Figure 32: Computer renderings of CSSWE.

integrated little experiment (REPTile) [*Schiller and Mahendrakumar*, 2010], is a miniaturized version of the Relativistic Electron and Proton Telescope (REPT) [*Baker et al.*, 2013] on board NASA's Van Allen Probes mission [*Mauk et al.*, 2012]. REPTile measures energetic electrons and protons within Earth's magnetosphere from a low Earth orbit (LEO) altitude of 478 km x 786 km and a 64.7 degree inclination. The measurements compliment the Van Allen Probes mission, as well as other spacecraft, balloon, and ground-based measurements.

As with many CubeSat projects, there are parallel science and educational goals. CSSWE's educational objective required a student-led team to deliver the CubeSat system. To fulfill this requirement, CSSWE was designed, built, tested, and operated by students at the University of Colorado. Over 60 multidisciplinary students were involved in the mission during their undergraduate or graduate student careers. Professors in the Aerospace Engineering Department and professionals at LASP, and other facilities, provided mentorship for the students.

On September 13, 2012, CSSWE was launched from Vandenberg Air Force Base as the sixth of NASA's Educational Launch of Nanosatellites (ELANA)

program [*Skrobot et al.*, 2012]. It was, along with 10 other CubeSats, a secondary payload to a National Reconnaissance Office (NRO) satellite. The launch vehicle was an Atlas V-401 operated by the United Launch Alliance (ULA). REPTile, the science payload, was activated on October 4, 2012, after a three-week spacecraft commissioning phase. As of the writing of this paper, CSSWE continues to operate and return quality science data. To date, CSSWE has taken almost 300 days of science data, more than tripling the three-month expected mission lifetime. Operationally, the mission is a resounding success. Moreover, the quality of science data returned, as well as the tenacity of a student-developed mission, far surpasses the expectations for any CubeSat mission.

3.4.2 Science Background

In the modern era there is considerable investment in aircraft. Applications range from commercial to recreational and military to scientific. One commonality among aircraft is that airplane pilots constantly check the weather report to minimize environmental risk to themselves and the airplane. Like aircraft, spacecraft are also subject to hazardous environmental conditions. These conditions can be adverse to both spacecraft and astronauts, but the near-Earth space environment lacks a reliable and accurate space weather report.

The lack of predictive capability is caused by the immaturity in understanding the dynamics in Earth's magnetosphere, and beyond that, the Sun's heliosphere. In fact space weather, which can be equally as hazardous as its terrestrial counterpart, is far less understood. Society's increasing dependence on space-based technology motivates the major investment being put into risk mitigation for space-based assets. A significant portion of which is applied to

understanding exactly what physical processes are responsible for the adverse space weather effects.

The first space weather threat is relativistic electrons, moving close to the speed of light and having energies on the order of one million electron volts (MeV). These particles can damage to spacecraft components via surface charging or deep dielectric discharging. A second threat is energetic ions, with energies up to GeVs, that can disrupt electronics or cause single event upsets (SEUs) in component memory. Very high-energy protons can have harmful, potentially lethal, radiation effects on astronauts in space [*Baker*, 2002]. Unfortunately, unlike terrestrial weather, the governing dynamics are currently not sufficiently understood to accurately and reliably predict these dangers. In fact, there are two major outstanding questions concerning the hazardous populations.

The first concerns source, loss, and transport processes of hazardous energetic electrons in Earth's Van Allen radiation belts. The Van Allen radiation belts consist of two torus shaped regions which encircle the Earth; the inner radiation belt is confined to approximately 1.2 to 2 Earth radii (R_E) and the outer radiation belt extends from roughly 3 to 7 R_E. Both belts contain relativistic electrons; the inner belt contains a moderate but persistent population (stable on the timescale of years) while the outer belt can be far more intense, but it is extremely variable. The relativistic electron population in the outer belt can be created or eliminated in a matter of hours. Definitive answers to questions like "what mechanisms cause sudden enhancements or precipitation into the atmosphere?", "what is the intensity of the atmospheric precipitation?", or "is activity correlated with solar or geomagnetic activity?" will be significant

breakthroughs in predicting space weather. Moreover, the outer belt region is of particular interest because it contains many popular spacecraft orbits, such as geosynchronous orbit (GEO) and global positioning system (GPS). These orbits reside in the heart of the outer radiation belt and, as a result, are especially exposed to energetic electron space weather effects.

A second outstanding topic is in regards to solar flares and their relationship with solar energetic particle (SEP) events. Ultimately, like terrestrial weather, even Earth's magnetospheric system is driven by the Sun. When solar magnetic field lines are violently reconfigured near the Sun's surface, they can cause a sudden and rapid release of up to 10^{25} J of energy. These events are known as solar flares and they can also propel electrons and protons to velocities close to the speed of light. This release of relativistic particles is known as a SEP event. If they are directed Earthward, SEP events can penetrate deep into the Earth's atmosphere, guided by magnetic fields at high-latitudes. The result can disrupt radio and GPS communication and increase radiation doses for crews and passengers on polar flights. The relationships between solar flares and SEPs are not fully understood. An outstanding question is: how does flare location and magnitude relate to the timing, duration, or energy spectrum of SEPs reaching Earth?

Addressing these critical space weather questions requires in-situ measurements of relativistic outer belt electrons and energetic solar protons. Multiple observational spacecraft to sample an array of latitudes, longitudes, and radial extents would be an ideal configuration. In reality, however, quality in-situ space weather measurements are few and far between. Currently, CSSWE provides the only differential LEO observations of both SEP protons and

radiation belt electrons. Furthermore, conjunctive measurements between CSSWE and other missions, such as GOES, THEMIS [*Angelopoulos,* 2008], the Van Allen Probes, and BARREL [*Millan et al.,* 2013] will provide the opportunity for multi-point observations of radiation belt electrons and SEP protons.

Specifically, many of CSSWE's measurements are directly relevant to instruments from the Energetic Particle, Composition, and Thermal Plasma (ECT) suite the Van Allen Probes [*Spence et al.,* 2013], particularly for radiation belt electrons. The Van Allen Probes, in a GEO-transfer-like orbit (700km x 5.8 R_E, 10° inclination), traverse the heart of the radiation belts near the geographic equator. Although the mission provides the most sophisticated measurements of the radiation belts to date, the onboard instruments cannot resolve which electrons will precipitate into the atmosphere. At the equator, precipitating outer belt electrons have pitch angles (the angle between the momentum vector and the local magnetic field line) of less than roughly 5 degrees. These electrons travel along magnetic field lines and are lost to collisions with neutrals near the footpoint of the magnetic field line in the polar regions. Similar processes for lower energy electrons cause the aurora. CSSWE directly measures the precipitating particles as they pass by the CubeSat on their way into the atmosphere. These measurements quantify the number of electrons lost at a given time, and conjunctive measurements with the Van Allen Probes in the heart of the radiation belt allow for a quantitative estimate of precipitation loss and its impact on the total population, and thus a better understanding of full electron dynamics.

CSSWE also measures the energy spectrum and time evolution of SEP particles at LEO. These measurements are used to better understand the

relationship between flares and the deeply penetrating SEP particles at Earth. Ultimately, they provide insight to the dynamics of SEP particles in the magnetosphere and will lead to a better understanding of their behavior to improve models and predictions.

3.4.3 Science Payload – REPTile

Instrument Design

To measure SEP protons and radiation belt electrons, the students on CSSWE miniaturized the REPT instrument [*Baker et al.*, 2013] onboard the Van Allen Probes. The resulting payload, the Relativistic Electron and Proton Telescope integrated little experiment (REPTile), measures protons from 9 to 40 MeV and electrons from 0.58 to >3.8 MeV in three energy channels as outlined in Table 5.

REPTile is a loaded-disc collimated solid-state particle telescope. It consists of four doped silicon detectors (labeled 1 in Figure 33) housed in a heavy tungsten (atomic number [Z] = 74; atomic symbol = W) shielding chamber (labeled as 2), which is in turn encased in an aluminum (Z=13; Al) outer shield (labeled as 3). At the front of the detector stack is a 0.5mm thick beryllium (Z=4; Be) window, which acts as a high-pass filter by absorbing low energy particles that would saturate detector electronics. The Be window (labeled as 5) absorbs electrons with energy less than ~0.4 MeV, and protons with energy less than ~8 MeV. Higher energy particles punch through the Be window and into the detector stack. The instrument's field of view is 52 degrees, which is defined by
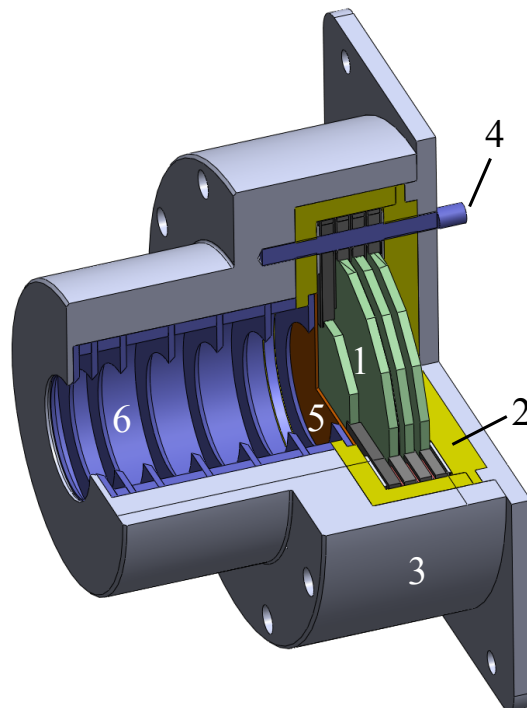
Figure 33: Computer rendering of REPTile instrument

the tantalum (Z=73, Ta) lined Al collimator (labeled as 6). Seven knife-edged Ta collimator baffles prevent stray particles from scattering off of the collimator walls and entering the detector stack. The particles to be measured by REPTile are capable of penetrating through relatively large amounts of shielding (which is how they are able to damage internal spacecraft components). Measuring them is a trade-off between shielding mass and measurement noise caused by shield-penetrating particles. Thus, energetic particle measurements are challenging from the mass-restrictive CubeSat platform. As a result, the total mass of the REPTile instrument is 1.25 kg, approximately 42% of the total spacecraft mass. The instrument is contained in a cylindrical volume of 4.6cm (diameter) x 6.0cm (length) and is held straight by three Ta alignment pins (labeled as 4 in Figure 33).

Data are returned from CSSWE as raw six-second count rates in four energy channels for both electrons and protons. It is of note that only three of REPTile's four detectors survived launch; the third detector in the stack failed to operate consistently post-launch. The loss of the detector rendered one electron energy channel and one proton energy channel invalid. However, due to the simple yet robust design doctrine engrained in the program, REPTile was able to operate with the remaining three detectors and the data are recalibrated accordingly on the ground.

The onboard binning logic automatically determines the species and energy of the incident particle, accumulates the counts over six seconds, and stores the eight count rates (four electron energy channels and four proton energy channels) in the onboard SD card. When requested, the raw counts are transmitted to the ground where they are processed into differential flux units. Details of this conversion are specified in *Li et al.* [2013].

Species	Channel 1	Channel 2	Channel 3
e-	0.58–1.63 MeV	1.63–3.8 MeV	>3.8 MeV
H+	9–18 MeV	18–30 MeV	30 – 40 MeV

Table 5: REPTile Species and Energy Channels

Traditional testing tactics for particle telescopes are not within the scope of CSSWE's relatively small $840k budget. Methods typically include beam tests using a high-energy particle beam to simulate the radiation environment encountered in orbit. The particle flux from the beam can be compared with instrument results to characterize the behavior of the instrument. Instead, CSSWE uses a software package called Geant4 [*Schiller and Mahedrakumar*, 2010].
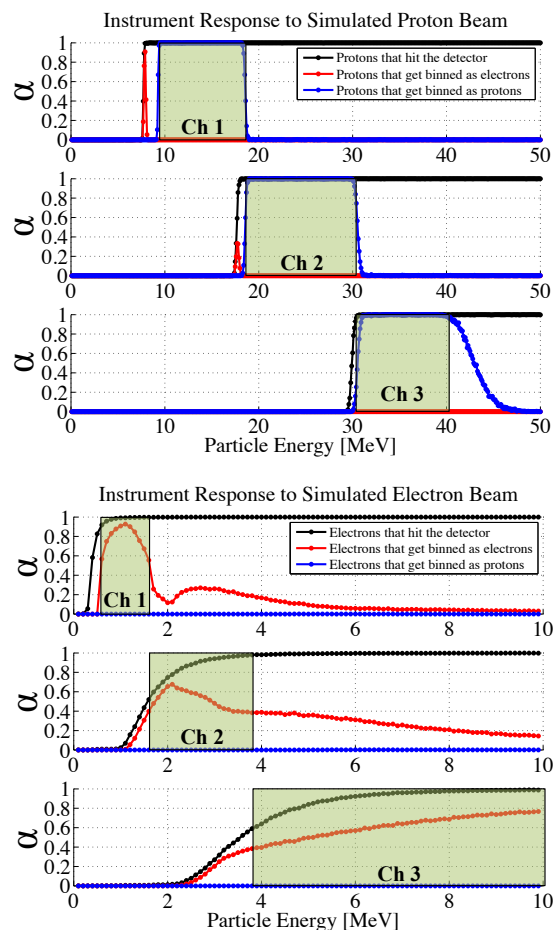
Figure 34: Instrument response, as simulated using Geant4, for protons (top) and electrons (bottom). The top panel of each set corresponds to the first detector, middle to the second, and bottom to the fourth. The black line represents the % of particles as a function of energy that impact the detector, blue the % binned as protons by the onboard binning logic, and red the % binned as electrons. Energy channel widths are highlighted in green.

Geant4 was developed by physicists at the European Organization for Nuclear Research (CERN) to simulate particle-matter interactions for particle instruments and is the most advanced modeling package available [*Agostinelli et al.*, 2003].

Traditional particle telescopes use pulse height analysis to determine the incident energy of the particle. That is, a particle travels down the collimator, through the Be window, impacts the detector stack, and deposits some of its

energy into the detectors. The amount of energy deposited, or pulse height, on each of the detectors is analyzed to determine species and incident energy. However, this requires either a complex and power-hungry onboard binning logic scheme to analyze the pulse heights in real-time, or a large communication link margin to transmit every particle impact to the ground for analysis. With neither of these options a feasible solution with the limited budgets of CSSWE, REPTile alternatively uses a unique onboard binning scheme.

Instead, REPTile uses the pulse height of each particle to determine species. It uses the depth of penetration into the detector stack to determine particle energy. Based on extensive simulations with Geant4, it was shown that electrons typically deposit less than 1.5 MeV into a detector, and protons typically more than 4.5 MeV. Thus, the binning logic counts particles depositing 0.25 MeV < E < 1.5 MeV as electrons, and particles depositing E > 4.5 MeV as protons. Particles which deposit 1.5 MeV < E < 4.5 MeV are indeterminate and discarded as noise, but accounted for in post-processing. The depth of penetration into the detector stack is then used to determine incident energy, as more energetic particles are able to punch deeper into the detector stack.

The channel energy thresholds are determined using Geant4 and an onboard coincidence logic scheme [*Blum and Schiller*, 2012], and are outlined in Table 5 and Figure 34. α in Figure 34 represents the normalized response efficiency for each detector, which can be thought of as "% of simulated particles". The energy channel widths are determined using the instrument response and are shown in Figure 34 with green boxes. The third detector response is omitted due to its post-launch failure. Note the contrast between the

well-behaved protons and the more random behavior of the electrons. The statistical response of electron interactions with matter is a driving factor for the detailed characterization of the instrument.

Instrument Validation

Beam tests, as previously described, are an efficient way to characterize and validate instrument performance. Although beam tests were not available due to CSSWE's restrictive budget, REPTile was still tested end-to-end. Two methods were used instead: 1) measurements of naturally occurring muon populations and 2) testing with a radioactive source [*Blum and Schiller*, 2012].

Muons, which are a natural byproduct of cosmic ray collisions with Earth's atmosphere, reach the surface of the Earth and do not interact significantly with matter, which means they can penetrate instrument shielding. Thus, muon count rates are proportional to detector size, as opposed to instrument pointing for example. To measure muons, the instrument is simply turned on and allowed to collect statistics. The results of the REPTile muon test are detailed in Table 6. The detectors are circular, with diameter shown in the first column. Expected values are calculated using the measured value of 0.01 muon/s/cm^2/sr [*Rossi,* 1948]. The actual ambient muon rate depends on only a few factors, such as elevation and solar cycle.

Detector	Measured	St. Dev.	95% Conf.	Expected
1 (20mm)	1.07	1.03	0.02	~1.2
2 (40mm)	3.67	1.93	0.04	~4.7
3 (40mm)	3.47	1.85	0.04	~4.7
4 (40mm)	3.42	1.85	0.04	~4.7

Table 6: Averaged Muon Countrates (#/6s)

Radioactive source testing is another alternative to beam testing. REPTile's radiation source was a strontium 90 (^{90}Sr) radiation source. ^{90}Sr decays into ^{90}Y by beta decay (electron release) with maximum energy of 546 keV with half-life of 28 years. ^{90}Y decays into zirconium 90 (^{90}Zr) with half-life of 2.7 days via beta decay with maximum energy of 2.28 MeV. The electrons from beta decay are released in an exponential decay spectrum, which was independently measured prior to the test. The radiation source test was done in flight configuration, including the Be window. The results of the test are shown in Figure 35 for original, four detector processing (top) and the recalibrated on-orbit processing for the three remaining detectors. Agreement between measured counts and expected counts closely agree. Over counting in the second and fourth detector (top panel: channels 2 and 4; bottom panel: channels 2 and 3) is likely due to residual electronic noise on the signal chains. Both muon and radiation source tests verified REPTile system performance.

3.4.4. CSSWE Validation

In addition to instrument tests, rigorous system level validation was performed on the complete CSSWE system. The radio frequency (RF) link, including ground station packet decoding and parsing, was used whenever possible during top-level validation testing, including aforementioned instrument tests.

On orbit, the spacecraft is operated from a ground station at the LASP. The ground station consists of two phased and circularly polarized Yagi antennas operating single-duplex at 437.350 MHz in the amateur frequency band
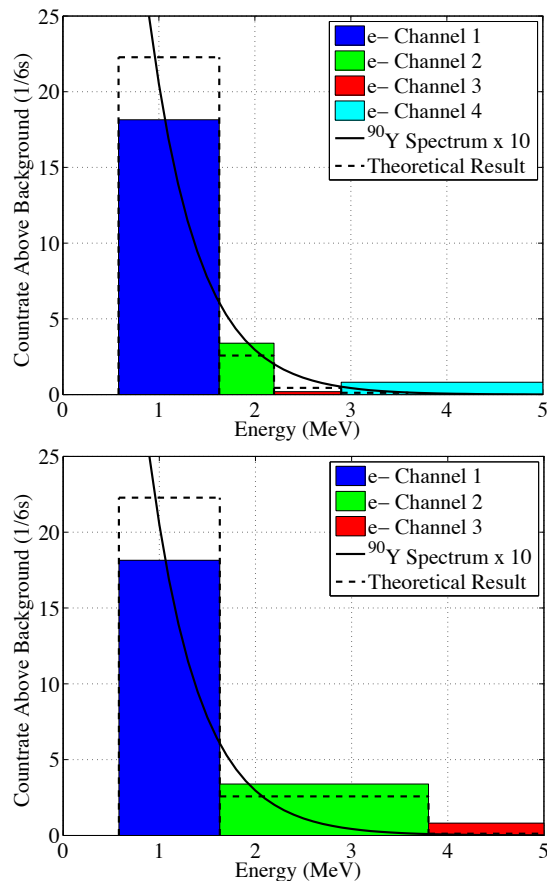
Figure 35: Instrument response to the ^{90}Sr radiation source test. Top panel: results using data from all four detectors. Bottom panel: recalibrated results using data from the three operational detectors on-orbit with the reconfigured instrument response.

with a bandwidth of 15kHz and capable of 9600bps data rates. This system was designed and built by CSSWE students, with input from local amateur radio operators, specifically for the CSSWE mission, but is also adaptable to be used in future CU small satellite missions. The end-to-end RF link, which employs communication between the onboard radio (via the spacecraft antenna) and the decoding software (via the ground station), was also tested repeatedly. These tests often included a simulated on-orbit deployment from the launch vehicle. To perform the long-distance communication tests, the spacecraft was driven to a

location with a line-of-sight distance of approximately 5 miles to the LASP ground station. The spacecraft was "ejected" from the launch vehicle by the release of a mechanical switch on a footpeg of the structure. As designed, the antenna deployed two hours after power up and began transmitting with the ground station and receiving commands. Additional attenuation was added to match orbit-to-ground communication conditions after the link was established. The satellite performed well throughout the test, even with attenuated communication.

Unlike most CubeSats, CSSWE also underwent thermal vacuum (TVAC) chamber testing. It experienced eight temperature cycles in the chamber covering both operational extremes. The system was required to perform functionality tests at hot dwell, cold dwell, and in transition. It passed all functionality milestones during TVAC testing. A whip antenna and RF-attenuator tiles were also included within the TVAC chamber, allowing CSSWE to test RF performance while in the TVAC chamber. The successful results in temperature and vacuum conditions validated system performance in the real on-orbit environment

3.4.5. On Orbit Performance

The rigorous validation procedures provided confidence that the spacecraft would operate successfully on orbit. Furthermore, they generated a baseline for comparison during spacecraft operations. After the launch on September 13th, 2012, comparisons were made between on-orbit results and the ground-based nominal operations data. The two were homologous, verifying
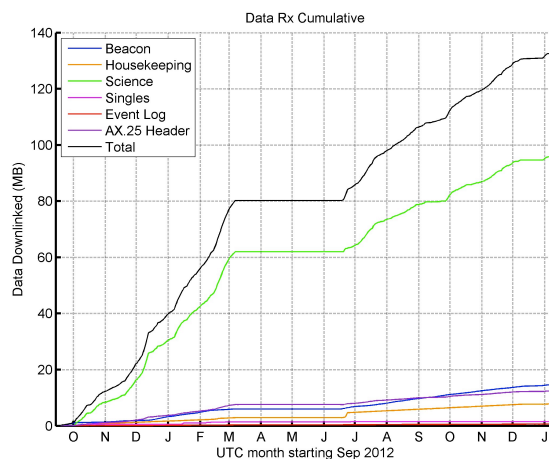
Figure 36: Cumulative data received from the spacecraft from launch to mid-November 2013.

successful on-orbit spacecraft operations. In-detail descriptions of on-orbit performance are outlined in *Gerhardt et al.* [2014]. The most significant anomaly during spacecraft commissioning was the recognition that the third detector in the REPTile detector stack suffered a complete failure. However, CSSWE's robust design allowed continuing operations with the remaining three detectors.

Anomalies and Current Operations

Contact was temporarily lost with the CubeSat on March 7, 2013, when the onboard radio ceased responding to internal or external commands. During this anomaly, the spacecraft could not transmit or receive communication. However, all other subsystems were nominal; in fact, REPTile continued to take science data for an additional few days after communication was lost. The radio returned to nominal operation on June 18, 2013, when low battery voltage caused a full system reset. Within days of reestablishing contact, REPTile was activated
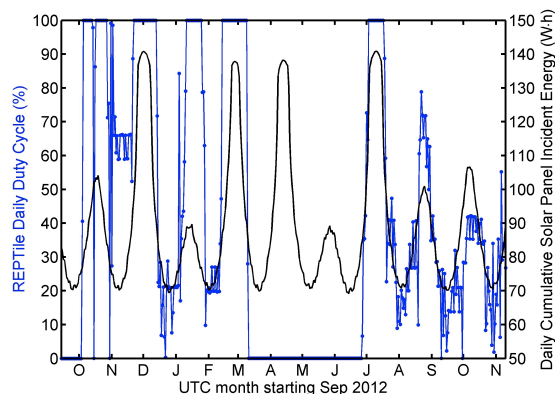
Figure 37: Daily averaged % time REPTile was on (duty cycle) in blue and daily averaged incident energy acquired by the solar panels in black.

after 110 days of inactivity.

Figure 36 shows the amount of data received from the spacecraft since launch. The radio malfunction is apparent, as is a noticeable increase in downlinked housekeeping data immediately after communication was reestablished. REPTile went through a prompt re-commissioning and was quickly reactivated. Notice that the majority of the data down linked over the course of the mission is in the form of science packets, which reflects on the overall success of the mission.

Current mission operations are dictated heavily by the spacecraft's solar beta angle, which is defined as the angle between the orbital plane and the sun vector. Primarily, solar beta angle determines the amount of sunlight the spacecraft receives. This angle varies over time for all spacecraft orbits, but most strongly affects LEO spacecraft, which can spend more of their orbit in eclipse. With an already thin power budget, a low beta angle often determines whether CSSWE is power positive with REPTile activated.

During periods of especially low beta angle, the incident energy on the solar panels is insufficient to allow REPTile to run 100% of the time. Thus, REPTile is duty-cycled to help conserve battery capacity. The effect of the solar beta angle on REPTile duty cycling can be understood better in Figure 37, which shows the daily averaged percent of time REPTile was on, plotted with the daily averaged solar energy received. In general, less than 90 W·h causes the system to be power negative. However, as the battery and solar cell performance degrades over time, the spacecraft requires more incident energy to remain power positive. To maximize mission longevity, CSSWE spends less time in science mode as these components deteriorate. The system is designed so that, in a power negative state, REPTile is shut off automatically to prevent significant battery discharge. This happens when the battery voltage falls below an adjustable threshold, which was set to 6.8 V in early mission and then to 7 V to improve battery longevity. Extreme variations in REPTile's duty cycle (e.g. mid- and late-October 2012) are due to other anomalies, such as component latch-ups or changes in ground control algorithms [*Gerhardt et al.,* 2014].

3.4.6. Science Results

After the reentry of the SAMPEX spacecraft on November 11, 2012 [*Blake et al.,* 1996; *Baker et al.,* 2012], CSSWE is the only spacecraft in LEO to measure differential flux of energetic protons and electrons in specified energy ranges. REPTile measurements are clean, as can be seen by the clear species separation, which will be discussed later in this section. Additionally, the data have a low
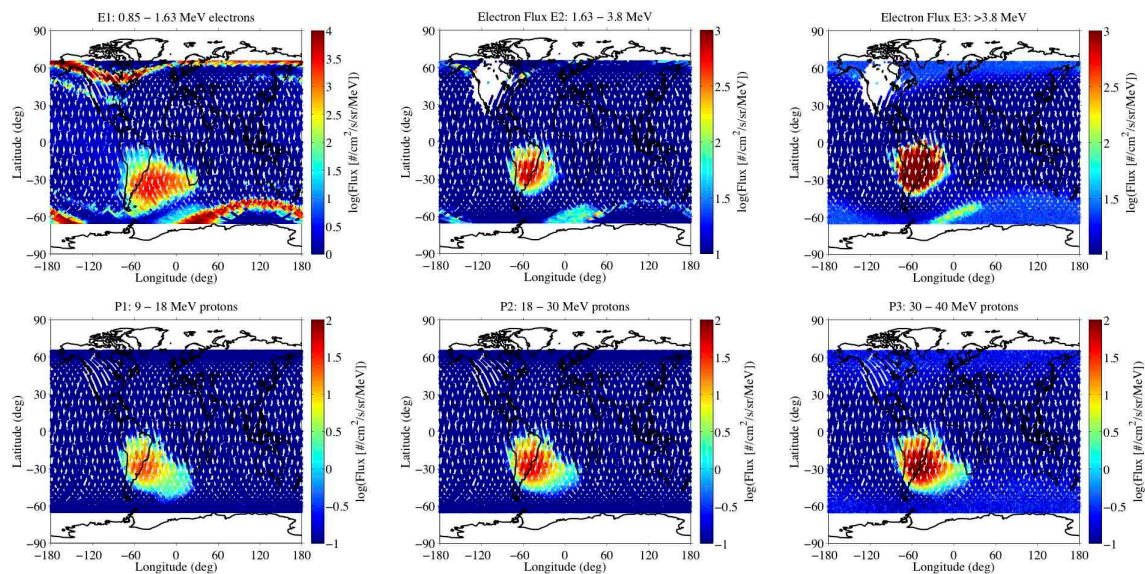
Figure 38: Science results from January 18 to 23, 2013. Spacecraft position is plotted in geographic longitude (x-axis), geographic latitude (y-axis), and flux in color. Electrons are plotted in the top row, protons in the bottom row. Energy channels are increasing to the right. Data was removed for E2 and E3 during transmission, as these channels are sensitive to transmission noise.

noise floor (~1s-10s counts per sec) and high dynamic range (over 4 orders of magnitude). These qualities are critical to produce accurate and reliable measurements of high-energy particles and verifying that REPTile measurements are adequate for scientific use. Specifically, flux observations measured from low altitude are used to quantify atmospheric precipitation loss; in this regard, CSSWE fills a valuable scientific niche. The data have been used in long-term and event specific studies, which will be discussed in this section.

Electrons in the Radiation Belts – Observations

An example of typical REPTile science results, plotted in geographic coordinates, is shown in Figure 38. These data are from January 18-23, 2013, and are taken during a period with a relatively static, but intense, outer radiation belt.

The region of increased flux over South America is due to low magnetic field strength caused by the offset nature of Earth's magnetic field. This phenomenon is commonly known as the South Atlantic Anomaly (SAA). The ribbons of electron flux towards the poles are the outer radiation belt. The inner radiation belt is just equator-ward of the outer radiation belt, noticeable only in the upper left panel (E1). While there is some cross contamination (specifically >100 MeV, shield-penetrating protons), the measurements are still clean, as can be seen by the different morphologies presented by the two populations in the SAA. Fortunately, shield-penetrating protons are short lived outside of the inner radiation belt and contamination of outer belt measurements is trivial.

Spacecraft in LEO can observe the Van Allen radiation belts, the heart of which is located at 3-6 R_E, because of basic electromagnetism principles. Most relevant is the magnetic trap, which is a uniform magnetic field that is then compressed on either end, creating regions of increased magnetic field strength called mirror points. Charged particles in the presence of a magnetic trap bounce between mirror points. Earth's magnetic field is a type of magnetic trap, where the mirror points are near the poles. Particles map out the torus shape of the radiation belts while bouncing from pole to pole, passing through the heart of the radiation belt at ~5 R_E as they do so. The radial distance of their equatorial crossing is quantified in the L parameter, which, although dimensionless, is essentially in units of Earth radii [*Roederer*, 1970]. For every measurement at LEO, the particles trajectories can be mapped to the equator to determine the L value measured by CSSWE. This concept is shown in Figure 39.
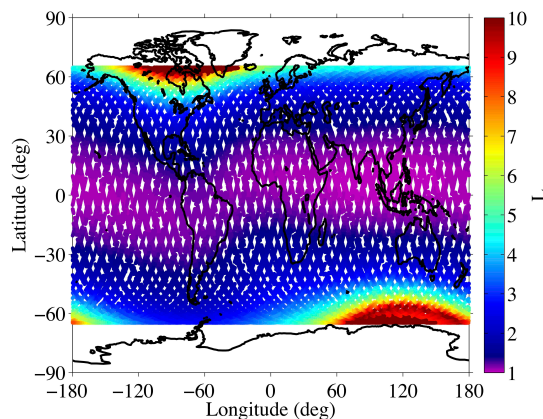
Figure 39: Spacecraft geographic coordinates mapped to L, where L is the radial distance in Earth radii of the particle's equatorial crossing.

A similar visualization of the flux data to Figure 38 can be seen in Figure 40. Figure 40 incorporates the distance to the measured particle's radial crossing, or L, which is a more physical parameter than the geographic location of the measurement. It shows the electron flux as a function of L for all three of REPTile's electron energy channels. The data in Figure 40 are for the same period as Figure 38: during a relatively stable period from Jan 18 to 23, 2013. The intensity of the outer belt has an apparent daily fluctuation that is closely related to the picket fence-like sampling at higher L. Both of these phenomena are caused by a combination of CSSWE's orbit and the variation in longitudinal sampling, which is more apparent in Figure 38. For example, the inner radiation belt is most visible when the spacecraft crosses through the SAA and can measure the inner belt population. Similar effects occur on orbits that pass over Russia and the southern tip of South America, where the CubeSat cannot sample measurements above L~4.5. An interesting feature during this period, which is not always the case, is the inner belt which can be seen in the first electron channel near L=2 in Figure 40, but only to the west of the SAA in Figure 38.
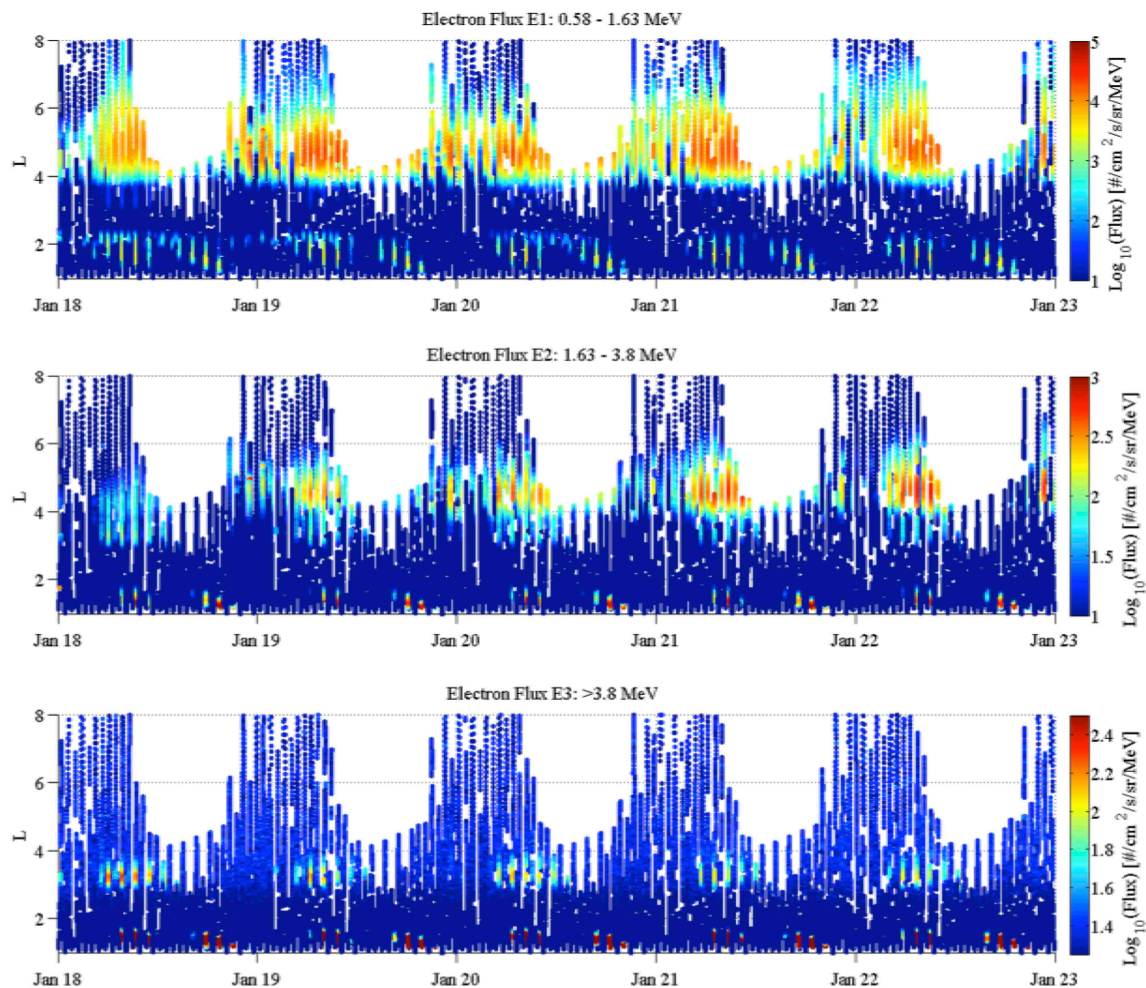
Figure 40: Electron flux as a function of time and L for January 18 to 23, 2013.

Electrons in the Radiation Belts – Applications

As previously discussed, loss, acceleration, and transport mechanisms in the outer belt are intensely entangled. Only by measuring each process individually can the full system dynamics be unraveled. CSSWE's measurements are critical in quantifying atmospheric precipitation, a major loss mechanism. Ultimately, precipitation rates vary depending on geomagnetic conditions. Typically, increased geomagnetic activity increases precipitation, but

it also increases acceleration and transport mechanisms that are closely tied to the location, magnitude, and cause of precipitation.

Geomagnetic storms, which play a pivotal role in magnetospheric dynamics, can be measured by the Dst index [*Sugiura et al.*, 1991]. The Dst index is a quantification of the storms' perturbation on the horizontal component of Earth's magnetic field at the equator. Specifically, it is the difference between the decreased magnetic field due to storm processes and the nominal magnetic field strength, which is approximately 31,000 nT. Stronger storms have a larger effect, and thus are indicated by a more negative index. For reference, a Dst index of < -100 nT (a perturbation of ~0.3%) is considered an intense geomagnetic storm [*Gonzalez et al.,* 1999]. However, the presence of a storm does not guarantee certain effect on the radiation belts. In fact, only half of geomagnetic storms have a net increase on the electron population, 20% cause a net decrease, and 30% result in no change [*Reeves et al.,* 2003]. REPTile observations during the large Oct. 9th, 2012, storm provide insight towards which storms have the net effect of erasing the outer belt content and which storms amplify it by quantifying the relative contributions of loss and source.

A large geomagnetic storm (Dst < -100 nT) occurred on Oct. 9th, 2012, within a week of turning REPTile on. This storm caused an enhancement in the outer radiation belt electron flux of nearly three orders of magnitude in 18 hours [*Reeves et al.,* 2013], as measured by the Van Allen Probes. Although a net intensification, REPTile measurements during this storm separate the contribution of loss mechanisms from the net acceleration that occurred, specifically by quantifying the relative contribution from precipitation loss. Results from CSSWE analysis for the storm and succeeding electron flux increase

are published in *Li et al.* [2013]. The authors showed that, when including atmospheric precipitation, the enhancement was at least 12.7% and 14.6% stronger for 0.58 MeV and 1.63 MeV electrons, respectively. The findings suggest that the mechanism responsible for the sudden flux enhancement was significantly larger than the Van Allen Probe measurements indicate.

While storm-time conditions have a more volatile impact on outer belt electrons, a recent study found that rapid outer belt enhancements occur during non-storm times as well [*Schiller et al.,* 2014a]. The study investigated an enhancement on January 13-14, 2013, that occurred with very little geomagnetic activity yet enhanced outer belt fluxes by more than 330x. Using CSSWE to measure atmospheric precipitation, the authors showed that enhancement was even larger than the flux measurements suggest: 5% and 16% larger for 0.6 MeV and 1.8 MeV electrons, respectively. This study directly addresses the outstanding question regarding correlations between radiation belt enhancements and geomagnetic activity.

CSSWE's measurements are also used to map the physical extent of precipitation regions. *Blum et al.* [2013] used REPTile measurements in conjunction with high-altitude balloon measurements to do this analysis. The Balloon Array for Radiation Belt Relativistic Electron Losses (BARREL) observed relativistic electron precipitation simultaneously with REPTile on January 18-19, 2013. The authors combined the measurements from the two missions to create a spatial and temporal map over which the electron precipitation occurred. Finally, incorporating the precipitation map with estimates of the total outer belt
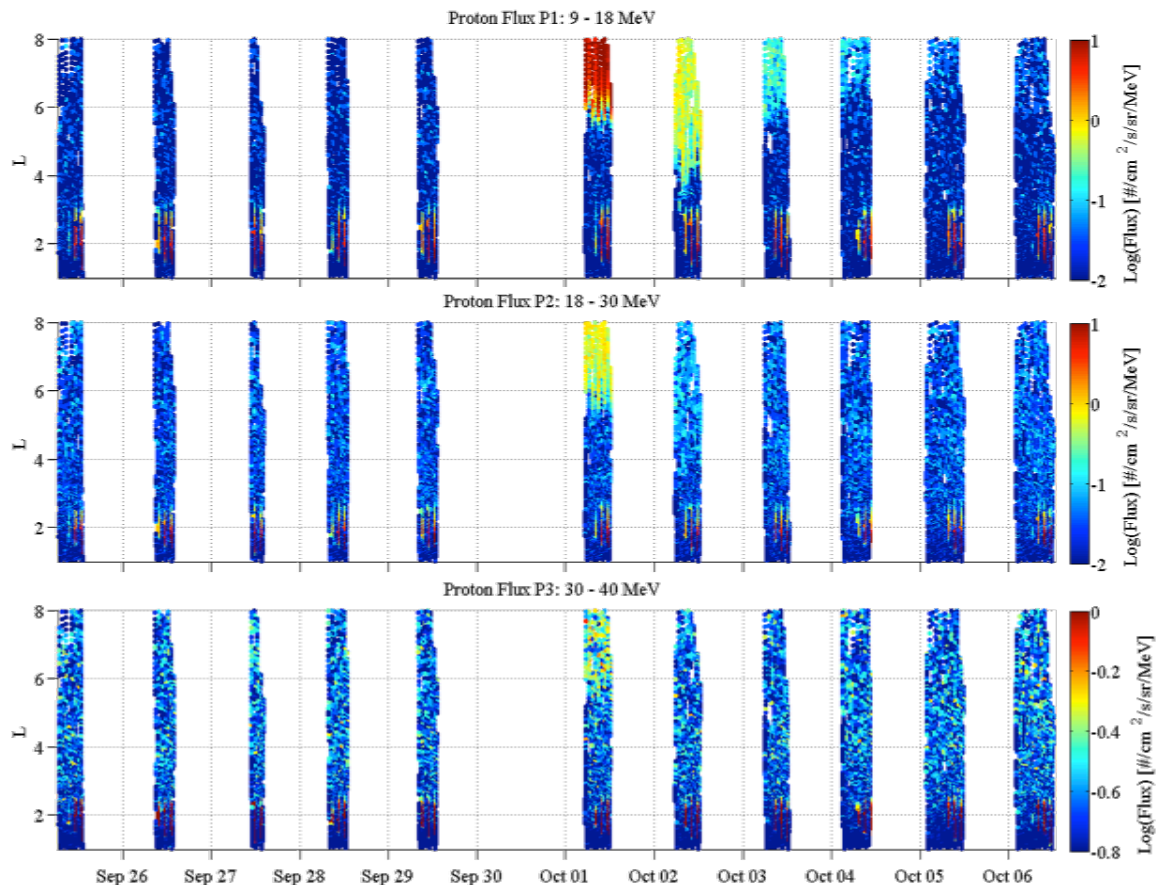
Figure 41: Proton flux for the September 30 SEP event.

electron population, the authors calculated that just one of the observed precipitation events was strong enough to precipitate at least 5% of the total outer belt content for 0.58 and 1.63 MeV electron populations. Only ~20 of these relatively common events would be sufficient to remove the entire outer belt, suggesting that precipitation loss is a significant loss mechanism for outer belt electrons, and directly addressing the science question of quantifying electron precipitation.

As demonstrated in the *Blum et al.* study [2013], storm-time conditions drastically strengthen the mechanisms that cause precipitation loss. However, in

addition to the storm-time precipitation, there is also a constant slow diffusion of particles into the atmosphere that occurs even during non-storm time conditions. Quantifying this diffusion rate separates the variable, storm-time processes from the underlying background precipitation. CSSWE's measurements were used in quantifying the quiet-time diffusion rates in *Jaynes et al.* [2014]. They found that 97.7% of radiation belt electrons were lost due to the background diffusion, specifically broadband wave-particle interactions known as plasmaspheric hiss [*Thorne et al.*, 2005], during an extended quiescent period from December 22, 2012, to January 13, 2013. These findings constrain current radiation belt flux models and forecasts by providing more realistic hiss-induced precipitation loss timescales.

Energetic Protons from SEPs

Unlike energetic electrons, which are nearly always measurable in the Van Allen radiation belts, SEP protons can only be measured when the Sun provides a SEP event. Fortunately, on September 30, 2013, the Sun emitted a large SEP event. Although REPTile was operating at a ~%30 duty cycle, its measurements of the SEP event are depicted in Figure 41. REPTile was not active during the onset of the event, but it still took measurements for the ensuing days. The inward penetration of the protons can be seen progressing from L~6 on October 1 to L~4 on the 2nd before retreating to L~6 on the 3rd and then to L>6 on the 4th. On October 5, the protons are no longer observed. As CSSWE is the only spacecraft in LEO capable of measuring the differential particle flux, the REPTile observations are critical in advancing the models of this event, as well as the models to predict the evolution of SEP penetration into Earths magnetosphere.

3.4.7 Summary

Recently, the satellite community has progressed considerably in regards to small, low cost missions and their access to space. A major player in the small satellite arena is the CubeSat. Although CubeSats are often considered as proof-of-concept missions, methods to increase TRL for commercial products, or simply educational platforms, the recent successes of the Colorado Student Space Weather Experiment has shattered this existing conviction.

The National Science Foundation awarded funding to the CSSWE team for $840k in January 2010. Within budget, CSSWE was designed, built, tested and operated by students at the University of Colorado at Boulder with mentorship from professionals in the Aerospace Engineering Sciences Dept., LASP, as well as other sources. Despite the heavy student involvement and high CubeSat infant mortality rates, CSSWE has exceeded full mission success in all categories.

Most importantly, CSSWE's science payload, the Relativistic Electron and Proton Telescope integrated little experiment (REPTile), continues to take valuable science measurements of the near-Earth plasma environment. A number of papers have been accepted to peer-reviewed scientific journals, demonstrating that CSSWE returns publication-quality measurements regarding electrons in Earth's radiation belts and protons in Solar Energetic Particle events. While CSSWE does not directly offer predictive capabilities, the mission directly improves the understanding of these space weather affects and in turn, risks and costs associated with space weather operations are reduced. CSSWE's science mission success, in tandem with the full mission success, proves that CSSWE is the paradigm for big science on a small budget.

3.5 Current Scientific Results

3.5.1 Introduction

In this section we present a brief overview of the scientific contributions that CSSWE measurements have made to the field. REPTile can make direct measurements of radiation belt particles, but the observations are similar to other LEO spacecraft in high inclination in that they can be used to directly observe atmospheric precipitation of relativistic particles. Studies that use the measurements to either directly infer electron precipitation or the presence/absence of radiation belt particles are presented in Section 3.5.2. In combination with detailed modeling, REPTile data can also be used to estimate radiation belt electron lifetimes (see *Selesnick* [2006], *Li et al.* [2013a, 2013b], and Section 6.2). Studies that use REPTile observations in conjunction with modeling are presented in Section 3.5.3. Since my involvement with many of these studies was supportive, I will merely summarize their contributions.

3.5.2 Direct Analysis of REPTile Observations

Blum et al. (2013) use CSSWE conjunctions with the Balloon Array for Radiation belt Relativistic Electron Losses (BARREL) [*Millan et al.,* 2013]. Using both platforms, they analyze an electron precipitation band event that occurred in the dusk sector. Precipitation bands are 5-30 seconds of rapid atmospheric particle precipitation associated with scattering caused by EMIC waves [*Thorne and Kennell*, 1971]. A precipitation band event was observed by both CSSWE and BARREL on January 18-19, 2013. Using CSSWE to temporally constrain the event, and BARREL to spatially constrain it, the authors determine that this

single event could precipitate as much as 50% of the electron population in the precipitation region (~L=5.5-5.8) and up to 5% of the entire outer belt population.

Baker et al. [2013] observe an ultrarelativistic (>2 MeV) electron impenetrable barrier using REPT and REPTile observations. The impenetrable barrier occurs at L~2.8, where transport processes become significantly slower than the loss timescales. The result is a sudden drop in flux and PSD levels that occurs inside of L=2.8, which remains devoid of ultrarelativistic electrons even during periods of strong geomagnetic activity. While an inner boundary of relativistic electrons can be expected, the steepness of the gradient between the two regimes is very interesting. The authors use CSSWE data to decisively show that the barrier is not caused by particles precipitating into the atmosphere. This process can occur as particles drift around the Earth and encounter regions of low magnetic field strength, which are due to higher order moments in Earth's internal dipole field.

Li et al. [2015] use REPTile measurements to better understand energetic electron behavior in the inner belt. The authors take advantage of high energy protons, which can penetrate instrument shielding and incorrectly be categorized as electrons. The high energy proton contamination is only relevant in regions of high proton fluxes, such as the inner belt, where the contamination is significant. *Li et al*. [2015] use the contamination to disentangle a real electron signal where the proton signal is absent. Initially, they observe the morphology of the low altitude precipitation regions around the South Atlantic Anamoly (SAA) using REPTile observations. They recognize a similar morphology between the high energy electrons and protons, but a different morphology between low energy electrons and protons, suggesting contamination in the high energy electron

signal. The authors use detailed analysis of REPT measurements, specifically using pulse height analysis of individual particle impacts, to show that there is not a significant population of electrons with E>0.5 MeV in the inner belt as previously thought.

3.5.3 REPTile Measurements Combined with Detailed Modeling

The three papers presented in this section use REPTile observations in a consistent manner; they use detailed modeling to extract electron lifetimes from the REPTile measurements. Electron lifetimes can be calculated using in-situ LEO relativistic electron observations by taking advantage of the higher order moments in Earth's magnetic field. As a particle drifts around the Earth, it maintains a mirror point at constant B. However, because of the tilted, offset nature of the dipole field, the points of constant B are at different geographic altitudes. In regions of low surface magnetic field strength, such as the SAA region, particles can mirror sufficiently low enough to be lost by collisions with the neutral component of Earth's atmosphere.

Similarly, a spacecraft in low Earth orbit measures particles at different points in their bounce and drift phases. The measurements can be made in regions of low magnetic field strength such that the particles are stably trapped, that is they remain in the system for longer than a drift period (Figure 42 (d)); they can be in regions of high magnetic field strength such that the particles are lost in the conjugate hemisphere within one bounce period (the bounce loss cone [BLC] – Figure 42 (b)); or the particles that are measured can be lost within one drift period and are considered in the drift loss cone (DLC – Figure 42 (c)).
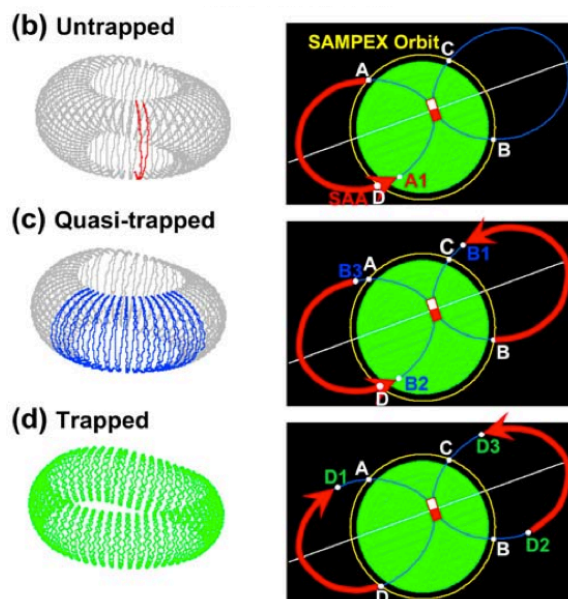
Figure 42: An illustration of the bounce loss cone (b), the drift loss cone (c), and stably trapped particles (d). [*Tu et al.*, 2010].

Selesnick et al. [2003, 2004] and *Selesnick* [2006] introduced a drift diffusion model to directly estimate electron loss rate from SAMPEX. In these works, the authors use steady decay to numerically fit various observations periods to balance azimuthal drift and pitch angle diffusion. *Selesnick* [2006] shows that the numerical model solutions can be estimated as $\tau \approx \tau_d/7F$, (where the correction from the original equation $7\tau_d/F$ was made after discussion with Dr. Selesnick), where τ is the electron lifetime, τ_d is an electron drift period, and F is the ration of quasi-trapped population to the total locally measured population averaged over half a day. This approximation is known as the Loss Index Method (LIM), and can be applied to the CSSWE mission to quantify the rate of precipitation loss for periods of slow diffusion. More on this method is presented in Chapter 6.

Jaynes et al. [2014] are able to quantify electron precipitation due to hiss interactions during an extended quiescent period between December 22, 2012, and January 13, 2013. Using the LIM, the authors found that the aggregate loss of the outer belt electron content for this period was 92.9% at L = 5.5 and 97.7% at L = 5.0. The LIM results compared well to the ratio of measured flux at the beginning and end of the period. Furthermore, lifetimes found at L = 4.5 were as short as 2.7 days, shorter than currently used theoretical lifetimes inside the plasmasphere. This study provided insight towards hiss interactions with the outer belt population and showed that electron lifetimes due to hiss may be shorter than previously thought.

While quantification of electron losses is valuable in itself, it can also lead to more accurate estimate of acceleration processes. *Reeves et al.* [2013] present a detailed analysis of the October 9-10, 2012, double-dipped storm enhancement. They show that the net result of the storm was an enhancement in the outer belt fluxes of almost 3 orders of magnitude in less than 24 hours. However, they are unable to separate the loss processes from acceleration processes and, as a result, cannot determine the true strength of the acceleration mechanism. *Li et al.* [2013] use CSSWE observations in combination with the LIM to estimate the electron loss rate, thus showing that the acceleration mechanism was 12.7% and 14.6% stronger for 0.58 and 1.63 MeV electrons respectively.

Similarly, *Schiller et al.* [2014a] observe a non-storm time enhancement on January 13-14, 2013. This sudden, extreme event enhanced outer belt fluxes from 0.6 - 1.3 MeV by more 336x in less than 13 hours. Using CSSWE and the LIM they determine that the acceleration mechanism responsible for this enhancement was actually 5% and 16% larger for 0.6 and 1.8 MeV electrons

respectively due to the concurrent precipitation into Earth's atmosphere. More on this study is presented in Chapter 4.

3.6 Conclusions

In this chapter I have introduced and discussed the Relativistic Electron and Proton Telescope integrated little experiment (REPTile) onboard the Colorado Student Space Weather Experiment (CSSWE) CubeSat. REPTile has been proven to reliably measure energetic electrons and protons from a low-Earth orbit with high inclination. The instrument and mission provide the first differential observations of precipitating electrons from a low-Earth orbit. Its observations, in conjunction with other missions such as the Van Allen Probes and BARREL, provide a unique scientific opportunity to understand electron losses in Earth's radiation belts and have been used in numerous scientific publications. CSSWE is an prime example of how small and inexpensive spacecraft can be used to benefit and enrich the science results of larger, more resource intensive, space missions. It proves two critical points: that publication-quality science can be done 1) from a small spacecraft platform and 2) from hardware developed by students.

REPTile is an innovation in design that marks the beginning of a new era in which reliable measurements of energetic particles can be made from miniaturized telescopes onboard nano- and picosatellites. However, only with comprehensive simulations can an instrument with such restrictive resources be proven reliable. REPTile's observational reliability stems from unprecedented instrument performance analyses and system characterizations. This work employs Geant4 to rigorously model and thoroughly quantify the instrument

performance, exceeding even the depth of analysis performed on NASA's REPT instrument. The simulation and validation efforts have verified the instrument's ability to make reliable measurements of outer belt electrons, and developed a blueprint for future miniaturized particle telescopes to characterize their instruments.

Extensive simulation efforts are required because of the challenges inherent in measuring relativistic electrons from space. Despite the challenges, however, these observations are required to develop an improved understanding of radiation belt dynamics. In the subsequent chapter, I discuss using REPTile observations, in combination with larger NASA missions, to better understand mechanisms that accelerate outer belt electrons to relativistic energies.

CHAPTER 4

OBSERVING A NON-STORM ENHANCEMENT

4.1 Introduction

In the previous chapter I introduced, in detail, how measurements of outer belt electrons are made. In this chapter I analyze these measurements to investigate outstanding science questions regarding outer belt electrons. In Section 4.2 I present work done for publication in the Geophysical Research Letters [*Schiller et al.,* 2014]. The analysis focuses on an unusual, but very intense, non-storm time enhancement event. I summarize the conclusions from the study in Section 4.3.

For the ensuing section, it is worthwhile to note that assigning a numerical threshold to qualify a storm as low, medium, or intense, may not be the best technique. The Dst index may be an especially poor metric, since it requires numerous corrections to achieve a final value, which often takes years to release. Furthermore, recent findings by *Temerin and Li* [2015] show that even the final Dst value could be off from the true deviation of Earth's background field by as much as 20nT. In their study, they analyze secular variations of the Dst index and imply that the baseline Dst underestimates ionospheric currents that are solar cycle dependent. Their resulting corrections are at least -15 nT during solar minimum and as much as -30 nT during solar maximum.

4.2 *A nonstorm time enhancement of relativistic electrons in the outer radiation belt*

by Q. Schiller, X. Li, L. W. Blum, W. Tu, D. L. Turner, J. B. Blake, published in *Geophysical Research Letters*, 2014

Abstract

Despite the lack of a geomagnetic storm (based on the Dst index), relativistic electron fluxes were enhanced over 2.5 orders of magnitude in the outer radiation belt in 13 hours on January 13-14, 2013. The unusual enhancement was observed by MagEIS, onboard the Van Allen Probes; REPTile, onboard the Colorado Student Space Weather Experiment (CSSWE); and SST, onboard THEMIS. Analyses of MagEIS phase space density (PSD) profiles show a positive outward radial gradient from 4<L<5.5. However, THEMIS observations show a peak in PSD outside of the Van Allen Probes' apogee, which suggest a very interesting scenario: wave-particle interactions causing a PSD peak at ~L^*=5.5 from where the electrons are then rapidly transported radially inward. This letter demonstrates, for the first time in detail, that geomagnetic

storms are not necessary for causing dramatic enhancements in the outer radiation belt.

4.2.1 Introduction

The relativistic electron population in the outer radiation belt is extremely volatile during periods of enhanced geomagnetic activity. During these times, it is constantly subjected to processes, such as loss, transport, and acceleration, which all compete and blend to affect the net electron population in the outer belt. The result is that geomagnetic storms can deplete, enhance, or cause little effect on the outer radiation belt [*Reeves et al.*, 2003]. A detailed understanding of loss, source, and transport is required to fully understand the dynamics of Earth's natural particle accelerator.

Acceleration mechanisms, which replenish the relativistic electron content, can be classified into two broad categories: radial transport and internal acceleration. Radial transport mechanisms can again be broadly classified into two sub-categories: radial diffusion and sudden injection, both of which violate the third adiabatic invariant. Radial transport requires an electron source population at high L, such as the plasma sheet in the tail of the magnetosphere [e.g., *Ingraham et al.*, 2001]. Radial transport by diffusion in the third adiabatic invariant is a result of incoherent scattering by ULF waves in the Pc4-5 band [e.g., *Tu et al.*, 2012]. Sudden injection, which is non-diffusive, can occur from a strong interplanetary shock, for example. Both of these mechanisms are well associated with geomagnetic activity [e.g., *Elkington et al.*, 1999; *Li et al.*, 2003]. Both also result in a smoothing of the PSD radial profile and thus cannot by themselves create local peaks in PSD.

Local acceleration, on the other hand, is a result of the violation of electrons' first or second adiabatic invariant. This process is also well associated with geomagnetic activity. One local acceleration mechanism is VLF chorus waves, which can resonate with the electrons' gyration period to accelerate them to relativistic energies [e.g., *Meredith et al.*, 2003]. Unlike radial transport, this mechanism produces a peak in PSD where the resonant interaction is occurring [e.g., *Chen et al.*, 2007; *Reeves et al.*, 2013]. Gyro-resonant wave-particle interactions are theorized to be a significant contributor to accelerating electrons to relativistic energies [e.g., *Horne and Thorne*, 1998].

Electron acceleration mechanisms in the magnetosphere, and thus enhancements in the outer radiation belt, are strongly correlated with geomagnetic activity. This relation has been recognized for decades, especially in association with the Dst index [e.g., *Dessler and Karplus*, 1961]. More recently, *Li et al.* [2001] further substantiate the association by finding a strong correlation between the Dst index and SAMPEX 2-6 MeV electron enhancements near geosynchronous orbit (GEO). *Reeves et al.* [1998] investigate electron flux measurements of 0.7 to 7.8 MeV using LANL-GEO spacecraft. Their study, which looks at 43 enhancements from 1992 to 1995, finds that every relativistic electron enhancement in the study is associated with a magnetic storm.

Geomagnetic storms are typically defined as when Dst < -30 nT]*Gonzalez et al.*, 1999], but sometimes a lower threshold is used. For example, *O'Brien et al.* [2001] do a thorough statistical analysis of electron enhancements of 0.3 – 1.5 MeV and >2 MeV electrons from LANL GEO from 1992 to 2000. They attempt to correlate electron enhancements with both internal and external drivers and find that long-duration Pc-5 ULF wave activity is an indicator of electron

enhancement. However, the study only selects events with Dst < -50nT, which omits events with little geomagnetic activity, and thus potentially neglects acceleration mechanisms that cause the enhancement of radiation belt electrons during relatively quiet geomagnetic conditions. Events such as the one described in this letter demonstrate that filtering by geomagnetic activity can exclude some significant enhancement events.

Perhaps due to imperfections in the Dst index, selection criteria, or to the strong association between electron enhancements and geomagnetic activity, there has not been a detailed reported case of a sudden (<13h), extreme (>330x) enhancement of electron flux in the outer belt that is not associated with a geomagnetic storm. Some recent studies have begun to allude to the separation between enhancement events and Dst; for example, *Borovsky and Denton* [2006] argue that the Dst index is a poor indicator of storm properties. *Miyoshi and Kataoka* [2008] use a -50 nT threshold in Dst to conclude that magnetic storms are not essential for >2 MeV electron flux enhancements at GEO. *Lyons et al*. [2005] state that >2 MeV electron fluxes at GEO during August to December 2003 increase for every high velocity solar wind speed event (>500 km/s) regardless of an associated storm. They point out two events with small Dst signature and a corresponding relativistic electron enhancement. However, neither event is investigated in detail. Similarly, *Kim et al.* [2006] find two GEO >2 MeV electron enhancement events with Dst > -30nT from 1999 through 2002. With these two events, they also suggest that storm time conditions are not required to create a MeV electron flux enhancement at GEO.

Expanding on these previous studies, this letter is the first to detail a sudden, extreme relativistic electron enhancement at and inside GEO that occurs

during non-storm time conditions. The enhancement increases flux levels by a factor of >330 in less than 13h at L=5.5. We employ a unique multipoint measurement configuration to observe the outer radiation belt, which provide unprecedented spatial and temporal coverage and instrument quality. These quality measurements enable a detailed investigation of the timing, energy dependence, and potential causes of the relativistic electron acceleration during this non-storm enhancement (there are at least two other similar, but less intense, events that are also observed by the Van Allen Probes in its first year). We calculate radial PSD profiles to determine the likely cause of rapid electron acceleration during this non-storm time event. Additionally, we quantify the relative contribution of concurrent precipitation loss since, ultimately, the enhancement results from energization processes dominating over losses.

4.2.2 Data

Electron measurements from the Van Allen Probes mission/RBSP-ECT suite [*Spence et al.*, 2013], namely from the Magnetic Electron Ion Spectrometer (MagEIS) instruments [*Blake et al.*, 2013], are used for in-situ relativistic electron flux and phase space density (PSD) measurements. Spin-averaged fluxes from the MagEIS Medium M75 and High instruments are converted to PSDs for fixed first and second adiabatic invariant for a range of μ centered at 750 (735-765) MeV/G (corresponding to ~550 keV at GEO) and K<0.13 $G^{1/2}R_E$ (mirroring electrons with pitch angles from 90 +/- ~35 deg.) via the method described in *Chen et al.* [2006]. Analysis shows that the pitch angle distribution is heavily peaked near the magnetic equator, thus we can treat the spin-averaged flux

measurements as locally mirroring electrons. Background counts due to cosmic rays, solar particles, bremsstrahlung, or electron backscatter have not been removed from the data, but are expected to be small during this event.

Additional electron measurements are analyzed from the Solid State Telescope (SST) instruments onboard the THEMIS mission [*Angelopoulos*, 2008]. Flux measurements from the 4 highest energy-channels (from ~400 keV to several MeV) on probes D and E are converted to PSD coordinates for fixed fist and second adiabatic invariants $\mu=750$ MeV/G and K <0.01 $G^{1/2}R_E$ (nearly equatorially mirroring electrons with pitch angles from 90 +/- 15 deg.). Details on the THEMIS PSD conversion can be found in *Turner et al.* [2012b]. THEMIS and MagEIS PSDs have not been cross-calibrated, so variation in the absolute magnitude is expected. The T89 magnetic field model [*Tsyganenko*, 1989] with real Kp input is used for both MasgEIS and THEMIS PSD calculations.

Finally, electron flux measurements are also used from the Colorado Student Space Weather Experiment (CSSWE), a 3U CubeSat in low-earth orbit. These measurements provide insight into the bounce- and drift-loss cones, which cannot currently be resolved from equatorial orbiting measurements like those of the Van Allen Probes or THEMIS. The instrument onboard CSSWE is the Relativistic Electron and Proton Telescope integrated little experiment (REPTile), which measures six-second directional fluxes of energetic electrons from 0.58 MeV to >3.8 MeV in two differential and one integral channel. Details of the mission and instrument can be found in *Li et al.* [2013a, 2013b].

Solar wind data and geomagnetic indices are acquired from the OMNI dataset. The T89 magnetic field model [*Tsyganenko*, 1989], with real Kp inputs, is

used in the ONERA IRBEM-LIB toolset for all PSD calculations. The Dst index is calculated every hour and available in near-real time. Provisional and final versions of the Dst index, which are respectively more accurate than the previous versions, are released within a few years of the real time Dst index. Predicted Dst, as seen in Figure 43 panel 9, is obtained from the *Temerin and Li* [2002, 2006] model and is available online (http://lasp.colorado.edu/space_weather/dsttemerin/dsttemerin.html). The predicted value has a 0.956 correlation with final Dst, and is potentially a more accurate representation of final Dst than the real-time or provisional indices, as demonstrated in *Temerin and Li* [2002].

4.2.3 Detailed Event Analysis

The period of interest terminates an extended quiet period for outer belt electron fluxes beginning around Dec 10, 2012. Solar wind and geomagnetic parameters are shown in Figure 43, along with electron flux measurements from the Van Allen Probes A and B MagEIS instruments (MagEIS A + B) 0.6 MeV channel and the REPTile 0.58 -1.63 MeV channel. A weak high-speed stream (HSS) with maximum velocity reaching almost 600 km/s can be seen to arrive late on January 13, 2013. For this event, the real-time and predicted Dst indices peak at -30 nT and -27 nT, respectively, and the Kp index peaks at 4-. Additionally, the HSS lacks a strong stream-interface (SI) region, which can be seen by the modest increase to 10 #/cc in the solar wind density and increase of
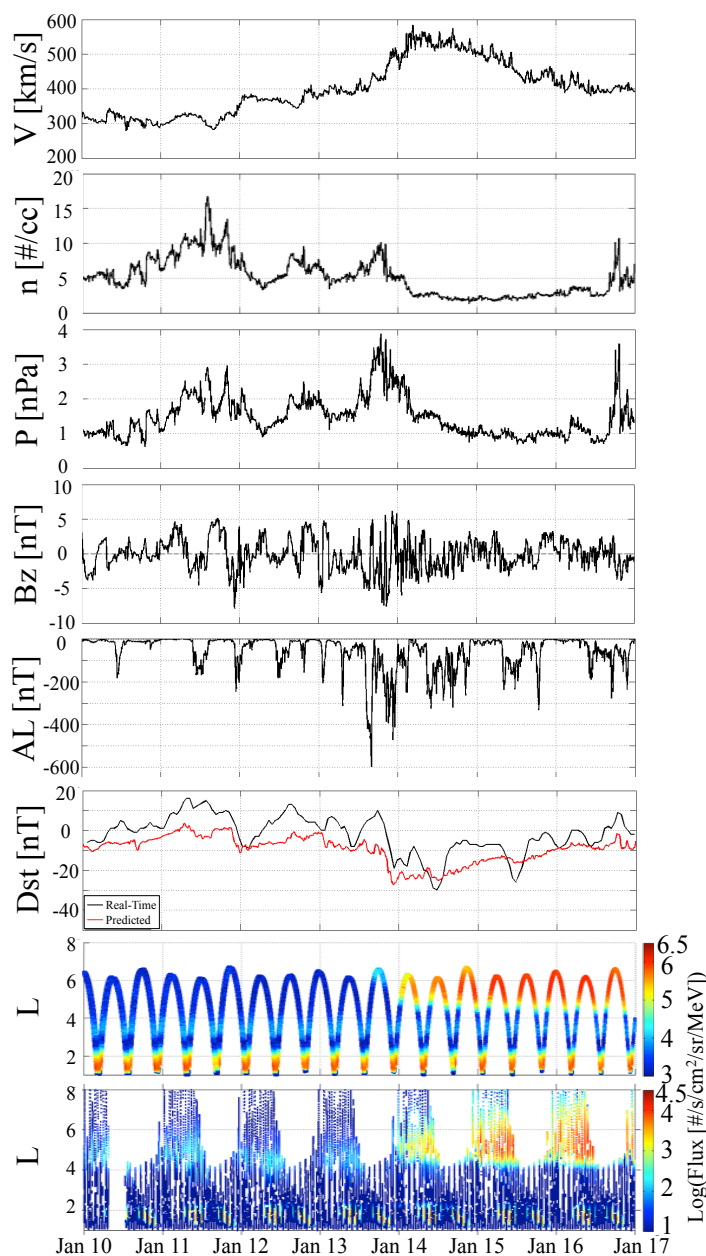
Figure 43: Electron flux measurements and solar wind parameters during the January 2013 enhancement event. (a) Flux measured by THEMIS probes D and E 0.65 MeV electron channel. (b) Flux measured by the MagEIS ~0.6 MeV electron channel on both Van Allen Probes A and B. THEMIS measurements below L = 4 and MagEIS measurements below L = 3 are not included due to electron and proton contamination, respectively. (c) Electron flux measurements from the CSSWE CubeSat's 0.58–1.63 MeV channel. (d–g) Solar wind parameters, with (h and i) geomagnetic indices AL and Dst. The predicted Dst index (red) can be a more accurate representation of the final Dst index than the real-time Dst index [*Temerin and Li*, 2002, 2006].

just 1 nPa in solar wind pressure. For comparison, in a statistical analysis of 32 CIR driven events from 1994 to 2002, *Denton et al.* [2006] find the mean peak Dst and Kp indices to be ~-59 nT and 5[-], respectively. *Morley et al.* [2010] examine 67 SIs from 2005 through 2008, and find the median density to be ~20 #/cc, with 10 #/cc falling well outside of the interquartile range. There is isolated substorm activity concurrent with the HSS impact, as indicated in the AL index.

An enhancement of relativistic electrons is observed by MagEIS near L~6 on its inbound orbit during the second half of January 13, nearly simultaneous with the arrival of the HSS, as seen in panel 2 of Figure 43. On the subsequent orbit, near Jan 14 00:00, the enhancement is seen inside of L=5. REPTile observations also measure the enhancement inside of L=5 just prior to Jan 14 00:00. At L=5.5, the MagEIS 0.58 MeV flux is enhanced 336x in under 13 hours, from the outbound orbit around Jan 13 15:30 to the inbound orbit near Jan 14 04:30. The sudden electron enhancement can be seen on all MagEIS channels up to 1.3 MeV, as well as REPTile E1 channel: 0.58 to 1.63 MeV, as seen in Figure 44.

The immediate and rapid enhancement is seen in neither MagEIS nor REPTile energy channels above 1.3 MeV, although these energies are gradually enhanced over the ensuing days. Some potential explanations are that the acceleration mechanism has upper energy threshold, beyond which the electrons are not as effectively accelerated; that the acceleration mechanism is not active for long enough to accelerate the electrons to higher energies; or that the inward radial transport from L~6.5, which is likely the cause of the relativistic electron flux enhancement measured by MagEIS, occurs more rapidly for the lower energy electrons. It is of note that in both Figures 43 and 44 the measured particle flux is one to two orders of magnitude lower as observed by REPTile
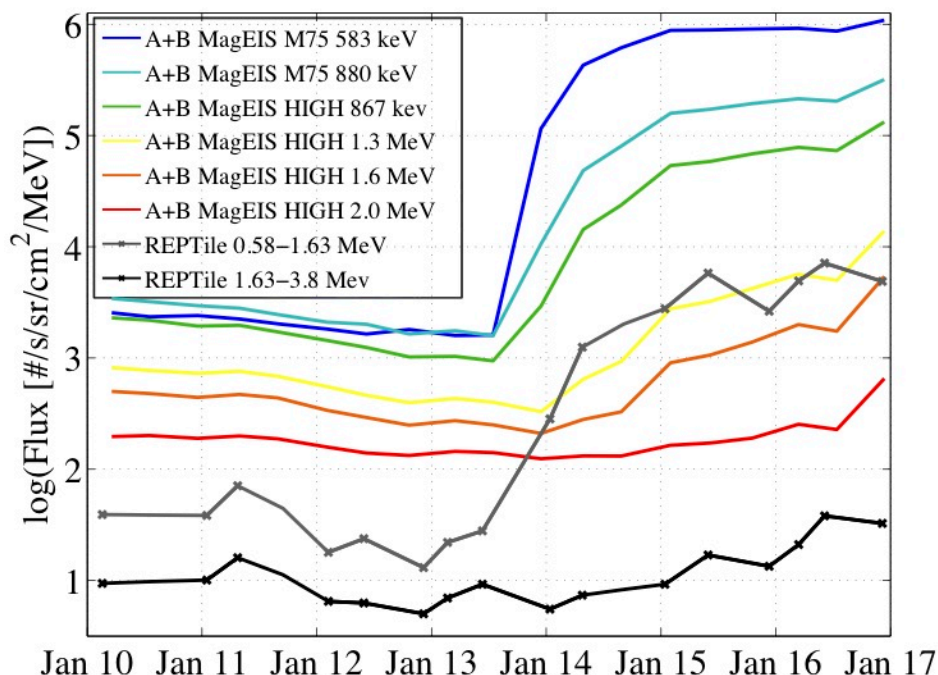
Figure 44: Nine hour flux averages for various MagEIS and CSSWE energy channels. The averages are taken at L = 5.5. The sudden and intense electron enhancement late on 13 January is most pronounced at energies from ~0.6–0.9 MeV. The higher-energy electrons are enhanced more gradually over the subsequent few days. Discrepancies between MagEIS M75 and HIGH instruments are expected; MagEIS HIGH channel thresholds were changed after this period to improve agreement between the instruments.

than MagEIS. Since REPTile is in a low Earth orbit, as compared to the geo-transfer-like orbit of MagEIS, it measures only the tail-ends of the pitch angle distribution, corresponding to <~6 deg. equatorial pitch angle at L=6.

The phase space density (PSD) profiles for μ~750 MeV/G and K<0.13 $G^{1/2}$ R_E, as measured by MagEIS and depicted in panel 1 of Figure 45, show a positive radial gradient through L*=5.5 during the enhancement (as the Van Allen Probes' apogees are at ~5.8 R_E, they cannot measure much beyond L*~6). A positive radial gradient suggests radial transport as the acceleration mechanism:
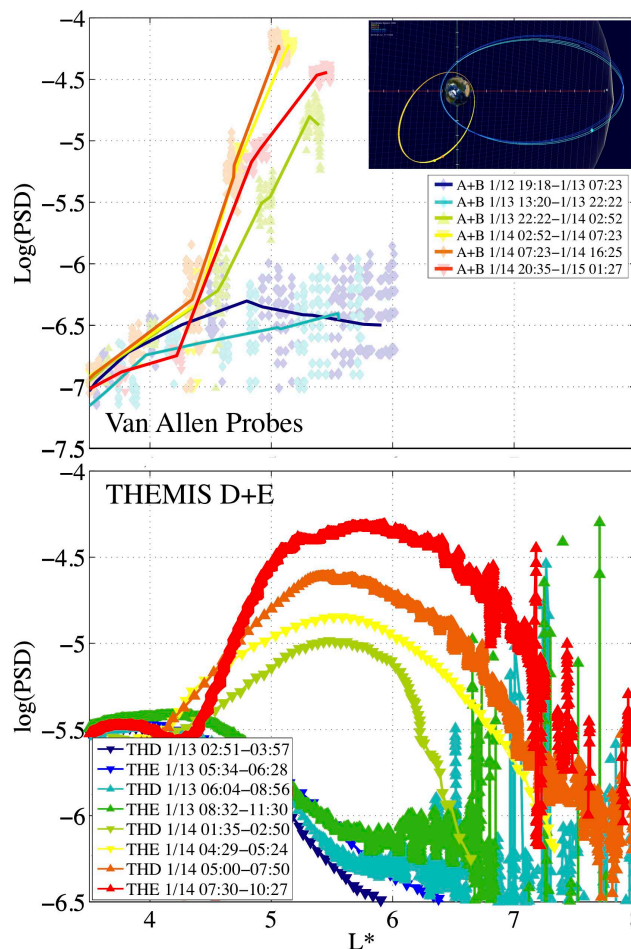
Figure 45: PSD gradients for constant μ and K during the 12–15 January 2013, enhancement event. Cool colors correspond to earlier times in the period and warmer colors to later times in the period. Upward triangles indicate outbound passes, downward triangles inbound passes, and diamonds from both inbound and outbound portions of the orbit. (top) PSD radial gradients from MagEIS Medium M75 and HIGH instruments on both Van Allen Probe space-craft for μ = 735–765 MeV/G and K < 0.13 $G^{1/2}R_E$. The profile is shown with the opaque line and the data points used to calculate the profile are shown in transparent triangles/diamonds. The inset depicts the orbits of the Van Allen Probes (yellow and orange) and THEMIS D and E (cyan and blue) in the GSE x–y plane, with the Sun to the right. (bottom) PSD radial distributions from THEMIS D and E spacecraft for μ = 750 MeV/G and K < 0.01 $G^{1/2}R_E$. Passes after 14 January 01:35 show peaks in PSD between 5 < L* < 6. Noise at higher L is due to poor statistics in the counts-to-PSD conversion. THEMIS and MagEIS have not been intercalibrated for this study, which can result in absolute and scaling differences. Additionally, THEMIS PSD measurements below L = 5 are susceptible to contamination from higher-energy electrons. The local PSD peak near L* ~ 4 during this period is likely due to this contamination.

either sub-storm related injections from the tail or radial diffusion from higher L. However, a more complete understanding can be had through the use of THEMIS PSD measurements for constant $\mu=750$ MeV/G and K<0.01 $G^{1/2}$ R_E, shown in panel 2 of Figure 45. During this period, with apogee near 13 R_E, each THEMIS spacecraft cuts through the full extent of the outer belt twice every ~24 hours. The THEMIS PSD gradients show a clear peak between 5<L*<6 on four consecutive passes through the outer belt between 01/14 1:35 UT and 01/14 10:27 UT. A local peak in the PSD profile such as this suggests a local acceleration mechanism occurring, such as VLF chorus. This event agrees with other recent studies that determine that PSD peaks are typically found inside of GEO [e.g., *Shprits et al.,* 2012; *Schiller et al.*, 2012; *Reeves et al.*, 2013]. Note that THEMIS PSD measurements are susceptible to high-energy electron contamination. During this period there is an enhanced high-energy electron population at L<5, so the discrepancy between MagEIS PSD and THEMIS PSD in this region for this period is likely due to this contamination.

Another possible cause for a peak in PSD is magnetopause shadowing [*Chen et al.*, 2007; *Turner et al.*, 2012a]. However, THEMIS PSD profiles prior to the enhancement do not show significant PSD at high L, which is required for magnetopause shadowing to be the cause of a peak in PSD. Furthermore, the magnetopause is ~9.3 R_E at the subsolar point based on *Shue et al.* [1997] magnetopause model, which would cause the PSD peak to be measured at much higher L than observed by THEMIS.

The average Bz for the period following the SI is negative, qualifying the event as a southward interplanetary magnetic field-dominant HSS (SBz-HSS).

There are similarities between this event and the statistical result of 108 SBz-HSSs analyzed in *Miyoshi et al.* [2013] and *Miyoshi and Kataoka* [2008]. Their findings show that hot electrons (30-100keV) provide energy for the generation of whistler waves, which in turn enhance outer radiation belt electrons. This statistical analysis provides further evidence that VLF whistler mode chorus waves are the cause of the accelerating electrons to relativistic energies.

Since these measured flux and PSD values are the net result of the balance between acceleration and loss mechanisms, further analysis of low Earth orbit (LEO) precipitation measurements can provide a direct estimate on the electron precipitation rate to better quantify the magnitude, energy, and location of the acceleration mechanisms occurring during this enhancement event. To provide an estimate of loss rates, we employ CSSWE measurements and the Loss Index Method [*Selesnick et al.*, 2006; *Tu et al.*, 2010; *Li et al.*, 2013b]. This method relies on the tilt and offset of Earth's dipole magnetic field, which allows three populations to be measured by CSSWE from LEO: trapped, quasi-trapped, and untrapped. The trapped electrons are trapped in the magnetosphere beyond a drift orbit timescale, the quasi-trapped electrons are in the drift loss cone and precipitate within a drift period, and the untrapped electrons are in the bounce loss cone and are lost within a bounce period. Separating the different populations, under the assumption that electrons are locally mirroring if measured at the spacecraft and are lost if they reach 100 km altitude, allows the method to model pitch angle diffusion rates from CSSWE measurements and, ultimately, electron lifetimes. During the first half of January 14 (00:00 to 12:00), 0.6 MeV electrons at L=5.5 had a lifetime of 10.5 days, and 1.8 MeV electrons a lifetime of 3.6 days. The mechanism that causes the observed enhancement must

consequently have accelerated 5% and 16% more electrons with energies of 0.6 MeV and 1.8 MeV, respectively, to account for atmospheric precipitation. Thus, measurements at low altitude, which are capable of resolving the loss cones, are essential to properly quantify the relative contribution between source and loss processes.

4.2.4 Summary

The Van Allen Probes, THEMIS, and the CSSWE CubeSat observe a relativistic electron enhancement on January 13-14, 2013, associated with a HSS. Observations of the radiation belts during this period are unprecedented in energy resolution, radial distribution, and latitudinal coverage. This particular enhancement, which was greater than 2.5 orders of magnitude for 0.6 MeV electrons in less than 13 hours, is of considerable interest due to the relatively benign geomagnetic conditions during which it occurred. Small but isolated substorm activity is present, but there is no geomagnetic storm as measured by the Dst index. The existence of this event, and others like it, demonstrate that large enhancements can occur independent of geomagnetic storms.

The sudden, extreme enhancement (>330x in <13h) is seen in all energy channels from ~0.6 - 1.3 MeV, but not observed at greater energies. The acceleration mechanism is estimated to be 5% and 16% larger for 0.6 MeV and 1.8 MeV electrons, respectively, than what MagEIS measurements alone indicate, due to concurrent precipitation loss into Earth's atmosphere. Radial phase space density (PSD) profiles from MagEIS observations alone do not capture the location of the PSD peak. Analysis of THEMIS PSD profiles, however, shows a local peak in PSD near L^*~5.5, which indicates that local acceleration is the

source of the relativistic electrons. Consequently, the flux enhancement observed by MagEIS is dominated by rapid inward radial transport from this peak at higher L. By using both spacecraft, we observe that the initial acceleration source of relativistic electrons is due to local heating, but the sudden and extreme flux enhancement observed by MagEIS is a direct result of a fast transport mechanism bringing relativistic electrons radially inward.

4.3 Conclusions

In this chapter I analyze a non-storm time enhancement event using data from CSSWE, THEMIS, and the Van Allen Probe missions. The event is the largest non-storm time enhancement to be reported on; electrons of 0.6 MeV were enhanced over 2.5 orders of magnitude in less than 13 hours.

Local heating, rapid radial transport, and extreme flux enhancements are commonly associated with geomagnetic activity. However, in the event described in this letter, we observe all three processes occur during non-storm time conditions. This event, and others like it, compels investigators to include all enhancement events in their studies, rather than relying on the assumption that storm-time conditions are required for relativistic electron enhancements in the outer radiation belt. Furthermore, we advise caution when using absolute thresholds to indicate storm-time conditions. Especially when including the Dst index, as recent results [*Temerin and Li,* 2015] suggest that annual biases in the index could be significant. Finally, this study demonstrates the importance of substorm activity, rather than geomagnetic storm signatures, to create enhancements in the outer belt (for further discussion see Section 7.2.3).

While in this chapter I directly analyze spacecraft data to diagnose an acceleration event, in the following chapter I present unique method to model acceleration events. This novel method provides insights to acceleration mechanisms responsible for enhancing radiation belt fluxes.

CHAPTER 5

DATA ASSIMILATION

5.1 Introduction

The previous chapter uses phase space densities as a tool to investigate an outer belt electron enhancement. However, it also briefly discusses some limitations in using the observations, such as uncertainties inherent in an under-sampled system. This chapter discusses a technique to combine the sparse observations with a physical model to recreate the full system state. In this case, the state is the globally averaged phase space density profile. A unique method is also presented that, in addition to estimating the full radial phase space density profile, can also estimate aspects of the source rate term. The work is presented in a publication for the Journal of Geophysical Research [*Schiller et al.*, 2012a], which Section 5.2 is based from. Section 5.3 is a supplementary report published in the Los Alamos National Laboratory (LANL) Space Weather Summer School Reports [*Schiller and Godinez*, 2012] that further discusses analysis to verify the methods used in *Schiller et al.* [2012]. Section 5.4 discusses improvements to the method. Particularly, Section 5.4.2, based off an internal LANL report, presents a method to optimize the technique by intelligently exploring the cost function, rather than mapping the entire parameter space. Section 5.4.3, also based from another LANL report, expands this idea into three

dimensions and discusses the limitations and uses of the expansion. Finally, the scientific contributions of this work are summarized in Section 5.5.

5.2 *A parametric study of the source rate for outer radiation belt electrons using a Kalman filter*

by Q. Schiller, X. Li, J. Koller, H. C. Godinez, and D. L. Turner, published in *Journal of Geophysical Research*, 2012

Abstract

Data assimilation methods have become increasingly popular to describe the outer radiation belt energetic electron environment. We use a Kalman filter with inputs of 1) electron phase space density (PSD) for constant first and second adiabatic invariants, $\mu = 2083[MeV/G]$ and $K = 0.03[G1/2RE]$ respectively, from a five satellite data set (three LANL-GEO, one GPS, and Polar), and 2) a one-dimensional radial diffusion model with loss and source terms included. We augment the Kalman filter to include the intensity of local acceleration in the state vector. The output is an estimate of PSD for the radial range of the outer radiation belt and the time-dependent amplitude parameter of a Gaussian shaped source rate term for given location and width. To further constrain the source rate parameters, a root mean square (RMS) analysis of the observation

residual vector (a.k.a. innovation vector) is performed in a parameter space of source location and width. We analyze five storm periods spanning from July 30th to October 24th of 2002, and each period's unique solution in the location-width parameter space is assimilated with the Kalman filter for a continuous reanalysis of the full 87 day period. The source amplitude parameter is analyzed for insight into time periods of enhanced local heating, suppressed loss, or, as the parameter can take negative values, additional loss. The source is found to peak in the recovery phases of the storms where the rate is sufficient to repopulate the radiation belt in approximately one day, suggesting that local heating is a major contributor to the electron radiation belts during the recovery phase.

5.2.1. Introduction

Understanding the Electron Radiation Belt

The electron radiation belt, or outer Van Allen belt, is a toroidal region in space populated by relativistic electrons. These particles are trapped in the Earth's magnetosphere, but are constrained to 3 ~ 7 Earth radii (R_E) and often have peaks in intensity between 4 and 5 R_E. The outer radiation belt is separated from the inner radiation belt, which consists of mostly energetic protons populating approximately 1.2 to 2.5 R_E, by a region of space generally empty of energetic particles called the slot region.

The highly energetic electron environment in Earth's magnetosphere poses an incessant risk to spacecraft and organic tissue alike [*Baker*, 2001]. Furthermore, the particles overlap an array of commonly used spacecraft orbits, such as low-Earth, Global Positioning System (GPS), and geosynchronous (GEO).

Understanding the physical processes in this environment is not only a scientific challenge but also critical to mitigate the risk to spacecraft and astronauts.

The energetic electron environment changes continuously by various complex and not well-understood processes, such as localized heating (source), loss, and radial transport [e.g., *Li and Temerin*, 2001]. For example, whistler mode chorus waves, associated with increased geomagnetic and substorm activity, are believed to be a major contributor in locally accelerating 100 keV electrons to MeV energies [e.g. *Horne et al.*, 2007]. Recently, numerous studies have been published on modeling the waves' effects on the radiation belts [e.g. *Shprits et al.*, 2006; *Summers et al.*, 2007]. The source location has been characterized [*Meredith et al.*, 2002, 2003a, 2003b; *Santolik et al.*, 2005, 2009; *Li et al.*, 2009] to occur preferentially from approximately $4<L<6$, but can occur from $3<L<10$ [*Li et al.*, 2009].

However, each individual process is difficult to quantify and understand its net contribution to the state of the system. *Reeves et al.* [2003] showed that geomagnetic storms can affect the delicate balance of these processes, resulting in a net increase or decrease of radiation belt electron fluxes, or sometimes no change at all, if comparing the post-storm level with the pre-storm level. Further complication of the problem lies in the restricted, single-point in-situ measurements of spacecraft. These measurements have limited spatial and temporal coverage, often with large uncertainties. To address these challenges, the radiation belt community has turned to data assimilation to attempt to fill in the data gaps in space and time.

Data Assimilation and Recent Applications to Radiation Belts

Data assimilation is methodologies that approximate, as accurately as possible, the true state of a system. They do so by blending observations with dynamical models of the system to optimally combine all available information. Data assimilation has been used extensively where sparse data is typical, such as applications in terrestrial weather [*Kalnay*, 2003], satellite orbit determination [*Tapley et al.*, 2004], unmanned aerial vehicle control [*Stachura and Frew*, 2011], and oceanography [*Evensen*, 1994]. The sparse and restricted measurements of the energetic electron environment make data assimilation a natural approach for us to form a global picture of the radiation environment around Earth.

Data assimilation is a proven method to reconstruct aspects of the energetic electron environment in the outer radiation belt. One method, known as direct insertion, runs a physics-based model while substituting the in-situ observations as they become available. The model then propagates the measurements into regions of interest that lack observations. Work by *Maget et al.* [2007] and *Bourdarie et al.* [2005, 2009] used the Salammbô code, developed at the Office National d'Etudes et de Recherche Aérospatiales in Toulouse, France [*Beutier and Boscher*, 1995], to directly insert PSD data in a 3D radiation belt model (see Section 2.2 for discussion on radiation belt modeling). A 3D model more accurately describes the physical dynamics of the environment, but introduces additional challenges, such as requiring conjunctions between satellites to determine pitch angle distributions. On storm timescales, this limitation hinders the 3D code from reproducing the full dynamics of the environment and thus, 1D diffusion is a reasonable approach despite the inherent limitations in describing system dynamics.

Another method of data assimilation is the Kalman filter [*Kalman*, 1960]. An early study by *Naehr and Toffoletto* [2005] showed that, for a simple one dimensional radial diffusion model, an extended Kalman filter (EKF) [*Jazwinski*, 1970] outperforms direct insertion for a highly idealized case. Furthermore, using an identical twin experiment (a method of assimilating a synthesized radiation belt environment to measure the performance of the filter), *Naehr and Toffoletto* [2005], as well as others [e.g. *Koller et al.*, 2007, *Shprits et al.*, 2007, *Kondrashov et al.*, 2007] show that the Kalman filter technique accurately reproduces the synthesized electron phase space density (PSD) environment. These studies are generally performed for simplified cases with clearly specified dynamics, but they verify the robustness and functionality of Kalman filters to reproduce 1D radial diffusion.

One such study was performed by *Ni et al.* [2009a], who demonstrated that the Kalman filter is able to reproduce the location and magnitude of PSD peaks and dropouts using two independent datasets. Another example verifying the Kalman filter's practicality was completed by *Daae et al.* [2011], who examined the Kalman filter's robustness to initial conditions, boundary conditions, and loss timescales. This study explicitly demonstrates the Kalman filter technique can reproduce radiation belt dynamics regardless of choice of initial conditions, boundary conditions, or loss timescales. Additionally, they showed that the difference in PSD between drastically different initial conditions is reduced to 15% after one day, and slowly decays to zero on the order of 14 days, quantifying the memory span of the filter. These studies, as well as others [e.g. *Ni et al.*, 2009b], indicate that the Kalman filter is robust to various data, input, and model parameters.

Another data assimilation tool is the observation residual vector, or the innovation vector, which is a measure of the processes that exist in the measurements but are not present in the physical model. *Koller et al.* [2007], *Shprits et al.* [2007], and *Daae et al.* [2011] used the innovation vector to infer enhancements in local acceleration and/or loss. *Shprits et al.* [2012] used the innovation vector to perform a statistical analysis and found a strong correlation between the plasmapause and the location of an inferred source region.

Physical processes can also be estimated directly by including model parameters in the Kalman filter's state vector. This allows for an estimate of, for example, source rate or loss timescale. *Kondrashov et al.* [2007] included loss parameters in the state vector of an EKF. They used an electron PSD dataset to estimate the loss timescale inside and outside the plasmasphere for a radial diffusion model with loss. *Reeves et al.* [2012] demonstrated the ability to estimate the time-dependent amplitude parameter of a Gaussian shaped source term for a single storm.

However, until the study presented here, the Kalman filter has not been used to directly estimate source rate location or width, or to estimate the intensity of local heating for more than one storm. In this study, we include a parameterized source rate term in the radial diffusion model and augment the state vector to include source rate parameters. The Kalman filter reconstructs the electron PSD for the full radial range of the outer radiation belt, thereby filling in data gaps in time and space, and estimates the time-dependent intensity of local heating. We perform a parametric study to discern the most likely location and width of the acceleration region for five storm periods. We then use the solutions in a reanalysis of the full 87-day period. The result is a time dependent

estimate of the location, extent, and magnitude of local heating. We describe the inputs of the data assimilation scheme in Section 5.2.2 and the Kalman filter technique in Section 5.2.3. The detailed results of the parametric study and reanalysis are presented in Section 5.2.4, which are then discussed in Section 5.2.5.

5.2.2. Data Assimilation Inputs and Methodology

INPUT: DATA

We use energetic electron data from the Synchronous Orbit Particle Analyzer (SOPA) instrument aboard Los Alamos National Laboratory satellites at geosynchronous orbit (LANL-GEO: 97a, 1991-080, 1990-095) [*Belian et al.*, 1992], the Burst Detector Dosimiter (BDD) II aboard a Global Positioning System (GPS) satellite (GPS-ns41) [*Feldman et al.*, 1985], and the Comprehensive Energetic Particle and Pitch Angle Distribution Experiment on Polar (CEPPAD) [*Blake et al.*, 1995]. The data spans an 87-day period from June 30th to October 24th, 2002. The data are averaged to the center of each discrete mesh grid point with dimensions 0.25[L]x120[min]. The conversion to PSD and intercalibration [*Friedel et al.* 2005] is done for constant first and second adiabatic invariants: $\mu = 2083$ (MeV/G) and $K = 0.3$ (G$^{1/2}$R$_E$), corresponding to ~1 MeV at GEO. It is performed in two steps: 1) transforming the spacecraft coordinates into phase space coordinates and 2) converting the measured fluxes into PSD values [*Chen et al.*, 2005; *Chen et al.* 2006]. The electron flux, j(E, α, $\vec{r}$), as a function of energy (E), pitch angle (α), and satellite position ($\vec{r}$), is converted into PSD following *Hilmer et al.* [2000].

INPUT: PHYSICAL MODEL

The energetic electron population is often described in phase space coordinates. Phase space corresponds to a six dimensional position-momentum space, but can be reduced to three dimensions by averaging over the three periodic motions: gyration, bounce, and drift. Relativistic electron populations can be described by their PSD: $f(\mu,K,L,t)$ [*Schulz and Lanzerotti*, 1974], where μ is the first adiabatic invariant associated with gyration around a field line, K is the second adiabatic invariant associated with particle bounce motion between magnetic mirror points, and L is the Roederer L* parameter [*Roederer*, 1970] related to the third adiabatic invariant ϕ, which is associated with the drift motion of the particle about the Earth. Phase space coordinates are useful because the particle distribution function is constant along a dynamical trajectory in absence of external or internal sources or losses (such as diffusion, wave-particle interactions, etc.), aiding in the identification of system dynamics. When the distribution function is not conserved, phase space coordinates can help identify non-adiabatic heating or loss mechanisms, including location and magnitude.

Radial diffusion in energetic electron populations can be described in PSD coordinates with a Fokker-Plank equation for constant μ and K. We use a one-dimensional Fokker-Plank equation to describe the radial diffusion in L

Equation 14: Fokker-Plank

$$\frac{\partial f}{\partial t} = L^2 \frac{\partial}{\partial L}\left(\frac{D_{LL}}{L^2}\frac{\partial f}{\partial L}\right) - \frac{f}{\tau} + S ,$$

where $D_{LL}(L,t)$ is the radial diffusion coefficient, $\tau(L,t)$ is the loss timescale, $S(L,t)$ is the source rate, where a three-dimensional model also includes diffusion in pitch angle and energy. We assume a Gaussian form for the source rate, i.e.

Equation 15: Source

$$S = Ae^{-\frac{(L-L_C)^2}{\sigma^2}},$$

where the source rate is centered at L_C, with width σ and amplitude A. This source function exists over all values in L, and thus does not introduce any artificial discontinuities. Note that we separate source rate and loss terms. The resulting PSD is the net result of the balance between radial transport, source, and loss for particles for only one specific combination of first and second adiabatic invariants, here $\mu=2083[\text{MeV}/\text{G}]$ and $K=0.3[\text{G}^{1/2}\text{R}_E]$.

The Crank-Nicolson method [*Crank and Nicolson*, 1947], which is unconditionally stable and 2nd order accurate, is used to solve the equations and does not need to satisfy the Courant condition [*Press et al.*, 1986]. We assume a discrete meshed grid of 32 points from $2 \le L \le 10$. We select a relatively large spatial resolution of L=0.25 to mitigate radial errors that could occur, for example, in the choice of magnetic field model [*Ni et al.*, 2009b], D_{LL} coefficient [*Brautigam and Albert*, 2000], satellite intercalibration [*Friedel et al.*, 2005] or PSD calculations [*Chen et al.*, 2005]. Our initial condition is a Gaussian fit to an average of the first 20 hours of GEO data. On a relevant note, work by *Daae et al.* [2011] show that the initial conditions are 'forgotten' in ~1 day. That is, the filter

takes ~1 day to 'spin-up', after which the PSD estimate is nearly identical regardless of the imposed initial condition.

We choose the widely used Kp dependent diffusion coefficient: $D_{LL}(Kp,L)$ = $10^{(0.506Kp-9.325)}L^{10}$ [*Brautigam and Albert*, 2000], where Kp is an index indicating the magnitude of geomagnetic activity. Since the loss is included separately in the model, we choose three L-dependent loss timescales. To represent plasmaspheric hiss, the loss timescale inside the plasmapause ($L<L_{PP}$) is $\tau = 8$ days [*Kondrashov et al.*, 2007]. For loss mechanisms occurring outside of the plasmapause, but inside the last closed drift shell ($L_{pp} \leq L < L_{MAX}$), we choose $\tau=3/Kp$ [*Shprits et al.*, 2005; *Kondrashov et al.*, 2007]. For particles at the last closed drift shell and beyond, we assign a loss timescale of $\tau = 10$ minutes as these particles will be lost to the magnetopause on the timescale of minutes (approximately ½ of a drift period).

We calculate the plasmapause and last closed drift shell using the Dst index, which is an indicator of geomagnetic storm activity. The plasmapause location is assumed to be $L_{PP}(Dst) = -1.57\log_{10}(\min_{-24,0}Dst) + 6.3$, where the notation $\min_{-24,0}Dst$ represents the minimum Dst value for the past 24 hours [*O'Brien and Moldwin*, 2003]. We approximate the last closed drift shell with a second order polynomial fit as described in *Koller & Morley* [2010]. The fitted function is $L_{MAX} = 6.07 \times 10^{-5}Dst^2 + 0.0436Dst + 9.37$, which is derived from the last closed drift shell using the TS03 model [*Tsyganenko et al.*, 2003] during July – December 2002. The PSD at the inner and outer boundaries, L=2 and L=10, is set to 1×10^{-16} (c/MeV/cm)³ based on various studies where, during geomagnetically

active times, radial diffusion alone is insufficient to explain PSD peaks near GEO [*Brautigam and Albert*, 2000; *Green and Kivelson*, 2004; *Chen et al.*, 2007].

It is pertinent to recognize that the source rate in our model can have a negative value. In this case, the existing loss in the model is insufficient to match observations, and the filter creates additional loss in the form of negative source. When the source rate term has a positive value, it may indicate an enhancement of an acceleration process or a suppression of loss mechanisms, as the resulting PSD depends on the net contributions of both the loss and source terms, as well as radial diffusion. Actual observational data cannot distinguish between these various processes and measure only the net effect of all the processes in combination. Models, such as the one presented, are a justified attempt to separate and quantify their respective dynamics.

5.2.3 THE KALMAN FILTER

The Kalman filter [*Kalman*, 1960] is a sequential data assimilation method that uses weighted least square minimization based on the uncertainties in both the observations, y, and the model state, x. The algorithm is optimized for linear systems for which a Gaussian probability distribution is assumed. The variables used in the Kalman filter, as well as their descriptions and sizes, are outlined in Table 7. The filter consists of two major operations: an analysis step and a forecast step.

The first operation in the analysis step is to calculate the Kalman gain matrix $\mathbf{K}_i$ (Equation 16), which is a weighting matrix computed from the model error covariance matrix $\mathbf{P}_i$, and the observational uncertainty $\mathbf{R}_i$. The subscript i

represents the time step of operation. The Kalman gain matrix is used to weight the state and observation in subsequent analysis steps, and is defined as

Equation 16: Kalman Matrix

$$K_i = P^f(t_i)H^T_i[H_i P^f(t_i)H^T_i + R_i]^{-1}$$

where $R_i = \varepsilon_o I \times y_i$. Here, H_i is an observation operator that maps the model space into the observational space, the superscript f represents the forecasted state, and ε_o represents the uncertainty of the observations and is set to 30% of the measured PSD [*Koller et al.*, 2007]. I is the identity matrix.

The analysis state vector $x^a_{i,}$ and model covariance matrix P^a_i are given by the Kalman update equations

Equation 17: Assimilated State

$$x^a(t_i) = x^f(t_i) + K_i d_i,$$

Equation 18: Innovation Vector

$$d_i = y^o_i - H_i[x^f(t_i)],$$

Equation 19: Covariance Matrix

$$P^a(t_i) = (I - K_i H_i)P^f(t_i),$$

where the superscript a denotes the analysis state after the Kalman update. As can be seen from Equation 17, the analysis state vector x^a_i is computed through adjusting the forecasted state vector x^f_i by weighting the difference between the observations and the model forecast with the Kalman gain matrix. In Equation

18, d_i is called the observation residual vector or the innovation vector, and the product $\mathbf{K}_i d_i$ is known as the Kalman innovation vector.

The analysis state is then propagated forward in time using the linear forecast model operator $\mathbf{M}_i$, solved by the Crank-Nicolson method [*Crank and Nicolson*, 1947], to create the forecast state:

Equation 20: Forcast State

$$x^f(t_{i+1}) = M_i[x^a(t_i)]$$

Equation 21: Forecast Covariance Matrix

$$P^f(t_{i+1}) = M_i P^a(t_i) M^T_i + Q(t_i)$$

where $\mathbf{Q}_i = \varepsilon_m \mathbf{I} \times [x^f_i - x^a_i]$ is a diagonal error covariance propagating matrix and represents the decrease in confidence in the model as time evolves away from observation. Its value, $x^f_t - x^a_t$, is a good representation of the performance of the model; that is, a large (small) value indicates poor (good) performance, and thus the model covariance will increase faster (slower). The uncertainty of the model ε_m is a very difficult value to quantify. It is ambiguously set to ten times the observational uncertainty, or $\varepsilon_m = 300\%$, since our confidence in our simple one-dimensional model is much lower than observations. This observation error/model error ratio is roughly consistent with previous work [*Shprits et al.*, 2007; *Ni et al.*, 2009a; *Ni et al.*, 2009b; *Daae et al.* 2011; *Shprits et al.*, 2012]. In a future study, the model uncertainty will be replaced with a dynamic model automatically adjusting the model uncertainty as a function of the innovation vector as described in *Godinez and Koller* [2012].

Whereas most previous radiation belt Kalman filter studies define the state vector to be electron PSD for the full radial range, here we create an augmented system to also include source parameters as additional state variables [e.g. *Lainiotis*, 1971; *Ljung*, 1979]. Since Equation 14 is linear in *A*, we are able to simply append the state vector (*x*), state error (ε), and forward linear model operator (**M**) to include this additional parameter for assimilation; that is, we define an augmented state vector, error, and forward model operator as

$$x = \begin{bmatrix} f_1 & f_2 & \cdots & f_n & A \end{bmatrix}^T \quad \varepsilon = \begin{bmatrix} \varepsilon_{f_1} & \varepsilon_{f_2} & \cdots & \varepsilon_{f_n} & \varepsilon_A \end{bmatrix}^T$$

$$M = \begin{bmatrix} \overline{M} & 0 \\ 0 & 1 \end{bmatrix}$$

where ε_{f1} … $\varepsilon_{fn,}$ and ε_A correspond to the flux uncertainties at the 1st … n^{th} grid points and the uncertainty in A, respectively.

Model Variables	Description	Dimension
x_a	Analysis state vector	n×1
x_f	Forecast state vector	n×1
$\mathbf{P}_a$	Analysis covariance matrix	n×n
$\mathbf{P}_f$	Forecast covariance matrix	n×n
Q	Model covariance propagating matrix	n×n
H	Observation mapping operator	m×n
K	Kalman gain matrix	n×m
M	Forecast model operator	n×n
Observation Variables		
y	Observation vector	m×1
R	Observation covariance	m×m

Table 7: Description and dimension of vectors, matrices, and operators used in the Kalman filter. The value n represents the number of values being estimated by the filter and m is the number of observations at a given time t_i.

5.2.4 PARAMETRIC STUDY OF SOURCE PARAMETERS

The augmented Kalman filter algorithm is only capable of estimating the amplitude parameter of the source term. We must assign values for the location and width parameters. However, these terms are physically dynamic, most likely changing throughout individual storms. To find the most accurate source term location and width for specific periods we employ the observation residual, or the innovation vector, $(y_i - \mathbf{H}_i x^f_i)$, which represents the residual between the observations at time i and the model's forecast of the state at time i. It is a measure of the fidelity of the model or, in other words, it is an attempt to quantify physics that are present in the observations but absent from the model.

The RMS of the innovation vector is defined as

Equation 22: Innovation RMS

$$RMS_{INNOVATION} = \sqrt{\frac{1}{m}\sum_{i=1}^{T}\left(y_i - H_i x_i^f\right)^2}$$

where T is the total number of timesteps over the considered storm period and m is the number of observations. It is a reliable method to quantify the accuracy of the model, by measuring the discrepancy between model forecast and observations. A low (high) innovation vector RMS indicates that the model, including the location and width of the source rate, more (less) accurately predicts the actual measurements. Thus, the lowest innovation vector RMS establishes the solution in location-width parameter that can best reproduce the observed measurements.
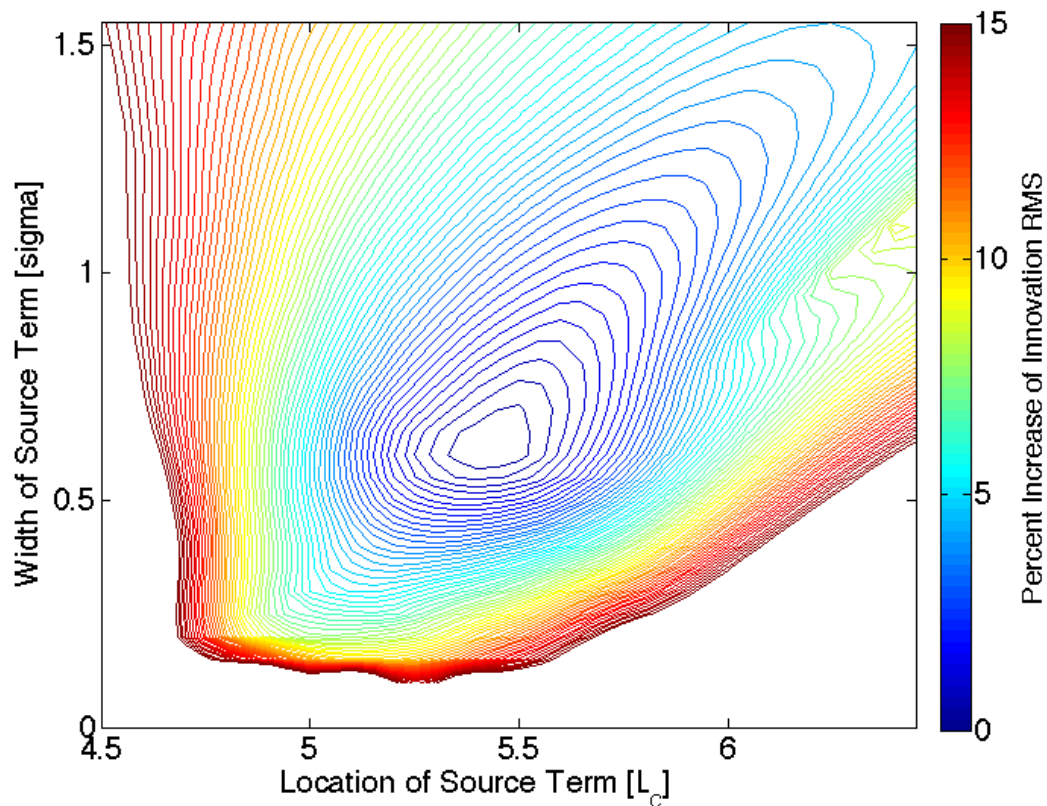
Figure 46: The innovation vector RMS parameter space as a function of the Gaussian source width (y axis) and location (x axis) for July 30th 04:00 to August 21st 00:00. Although the rest of the parameter space is not shown, the minimum depicted is a global minimum.
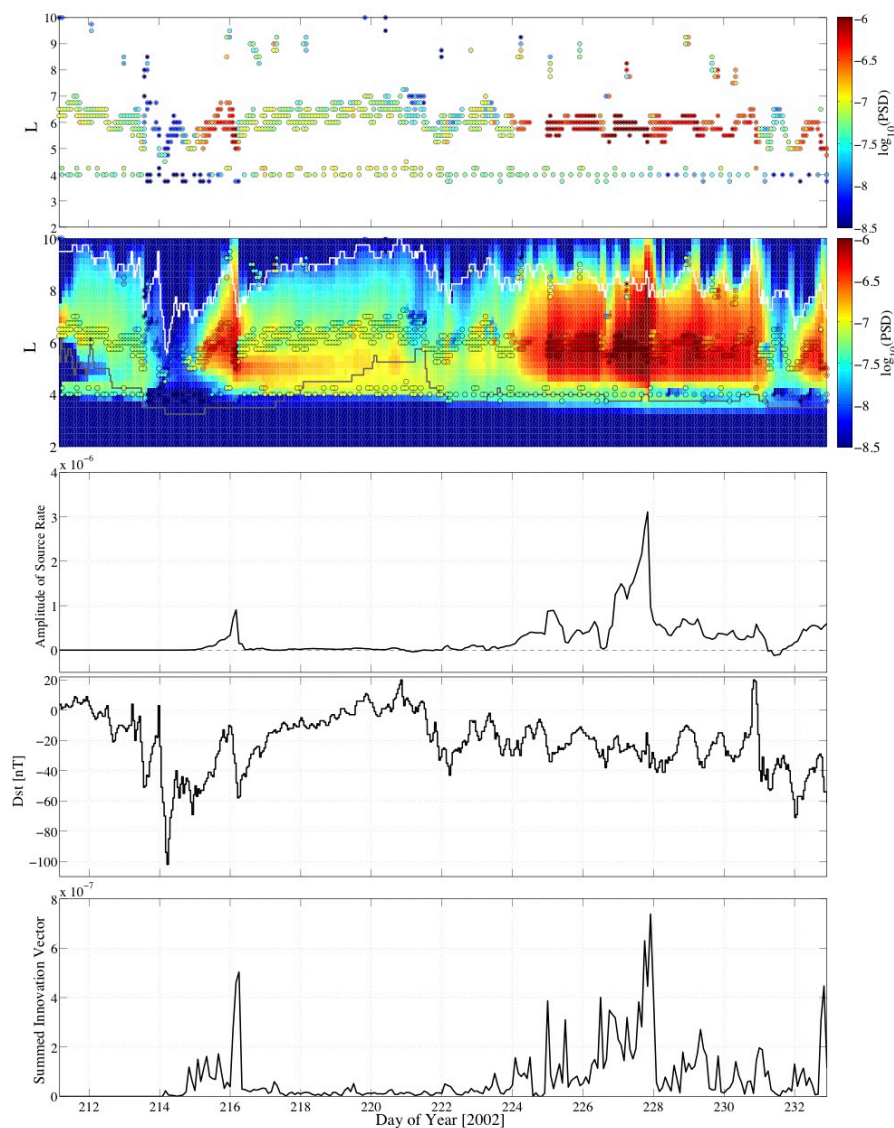
Figure 47: Data reanalysis from July 30ᵗʰ 04:00 to August 21ˢᵗ 00:00 with the source term at L_C=5.4 and width σ=0.6. Panel 1: Electron PSD dataset used in the assimilation. Panel 2: the reanalyzed PSD dataset with the data over-plotted for comparison. The white line represents the last closed drift shell and the grey line represents the plasmapause location. Panel 3: the amplitude parameter of the source rate term. Panel 4: the Dst index. Panel 5: the sum of the innovation vector at each time step, averaged by the number of observations (m).

Figure 46 represents the innovation vector RMS parameter space for July 30th 04:00 to August 21st 00:00 (which represents storm period 1 - see Table 8). To generate this figure, a series of simulations are performed, each with a discrete pair of source region parameters ranging from L_C=4.5-6.6 and σ=0.01-1.6. The innovation RMS is calculated for an individual model run, as each run corresponds to a unique source region. The minimum, located at L_C=5.4 and σ=0.6, represents the parameters that best reproduce the observations. These parameters are then applied to the source rate term and used in the reanalysis presented in Figure 47. The first panel of Figure 47 shows the gridded PSD measurements used. The second panel shows the reanalyzed dataset with the gaps across space and time filled in, plotted with the real observations. The source rate amplitude parameter *A* is estimated through the assimilation and plotted as a function of time in the third panel. Together with the ascertained location and width, the amplitude parameter completes the prediction of the source rate term and quantifies the location, extent, and magnitude of local heating during this period.

An important note is that the innovation vector RMS is a relatively stable measure of the accuracy of the assimilated results and not sensitive to the variable parameters. That is, small changes in innovation vector RMS are associated with significant changes in source rate parameters. For example, in Figure 46, a 1% change in RMS corresponds to a 0.4 variation in L_C and a 0.35 change in width. However, the innovation RMS for the same period without a source term is 28.9% higher than the same analysis including the source term. In other words, the model performs unquestionably better when the filter is

allowed to adjust the amplitude of the source parameter, decidedly justifying its inclusion.

The period of July 30th to October 25th is divided into storm periods, where each storm period begins upon achieving the two criteria: 1) Dst < -80 nT and 2) the first criterion has not been met in the previous four days. Each storm period is assimilated including three days preceding the achievement of the criteria to allow sufficient time for the filter to calibrate. The specifics for the resulting five periods are outlined in the first four columns of Table 8. An innovation RMS parametric study is performed for all five storm periods and the results are outlined in the right two columns in Table 8.

Storm Period	Reanalysis Start Date	Storm Criteria Achieved	Reanalysis End Date	L_C	σ
1	July 30th 04:00	Aug. 2nd 04:00	Aug. 21st 00:00	5.4	0.6
2	Aug. 18th 00:00	Aug. 21st 00:00	Sept. 4th 04:00	5.4	1.5
3	Sept. 1st 04:00	Sept. 4th 04:00	Oct. 1st 10:00	6.1	1.3
4	Sept. 28th 10:00	Oct. 1st 10:00	Oct. 14th 13:00	3.9-4.2	Likely <0.6
5	Oct. 11th 13:00	Oct. 14th 13:00	Oct. 24th 00:00	7.1	1.3

Table 8: The individual storm periods are outlined with the location and width of the source term to minimize the innovation vector RMS.

Whereas most periods result in a straightforward minimum in location-width space, storm period 4 presents distinctive results. A storm of Dst=-180nT occurs on October 1st (day of year [DOY] 274), and the resulting PSD peak occurs near L=4. Intuitively, one would expect that the residual RMS to be smallest for $L_C \approx 4$. Indeed, a source region centered between L=3.9-4.2 minimizes the innovation RMS. However, because of the proximity of this source region to the

plasmapause (which is already compressed to small L), source widths greater than σ≈0.6 considerably populate the slot region. Without measurements below L=3.5 to locally update the filter, the slot region accumulates PSD from the source term. Although rare, heating near L=3 is possible during periods of high geomagnetic activity [*Shprits et al.*, 2012]. Thus, without measurements in this region, we cannot specify the width of the source region for this period, although a width of σ<0.6 does not allow significant PSD accumulations inside of L=3.

Since source location and width parameters are specified for each period, reanalysis of the 87-day period is performed with the source parameters changing appropriately for each storm period. The resulting reanalysis is shown in Figure 48. The second panel portrays the data from the first panel superposed on top of the reanalyzed PSD dataset. The spatiotemporal gaps in PSD are filled, allowing for an estimate of electron PSD for the entire radial range of the radiation belt. The full source term, including all three parameters – L_C and σ from the innovation RMS analysis and *A* directly from the state vector – is pictured in the third panel. This panel visualizes the magnitude and extent of local heating occurring during this period. Notice that discontinuities do not occur in the state vector, which allows for a space- and time-continuous estimate for PSD and source rate amplitude, even over boundaries between storm periods. Panel four depicts the amplitude term only and quantitatively conveys the intensity of the heating.

The source rate function, which consists of time series estimates of three source rate parameters, is used in a simple one-dimensional diffusion model Equation 14 without assimilation for comparison. Identical diffusion rates and
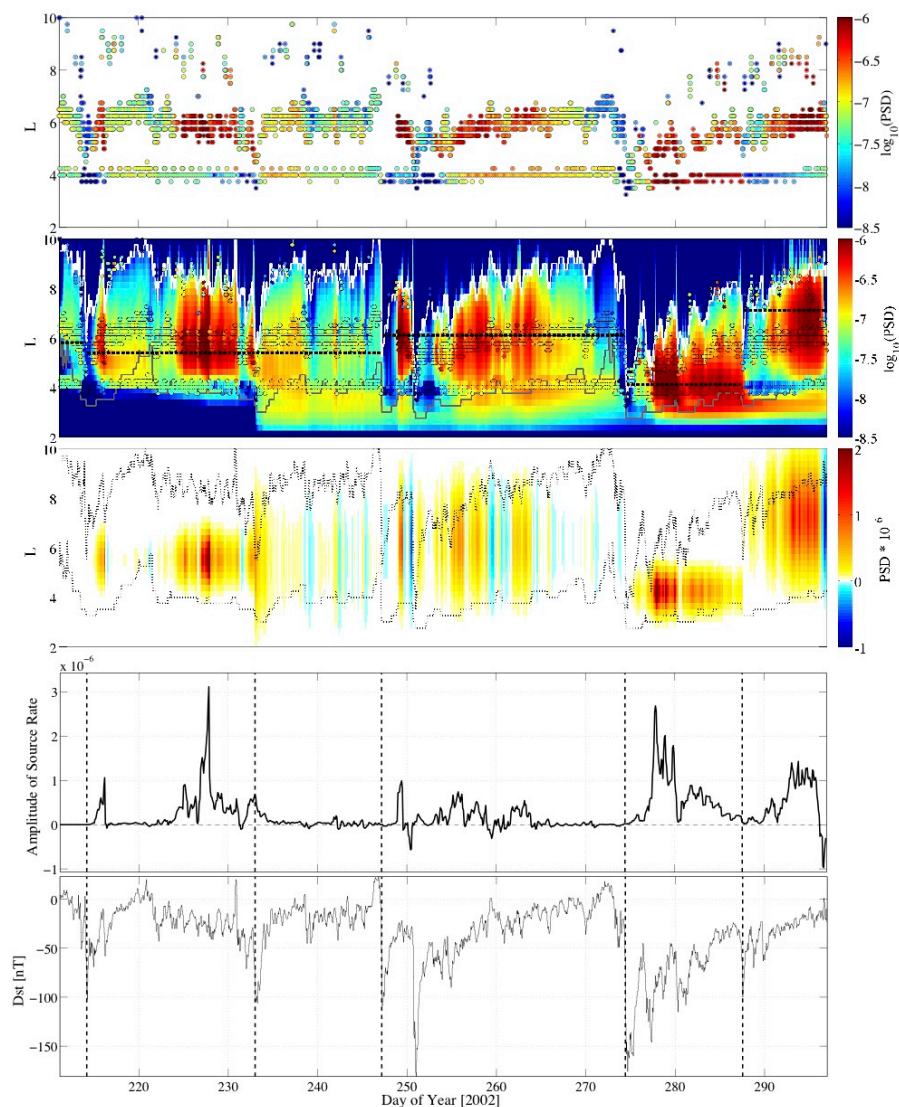
Figure 48: Panel 1: electron PSD dataset used in the assimilation. Panel 2: reanalyzed PSD with data overlay. The white line corresponds to the last closed drift shell and the grey line to the plasmapause location. Panel 3: the source term, where red/yellow colors represent a positive source term and blue values represent a negative source term. For reference, the upper dotted line represents the last closed drift shell and the lower dotted line represents the plasmapause. Panel 4: the source amplitude parameter. Panel 5: the Dst index. In both Panel 4 and Panel 5, the vertical dashed lines represent the boundary between consecutive storm periods.
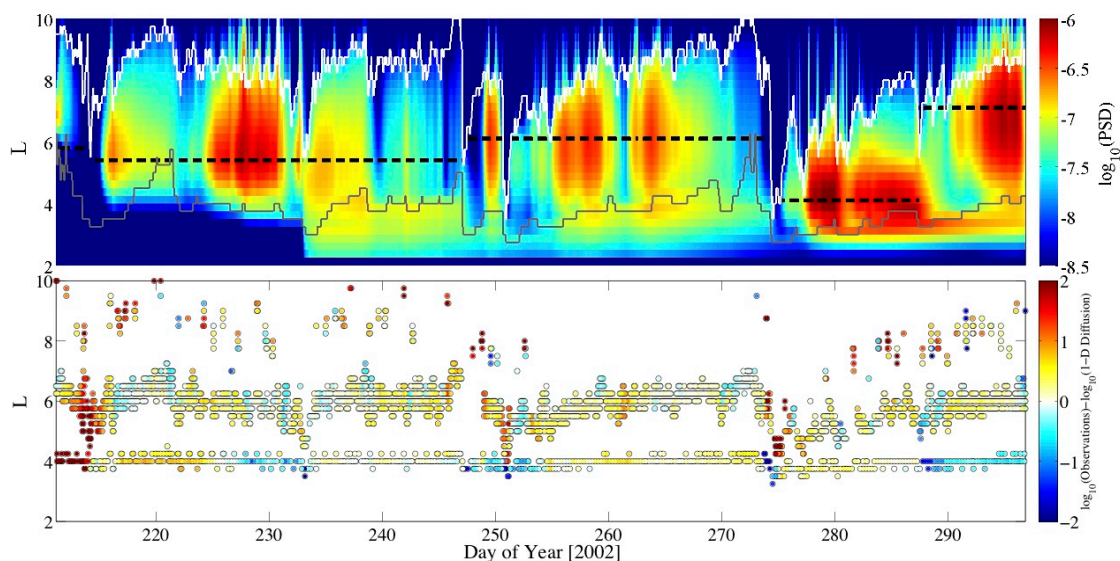
Figure 49: Panel 1: One-dimensional radial diffusion model with no assimilation. The diffusion coefficient and loss terms used are outlined in Section 2.2. The full source term from the parametric study is included. Panel 2: The difference between satellite data (Figure 48, Panel 1) and the radial diffusion model without assimilation.

loss timescales are used, as described in Section 2.2. The time series of the local acceleration function (visualized in Figure 48, Panel 3) is applied in the model.

The results are shown in Panel 1 of Figure 49. As expected, the resulting PSD from the 1D diffusion model is very similar to the reanalyzed PSD. We quantify the 1D diffusion model's ability to reproduce the observations in Panel 2, where the PSD observations (Figure 48, Panel 1) are directly compared to the results of the simple 1D diffusion model. The diffusion model with no assimilation is able to reproduce the majority of the observations within a factor of 2.

5.2.5 DISCUSSION

This study is performed for only a single pair of first and second adiabatic invariants, μ and K, and captures only a small subset of the dynamics of the radiation belts. A reanalysis of all available μ and K combinations is beyond the scope of this study, but will be performed to gain insight on a more comprehensive global picture. The presented analysis demonstrates the pertinence of using data assimilation techniques to do science on the observationally sparse radiation belts, and also allows us to perform science on this particular set of energetic electrons.

Upon closer inspection of the acceleration enhancements in Figure 48, it is apparent that the energization of outer belt electrons generally occurs in the recovery phase of the storms, as expected from elevated ULF wave [e.g., *Elkington et al.*, 1999] and chorus wave activity [e.g., *Li et al.*, 1997; *Bortnik and Thorne*, 2007]. Additionally, the source region occurs inside of GEO for four of the five storm periods analyzed and the widths vary appreciably between $\sigma=0.6$-1.5. The fluctuation in source rate magnitude is significant, changing orders of magnitudes over hours to days, but the timescale could be limited to the resolution of the analysis. The maximum rate of approximately 3.0×10^{-6} $(c/cm/MeV)^3day^{-1}$ occurs on August 14th at 20:00 (DOY 226), but local maxima are varied for each storm period. This maximum rate, if sustained, is capable of completely repopulating the radiation belt to the largest observed value in ~17 hours. The third storm period (August 21st 00:00 to September 4th 04:00 [DOY 233-247]) has the smallest enhancements, the largest of which is 2.1×10^{-7} $(c/cm/MeV)^3day^{-1}$, which would repopulate the radiation belt in ~10 days, if

sustained. The source rates are sufficient to show that local heating is a major factor in populating the electron radiation belts during storm recovery phases. An interesting extension of this work will be to determine the relationship of the source term between multiple combinations of first and second invariant pairs in addition to higher temporal resolution and correlation between solar wind drivers. The temporal evolution between low-energy and high-energy electrons could be examined as per *Turner and Li* [2008b], for example.

We briefly investigate the effect of magnetopause loss timescales by rerunning the simulation with loss timescales two times larger and two times smaller for $L>L_{MAX}$. That is, we perform the same analysis, but with loss timescales above the last closed drift shell equal to $\tau=5$ minutes and $\tau=20$ minutes (instead of $\tau=10$ minutes). The locations and widths of the source terms are reproduced identically for all storm periods except for the 20-minute timescale, where for storm period five L_C changes from 7.1 to 6.7 and the width from 1.3 to 1.1, and for storm period three where the width changes from 1.3 to 1.2. The other storm periods are unaffected by either a 5 or 20 minute loss timescale above L_{MAX}.

Estimation of source rate location and width is completely novel in data assimilation applications of the electron radiation belts. However, other Kalman filter studies, which also use 1-D models for a single first and second adiabatic invariant pair, have constrained the source region's location and width. The results of our parametric study agree with previous data assimilation in principle. *Shprits et al.* [2007] used a CRRES PSD dataset (for less energetic particles of $\mu=700[MeV/G]$ and $K=0.11[G^{1/2}R_E]$) from August 18th to October 7th,

1990 and averaged the Kalman innovation vector to find missing source region resembling a positively skewed Gaussian centered at L=5.5 with width σ≈0.3-0.8. *Daae et al.* [2011], using a similar PSD dataset (Polar, GPS, and three LANL-GEO for μ=2083[MeV/G] and K=0.33[$G^{1/2}R_E$]), inspected the Kalman innovation vector for a variety of different model conditions from June 6th to December 31st, 2002 and repeatedly found evidence of pseudo-Gaussian acceleration occurring between 5≤L≤6, with widths between σ≈0.6-0.9. However, both of these studies assimilated multiple storms, so the results are a long-term average of source processes. *Koller et al.* [2007] used a similar PSD dataset (Polar, GPS, and three LANL-GEO for μ=2083[MeV/G] and K=0.1[$G^{1/2}R_E$]) for the October 24th, 2002 storm (October 25th -November 2nd [DOY 298-306]) and summed the Kalman innovation vector to find a Gaussian-shaped source region close L=5.5 with width σ≈0.3.

Reeves et al. [2012] demonstrated that the Dynamic Radiation Environment Assimilation Model (DREAM) has the capabilities to estimate the amplitude of a Gaussian source region in a comparable method to that presented here. They used a similar dataset (Polar, GPS, and three LANL-GEO), for μ=2083[MeV/G] and K=0.03[$G^{1/2}R_E$], and an ensemble Kalman filter [*Evensen*, 2003], to provide an amplitude estimate for the same storm period as *Koller et al.* [2007]: October 21st to November 4th, 2002. *Reeves et al.* [2012] chose the source location and width to compensate for the dual-peak nature of the reanalyzed PSD, which is caused by observations at GEO and GPS with extensive data gaps in the region L~4-6. Hence, they choose a source location of L=5 with width of σ=1, which eliminates the PSD trough between GEO and GPS observations. The intensity of local

heating peaks in the pre-storm phase, which is an artifact of the filter using the source term to compensate for the dual-peaked initial condition. They find, as presented in this study, that the source rate intensifies in the recovery phase.

Our findings agree with results from non-assimilative studies that find peaks in electron PSD below GEO. Modeling done with the 3-D VERB diffusion code [*Shprits et al.*, 2008], including chorus wave interactions, found peaks in PSD at L ~ 4-6 for electrons with mu = 700 MeV/G. Similarly, modeling done with the 3-D Salammbo code [*Beutier and Boscher*, 1995], including interactions with chorus waves, found PSD peaks for 3100 MeV/G electrons near L=5.5 during the recovery phase [*Varotsou et al.*, 2005]. These physics-based models are consistent with our findings.

Investigations of electron PSD radial gradients using LANL-GEO data conclude localized acceleration occurring inside of GEO for electrons with μ=2000[MeV/G] [*Turner and Li*, 2008a; *Turner et al.*, 2010] and for electrons with 1.1-1.5 MeV [*Shi et al.*, 2009]. More comprehensively, *Green and Kivelson* [2004] (for electrons with μ=2000[MeV/G] and K>500[$G^{1/2}R_E$]) and *Chen et al.* [2006] (for electrons with μ=2083[MeV/G] and K=0.1[$G^{1/2}R_E$]) were able to estimate local heating occurring near L=5 and L=5-6, respectively. Additionally, *O'Brien et al.* [2003] found associations between acceleration and VLF/ELF chorus waves occurring near L~5 for electrons of 1.8-3.5 MeV and >1.5 MeV. These studies, which arrive at similar conclusion for a variety of *µ* and K pairs, but in different ways, reinforce the theory of internal acceleration mechanisms occurring near GEO.

5.2.6 SUMMARY

We use a Kalman filter, which blends energetic electron measurements of a specific pair of first and second adiabatic invariants with a one dimensional radial diffusion model, to produce an estimate of the outer radiation belt environment that is more accurate than either independently. Although the in-situ energetic electron measurements are sparse, the Kalman filter technique is capable of filling in spatiotemporal data gaps for constant μ and K and has proven robust for this application [*Naehr and Toffoletto*, 2005; *Ni et al.*, 2009; *Daae et al.*, 2011; etc.]. Previously, PSD values, loss timescales, and source rate have been determined using a Kalman filter, but this is the first attempt to quantitatively estimate source location and width, as well as the source rate over multiple storms. Specifically, we calculate the location and extent of the heating regions and quantify the time-dependent intensity of the enhancements.

Electron phase space density (PSD) observations from five satellites (three LANL geosynchronous, a GPS, and Polar) for μ=2083[MeV/G] and K=0.3[$G^{1/2}R_E$] are combined with a one-dimensional radial diffusion model that includes loss and parameterized local acceleration. The state vector is augmented to include an estimateable amplitude parameter for a Gaussian source rate term; thus, we are able to estimate the rate of local heating as a function of time. Other source term parameters include location and width, which are assigned values for each simulated period and are not directly estimated by the filter. However, we are able to estimate them using a parametric study, in which we use the innovation vector to find the most accurate solution in location-width parameter space. The innovation vector is a tool that measures of the performance of the model with

respect to actual observations, and is used to quantify physics that are present in the observations but absent in the model.

The analysis period, July 30th to October 24th, is divided into five storm periods (based on Dst criteria), and for each period the root mean square (RMS) of the innovation vector is calculated for various locations and widths. The RMS minimum indicates source rate parameters that best match the observations, consequently defining the most likely location and width of the source region. A detailed analysis of July 30th 04:00 to August 21st 00:00 (DOY 211 to 233), 2002, is presented as an example. We find that the minimum innovation vector RMS for this period occurs with source occurring at L=5.4 with width σ=0.6. The analysis is performed for all five periods and the results are included in a reanalysis of the full 87-day period. The resulting assimilated data consists of constant μ and K PSD for the full radial range, with spatial and temporal observational gaps filled, and an estimate of the source rate amplitude parameter as a function of time.

The source regions are found to occur within GEO for four of the five periods analyzed. Furthermore, close inspection of its intensity shows orders-of-magnitude fluctuations on the timescales of hours. The magnitude of the enhancements increases during the recovery phase of many of the storms, consistent with occurrences of ULF and chorus wave activity [e.g. *Li et al.*, 1997; *Elkington et al.*, 1999; *Bortnik and Thorne*, 2007]. Additionally, local peaks of the acceleration enhancements are almost exclusively found during the recovery phase. The magnitude of the enhancements indicates that local heating is a significant contributor to the energetic electron population. In fact, the rate

shows that local heating is capable of completely repopulating the radiation belt after a full dropout.

The presented Kalman filter results are consistent with past data assimilation studies and previous PSD gradient studies, and confirm the importance of local electron heating near GEO in repopulating the outer radiation belt during the recovery phase of geomagnetic storms. Furthermore, this novel technique advances the applications of Kalman filters to Earth's energetic electron environment and provides a unique perspective on the dynamics of the outer radiation belt.

5.3 *Determining source rate parameters of energetic electrons in the outer radiation belt using a Kalman Filter*
by Q. Schiller and H. C. Godinez, published in Los Alamos Space Weather Summer School Research Reports, edited by J. Koller, J. R. Terry, and R. D. Gurule, 2012

Abstract

The following is a continuation of the work presented in the previous section [*Schiller et al.*, 2012]. Data assimilation methods are becoming increasingly popular to describe the observationally sparse environment in Earth's magnetosphere. As energetic electrons pose a number of hazards to manned and unmanned spacecraft, the outer radiation belts are an especially high profile candidate for data assimilation techniques. Energetic electron diffusion can be simplified with a Fokker-Plank equation, which also allows for the ability to include loss or source terms. We use a one-dimensional radial

diffusion model and a conventional Kalman filter (CKF) to describe the energetic electron PSD for the full radial range of the outer radiation belt. Additionally, we augment the state vector to include the magnitude of a Gaussian-shaped local acceleration term. The result of the analysis is an estimate of electron PSD, as well as a time-dependent heating rate for specified location and width. To further constrain the source rate parameters, such as the location and width of the acceleration region, additional analysis is performed using the observational residual vector (or innovation vector) by quantifying the root mean square (RMS) of the vector in a location-width parameter space. We prove the functionality of the innovation vector RMS method with three identical twin experiments, in which the method proves robust and is able to reproduce the synthesized source rate parameters and PSD. We then apply the method to real spacecraft observations, consisting of a five satellite Phase Space Density (PSD) dataset (three LANL-GEO, one GPS, and POLAR) for constant first and second adiabatic invariants, $\mu = 2083[MeV/G]$ and $K = 0.03$ [G 1 R]. In a data denial experiment, we show that the intensity of local 2E heating is robust to removing satellites from the dataset. Using the satellite observations we estimate the PSD and full source rate term (including amplitude, location, and extent of the local heating) for the entire period. Finally, we attempt to find a correlation between the plasmapause location and the location of local heating. However, a concrete correlation will require further investigation.

5.3.1 Identical Twin Experiments

The following identical twin experiments are a continuation of the work

done by *Schiller et al.* [2012]. For this part of our study, we run identical twin experiments to prove the functionality of the model. The first step of the experiment is to synthesize a dataset to act as the 'true' data the model is trying to recreate. In this case, there is a source term included which has constant amplitude, but changes in width and location every 3 days (Figure 50). Observations are taken of the 'true' data with ±10% error included (Figure 51). The observations are an attempt to recreate a hypothetical satellite in an idealized orbit flying through the radiation belts. Using the method described above, we attempt to recreate both the PSD for the full radial range as well as the amplitude, location, and width of the source term. The results can be seen in Figure 52.

We choose the source location to vary minimally, never by more than 0.4L, to verify the method works even during potentially 'worst-case' scenarios, where the filter would have difficulty distinguishing small variations in the parameters. The results confirm that our method works to estimate the amplitude of a constant source rate term, as well as accurately estimates the location and width. To determine the robustness of the method to more extreme gradients in the source term, we perform the same analysis for a source term that changes in intensity every three days by up to a factor of 3. A visualization of the synthesized term for this experiment can be seen in Figure 53, and the estimated source rate parameters can be seen in Figure 54.
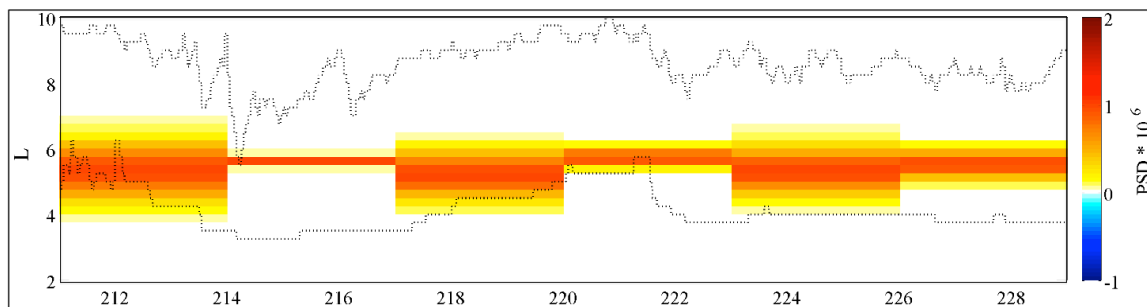
Figure 50: A visualization of the source rate. In this case, the amplitude is set to constant (1 × 10−6) for the full period, but the location and width change every three days.
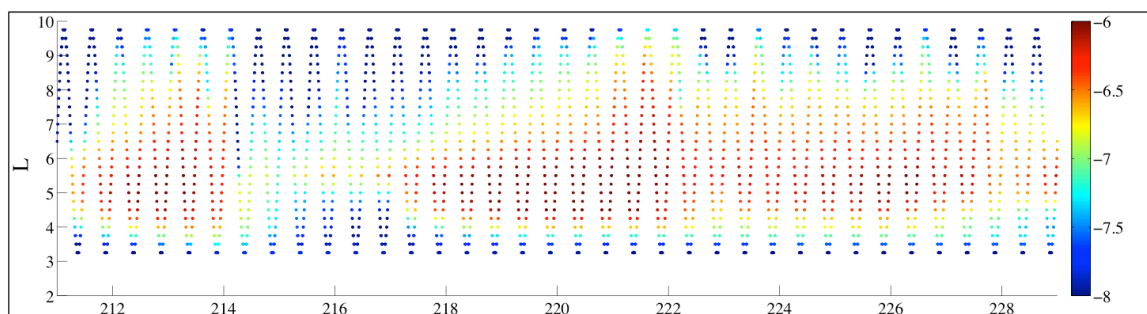
Figure 51: The sampling from the 'true' data (2), with ±10% error included, which are used as observations in the model.
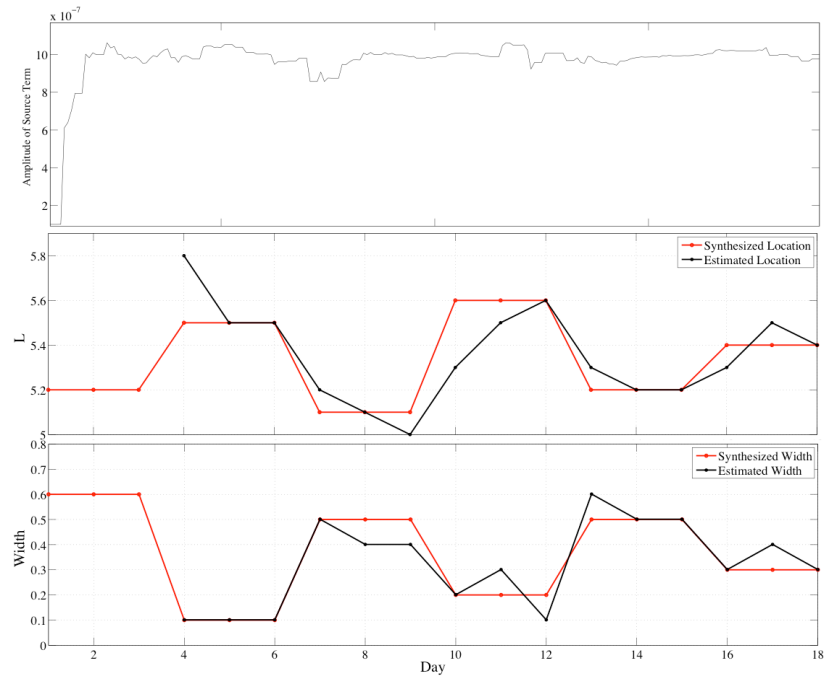
Figure 52: Results of the identical twin experiment - estimates of source rate parameters.
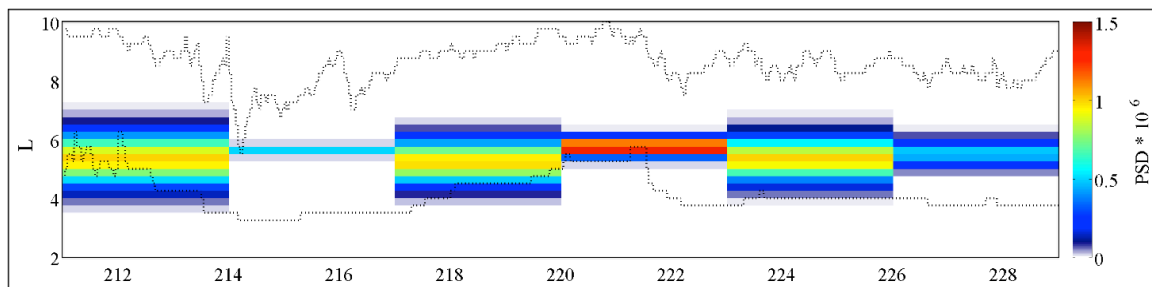
Figure 53: A visualization of the entire source term with variable amplitude. The amplitude varies from 0.5e-6 to 1.5e-6.
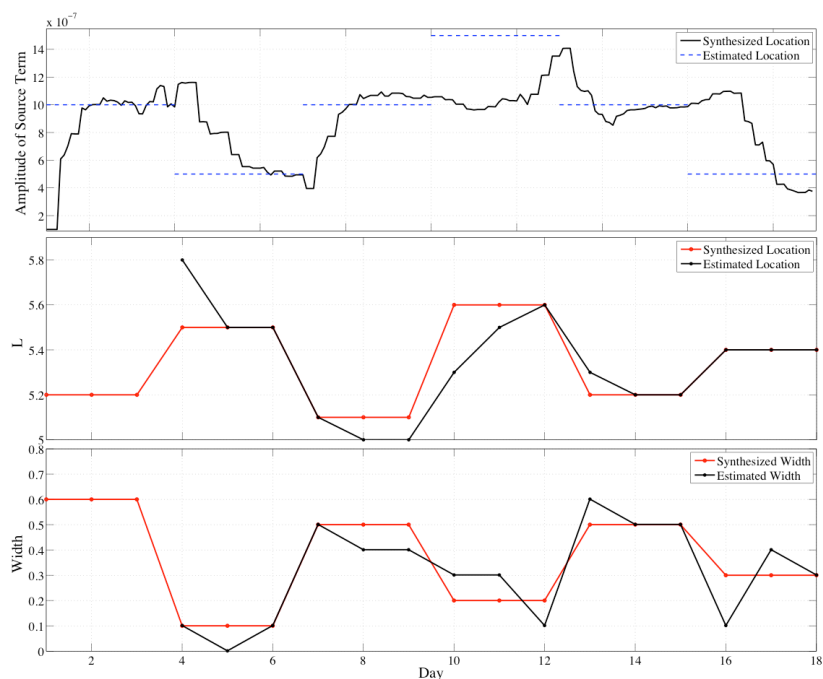
Figure 54: Estimate of source term parameters for the identical twin experiment with variable source rate amplitude as seen in Figure 53. The top panel shows the actual source rate amplitude in blue and the estimate of the parameter in black. The middle and bottom panels show the actual source term location and width, respectively, in red and the estimate of the terms in black.
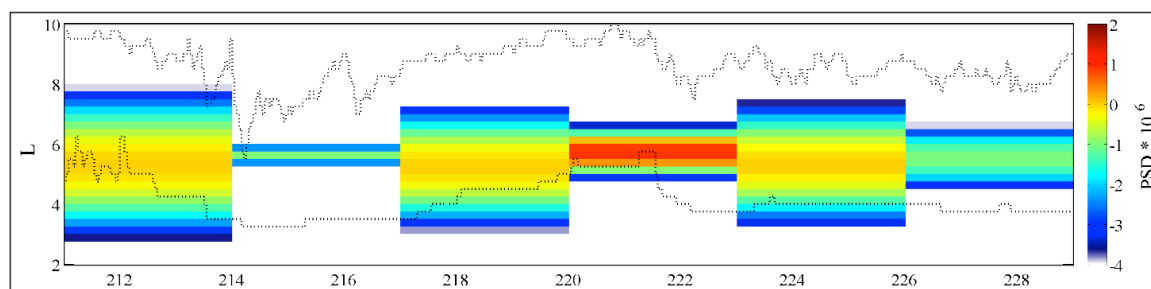
Figure 55: The entire source term with variable amplitude. The amplitude varies from 0.1e-6 to 10e-6. The label on the colorbar axis should read log10 (PSD*10⁶).
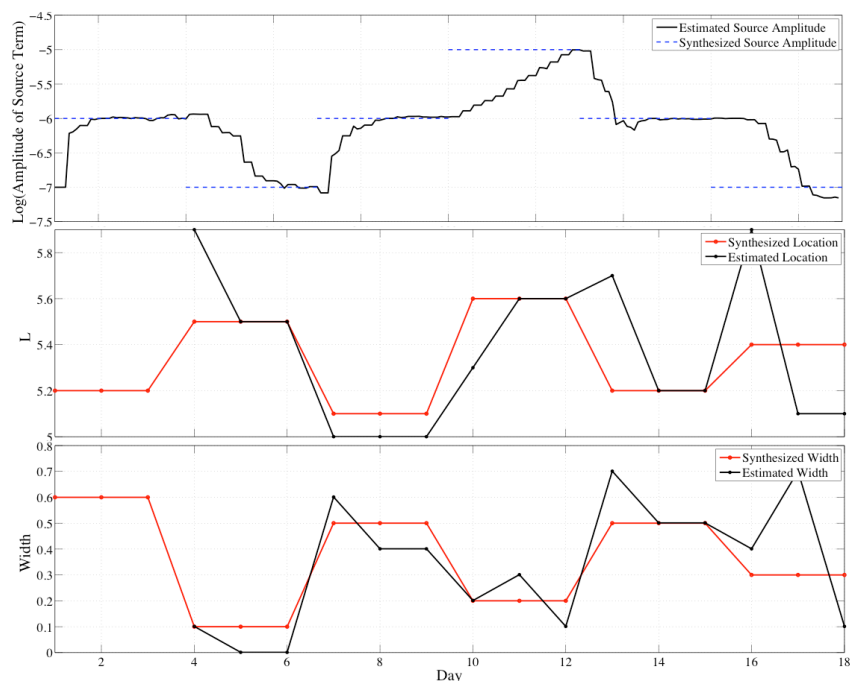
Figure 56: Estimate of source term parameters for the identical twin experiment with variable source rate amplitude as seen in Figure 55. The top panel shows the actual source rate amplitude in blue and the estimate of the parameter in black. The middle and bottom panels show the actual source term location and width, respectively, in red and the estimate of the terms in black.
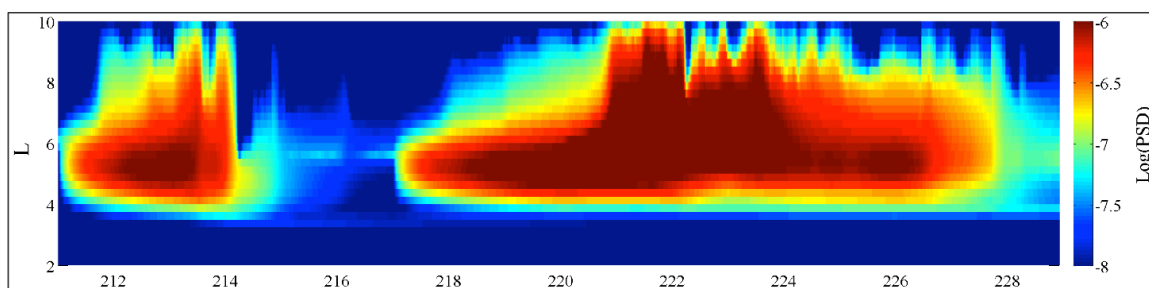
Figure 57: Synthesized data from the identical twin experiment which includes the source term which varies by two orders of magnitude.
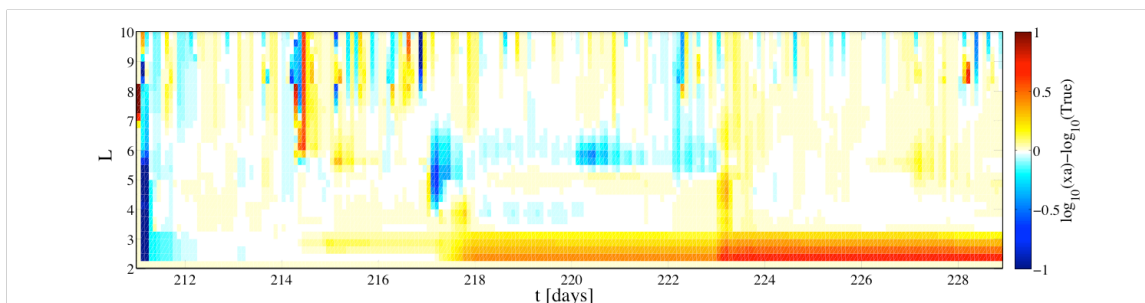
Figure 58: **The difference between the log of the PSD estimate and the log of the true PSD state, with source rate from Figure 55 included.**
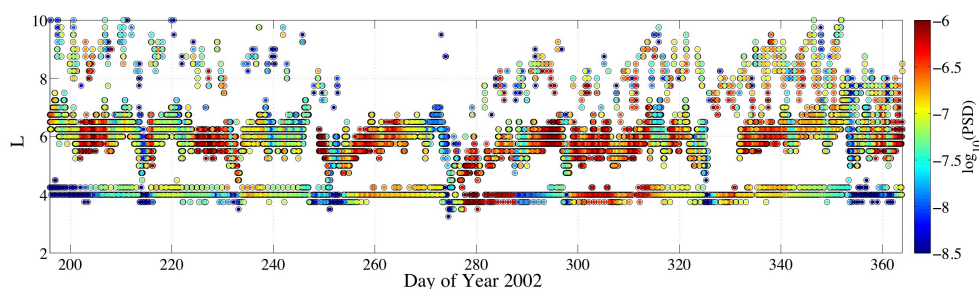
Figure 59: The full dataset in consideration, including observations from three LANL-GEO, POLAR, and a GPS spacecraft.

The results are very similar to the previous results. However, there is ~1 day delay for the amplitude estimate to converge on the correct value. These results agree to *Daae et al.* [2011], who find that the model 'forgets' previous states in approximately one day. More specifically, the difference between two models with drastically different initial conditions is reduced to %15 after one day. These results confirm that the method is valid for local heating which varies in time. However, heating rate that varies by no more than a factor of three is not physical. In the next experiment, the intensity of local heating varies by two order of magnitude - a scenario that is more likely to be observed in the

magnetosphere. The source rate term can be seen in Figure 55, and the estimates of the source rate parameters in Figure 56.

The results for this experiment are more scattered than previous results. Generally, the model performs well with some minor exceptions. First, it takes ~2.5 days to converge to the largest amplitude, whereas closer to one day for the others. Second, when the maximum source rate lowers by an order of magnitude, the subsequent estimate of location and width is far less accurate. This is likely due to the strong gradients which occur as the high levels of PSD diffuse radially and saturate the source term, as can be seen in Figure 57. Finally, the final period (days 16-18) is decidedly the least accurate estimate of source location and width. Similar to the second point, this is likely due to the high levels of PSD which occur in the source region during this period, which originate from the period of highest source intensity (days 10-12) and continue through days 13-15. The high PSD mask any source that is occurring, and the high PSD gradients from radial diffusion (as opposed to local heating) make it difficult for the filter to distinguish the relative contribution of local heating.

The large absolute PSD and steep PSD gradients result in poor estimates of location and width for the last period in the study. We suspect that, given a few more days for the PSD to diffuse away and be lost to the boundaries, the filter would converge to the correct values of location and width, as it did for a similar period of low source rate during days 4-6. However, despite the inaccuracies involved with estimates of source rate term parameters, the filter is able to accurately estimate the PSD for the entire period, as seen in Figure 58. These experiments prove that the method of innovation vector RMS in a parameter space is capable of reproducing not only parameters in the state

vector, but also parameters estimated 'offline', such as source rate location and width.

5.3.2 Real Data

As seen in the previous section, the method estimates all three parameters for a Gaussian-shaped source rate term - amplitude, location, and width - is also capable of reproducing synthesized PSD, both for a synthesized dataset. The next step is to apply this method to real satellite observations. The observations themselves are described in the following subsection, followed by a brief study to determine the robustness of the Kalman filter to different satellite observations, and finally the results of the method applied to the satellite PSD dataset.

PSD Observations

The data used in the assimilation process is a PSD dataset provided by Yue Chen at Los Alamos National Lab [*Chen et al.*, 2005; 2006]. It consists of particle measurements from five spacecraft: three LANL-GEO (97a, 1991-080, 1990-095), one Global Positioning System (GPS-ns41), and POLAR. The particle detectors onboard the satellites are: LANL-GEO - Synchronous Orbit Particle Analyzer (SOPA) instrument [*Belian et al.*, 1998], GPS - Burst Detector Dosimiter (BDD) II [*Feldman et al.*, 1985], and POLAR - Comprehensive Energetic Particle and Pitch Angle Distribution Experiment (CEPPAD) [*Blake et al.*, 1995]. In total, 87 days of data are available from June 30th to October 24th, 2002. Data from all spacecraft are averaged to the center of each discrete mesh grid point with dimensions 0.25[L] x 120[min]. The conversion from flux to PSD is done for

constant first and second adiabatic invariants, μ 2083 [MeV/G], and , K = 0.03 [G$^{1/2}$ R$_E$] respectively, and is performed in two steps following *Chen et al.* [2005, 2006] and *Hilmer et al.* [2000]. These particles correspond to ~1 MeV at GEO. The entire dataset can be seen in Figure 59.

Data Denial Experiments

A very brief study was conducted to determine the affect different satellites have on the overall PSD estimate of the state space. To conduct this experiment, a period from DOY 211 to 233, 2002 was reanalyzed with the augmented state space vector (to estimate the amplitude of the source rate term). The location was set to L=5.5, with width set to 0.3. These parameters were constant over the interval. A comparison was done between the reanalysis using all satellite observations; the reanalysis using only POLAR and GEO spacecraft (Figure 61); and the reanalysis using POLAR, the GPS spacecraft, and two of the three GEO spacecraft (Figure 60). The results for each are as expected: the larges differences in PSD occur where the data from the absent spacecraft is no longer available.

For the data denial experiment with the GEO spacecraft removed, the differences occur between the GPS observations and the magnetopause. The largest differences occur between DOY 225 and 230, during an enhancement in the radiation belts. During this time, the differences are magnified when 97A provided the only data for a particular observation time step, or when 97A observed significantly different PSD than the other GEO spacecraft for the same
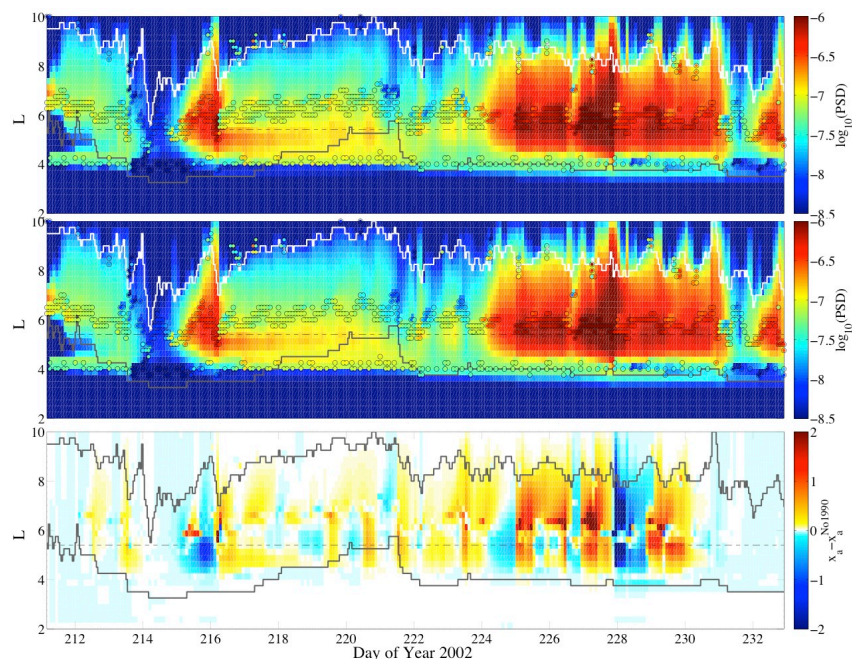
Figure 60: Top panel: Reanalysis with observations from all five spacecraft. Middle panel: Reanalysis performed with all observations except LANL-GEO 97A. Bottom panel: The log difference between the the two reanalyses. The dashed line corresponds to the location of the estimatable source term.
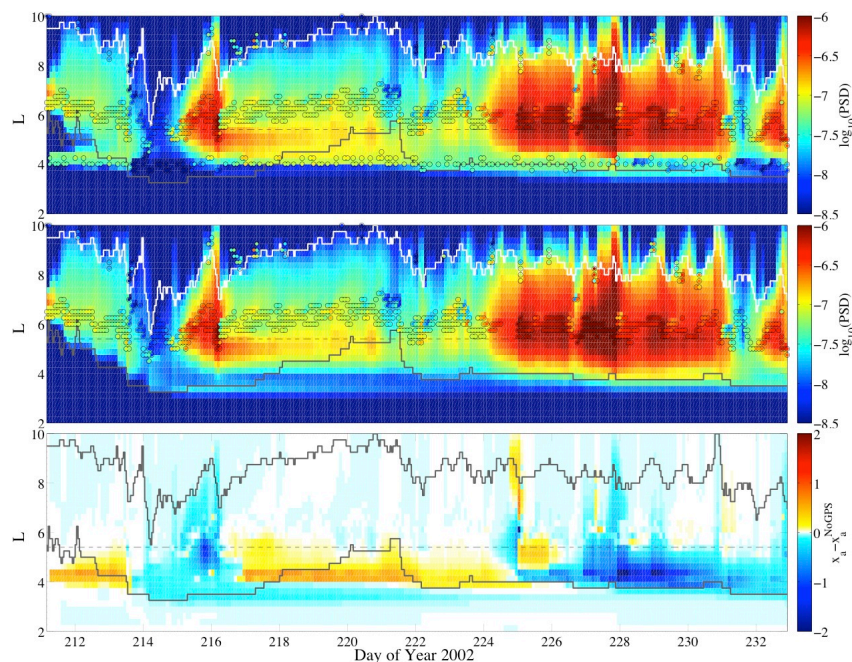
Figure 61: Top panel: Reanalysis with observations from all five spacecraft. Middle panel: Reanalysis performed with all observations except GPS. Bottom panel: The log difference between the the two reanalyses. The dashed line corresponds to the location of the estimatable source term.
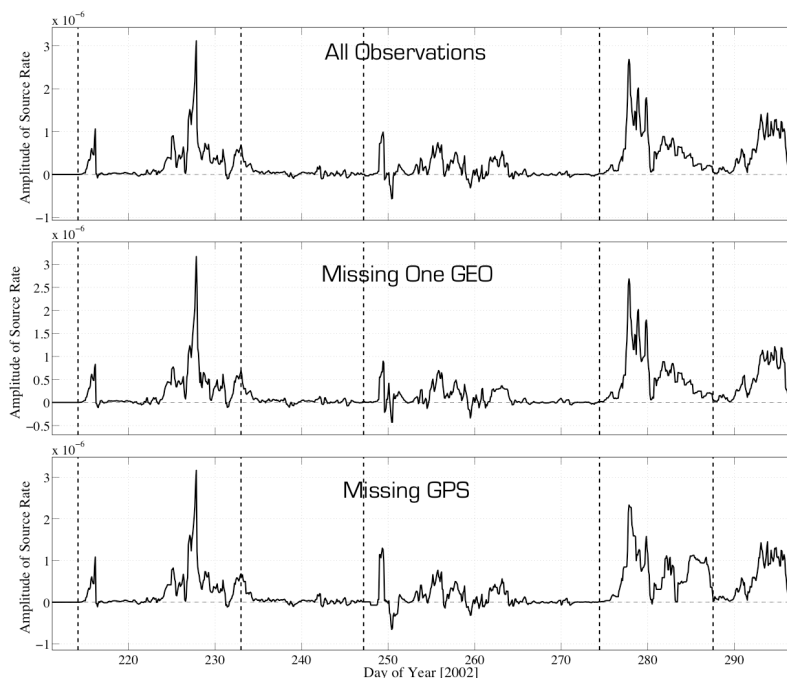
Figure 62: The estimate of the amplitude parameter for reanalysis performed with observations from all five spacecraft (top panel), all spacecraft except for one LANL-GEO (97A - middle panel), and all spacecraft except for GPS (bottom panel). The dashed line corresponds to the location of the estimatable source term.
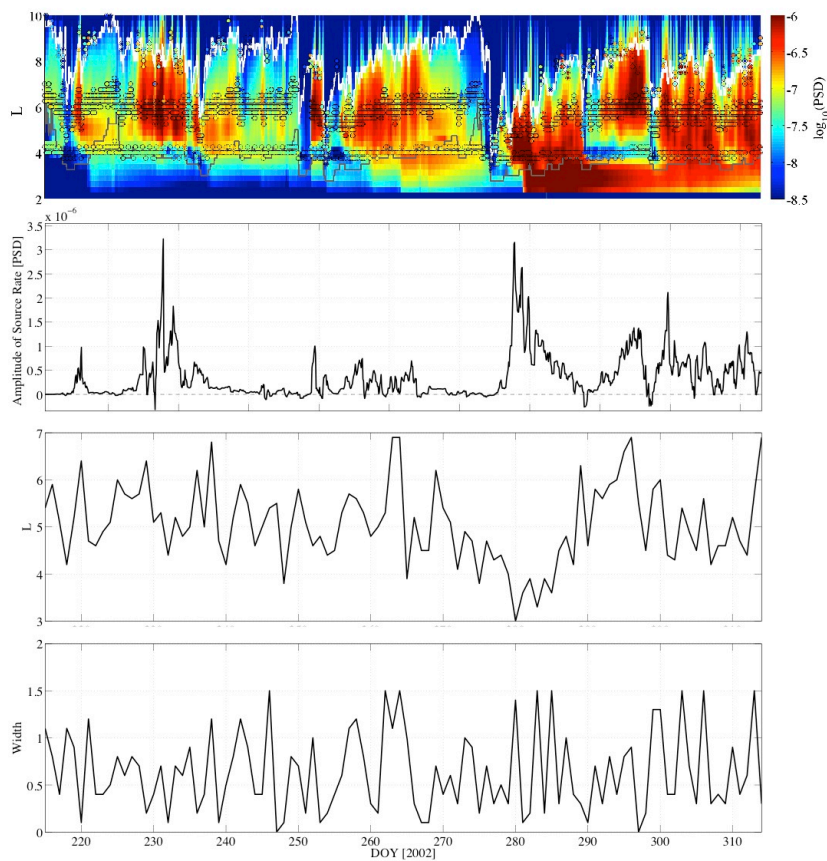
Figure 63: The results of the reanalysis and parametric study on actual observations, as depicted in Figure 59. The top panel shows the PSD estimate with observations overlain, with source term included with parameters from the following panels.. The second panel shows the estimate of the source rate amplitude given the locations and widths described in the following panels. The PSD and amplitude estimates have temporal resolution of 120 minutes, as they are 'online' estimate directly from the state vector. The third panel depicts the location parameter of the source term. The last panel represents the width parameter of the source term. The width/location combination was derived from the parametric study as described in Section 3 and performed in Section 4.
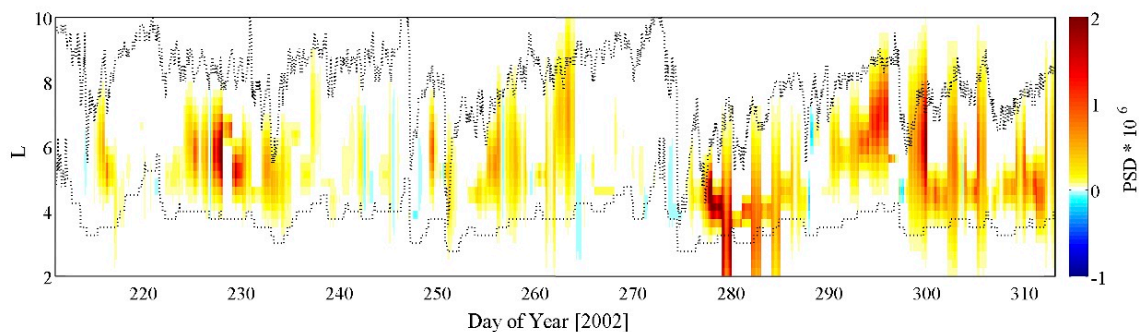
Figure 64: A visualization of the total source rate term, including location, width, and magnitude (color).
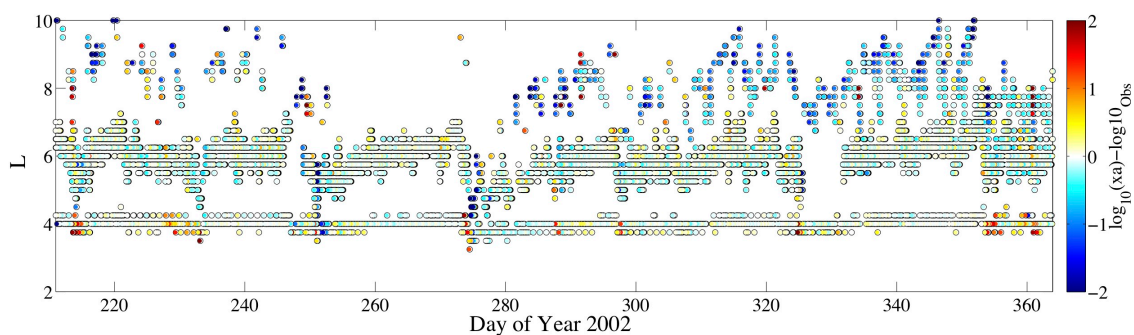
Figure 65: The differences between the log of the estimated PSD and observed PDS at each observation. White indicates a very good match, intense cooler colors an underprediction by the model, and intense warmer colors an overprediction by the model.
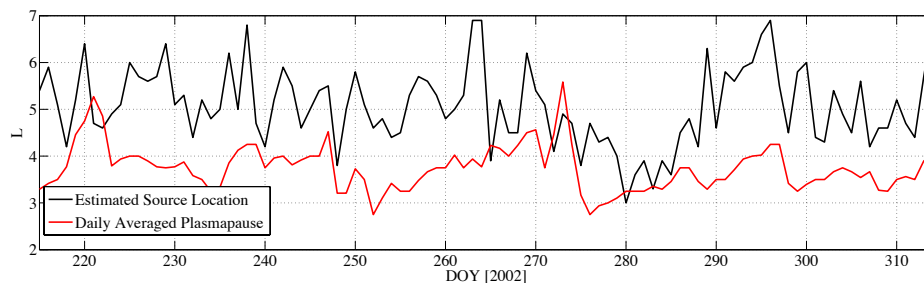
Figure 66: The location of the daily averaged plasmapause location (red) and the estimate of source region location (black).
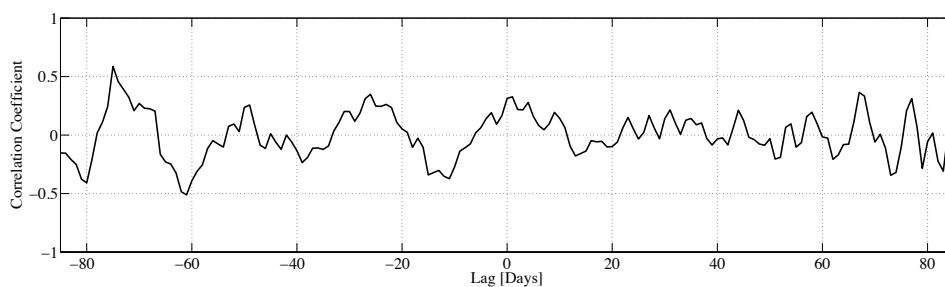
Figure 67: The correlation coefficient between the estimated source location and daily averaged plasmapause location (black and red, respectively), from Figure 66, as a function of lag between the two.

observation time step. This might be due to anisotropies in the electron drift population (where one GEO spacecraft will see high PSD, while other GEO spacecraft will be in regions of low PSD), localized acceleration occurring preferentially closer to one of the GEO spacecraft, injections of electrons from the tail region, or other physical or numerical causes. The variations in PSD can reach two orders of magnitude during this period of enhanced radiation belt intensities.

The experiment with data from the GPS spacecraft removed reveals similar results. The differences occur where the GPS spacecraft makes its observations, between L=4~5. The largest differences occur during the same

period of enhanced radiation belt intensities - DOY 225 to 230. However, the analysis with the GEO spacecraft removed sometimes over-predicted and sometimes under-predicted the PSD. The results of the analysis with the GPS data removed show consistent under-predicting during the period before the enhancement, and consistent over-predicting during the enhancement. This suggests that the GPS data was pulling the state vector up in the days before, and pulling the state vector down during the enhancement. Variations for this experiment also ranged to two orders of magnitude.

Whereas the previous studies observed the changes in PSD from the removal of one of the satellites in the dataset, a different analysis was performed to measure the effects on the estimate of the source rate amplitude. This analysis was performed for five consecutive periods during the interval from DOY 211 to 297, 2002, each with different source location and widths (as outlined in *Schiller et al.* [2012]). The results of this experiment can be seen in Figure 62. Despite the variations in PSD estimate, the estimate of the source rate amplitude is relatively unaffected by the removal of either dataset. The basic structure and magnitudes are preserved for all three cases. These results suggest that the PSD is sensitive to the data included in the observations, whereas the estimate of some source rate parameters is robust to data denial.

5.3.3 Application of Method to Real PSD Observations

We apply the methods to the real dataset described in the previous sections. The results are depicted in Figure 63. The authors warn the reader that the PSD estimate near DOY 280 may not be physical, as there are only a few examples of high energy electrons penetrating into the slot region (below L=2-3).

It is likely that the high PSD in the slot region is a result of numerics, as the source location is estimated to be very low: between L=3 and L=4 for multiple days. Such a source term could numerically populate the slot region as there are no observations inside of L=4 to decrease the filters estimate of PSD there. Despite this potential issue, the reanalysis agrees strongly with the observations. The comparison between the two can be seen in Figure 65. The vast majority of the observations are recreated within a factor of two. The largest differences between the reanalysis and the observations occur near the outer boundary, where we assume all particles are lost to the magnetopause.

Attempts to Find Correlation between Source Location and Plasmapause

Whistler mode chorus waves, for example, are believed to be a major contributor in accelerating lower energy electrons to relativistic levels [e.g. *Horne et al.*, 2007]. These waves are also believed to occur just outside the plasmapause. Thus, one would expect to see a correlation between the source location (region of high chorus wave activity), and the plasmapause. The daily averaged plasmapause, from the Dst-dependent plasmapause model by O'Brien and Moldwin [*2003*], and the estimated source location for the same period, can be seen in Figure 66 in red and black, respectively. Additionally, we calculate the correlation coefficient between the two. Since there may be some delay between the timing of local enhancements and the plasmapause location, we also calculate the correlation coefficient incorporating up to an 85 day delay. These results can be seen in Figure 67.

As can be seen in the figure, there does not seem to be any correlation, as the correlation coefficient is not higher than 0.4, except for a lag of -70 days

where it is only slightly higher than 0.5. (Interestingly, there is a 27-day period to oscillations in the correlation coefficient lag. This was not unexpected, as various solar wind features can have 27-day periods [e.g. CIRs], which directly affect the configuration of the magnetosphere.) The likely reason for no apparent correlation is that we use a daily averaged plasmapause location. The daily averaging washes out any variations, which occur on a smaller timescale. These variations can be significant, varying up to L=3 in a matter of hours. Thus, we conclude that the daily resolution at which we are calculating estimates of the source location is too coarse to resolve a plasmapause correlation, which likely happens on a timescale much less than a day.

5.3.4 Summary

In this paper, we discuss the specifics of estimating source rate parameters in the outer radiation belt electrons using data assimilation. We assume a Gaussian-shaped source region, an assumption, which should be improved upon in future studies, and attempt to estimate its radial extent, center location, and intensity.

The state vector of the model consists of the phase space density (PSD) for the full radial range and the amplitude parameter of the source rate term. These variables are estimated 'online', that is, they are direct outputs and have temporal resolution equal to the filter. The remaining source rate parameters, namely the location and width of the source region, are estimated 'offline'. To perform the offline estimation, we employ the innovation vector (or prefit observation residuals) to quantify the performance of the model to reproduce observations for a given location/width pair. We run the model over a large parameter space

(often a few hundred runs), and calculate the root mean square (RMS) of the summed innovation vector. The minimum in the RMS parameter space indicates the location/width pair, which best predict the observations, and thus are assumed to be the dimensions of the source region.

In the first part of our study, whose purpose is to verify the functionality of our model, we sample a synthesized dataset with a hypothetical spacecraft in an idealized orbit, which are used as the observations (a.k.a. an identical twin experiment). We then measure the performance of the model by quantifying how well the model reproduces the synthesized state. Three experiments are performed, each in increasing complexity. The model performs very well for the first two, accurately reproducing the PSD and the source rate parameters (amplitude, width, and location). The model begins to break down under the conditions imposed for the third experiment, but only when the existing PSD overwhelms the magnitude of the source rate. Overall, the method performs well in estimating PSD and all three dimensions of the Gaussian source term.

In the second part of our study, we apply this technique to actual satellite PSD observations. We first determine that PSD and source rate parameter estimation is relatively robust to the dataset. To do this, we remove one of the satellites from the observations and analyze the results. Since the satellites directly observe PSD, there are significant changes to the PSD estimate when denying a satellite's observations in the reanalysis. However, the estimate of source parameters, namely the intensity of the source region, is robust to which observations are included.

The PSD observations we use are from five satellites: POLAR, one GPS, and three LANL-GEO. We are able to estimate PSD and intensity of local

heating at relatively high temporal resolution. We are also able to estimate the location and width of the source region at daily cadence. Using this method, we are able to more accurately predict observed PSD measurements. Unfortunately, we suspect that daily cadence is too coarse to perform any rigorous analysis between the location of the source region and potentially relevant regions in space (e.g. the plasmapause). We do, however, see a 27-day period in the correlation between the plasmapause and the source region, verifying that the solar wind has a strong affect on the plasmapause, the source region, or both.

5.4 Improving the Data Assimilation Method

5.4.1 Introduction

We take a deferment from improving the estimates of the relative contributions of the loss, transport, and source terms to discuss its application. Specifically, the estimates of τ and D_{LL} are best used in Fokker-Planck type modeling. Here, we discuss application to the 1D simple radial diffusion Fokker-Planck model, and the data assimilation technique previously described in Chapter 5 and *Schiller et al.* [2012].

The previous analysis was capable of estimating source term parameters on large geomagnetic storm timescales. A more useful model will be able to estimate acceleration parameters on shorter timescales, with hours to days as a realistic goal. However, with the previous method, as illustrated in Chapter 5.3.1, there is a significant lag in the amplitude parameter. That is, it takes a few days for the amplitude term to spin up for large changes in the intensity of the

source rate, which one would expect during interesting sudden enhancement events. This lag must be removed before reducing the model timescale.

Our approach to reduce the lag is to estimate offline the amplitude along side the location and width of the source rate term. However, performing the parameter space estimation in three dimensions (amplitude, location, and width) increases the computation complexity of the problem exponentially. Doing a brute force approach, that is calculating the innovation RMS for every grid point in the parameter space, is not feasible. The model would require thousands of experiments and ultimately months of computation time on a dual-core laptop. A relatively simple solution is to optimize the parameter space. Instead of observing the entire cost function, we can observe a small part of it and optimize our exploration of the parameter space. We choose a straightforward downhill simplex method known as the Nelder-Mead technique [*Nelder and Mead*, 1965].

To verify functionality, we optimize the 2D parameter space in Section 5.4.2 before attempting a 3D optimization in Section 5.4.3. Both sections are based on work performed in the LANL Space Weather Summer School. The previous sections, as well as the subsequent two, develop a robust and reliable technique to estimate source parameters. The technique is applied for scientific investigation in Chapter 6.

5.4.2 Optimizing the source rate parameter estimation in two dimensions:

Determining source rate parameters of energetic electrons in the outer radiation belt using a Kalman filter

by Q. Schiller and H. C. Godinez, published in Los Alamos Space Weather Summer School Research Reports, edited by J. Koller and R. D. Gurule, 2013

Introduction

Based on the work from last summer [*Schiller and Godinez,* 2012], it was apparent that the offline method employed was a superior method for estimating all source rate parameters. In *Schiller and Godinez* [2012], source rate width and location were estimated offline, but source rate amplitude was estimated as a direct output of the Kalman filter. The downside of this method is that the Kalman filter requires a spin-up assimilation period of up to 36 hours prior to the estimate period to correctly estimate the amplitude parameter. If the source rate intensity changes on timescales less than 36 hours, which is likely to occur, the Kalman filter may not be able to respond quickly enough. Thus, a new method is required to estimate the amplitude parameter offline, increasing the number of dimensions in the parameter space to three - amplitude, location, and width. However, finding the minimum in two dimensional parameter space without an optimization technique can take hundreds, sometimes thousands of experiments. Increasing the dimension would exponentially increase the number of experiments required to find a solution. Performing so many experiments for each time step is unreasonable, so an optimization technique is required.

We choose the Nelder-Mead method [*Nelder and Mead*, 1965], which is a downhill simplex technique. Like other downhill simplex algorithm, the method samples the N dimensional parameter space randomly with N+1 samples. It uses the N+1 samples to determine the local gradient of the cost function. The method re-samples the parameter space based on the local gradient, 'walking' the sampling points downhill. The process continues until the samples find a local minimum and the end criterion is met, which for our case is that the standard deviation between the points is sufficiently small. Because the method

can mistake a local minimum for a global minimum, it is important to either visualized the cost function to verify a global minimum, or run the method repeatedly to ensure that it finds the same minimum with different initial conditions to verify it is, in fact, the global minimum. If the cost function has numerous local minima, more robust optimization schemes are available. However, for a clean cost function the simple Nelder-Mead method is sufficient (see discussion in Section 6.3.3).

Goal

We chose a reasonable goal to aim for: to choose an optimization method that would work for our problem; specifically, the technique must not require finding a derivative and can be used for three dimensions. We would then implement the technique in the existing two dimensional space (location, width) to verify its functionality. Finally, we would implement the scheme in the three dimensional space (location, width, amplitude).

Optimizing LANL Dataset in Two Dimensions

Almost immediately we saw problems with using the Nelder-Mead method on the parameter space from the LANL dataset we were assimilating. The topology of the parameter space had multiple minimums and wide, shallow valleys. The Nelder-Mean method cannot distinguish local minima from global minima, and can mistake the wide, shallow valleys for minima. *Reeves et al.* [2012] suggest that a source term is needed to account for the gap in observations between GPS and GEO satellites in that dataset. The filter could be confusing a source term accounting for absent data with a physical source term. We
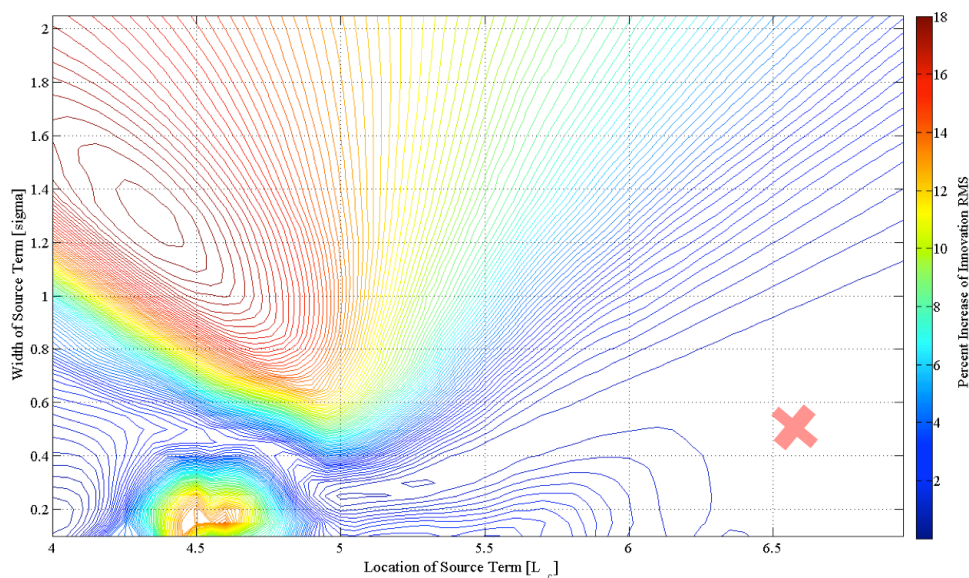
Figure 68: 2400 experiments run on the LANL dataset in the 4<Lc<6.5 and 0.1<Width<2.1 parameter space. The Nelder-Mead method often converges to the red 'x' at Lc=6.6 and width=0.5, when the true global minima exists at Lc=5.3 and width=0.3.
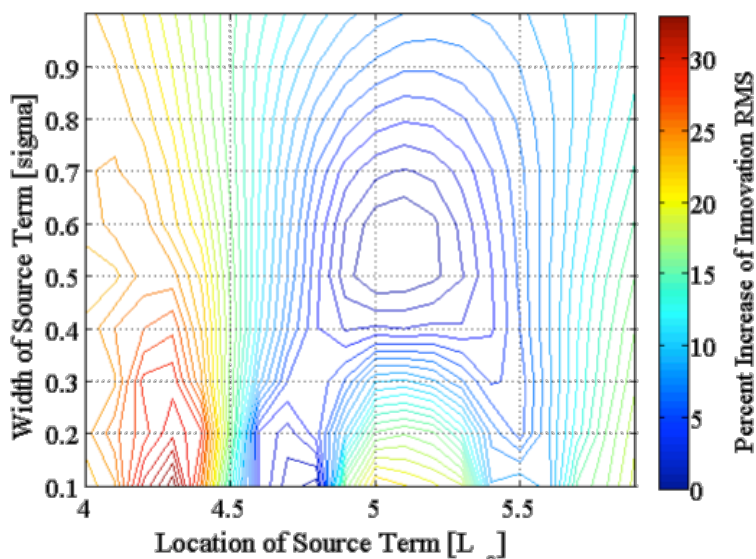
Figure 69: A common topology given the two source terms.
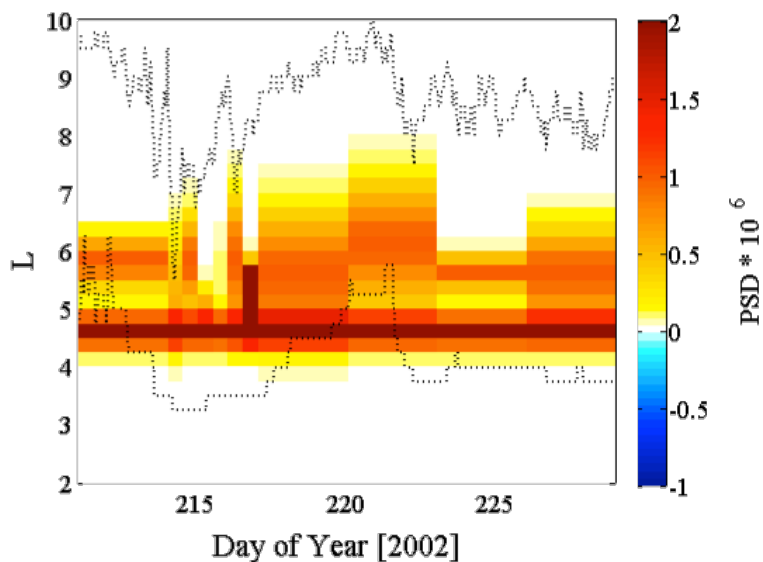
Figure 70: There are two source terms in this experiment: one unvarying at L=4.5 with width 0.2, and a second at higher L with varying location, width, and amplitude.
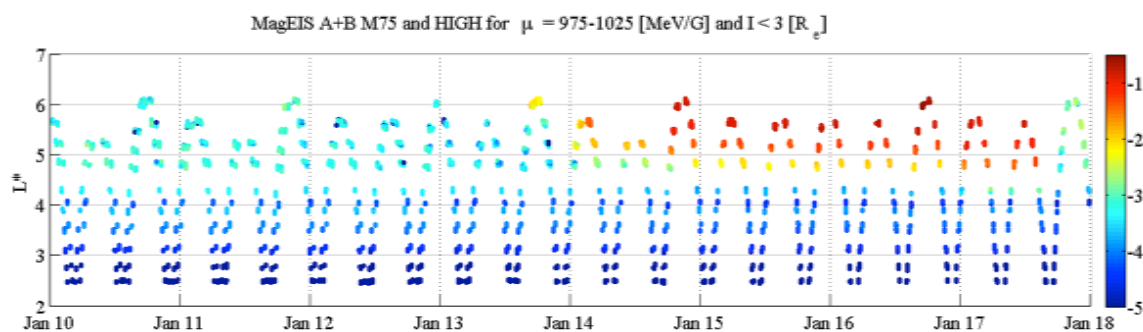
Figure 71: Phase space density measurements from the RBSP MagEIS M75 and HIGH instruments.
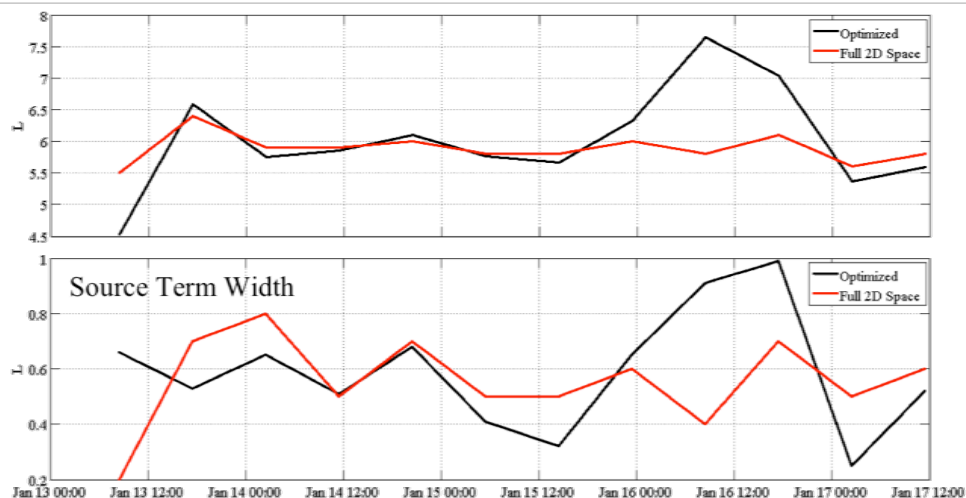
Figure 72: The results of running the 'old' method, where experiments are run for every grid point in 4<L<6.5 and 0.1<Width<2.1 parameter space in red, and the optimization method in red. The optimization method can find minima outside the bounds of the old method, as well as performing dozens of experiments to converge on a solution, as opposed to the thousands using the old method.
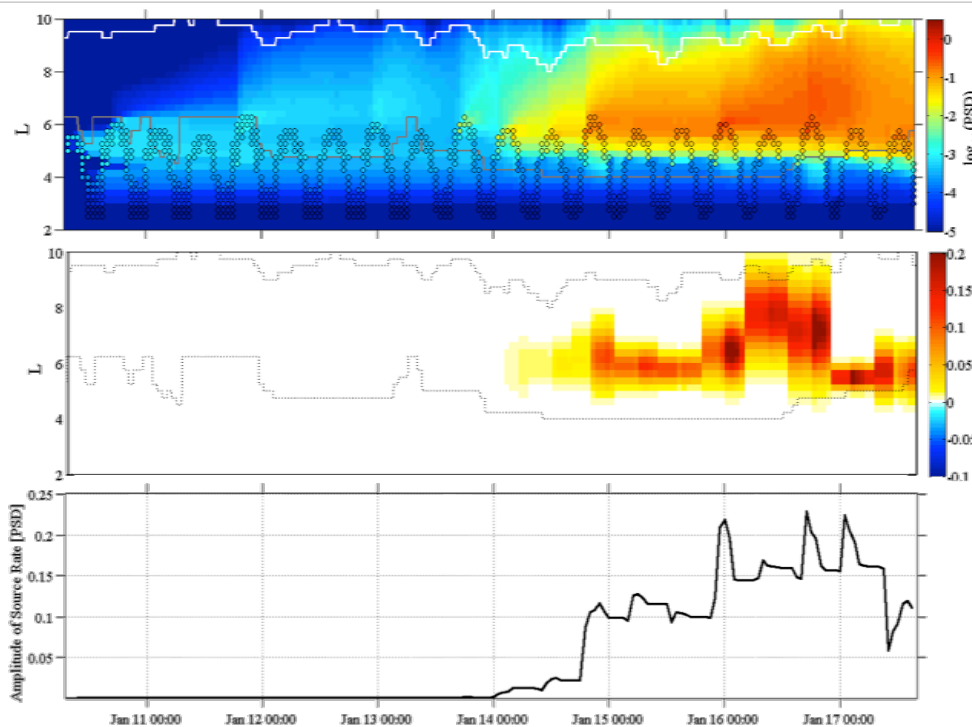
Figure 73: Results from the optimization method.
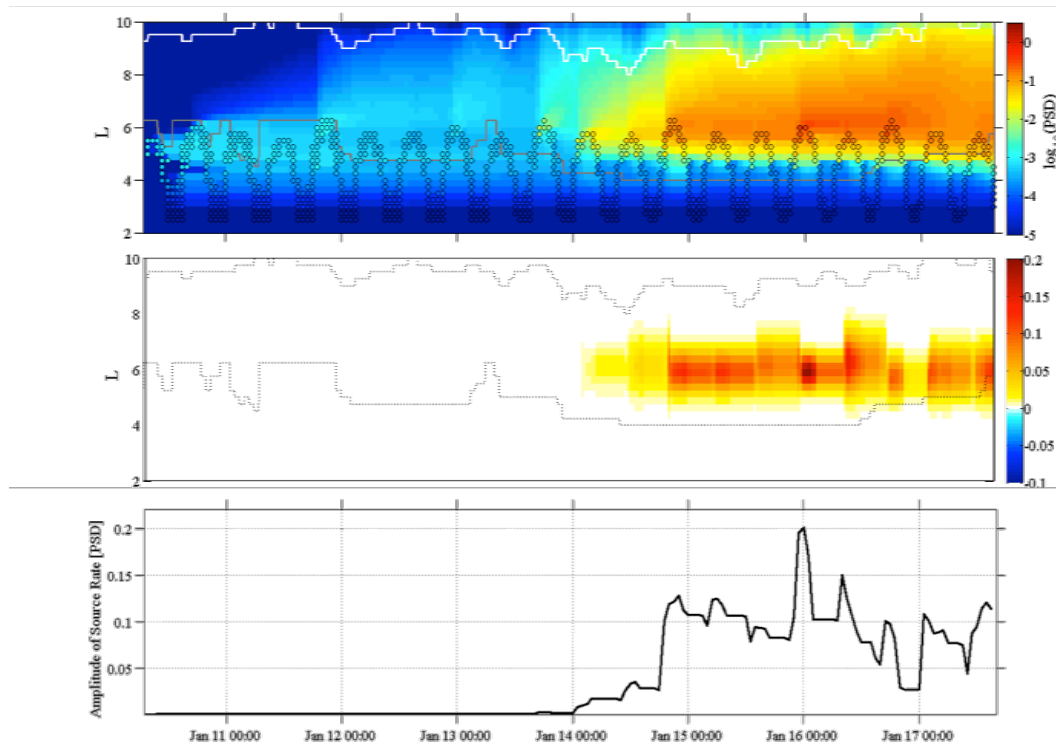
Figure 74: Results from the full method in a rigid parameter space.

performed identical twin experiments to see if the topology between the assimilated LANL dataset and a synthesized dataset with two source terms (Figure 70) were similar. They were, as can be seen in Figure 69, where there are multiple minima and shallow valleys. This motivated a change from the LANL dataset to a Radiation Belt Storm Probes dataset.

Optimizing RBSP Dataset in Two Dimensions

RBSP takes measurements from the outer electron radiation belt twice every 9-hour orbit. This dataset is ideal since a wide L range is sampled with relatively high frequency, and should not introduce non-physical source terms due to limited data range in L. The RBSP MagEIS M75 and HIGH instrument flux data is converted to PSD by binning flux measurements into $975 < \mu < 1025$

MeV/G and K < 0.13 [R_E]. The period of interest is Jan 10 to Jan 20, 2013, due to, among other reasons, a clear flux enhancement occurring near L=5, increasing the flux by 300x in <18 hours at L=5.5 [*Schiller et al.*, 2013]. The RBSP PSD data can be seen in Figure 71. The data was assimilated using both the 'old' brute-force technique, performing thousands of experiments to map the entire parameter space (4<Lc<6.5 and 0.1<Width<2.1) (Figure 72 and Figure 74), and the 'new' technique using the Nelder-Mead method (Figure 72 and Figure 73). The results are comparable, but the Nelder-Mead method finds solutions outside of the old method's specified parameter space. The parameter space for the old method can be extended, but at the cost of adding hundreds of experiments per timestep.

Summary and Future Work on this Topic

Three weeks spent at LANL was not enough time to get the 3-D optimization method in place. We were able to build up a 2-D optimization method, but quickly became sidetracked in issues with the PSD dataset being used. The first action item on the burn-down list is to implement a 3-D optimization scheme. There also wasn't enough time to do a proper PSD calculation with the RBSP flux data. Currently, there is not a scheduled release date for RBSP Level 4 PSD data. Thus, a home-grown conversion from L2 (spin-averaged flux) or L3 (pitch angle flux) is required. Thus, the future work summarizes in three action items:

1) Implement a reliable Nelder-Mead 3-D optimization scheme. This scheme should continue to be a stand-alone algorithm to allow for

optimization of any function, including assimilation of the existing LANL dataset or future RBSP datasets.

2) Gain confidence in the flux to PSD conversion of the RBSP data.

3) Combine the existing data assimilation technique with the RBSP PSD dataset. Estimate all three source rate parameters offline (location, width, amplitude) using the 3-D N-M optimization scheme.

5.4.3 Optimizing the Source Rate Parameter Estimation in Three Dimensions:

Estimating source rate parameters of outer radiation belt electrons using a Kalman filter variant: a progress report

by Q. Schiller and H. C. Godinez, published in Los Alamos Space Weather Summer School Research Reports, edited by M. Cowee, 2014

Abstract

We continue to explore the possibility of estimating source rate parameters of outer radiation belt electrons using a Kalman filter for timescales ~2 hours. We use a one dimensional radial transport equation with an electron phase space density dataset from the Van Allen Probes and THEMIS. Previously, we showed that some source rate parameters can be estimated accurately 'offline' with a simple optimization procedure. The 'offline' estimates are done by finding the minima of a cost function associated with the innovation vector rather than directly estimating the parameters as part of the data assimilation algorithm.

Here, we find that the current innovation vector cost function is not a good estimator, and propose an algorithm as an alternative.

Goal

The goal of this research is to characterize a Gaussian-shaped source rate term in a simple one-dimensional radial diffusion equation using data assimilation. Our approach is to minimize the innovation vector (y-Hx), where y is the observation vector, H maps the state space into the observational space, and x is the state vector. In this case, x is the phase space density as a function of radial distance and the observations are satellite particle measurements. The innovation vector represents physics that are missing from the physical model, and the theory is that changing state parameters to minimize the innovation vector is a way to estimate those state parameters. However, this method can require many different experiments to be run, since one has to try all the different state parameters to determine which set minimizes the innovation vector.

At the end of my last visit to Los Alamos [*Schiller and Godinez*, 2012; 2013], we had created a two-dimensional optimization technique to minimize the innovation vector in location,width space. We used a downhill simplex method known as the Nelder-Mead method [*Nelder and Mead*, 1965]. The parameter space can be represented as a cost function

$$J(x,L,\sigma) = ||\, y - Hx \,||_2$$

where L and σ are the location and width of the source rate term, respectively. Using an optimization technique reduced the number of experiments required by over two orders of magnitude, making a much more efficient use of computation time.

This 2D optimization method was used to estimate the location and width of the source term then estimate the final source rate term parameter, its amplitude (A), directly using the data assimilation and an augmented state vector to include this parameter. However, it was found that the data assimilation had a lag of ~24 hours, and that estimating any state parameters as a direct output of the assimilation would not capture dynamics on timescales shorter than this. We decided to approach the problem by optimizing a three-dimensional cost function

$$J(x,L,\sigma,A) = ||\, y - Hx\, ||_2$$

which would reduce the number of required experiments, from a brute-force full 3D mapping of the cost function, by many orders of magnitude.

Methodology

For this visit to Los Alamos, we extended the 2D optimization method to three dimensions. See below for examples. Investigation with simplified identical twin experiments showed that the 3D method was far less robust than the 2D method, as was expected with the inclusion of an additional dimension.
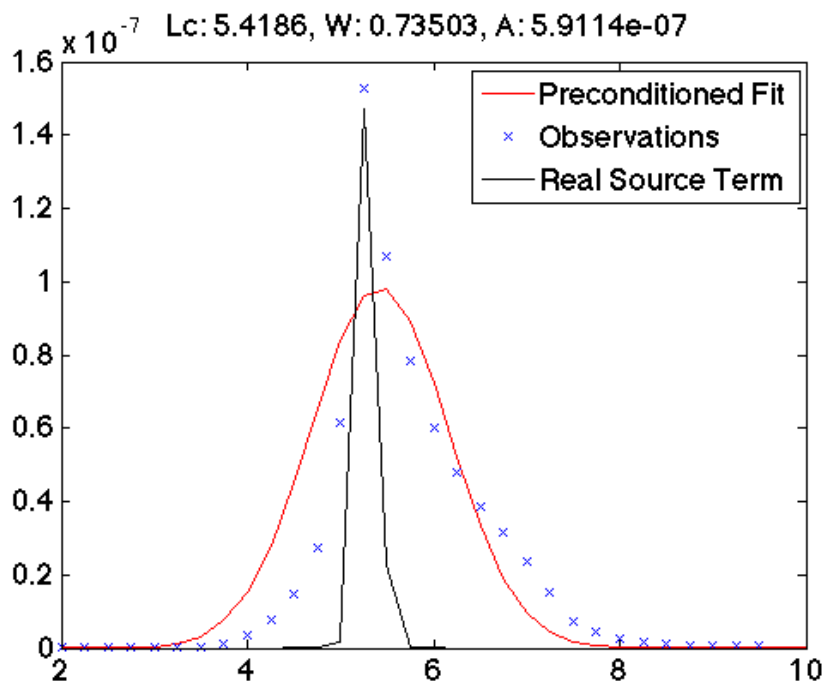
Figure 75: An example of preconditioning to determine the initial estimate for the 3D optimization. The black line is the actual source term over the period, the blue x's are the mean PSD within the period to be analyzed, the red curve is a Gaussian fit to the data, which amplitude, width, and location parameters (at top of the figure) are used to determine the initial parameter estimates for the source term. Notice that the fit Gaussian does not do a good job of representing the actual source term. However, in general, it is sufficient to condition the initial estimates so that the optimization scheme is able to find the global minimum if it exists.

Furthermore, the method is extremely sensitive to the initial parameter estimates made. As the method "walks" downhill, if the initial estimates are not on the downward slope to the global minimum, or if the estimates are separated enough in the parameter space that they do not sample the "valley" created by the global minimum, then the method fails to find the global minimum and the result is not close to the true parameter values. To account for this issue, we preconditioned the initial parameter estimates with a Gaussian fit to the radial PSD profile. We used the parameters from the fit to determine the initial

estimates. Note on the below plot, the y-axis should read "Phase Space Density", and the x-axis "L".

Using the 3D optimization scheme and preconditioned initial parameter estimates, we ran the method for a series of simplified identical twin experiments. For these experiments, we generated a PSD dataset with realistic loss and diffusion terms, which are Kp and Dst dependent, respectively. We created a simplified source term to include in the model. The full synthesized PSD dataset is depicted below. This dataset is sampled using a 5 spacecraft dataset to represent the Van Allen Probes (~1x6 R_E, 9 hour orbit) and three THEMIS spacecraft (~1x10 R_E, 12 hour orbit). The 'observations' are used in the data assimilation algorithm to attempt to recreate both the PSD for the full radial range as well as the Gaussian source rate term.

The 'observations' sample the synthesized dataset at a timescale of 4 minutes, and the filter assimilates the data at comparable timescales. This estimation method attempts to estimate the source term over timescales on the order of ~1 hour, comprising many observation and assimilation cycles. We can vary this period over which to estimate the source term to determine how many observations are required to gather enough information to accurately estimate the source term. The number of observations required depends on the number of dimensions to be estimated. Unfortunately, at least 3(6) hours of observations are required for the 2(3)D estimate, as presented below. In the Path Forward section, we discuss an idea to reduce the estimate timescale to an hour or less.
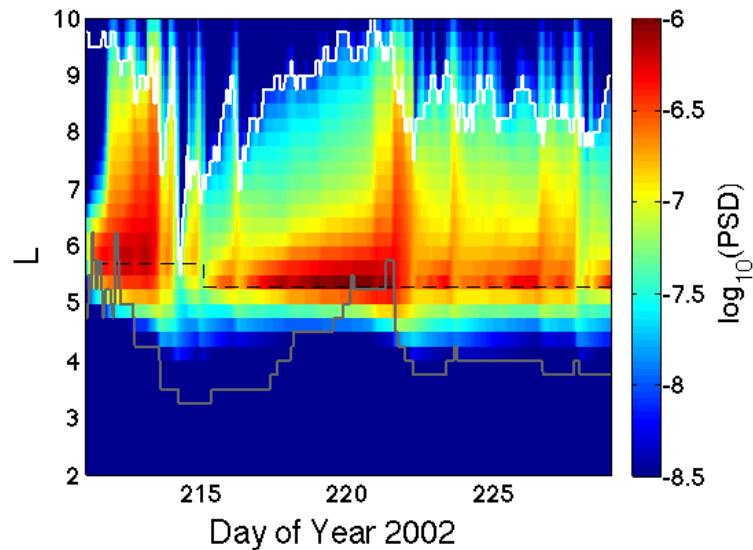
Figure 76: The synthesized PSD dataset. For reference, the last closed drift shell (as determined by *Koller and Morley* [2010]) is plotted in white, the plasmapause (as determined by *O'Brien and Moldwin* [2003]) is plotted in grey, and the source term center location in dashed black.
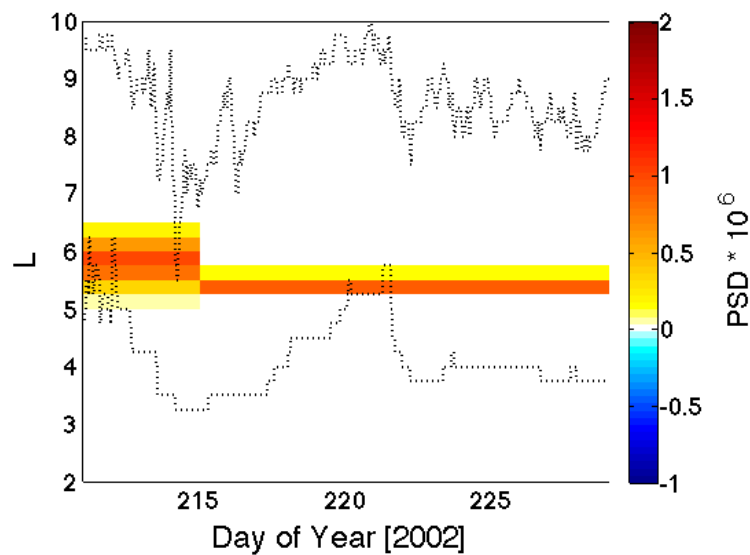
Figure 77: A visualization of the source term included in the PSD dataset. This source term is what this research is attempting to reproduce. The following analysis is focused on the step on DOY 215 from Lc=5.7, σ=0.3, A=1e-6 to Lc=5.3, σ=0.1, A=1e-6.

We assimilated the 'observations' in both the 3D and 2D algorithms to attempt to recreate the source term. All of the following 3D cost function optimization and 2D cost function figures begin on DOY 215, and finish 1-24 hours later, between DOY 215.042 to 216. The results, as explained later, show that the cost functions become more reliable with a longer time analyzed. Note that colorbar for these figures should read "Value of Innovation RMS". The initial parameter estimates are circled. The end criteria for the optimization is when the standard deviation of the most recent estimates fall below a certain threshold. These runs, this threshold is between 1e-13 and 5e-13.

Results

Below are figures diagramming the results of the analysis.

3D Cost Functions
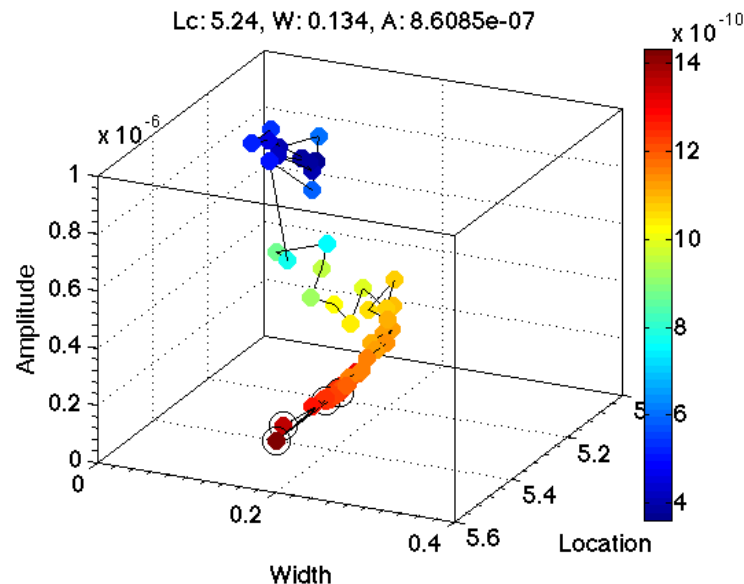
Figure 78: 3D optimization for a 24-hour period.
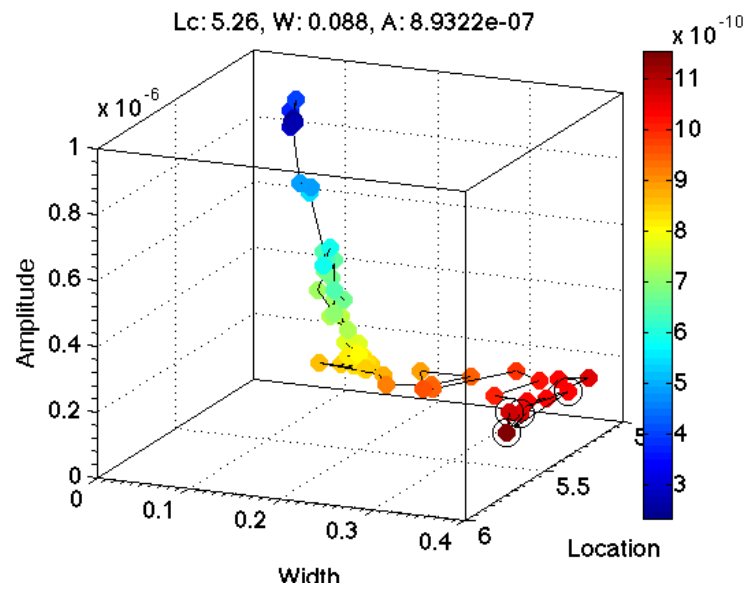
Figure 79: 3D optimization for a 12-hour period.
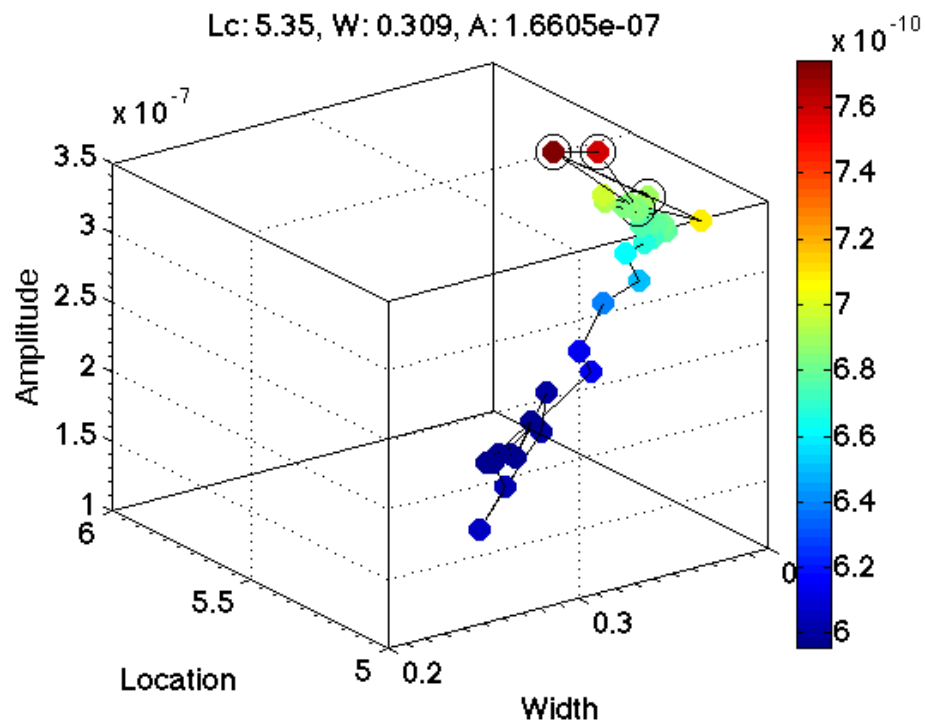
Figure 80: 3D optimization for a 6-hour period.
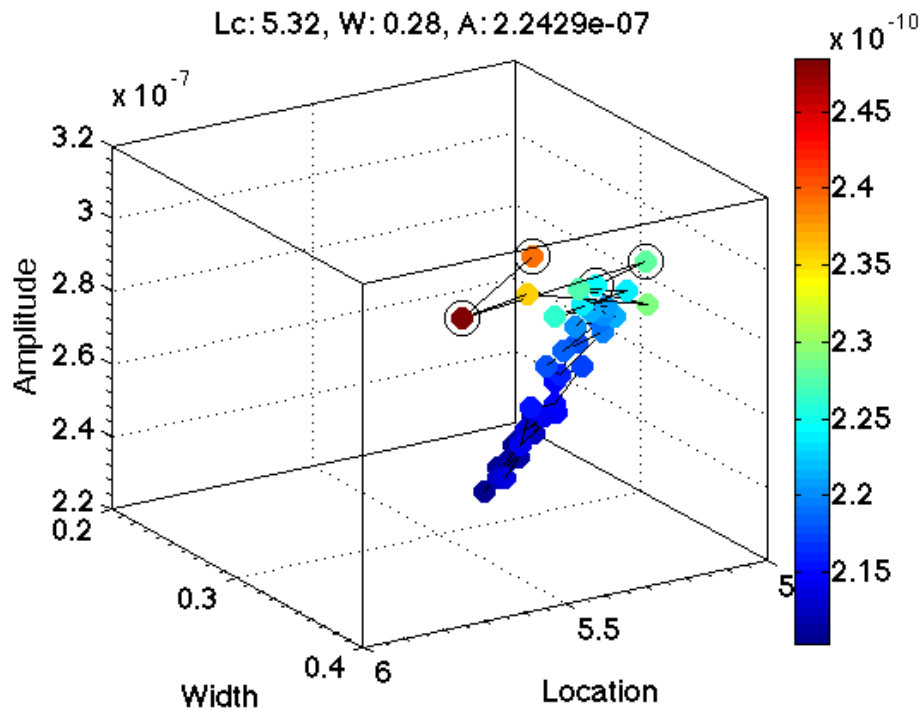
Figure 81: 3D optimization for a 4-hour period.
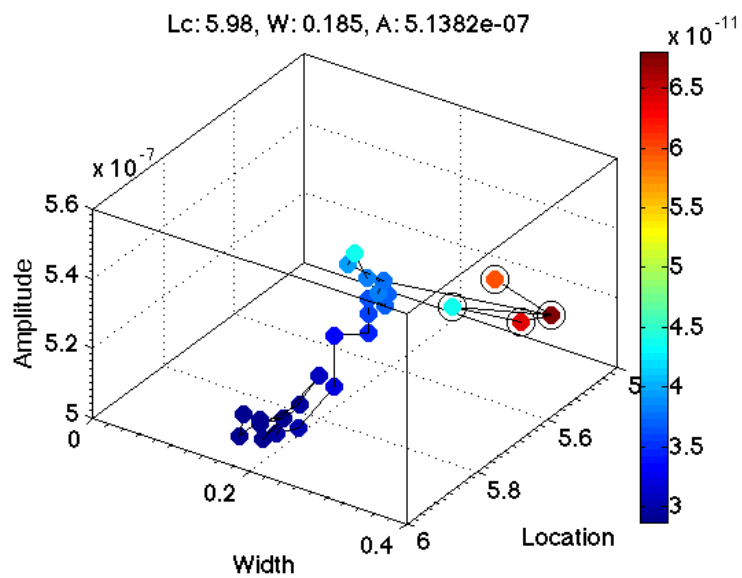
Figure 82: 3D optimization for a 2-hour period.

The previous figures show that the 3D optimization works well for the 12 and 24 hours periods. The method "walks downhill" to find the minimum of the cost function. However, it is not accurate in width or amplitude estimates for 6 or 4 hour periods, and does not estimate accurately at all for the 2 hour period. In short, the 3D cost function is not robust enough to provide an accurate global minimum without more than ~12 hours of data to assimilate. Unfortunately, visualizing the 3D cost function is difficult. In order to understand its behavior, we return to the 2D parameter space where visualizing the entire cost function is both visually and computationally easier.

2D Cost Functions

We investigated the 2D cost functions in location-width space. Note that the color bar for these figures should read "Value of Innovation RMS" as the values are absolute, not relative. Furthermore, the parameter space was mapped at coarse resolution, since it's full mapping is computationally consuming. Odd, angular features in the visualizations, as well as imprecise estimates of the location and width, can be artifacts of the coarse resolution.

The 2D cost functions, as presented above, are unable to reproduce the correct source term with less than four hours of data assimilated into the model. As expected, the 2D cost functions are more robust than the 3D cost functions. However, the 2D method is still unable to account for physics occurring on realistic timescales (~1 hour). To address this issue, we have decided to adjust the method to utilize a simpler cost function, with the hope that it will remain robust on shorter timescales.
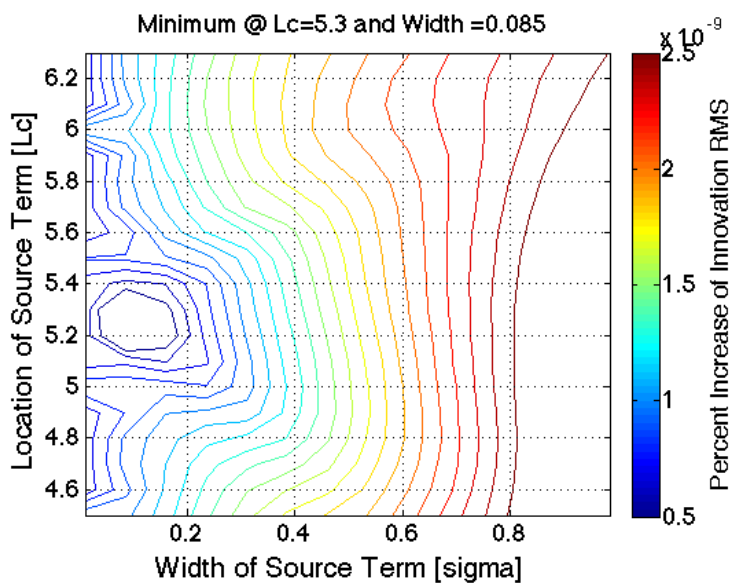
Figure 83: 2D cost function for a 12-hour period.
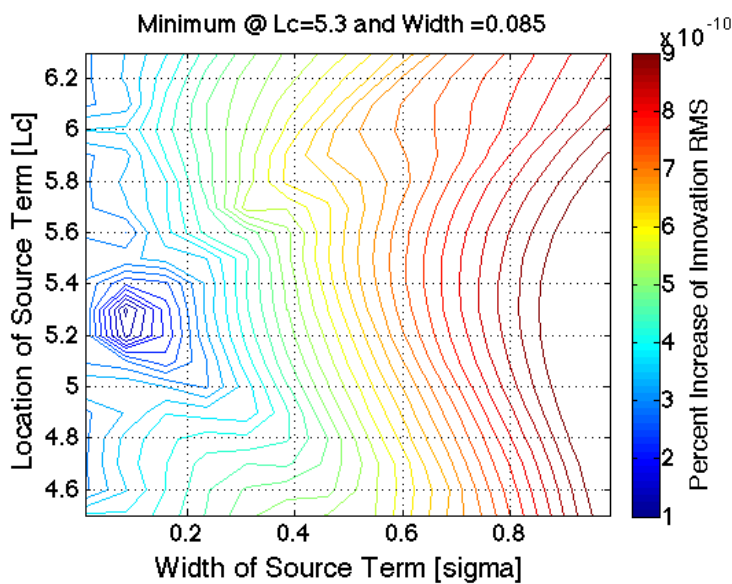
Figure 84: 2D cost function for a 4-hour period.
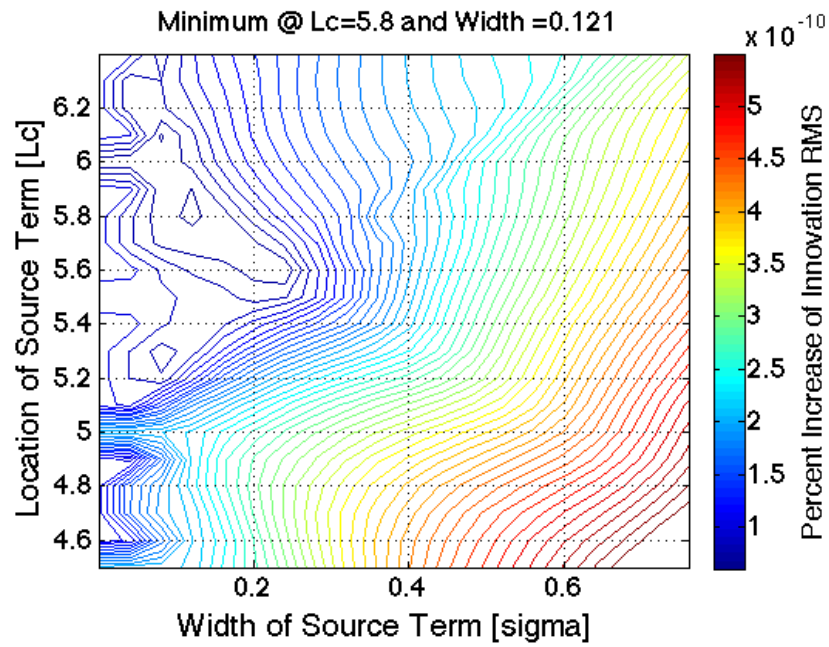
Figure 85: 2D cost function for a 3-hour period.
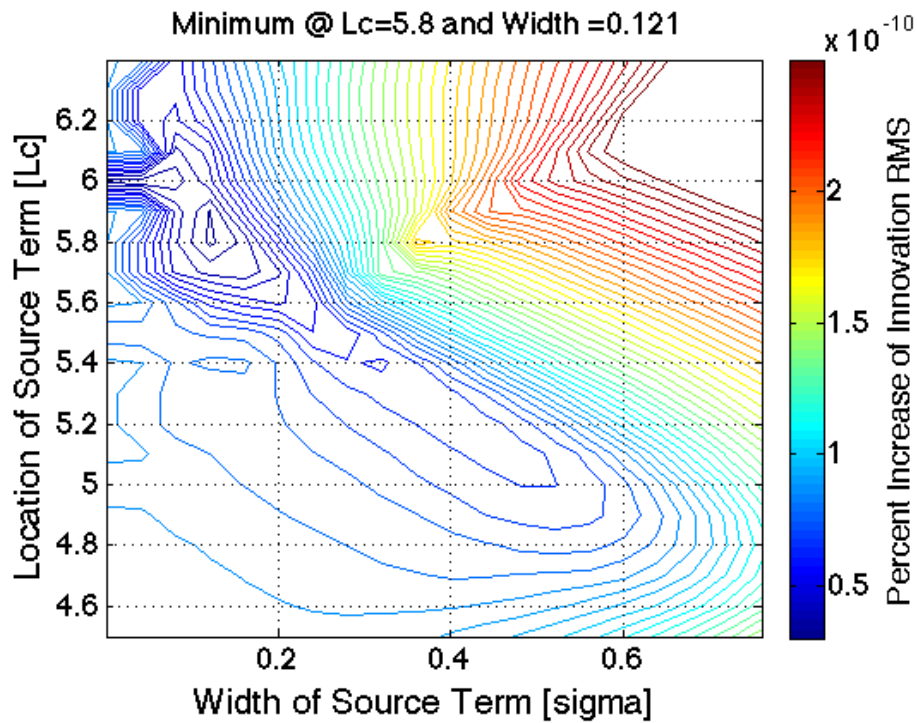
Figure 86: 2D cost function for a 2-hour period.
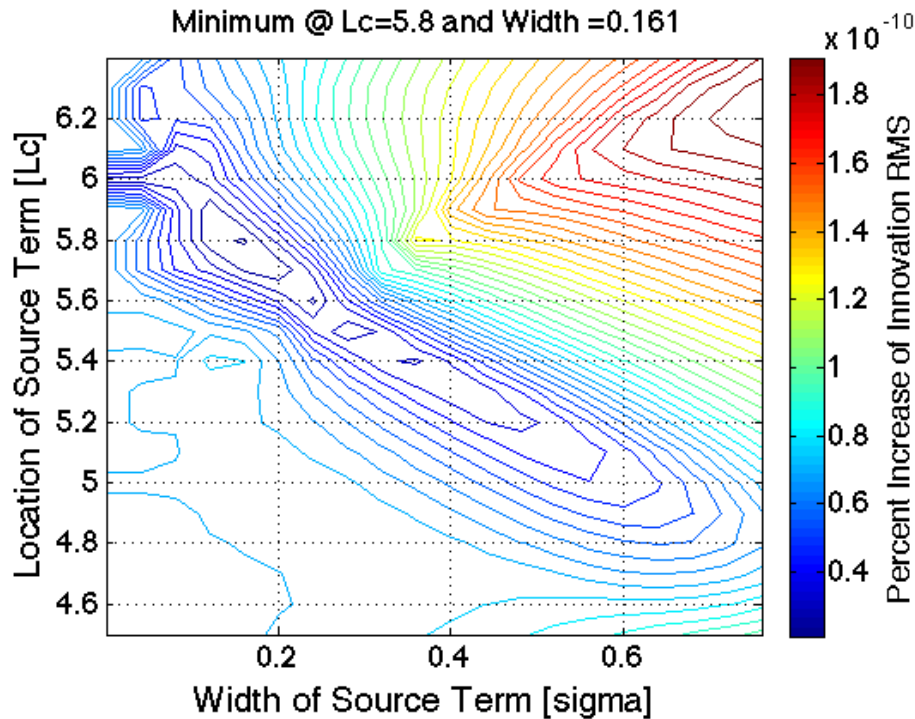
Figure 87: 2D cost function for a 1-hour period.

Summary and Future Work on this Topic

With the knowledge that the 3D cost function for analysis is not able to accurately estimate state parameters without at least 6 hours of data assimilated in the Kalman filter, we have decided to change how we define the cost function. If we can create a cost function that has the minimum at the correct source term parameters on shorter timescales, then we can implement the existing optimization scheme.

The short-term path forward is to remove the data assimilation component of the cost function. Instead, of using the Kalman filter to advance the assimilated state to a future timestep (t → t+1) in which to determine the value of the cost function, we will run only the physical model forward. Then, at

the future timestep (t+1), we compare the observations to the forecasted state to create the cost function. This method will have to be repeated many times to view the full 2D or 3D cost functions, but can be made more efficient using the optimization scheme to run the model forward for only a handful of different state parameter combinations. Once the correct location, width, and amplitude of the source term are determined through the global minimum in the cost function, then we assimilate the observations and forecasted state at t+1 to create an assimilated state.

In short:

1) Run physical model (1-D radial diffusion with loss + source) on x_a^t to x_f^{t+1}.

2) Determine cost: $J(x,L,sigma,A) = || y^{t+1} - H x_f^{t+1} ||$ for all different L, sigmas and A's. This can be done initially in 2D space to view topography of cost function.

3) Do steps 1) and 2) for different lengths (i.e. 12, 6, 4, 2, 1 hours separating t and t+1) and see if the new cost function is robust at short timescales.

If the method is capable of estimating correct source terms on short timescales, the next steps would be:

4) Assimilate observations (y^{t+1}) and forecasted state (x_f^{t+1}) to create assimilated state (x_a^{t+1}).

5) Set t+1 to t and repeat by returning to step 1).

The idea behind the new method is to remove assimilation between the forecasted state and the observations. Our reasoning is that the data assimilation reduces the impact of the source term by modifying the state vector to conform

to the observations. With an incorrect source term in the physical model, it will weight the observations more than the model, thus washing out or hiding the source term in the assimilation. By propagating the state vector forward using only the model, we hope to make the source term more obvious when the forecasted state is compared to the observations, in turn making the cost function more robust and hopefully improving our ability to estimate state parameters.

5.4.4 Summary

In the previous sections, we describe an improvement to the parameter estimation technique described in Chapter 5. The improvement introduces all three source rate terms (intensity, location, radial extent) in the offline estimate. The improvement also ensures that the lag present in the 2D estimate is removed, which allows for a drastic decrease in the timescales the method can be utilized for. The new method requires at least 12 hours of data to accurately reconstruct the global minimum of the cost function. The previous analysis shows that the new method is a feasible approach to estimating the source rate parameter of a simple 1D radial diffusion model.

5.5 Chapter Summary and Conclusions

In this chapter I present a unique approach to estimate system parameters, namely the intensity, location, and radial extent of the source term. However, this method can more generally be applied to estimates of state parameters in data assimilation models, and has potential applications across multiple disciplines.

In *Schiller et al.* [2012] we apply the method to five storm periods from July to November, 2002. We recreate the radial phase space density profile as well as make estimates of the source term. The source regions are found to occur within geosynchronous orbit for four of the five periods analyzed and show orders-of-magnitude fluctuations on hours timescales. Furthermore, as expected, the intensity of the source rate is found to increase during the recovery phase of many of the storms. All of these indicators are consistent with wave heating as the mechanism for the enhancement, with chorus a likely candidate. Finally, the estimated source rate shows that local heating alone is capable of completely repopulating the radiation belt after a full dropout event. In addition to gaining understanding of the contribution of the acceleration term in radiation belt dynamics, this study also advances the applications of data assimilation to outer belt electrons.

We also explore ways to optimize the technique such that it can be used to make more reliable estimates of all three source parameters. We show that the 3D estimate can be done, but has limitations related to the amount of data assimilated in a given timestep. Using identical twin experiments we find that, for well sampled 3D estimates, the optimized technique can accurately estimate location, extent, and intensity parameters on the timescales of ~1 day. However, this timescale is highly dependent on the amount of data assimilated; that is, how much information the Kalman filter can acquire from the observations. With this in mind, we choose to apply the method in the following chapter with 3-day resolution. This timescale is sufficient to capture the entirety of the enhancement process studied, without excess assimilation before or after to obscure the results. Furthermore, the method is proven robust for the three days

of input data. While this timescale cannot resolve small-scale processes occurring during the overall enhancement, it is a drastic improvement to the previous method in that 1) it reduces the timescale from ~weeks to days and 2) it simultaneously estimates all three source rate parameters. We apply the improved technique to an enhancement event in the next chapter.

CHAPTER 6

EVENT-SPECIFIC ELECTRON LIFETIMES AND MODELING

6.1 Introduction

The goal of this chapter is two-fold: 1) to present a novel technique to estimate electron lifetimes for radial diffusion models using in-situ LEO observations and 2) to use the lifetimes to simultaneously estimate loss, transport, and source rates. The lifetime estimates are an improvement to many current techniques, many of which use statistical wave models that incorporate months or years of data, to model individual events. We also use in-situ observations of ULF wave activity from the Van Allen Probes to determine radial diffusion rates. In combination, these two techniques provide the best possible estimate of the loss and diffusion term, allowing us to model radiation belt dynamics with confidence that the resulting flux changes are from the source term alone.

In the following section we outline the motivation and methods for this study. Specifically, we discuss how electron lifetimes are modeled from in-situ LEO satellite observations in Section 6.2.2. We discuss how diffusion rates are determined from in-situ Van Allen Probe wave data in Section 6.2.3. We then discuss the improved assimilative model in Section 6.3, which estimates the location, radial extent, and intensity of the source region. The various estimates are done for the January 13th non-storm time enhancement event. A brief

summary of analysis and subsequent conclusions drawn are presented in Section 6.4, and we close the chapter by discussing future work required before publication of this study.

6.2 Event-Specific Electron Lifetimes for Radial Diffusion Models

6.2.1 Motivation

A significant amount of resources have been expended to improve modeling efforts of radiation belt particles. Many models (as previously outlined in Chapters 2 and 5) use a version of the Fokker-Planck equation:

Equation 23: Generalized Fokker-Planck

$$\frac{\partial f}{\partial t} + \sum_i \frac{\partial}{\partial J_i}\left[\left(\frac{dJ_i}{dt}\right)_v f\right] = \sum_{ij} \frac{\partial}{\partial J_j}\left[D_{ij}\frac{\partial f}{\partial J_i}\right] - \frac{f}{\tau} + S$$

where τ is the electron lifetime [days] and f/τ is the loss timescale [1/days]. The electron lifetime is a difficult quantity to determine. Recently, the lifetimes have been separated by loss regimes [e.g. *Kondrashov et al.*, 2007; *Tu et al,* 2009], with different radial distances assigned to hiss, chorus, EMIC, and magnetopause losses; hiss losses typically assigned inside the plasmasphere, EMIC and chorus outside the plasmapause, and magnetopause shadowing outside of the last closed drift shell.

Accurate quantifications of each loss type remain elusive; so much, in fact, that modelers in the past have even resorted to visual estimates of lifetimes [*Shprits et al.*, 2005]. More comprehensive studies use theory to estimate electron

lifetimes [e.g. *Shprits et al.*, 2006; *Bornik and Thorne*, 2007 and references therein; *Santolik et al.*, 2009; *Thorne et al.*, 2013; *Ni et al.*, 2013], attempt to quantify losses by fitting parameters to observations [e.g. *Kondrashov et al.*, 2007; *Tu et al.*, 2009], or use statistical dynamic wave models to determine wave intensity for losses [e.g *Shprits et al.*, 2009; *Subbotin et al.*, 2010; *Albert et al.*, 2009; *Tu et al.*, 2013]. Many of these approaches perform well statistically, but their reliability can diminish when studying individual events as the loss term is trained on a large period. An improved approach is to use a loss term that is derived from in-situ observations during the event in question. Only recently has event-specific global wave models become available, such as *Chen et al.* [2014] and *Li et al.* [2013], but both indirectly infer wave activity from the POES electron 30-100 keV electron channel.

Recent investigations that use event-specific lifetimes have proven informative. *Tu et al.* [2014] use the inferred event-specific chorus amplitudes and seed population inputs to a 3D Fokker-Planck model and clearly demonstrate the importance, if not necessity, of using event-specific inputs. They show explicitly that models that utilize statistical wave amplitudes parameterized by AE fail to reproduce all of the major features in the October 9-10, 2012 event. However, despite emphasizing the importance of event-specific model parameters, *Tu et al.* [2014] use statistical wave models to derive their diffusion coefficients. Additionally, they do not use event-specific hiss amplitudes in the model. Without question, the most accurate model will utilize event-specific diffusion and loss. In this chapter, we attempt to provide the framework in which to do this.
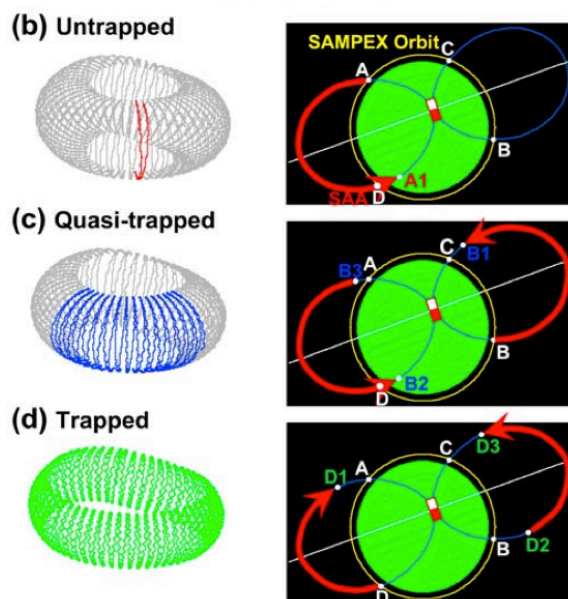
Figure 88: An illustration of the bounce loss cone (b), the drift loss cone (c), and stably trapped particles (d).

6.2.2 Determining the Loss Term

Electron lifetimes can be calculated using in-situ LEO relativistic electron observations. LEO spacecraft are most useful in determining electron precipitation loss rates because the bounce loss cone expands at low altitude and makes the precipitation particles significantly easier to measure.

The method used in this work takes advantage of higher order moments in Earth's dipole field. As previously described in Section 3.5.3, because of the tilted, offset nature of Earth's magnetic field, a spacecraft at constant altitude in low Earth orbit measures different magnetic field strengths throughout its orbit. It measures particles at different points in their bounce and drift phases as a result. The measurements can be made in regions of low magnetic field strength such that the particles are stably trapped, that is they remain in the system for longer than a drift period (Figure 88 (d)); they can be in regions of high magnetic

field strength such that the particles are lost in the conjugate hemisphere within one bounce period (the bounce loss cone [BLC] – Figure 88 (b)); or the particles that are measured can be lost within one drift period and are considered in the drift loss cone (DLC – Figure 88 (c)).

Selesnick et al. [2003, 2004] and *Selesnick* [2006] introduced a drift diffusion model to directly estimate electron loss rate from SAMPEX, a LEO spacecraft capable of measuring relativistic electrons [*Baker et al., 1993*]. In these works, the authors use steady decay to numerically fit various observations periods to balance azimuthal drift and pitch angle diffusion. *Selesnick* [2006] shows that the numerical model solutions can be estimated as $\tau \approx \tau_d/7F$, (where the correction from the original equation $7\tau_d/F$ was made after discussion with Dr. Selesnick), where τ is the electron lifetime, τ_d is an electron drift period, and F is the ration of quasi-trapped population to the total locally measured population averaged over half a day. This approximation is known as the Loss Index Method (LIM). Because of the fit to steady decay, the method breaks down for periods of strong diffusion.

The LIM can be done for constant energy, but to use electron lifetimes in a radial diffusion model the particles must be converted to phase space coordinates. To do this, we first choose a μ value; for this analysis we choose $\mu=750$ [MeV/G]. We then use CSSWE telemetry and fluxes in the E1=0.63-1.58 MeV and E2=1.58-3.3 MeV channels. Assuming a $E^{-\Upsilon}$ spectrum where Υ=2-4, the centroid energy is 0.64 MeV and 1.83 MeV for channels E1 and E2 respectively. The centroid energy is used in the LIM calculations. We map the spacecraft along field lines to the magnetic equator using the ONERA-IRBEM library and
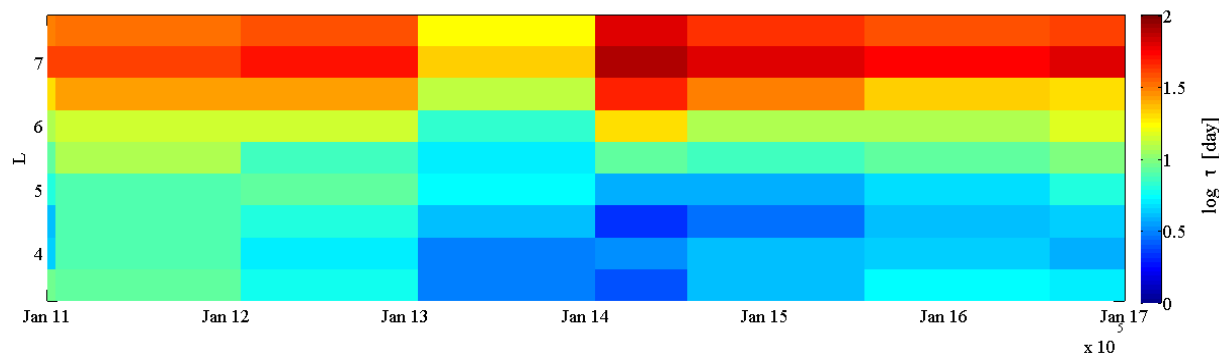
Figure 89: **Electron lifetimes for μ=750 [MeV/G], K<0.013 [$G^{1/2}R_E$] for the Jan. 11 – 17, 2013, non-storm time enhancement event determined from in-situ LEO observations and the loss index method [*Selesnick, 2006*].**

the T89 field model. We then fit the environmental energy spectrum to REPTile E1 and E2 fluxes and the instrument response curves. The spectra are constrained to exponential shapes in the form of AE^{-Y}, where Y is limited to fall between 2 and 6. We then find the energy required for the constant mu value at the new magnetic field strength at the magnetic equator and extrapolate REPTile fluxes using the environmental spectrum found in the previous steps. We store this flux value, and the spacecraft's L shell value, for input into the LIM. We repeat this process for each data point, and eventually have a dataset of fluxes corresponding to K ~ 0 and constant μ.

One major assumption required for the LIM to be valid is that only slow diffusive processes are occurring to replenish the bounce and drift loss cones. The method also assumes that diffusive processes affect all pitch angles equally. Especially for periods of low geomagnetic activity, these assumptions are valid. Additionally, the method requires sufficient longitudinal sampling. The temporal resolution of the estimate depends on the amount of time required for the spacecraft longitudinal coverage for all L values.

The estimate is performed for the Jan 13-14 2013, enhancement and the results are illustrated in Figure 89. The 24-hour resolution is caused by instrument duty-cycling during this period and full day of measurements is required to sufficiently sample all longitudes in each L bin. The estimate of the lifetimes calculated in this method represent the best possible estimate of electron lifetimes from pitch-angle diffusive processes. Furthermore, the estimate can be used as the loss term for a radial diffusion model, such as the 1D Fokker-Planck, described in detail in Chapter 5 and represented again here for convenience.

Equation 24: Simplified Fokker-Planck

$$\frac{\partial f}{\partial t} = L^2 \frac{\partial}{\partial L}\left(\frac{D_{LL}}{L^2}\frac{\partial f}{\partial L}\right) - \frac{f}{\tau} + S$$

.

We have now accomplished one third of our goal to completely disentangle the loss, source, and transport processes. We approach the transport term in the next section.

6.2.3 Determining the Transport Term

With an event-specific estimate of electron lifetimes, we can also generate an event-specific estimate of the diffusion coefficient as well. Radial diffusion in relativistic electrons is caused by drift-resonant fluctuations in the Pc5 range of ULF waves (2-7 mHz [*Kivelson and Russell,* 1995]). To extract these fluctuations, we use electric and magnetic field measurements from the Electric and Magnetic Field Instrument Suite and Integrated Science (EMFISIS) instrument [*Kletzing et*

al., 2013] and the Electric Field and Waves Instruments (EFW) [*Wygant et al.*, 2013] onboard the Van Allen Probes mission. We follow the method outlined in *Ali et al.* [2015] is used, which takes the following steps:

For the magnetic field, EMFISIS observations are processed as follows:

1) Remove data from $L^* < 2.5$.

2) Remove flagged data, invalid data points, and anomalous spikes of >3000nT. Interpolate over the removed data. If too much data is removed (>100 points), the entire orbit is removed.

3) Remove intervals during the thruster firings.

4) Down sample the 4 second Level 3 magnetic field data to 12 second resolution to match the electric field data. Compute a background field using a low pass digital filter with a cutoff at 0.8 mHz. Subtract the background and compute the compressional component of the field perturbations.

5) Estimate the power spectral density for a 20 minute intervals. The Multitaper method used to acquire spectra [*Thomson*, 1982], and the tapers used are the Discrete Prolate Spheroidal Sequences (DPSS), also known as the Slepian sequences [*Slepian*, 1978].

6) A L^* value is assigned to the center of each 20 minute window according to the center of each data segment. Then each spectrum is binned into the following six bins: $L \leq 3.25$, $3.25 < L \leq 3.75$, $3.75 < L \leq 4.25$, $4.25 < L \leq 4.75$, $4.75 < L \leq 5.25$, and $5.25 > L$.

7) The relativistic magnetic diffusion coefficient is then calculated, which

is: $D_{LL}^{B} = \dfrac{\mu^2 L^4}{8e^2 R_E^4 B_E^2 \gamma^2} \sum_m m^2 P_m^B (m\omega_d)$ (derived in *Fei et al.* [2006] and

consistent with *Falthammer* [1965]). Here, $D_{LL}{}^{B}$ is the magnetic diffusion

coefficient due to magnetic field perturbations, μ is the first adiabatic

invariant, e is the electron charge, B_E is the surface equatorial magnetic

field strength, γ is the Lorentz relativistic correction factor, ω_d is the drift

frequency, $P_m{}^{B}(m\omega_d)$ is the power spectral densities of the magnetic field

at the frequency m-times the drift frequency, and m is the azimuthal mode

number of the fluctuations. For this analysis, we assume that all of the

ULF power is in the first, m=1, mode.

8) The diffusion coefficient is calculated corresponding to constant μ,

including appropriate drift frequencies, such that it can be used in the 1D

radial diffusion code, which requires diffusion for particles of constant μ

and K.

For the electric field, EFW measurements are processed as follows:

1) Remove data from $L^* < 2.5$.

2) Remove flagged data, invalid datapoints, and anomalous spikes of >20

mV/m. Interpolate over the removed data.

3) E_y and E_z are provided in the Level 2 data. $E \bullet B = 0$ is used to compute

E_x and E_ϕ.

4) Estimate the power spectral density for a 20 minute intervals. The

Multitaper method used to acquire spectra [*Thomson*, 1982], and the tapers

used are the Discrete Prolate Spheroidal Sequences (DPSS), also known as the Slepian sequences [*Slepian*, 1978].

5) An L* value is assigned to the center of each 20 minute window according to the center of each data segment. Then each spectrum is binned into the following six bins: L ≤ 3.25, 3.25 < L ≤ 3.75, 3.75 < L ≤ 4.25, 4.25 < L ≤ 4.75, 4.75 < L ≤ 5.25, and 5.25 > L.

6) The electric diffusion coefficients are then calculated, and it is: $D_{LL}^E = \dfrac{L^6}{8R_E^2 B_E^2} \sum_m P_m^E(m\omega_d)$ (derived in *Fei et al.* [2006] and consistent with *Falthammer* [1965]). Here, $D_{LL}{}^E$ is the electric diffusion coefficient due to perturbations of the electric field, B_E is the surface equatorial magnetic field strength, $P_m{}^E(m\omega_d)$ is the power spectral densities of the electric field at the frequency m-times the drift frequency, and m is the azimuthal mode number of the fluctuations. For this analysis, we assume that all of the ULF power is in the first, m=1, mode.

7) The diffusion coefficient is calculated for the drift frequencies corresponding to constant μ.

8) Thruster firings, eclipsing, and charging events affect electric field measurements. Anomalies in $D_{LL}{}^E$ corresponding to eclipsing or charging events are determined and removed.

The diffusion timescale is calculated for the Jan 13-14 2013, enhancement event and shown in Figure 90 bottom panel. The resulting diffusion rate is
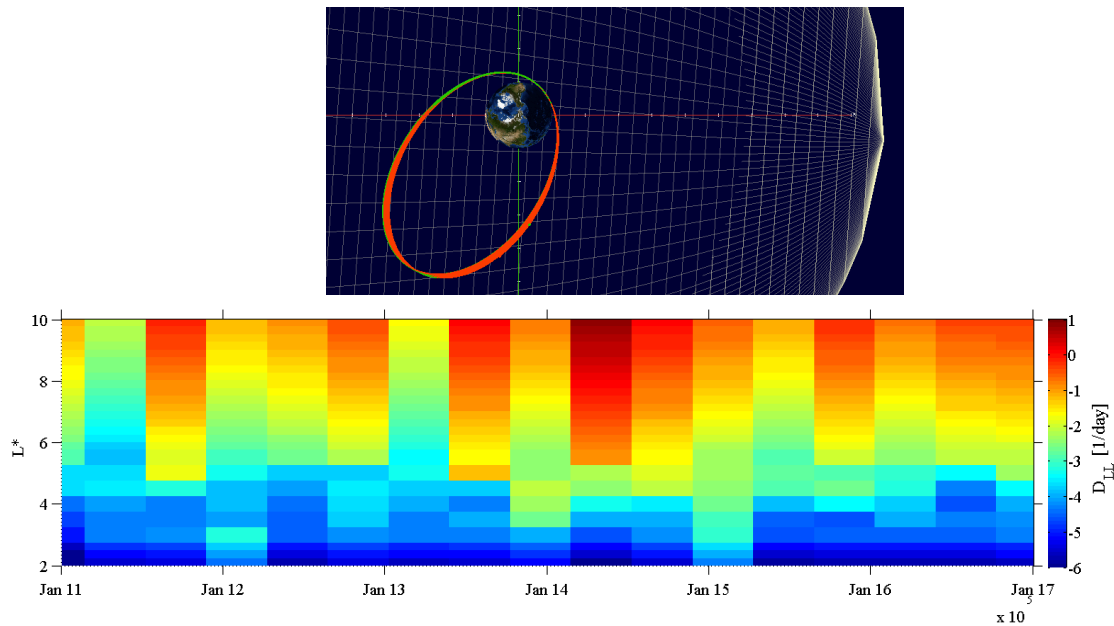
Figure 90: Top panel: Van Allen Probe orbit traces for Jan 11 – 17 2013, in the x-y plane (sun is to the right, looking from above). Bottom panel: D_{LL}^{total} for Jan 11 – 17 2013, as determined by Van Allen Probe field measurements

$D_{LL}^{total} = D_{LL}^{E} + D_{LL}^{B}$. For particles with constant first invariant μ = 750 MeV/G, the electric component of diffusion dominates. Although Figure 90 shows the total diffusion rate, it is essentially showing only the electric component. For L < 2.5 and L > 6, the diffusion rate is extrapolated from the outer boundary following a L^7 dependence, as determined roughly by the L dependences in the diffusion coefficient equations: explicit L^4 and L^6 dependencies, and implicit L dependence in γ and the wave power spectral densities.

It is worthwhile to note that the above terms are additive because they assume random phases between magnetic and electric perturbations. That is, they do not correspond to electrostatic and electromagnetic components. In fact, D_{LL}^{E} includes perturbations of the total electric fields, including convective and inductive fluctuations. D_{LL}^{B} is derived from the magnetic portion only. Thus, the

inductive electric fields are properly accounted for. However, the induced electric field cannot be separated from the total electric field with this methodology [*Tu et al.*, 2012].

Furthermore, this methodology assumes global wave activity, but ULF waves are known to have a local time biases. Ground observations of ULF oscillations are most prevalent in the dawn sector [e.g. *Anderson et al.*, 1990; *Glassmeier and Stellmacher*, 2000], possibly due to Kelvin-Helmholtz waves generated at the solar wind-magnetosphere boundary. With the Van Allen Probes sampling only the pre-dawn sector (Figure 90 top panel), it is possible that there is a spatial bias to the wave power measurements. The analysis here does not correct for this.

Now two thirds of our goal is accomplished: we have in-situ observational estimates of the loss and transport terms from Equation 24. With loss and transport known and accounted for, the remaining fluctuations in the outer belt phase space densities can be attributed to the source term. The next section is dedicated to estimating the source term.

6.3 Determining the Source Term with a Data Assimilation Model

6.3.1 Introduction

Combining in-situ particle and wave observations from CSSWE and the Van Allen Probes provides the best possible estimate of the diffusion and loss terms of the radial diffusion model. With the relative contributions of the loss and transport terms determined empirically, we can now estimate the source
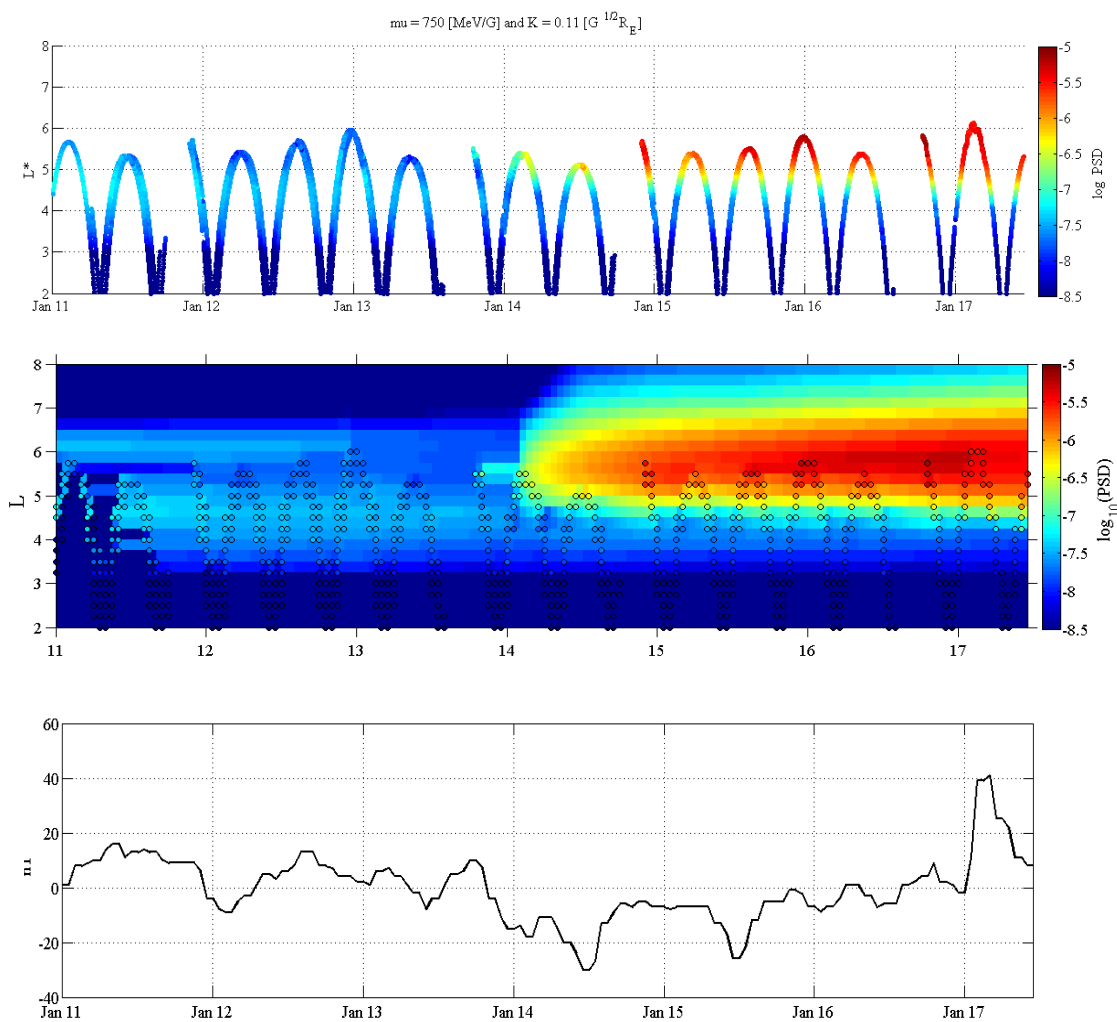
Figure 91: Top panel: electron phase space density for μ = 750 [MeV/G] and K = 0.11 [G$^{1/2}$R$_E$]. Middle panel: recreated full radial electron PSD with gridded observations over plotted. Bottom panel: the Dst index.

term with high reliability. With estimates of all three processes, we can determine the relative contribution of each term for a particular event.

6.3.2 General Methods

We use the method described in Section 6.2.2 to determine electron lifetimes and the method described in Section 6.2.3 to determine the radial diffusion rate. In this section, we use the improved data assimilation method described in Chapter 5 to reanalyze electron PSD observations with the 1D radial diffusion model (Equation 24). The method estimates the radial PSD profile as well as the location, extent, and intensity of the local acceleration term.

The PSD observations we use are calculated by the Los Alamos National Lab (LANL) Van Allen Probes Science Operations Center (SOC) for $\mu = 750$ [MeV/G] and $K = 0.11$ [$G^{1/2}R_E$] and are pictured in the top panel of Figure 91. The conversion from flux to PSD is done by fitting Van Allen Probe observations from the RBSPICE, MagEIS, and REPT instruments to an energy spectrum and a pitch angle spectrum. Constant values in first and second adiabatic invariants are generated by converting the spectral fits to PSD, rather than the observations themselves. L^* is determined using the TS04 storm-time magnetic field model [*Tsyganenko and Sitnov*, 2005].

We use three days to spin-up the filter (Jan. 11-14), and then perform the parameter space minimization on the subsequent thee days (Jan. 14-17). The recreated PSD profile for the full radial range is shown in the middle panel of Figure 91. The re-gridded observations are plotted on top of the reanalysis. The analysis period includes nearly the entirety of enhancement. A fully

comprehensive analysis to determine the smallest timescale the method can accurately determine the source rate has yet to be done (see Section 6.5). The results of the source estimate are shown in the following section.

6.3.3 Event Specific Source Estimates for a Non-Storm Time Enhancement

The downhill optimization approach successfully finds a minimum at (Amplitude = 2.2×10^{-6} [(c/cm/MeV)^{3}day^{-1}], Location = 5.8, Width = 0.5). As the downhill optimization approach is susceptible to finding local minima instead of the global minimum, it is important that the optimization scheme can reproducibly find the global minimum. This also ensures that enough data has been assimilated that the global minimum is well defined. Assuredly, the model is able to reliably reproduce the minimum for this period.

The full 3D parameter space is difficult to compute, as well as to visualize. As an alternative, we plot perpendicular 2D slices through the 3D parameter space in Figure 92. In each cross-section, the innovation RMS is fully sampled, and the intersection of the slices is at the global minimum. The resulting visualization shows a clearly defined global minimum with shallow gradients, which is an ideal parameter space for the downhill simplex method to sample. Note that the method was performed for all three dimensions and the figure represents only a fraction of the full parameter space.

The Van Allen Probes have an apogee near L*=6 and cannot take measurements on the farside of the radiation belts. As seen in the top panel of Figure 91, the spacecraft cannot resolve the full width of the outer belt, nor always the peak in PSD [*Schiller et al.*, 2013]. The THEMIS spacecraft, however,
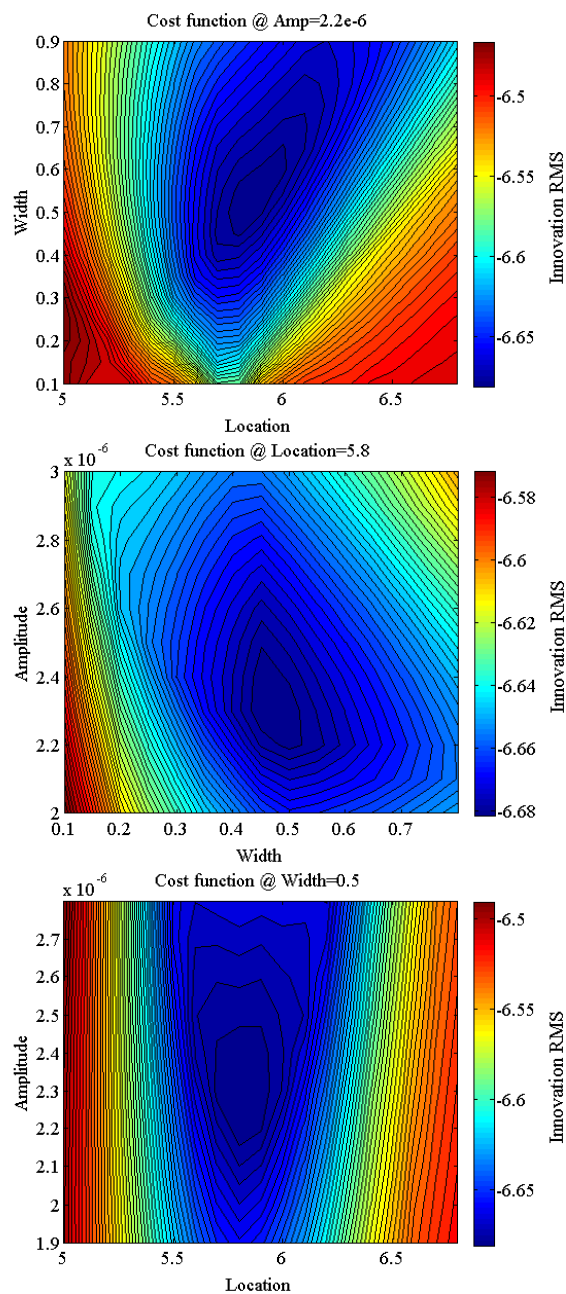
Figure 92: 2D cost function for the 3D parameter minimization at Amplitude = 2.6 x 10⁻⁶. (top panel), Location = 5.8 (middle panel), and Width = 0.5 (bottom panel).

have apogee near 12 R_E and fully sample the entire extent of the outer belt. So,

for independent verification, we turn to THEMIS observations.

Radiation belt fluxes were extremely low prior to the January 14th enhancement event. The radial profiles after the enhancement are thus a strong indication as to the shape of the enhancement region. We use THEMIS PSDs, calculated by Dr. Drew Turner (private communication), as an independent dataset to compare the results of the model against. While specifics of the conversion to PSC are not identical to the LANL SOC method (specifically, THEMIS uses the T89 magnetic field model [*Tsyganenko*, 1989] to calculate L*), a comparison can be seen in Figure 93. Here, the colored traces correspond to in- and out-bound passes by the THEMIS D spacecraft and the dashed black line corresponds to the results of the model. Note that the amplitude of the estimate is arbitrary, since the estimate is a rate $[(c/cm/MeV)^3/day]$ and the PSD profiles are in units of PSD $[(c/cm/MeV)^3]$. However, the peak location is nearly identical to what is observed by the THEMIS spacecraft. Furthermore, the shapes of the curves match extremely well inside of the peak. The curves disagree for the outward portion of the profile, which could be due to the fact that the THEMIS curves are subject to radial transport, and the dashed curve represents only the source term estimate. The PSD profiles diffuse rapidly towards the outer boundary at higher L, which could be the cause of the disagreement.

Surprisingly, despite only sampling L < 6, the method is still able to construct a source term located at L = 5.8. The result is well verified using the THEMIS dataset. These results are surprisingly agreeable and demonstrate the reliability of the method.
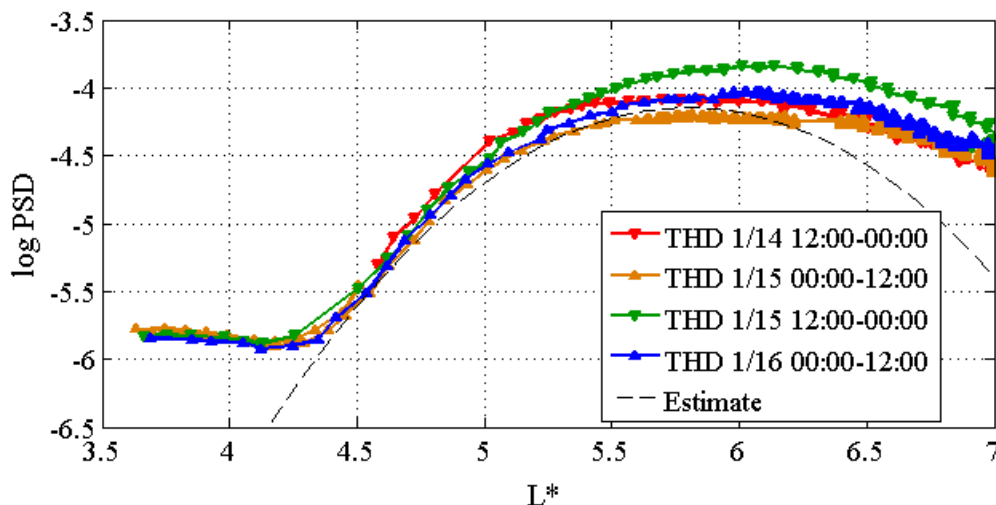
Figure 93: PSD radial profiles from four passes through the outer radiation belt by the THEMIS D spacecraft that correspond to the period during and after the enhancement. The source rate estimate is overplotted (dashed) for comparison between model and in-situ observations of the shape of the enhancement.

6.4 Summary

Untangling the respective strengths of various source, loss, and transport processes to the net flux is a scientific challenge. It is required, however, to fully understand radiation belt electron dynamics. In this chapter we present a method to determine the relative contributions of source, loss, and transport in the outer radiation belt. Specifically, we use in-situ measurements to quantify the loss and transport contribution, and then use a data assimilation model to estimate the contribution of the source term.

The loss term is determined using an approximation of numerical methods used to quantify the steady decay of electrons into the loss cone [*Selesnick,* 2006]. This technique, called the Loss Index Method, assumes that the drift loss cone is being replenished by scattering of electrons near the loss cone. The rate of precipitation loss can then be estimated by comparing the number of

particles in the drift loss cone to the total over a drift period. We use measurements from the Colorado Student Space Weather Experiment mapped to the magnetic equator to determine the lifetimes for constant first and second adiabatic invariants.

The diffusion term is determined from ULF fluctuations in the electric and magnetic fields in the Pc5 regime. The perturbations are measured by the EMFISIS and EFW instruments onboard the Van Allen Probes mission. The observations are converted into electric and magnetic diffusion rates following the procedure in *Ali et al.* [2015], and then converted into diffusion rates for constant invariant space.

Finally, with the loss and diffusion terms quantified, we use data assimilation to estimate the remaining state parameter – the source term. We compare the residuals between Van Allen Probe PSD observations and the forecast state of a Kalman filter. Because the residuals represent physics absent from the model, the smallest residuals correspond to the most likely physical processes occurring in the system.

We estimate the loss (Figure 89), diffusion (Figure 90), and source terms (Figure 93) for the January 13-14 non-storm time enhancement event. We show that the method results are reliable (see Figure 92) and reproducible. Furthermore, the results agree very well to independent observations from the THEMIS spacecraft.

This method is a groundbreaking way to disentangle the relative contributions of loss, source, and transport mechanisms for individual events, which is critical to thoroughly understand the processes occurring during radiation belt enhancement events. In the example presented, the timescales for

the loss and transport estimates are less than one day, and the source estimate is currently three days, sufficient to investigate the mechanisms for this case study. Additionally, moving to an event-specific modeling paradigm is a critical progressive step to understand magnetospheric dynamics on a per-storm basis. It provides more insight towards radiation belt dynamics than statistical models, and will lead towards answers of critical outstanding space weather questions; such as, why does each individual storms each have such unique effect on radiation belt fluxes?

6.5 Future Work

Understanding the relative contributions of source, loss, and transport is far from concluded. The work demonstrated here is only precursory and it is not yet complete. Additional investigation is required to gain confidence in the loss index method, namely, to address why electron lifetimes shown to increase with L. Theory and observation show that electron lifetime are typically highest inside the plasmasphere where hiss cause ~10 day lifetimes [e.g. *Ni et al.,* 2013]. In this regard, the LIM agrees with theory. However, although lifetimes outside of the plasmasphere are dependent on geomagnetic activity, electrons can have lifetimes ~1 day from chorus [*Thorne et al.,* 2005] and EMIC [*Summers and Thorne,* 2003] interactions. In this regard, the LIM seems to overestimate the lifetimes, suggesting that the electron lifetimes are ~20 days, not ~1.

Furthermore, electrons near the outer boundary are subject to a steep PSD gradient at the magnetopause as well as rapid radial diffusion rates (as D_{LL} has a $L^7 - L^{10}$ dependence [e.g. *Brautigham and Albert,* 2000; *Tu et al.,* 2012]). As a result, particles are quickly lost to the outer boundary and one would expect very short

lifetimes (< 1 hour) near the magnetopause. However, the LIM shows that electrons near the outer boundary (~L=8) have lifetimes longer than anywhere else in the magnetosphere. These issues indicate that additional analysis is required to understand the results of the model and verify the model reliability.

One method to better understand the LIM is to compare results obtained from CSSWE to that of another spacecraft. POES is an excellent example, as it has similar orbital properties (low altitude and high inclination), and measures similar particles (relativistic electrons with 90° local pitch angle). Performing the LIM on POES data and comparing the results to that of CSSWE can provide insight as to how reliable the CSSWE measurements are in comparison to POES, and increase our knowledge of how the LIM is performing.

Another important concept to fully understand is the error associated with the LIM. In this method, errors inherently scale with L; that is, we have lower confidence on the large lifetimes reported near the outer boundary. We must better understand and quantify the errors to determine, for example, during what geomagnetic conditions the LIM is reliable and at what radial distance it remains trustworthy.

The LIM's fundamental property is to quantify losses to the inner boundary in the form of precipitation loss. One could also quantify losses to the outer boundary with a simple radial diffusion model. A study could be conducted that directly compares losses at the atmosphere to losses at the magnetopause. Such a direct comparison has not been performed and it would shed light on the relative contribution of these two important loss processes. Also, the radial diffusion model requires a drift averaged D_{LL}, whereas the Van Allen Probe observations are localized in longitudinal coverage. Additional

work is required to properly convert the dawn sector measurements to represent global ULF activity.

Finally, the true limits of the data assimilation method we use have not been characterized. While we are confident that the timescales we use in this study are dependable (3 days), we have not determined the smallest time resolution that the method can reliably perform with. However, we do know that the method begins to break down around 12 hours of analysis, depending on specifics regarding the data available for assimilation. Additional analysis could be conducted to concretely understand what factors dictate the temporal limitations, as well as what the limitations are.

CHAPTER 7

SUMMARY, CONCLUSIONS, AND FUTURE WORK

This dissertation discusses various aspects regarding the Van Allen radiation belts. Much of the physics associated with the electron outer belt is not fully understood, especially in regard to the causes and reasons behind processes that accelerate electrons from benign energies to energies capable of damaging spacecraft. The work presented in this thesis aims to improve the way we measure, model, and understand outer belt electron dynamics.

The resulting narrative of the thesis begins by addresses the complexity of radiation belt dynamics and the challenges inherent in measuring them. Subsequently, I present unprecedented levels of verification for a unique, miniaturized particle telescope called REPTile. REPTile's measurements are used in combination with other datasets to investigate in detail an interesting non-storm enhancement event. In parallel, I develop a new data assimilative model that assists in understanding outer belt enhancements. Finally, I separate the loss and transport processes and use the model to thoroughly understand the contribution of local acceleration mechanism for the event.

7.1 Summary and Conclusions

The work in this thesis addresses the lack of a complete understanding of the acceleration mechanisms that create Earth's radiation belts. In particular, the role that acceleration plays, and how it is balanced by loss and transport mechanisms. How does acceleration vary during individual storm events? How does it vary between storms? How is the acceleration process balanced by outward radial transport and atmospheric precipitation? These are a handful of open questions that are addressed in this work. This work also address engineering questions like: how can we scale-down the intensive space-based observing process while maintaining confidence in our measurements?

Chapter 3 introduced the Relativistic Electron and Proton Telescope integrated little experiment (REPTile), a miniaturization of the REPT instrument onboard NASA's Van Allen Probes, developed and operated by students at the University of Colorado. REPTile is a novel design that miniaturizes a solid state particle telescope to make reliable and accurate observations of relativistic electrons from a low-Earth orbit. With the resource constraints of a student CubeSat mission, REPTile was developed using unprecedented detail in modeling of the instrument response and an exceptional level of data-processing to release a reliable dataset. REPTile's contributions to a number of peer reviewed journal articles are a testament to the mission's success. Its achievements indicate that the mission is a spearhead for making high-energy particle measurements from small, inexpensive spacecraft.

The subsequent chapters focus on data analysis and modeling of outer belt acceleration activity. We use REPTile measurements in Chapter 4 to help quantify an unusual enhancement event from January 13-14 2013, which occurs

without sufficient geomagnetic activity to categorize the event as a storm. The measurements are used along side Van Allen Probe and THEMIS observations to document in detail the largest non-storm enhancement event. We show that the enhancement is associated with both local heating inside of geosynchronous orbit as well as sudden inward transport. We also determine that precipitation loss is a significant contributor as well, affecting 5-16% of the relativistic electron population.

Chapter 5 focuses on modeling efforts of the outer belt, where we advance the application of data assimilation to electron dynamics. The technique we present uses residuals between the forecast state and observations to infer the size, location, and intensity of the enhancement region. Much of the chapter is dedicated towards developing and verifying the method. We also apply the novel method to a ~3 month period in 2002 to show that the source regions are commonly inside of GEO and are sufficient to completely repopulate the radiation belts after a full dropout. These estimates provide insight towards the role of electron acceleration and how it is balanced by loss and transport processes.

In Chapter 6 we disentangle the relative contributions of source, loss, and transport to generate the first event-specific, simultaneous estimate off all three processes. We use in-situ observations from REPTile of precipitating electrons to quantify loss and in-situ wave measurements from the Van Allen Probes to determine radial transport rates. The rate and location of local heating is determined using the data assimilative model. The result is a simultaneous, quantitative estimate of loss, transport, and acceleration mechanisms and the

relative contribution from each. We investigate the non-storm enhancement event as a case study using this method.

These investigations combine to generate a better understanding of the source rate of relativistic electrons. In fact, the balance between electron acceleration, loss, and transport processes is the principal motif that shadows each study. Understanding each individual event begins with knowing which physical processes dominate and dictate the electron response. Studying how electron acceleration fits into the larger picture helps untangle the various mechanisms. This work, as a whole, provides a more cohesive picture of how loss and transport are balanced by acceleration mechanisms during outer belt enhancements. It improves our understanding of the outer radiation belt and the role of the source region in relativistic enhancement events.

7.2 Potential Extensions

I present the reader with some ideas for potential extensions to the work outlined here.

7.2.1 Estimating Additional State Parameters

Data assimilation is a powerful tool. It has many applications to radiation belt physics, as demonstrated in this work and many other instances [e.g. *Koller et al.*, 2007; *Shprits et al.*, 2007; *Kondrashov et al.*, 2007; *Ni et al*, 2009a, 2009b; *Daae et al.*, 2011; *Kellerman et al.*, 2014]. There are many avenues in which data assimilation can be applied to electron dynamics that could potentially be useful to the community. However, the limits of the technique are not well understood.

Investigations that can explicitly show what observations or models are required to contribute to the field would be extremely useful.

An interesting route to pursue this research would be to see if data assimilation techniques could estimate more than one term, such as loss and source, in a simple 1D model. For example, could it simultaneously estimate a combination of the loss, source, and transport terms? If not, what observations are necessary, or what modifications to the physical model or the assimilation technique, are required to make simultaneous estimates of state parameters? The work presented here successfully estimates three parameters for the source term: How many parameters in each term can be estimated? Can state parameters be estimated in a 3D model? Finding the answers to these questions, and finding where the applications of data assimilation break down, would be an interesting avenue to pursue.

7.2.2 Expanding the Event-Specific Models

I believe that a much better understanding of radiation belt dynamics will be available with the use of event-specific analysis. In the Van Allen Probe era, we are fortunate to have simultaneous observations with low-altitude (POES, CubeSats), GEO-transfer (Van Allen Probes), GEO (GOES, LANL-GEO), and higher-Earth orbits (Cluster, MMS, Polar, THEMIS) spacecraft. By using a combination of these in-situ observations we can measure, instead of estimate, the relative contributions of various physical processes. For example, we estimate atmospheric precipitation, but we can also measure wave activity that causes pitch angle scattering that leads to atmospheric precipitation. Using these measurements in our modeling of radiation belt dynamics will refine our

understanding of the physical processes that result in the net measured flux. Moving to storm-by-storm investigations and modeling will help us better understand why not all storms result in enhancements, and what drivers and system preconditioning is required. Ultimately, predicting the response of the magnetosphere will be done by understanding individual driving events. As space weather prediction is a significant goal for the community, observing individual magnetospheric processes and their response to each individual event is required.

7.2.3 Investigating Source, Seed, and MeV Populations

When investigating outer belt enhancements, it is important to study cross-population processes. For example, to consider not only geomagnetic storms, but recognize the relative importance of substorm activity in radiation belt enhancements. While enhancements are often associated with large geomagnetic storms, it is extremely likely that there is significant substorm activitiy in the large events. An interesting hypothesis to test would be the contribution geomagnetic storms have to sudden radiation belt depletions, and the contribution substorm activity has on flux enhancements. Substorms are typically a better indicator of coupling between necessary wave and particle populations that generate enhancements. Geomagnetic storms, on the other hand, can be more associated with impulsive pressure events that cause sudden losses in combination with increased transport conditions. The non-storm enhancement event presented here further supports this general notion, as the enhancement is associated with substorm rather than geomagnetic storm activity.

The net flux of relativistic electrons observed by a spacecraft is a result of the delicate balance between transport, loss, and source mechanisms. Magnetospheric waves that can cause enhancements are typically excited by anisotropies in a 'source' population (10-100 keV electrons injected from the plasmasheet on the nightside), and can resonate with a 'seed' population (>100 keV electrons, such as ring current particles) to accelerate them to multi-MeV energies [e.g. *Summers et al.*, 1998].

Our understanding of the relationship between the source, seed, and 'energized' (>MeV energies in the heart of the outer belt) electron populations is tenuous. One current theory suggests that a source population of low energy plasma is required to generate wave growth by providing free energy to transfer energy into the waves. This plasma also acts as the medium through which these waves propagate. The waves then exchange energy with the seed population, if one is present, to accelerate them to relativistic energies [e.g. *Obara et al.*, 2000]. To illustrate, the evolutionary chain has three links:

Source (10s keV) -> EM Waves -> Seed (100 keV) -> Energized (MeV)

All three links are required to observe a MeV enhancement; a break in the chain should inhibit the sudden appearance of radiation belt electrons. This theory has been substantiated in multiple studies that find an strong association between larger flux enhancements and either larger fluxes of seed electrons [e.g. *Hwang et al.*, 2004; *Meredith et al.* 2003] or strong Auroral Electrojet (AE) activity, which is often used as a proxy for substorm activity and thus 10-100 keV particle injections [e.g. *Li et al.*, 2009; *Schiller et al.*, 2014b]. Studies have only just begun to empirically demonstrate the cross-energy prerequisites for MeV enhancements [*Boyd et al.*, 2013; *Jaynes et al.*, submitted to *Journal of Geophysical Research*].

Interesting science questions to address are: What is the correlation between the lower energy populations to the energized population? Does the correlation have a temporal or spatial component? Are both the source and seed populations required to observe an enhancement in the relativistic electrons? What are the roles of storms and substorms in these relationships?

BIBLIOGRAPHY

Abel, B. and R. M. Thorne (1998), Electron scattering loss in Earth's inner magnetosphere 1. Dominant physical processes, *J. Geophys. Res.* 103, A2.

Agostinelli, S., et al. (2003), Nuclear instruments and methods in physics research section A: accelerators, spectrometers, detectors and associated equipment, *Nucl. Instrum. Methods A*, **506**, 250–303.Allen, J. (2010), "The Galaxy 15 Anomaly: Another Satellite in the Wrong Place at a Critical Time," Space Weather, Vol. 8, No. S06008.

Ali, A. F., S. R. Elkington, W. Tu, L. G. Ozeke, A. A. Chan, and R. H. W. Friedel (2015), Magnetic field power spectra and magnetic radial diffusion coefficients using CRRES magnetometer data, *J. Geophys. Res. Space Physics*, 120, doi:10.1002/2014JA020419.

Anderson, B. J., M. J. Engebretson, S. P. Rounds, L. J. Zanetti, and T. A. Potemra, A statistical study of pulsations observed by the AMPTE/CCE magnetic fields experiment, 1, Occurrence distributions, *J. Geophys. Res.*, 95, 10,495, 1990.

Angelopoulos, V. (2008), The THEMIS Mission, *Space Sci. Rev.*, **141**, 5–34, doi: 10.1007/s11214-008-9336-1.

Baker, D. N., et al. (1986), Highly relativistic electrons in the Earth's outer magnetosphere 1. Lifetimes and temporal history 1979-1984, *J. Geophys. Res.*, 91, A4, 4265-4276.

Baker, D. N., G. M. Mason, O. Figueroa, G. Colon, J. G. Watzin, and R. M. Aleman (1993), An overview of the solar, anomalous, and magnetospheric particle explorer (SAMPEX) mission, *IEEE Trans. Geosci. Rem. Sensing*, 31(3), 531.

Baker, D. N. (2001), Satellite anomalies due to space storms, *Space Storms and Space Weather Hazards*, edited by I. A. Daglis, pp. 251-284, Springer, New York, NY.

Baker, D. N. (2002), "How to Cope with Space Weather," *Science*, Vol. 297, pp. 1486–1487.

Baker, D. N., J. E. Mazur, and G. Mason (2012), SAMPEX to reenter atmosphere: Twenty-year mission will end, *Space Weather*, **10**, S05006, doi:10.1029/2012SW000804.

Baker, D. N. et al. (2013), A long-lived relativistic electron storage ring embedded in Earth's outer Van Allen belt, *Science*, 340, 186.

Baker, D. N., et al. (2013), The relativistic electron-proton telescope (REPT) instrument on board the radiation belt storm probes (RBSP) spacecraft: Characterization of Earth's radiation belt high-energy particle populations, *Space Sci. Rev.*, 197:337-381, doi:10.1007/s11214-012-9950-9.

Baker, D. N., A. N. Jaynes, V. C. Hoxie, R. M. Thorne, J. C. Foster, X. Li, J. F. Fennell, J. G. Wygant, S. G. Kanekal, P. J. Erickson, W. Kurth, W. Li, Q. Ma, L. Blum, Q. Schiller, A. Gerrard and L. J. Lanzerotti (2014), An impenetrable barrier to ultra-relativistic electrons in the Van Allen radiation belt, *Nature*, 515, pp. 531-534, doi:10.1038/nature13956.

Belian, R. D., G. R. Gisler, T. Cayton, and R. Christensen (1992), High Z energetic particles at geosynchronous orbit during the great solar proton event of October, 1989., *J. Geophys. Res.*, 97, 16,897.

Beutier, T., and D. Boscher (1995), A three dimensional analysis of the electron radiation belt by the Salammboˆ code, *J. Geophys. Res.*, 100, 14,853 -- 14,861.

Blake, J. B., J. F. Fennell, L. M. Friesen, B.M. Johnson, W. A. Kolasinski, D. J. Mabry, J. V. Osborn, S. H. Penzin, E. R. Schnauss, H. E. Spence, D. N. Baker, R. Belian, T. A. Fritz, W. Ford, B. Laubscher, R. Stiglich, R. A. Baraze, M. F. Hilsenrath, W. L. Imhoff, J. R. Kilner, J. Mobila, D. H. Voss, A. Korth, M. Gull, K. Fisher, M. Grande and D. Hall (1995), Comprehensive energetic particle and pitch angle distribution experiment on polar, *Space Sci. Rev.* 71, 531–562, doi:10.1007/BF00751340.

Blake, J.B. et al. (1996), New high temporal and spatial resolution measurements by SAMPEX of the precipitation of relativistic electrons, *Adv. Space Res.*, **18**, (8)171-186.

Blake, J. B. et al. (1997), Correlation of changes in the outer-zone relativistic-electron population with upstream solar wind and magnetic field measurements, *Geophys. Res. Lett.*, 24, 8.

Blake, J. B., et al. (2013), The Magnetic Electron Ion Spectrometer (MagEIS) Instruments Aboard the Radiation Belt Storm Probes (RBSP) Spacecraft, *Space Sci. Rev.*, doi:10.1007/s11214-013-9991-8.

Blum, L. and Q. Schiller (2012), Characterization and testing of an energetic particle telescope for a CubeSat platform, *Proceedings of the AIAA/USU Conference on Small Satellites*, Frank J. Redd Student Scholarship Competition, SSC12-VIII-4.

Blum, L. W., Q. Schiller, X. Li, R. Millan, A. Halford, and L. Woodger (2013), New conjunctive CubeSat and balloon measurements to quantify rapid energetic electron precipitation, *Geophys. Res. Lett.*, 40, doi:10.1002/2013GL058546.

Borovsky, J. E., and M. H. Denton (2006), Differences between CME-driven storms and CIR-driven storms, *J. Geophys. Res.*, 111, A07S08, doi:10.1029/2005JA011447.

Bortnik, J. and R. M. Thorne (2007), The dual role of ELF/VLF chorus waves in the acceleration and precipitation of radiation belt electrons, *J. of Atmospheric and Solar-Terrestrial Physics*, 69, 378-386.

Bortnick, J., R. M. Thorne, and N. P. Meredith (2008), The unexpected origin of plasmaspheric hiss from discrete chorus emissions, *Nature*, 452, pg. 62-66.

Bourdarie, S., R. H. W. Friedel, J. Fennell, S. Kanekal, and T. E. Cayton (2005), Radiation belt representation of the energetic electron environment: Model and data synthesis using the Salammbo radiation belt transport code and Los Alamos geosynchronous and GPS energetic particle data, *Space Weather*, 3, S04S01, doi:10.1029/2004SW000065.

Bourdarie, S., A. Sicard-Piet, R. H. W. Friedel, T. P. O'Brien, T. Cayton, B. Blake, D. Boscher, and D. Lazaro (2009), Outer electron belt specification model, *Nuclear Science, IEEE Transactions on Nuclear Science*, vol.56, no.4, pp.2251-2257, doi:10.1109/TNS.2009.2014844.

Boyd, A. J., et al. (2014), Quantifying the radiation belt seed population in the March 17, 2013 electron acceleration event, *Geophys. Res. Lett.*, 41, doi:10.1002/2014GL059626.

Brautigam, D. H. and J. M. Albert (2000), Radial diffusion analysis of outer radiation belt electrons during the October 9, 1990, magnetic storm, *J. Geophys. Res.*, 105, 291–310, doi:10.1029/1999JA900344.

Bunch, N. L., M. Spasojevic, and Y. Y. Shprits (2012), Off-equatorial chorus occurrence and wave amplitude distributions as observed by the Polar Plasma Wave Instrument, *J. Geophys. Res.*, 117, A04205, doi:10.1029/2011JA017228.

Chen, Y., R. H. W. Friedel, G. D. Reeves, T. G. Onsager, and M. F. Thomsen (2005), Multisatellite determination of the relativistic electron phase space density at geosynchronous orbit: Methodology and results during geomagnetically quiet times, *J. Geophys. Res.*, 110(A10), A10210, doi:10.1029/2004JA010895.

Chen, Y., R. H. W. Friedel, and G. D. Reeves (2006), Phase space density distributions of energetic electrons in the outer radiation belt during two Geospace Environment Modeling Inner Magnetosphere/Storms selected storms, *J. Geophys. Res.*, 111, A11S04, doi:10.1029/2006JA011703.

Chen, Y., G. D. Reeves, and R. H. W. Freidel (2007), The energization of relativistic electrons in the outer Van Allen radiation belt, *Nat. Phys.*, 3, 614–617, doi:10.1038/nphys655.

Chen, Y., G. D. Reeves, R. H. W. Friedel, and G. S. Cunningham (2014), Global time-dependent chorus maps from low- Earth-orbit electron precipitation and Van Allen Probes data, *Geophys. Res. Lett.*, 41, doi:10.1002/2013GL059181

Crank, J., and P. Nicolson (1947), A practical method for numerical evaluation of solutions of partial differential equations of the heat-conduction type, *Proc. Cambridge Philos. Soc.*, 43, 50–67.

Daae, M., Y. Y. Shprits, B. Ni, J. Koller, D. Kondrashov, Y. Chen (2011), Reanalysis of radiation belt electron phase space density using various boundary conditions and loss model, *Advances in Space Research*, 48(2011), 1327-1334.

Dai, L., C. Wang, S. Duan, Z. He, J. R. Wygant, C. A. Cattell, X. Tao, Z. Su, C. Kletzing, D. N. Baker, et al. (2015), Near-Earth Injection of MeV Electrons associated with Intense Dipolarization Electric Fields: Van Allen Probes observations, *Geophys. Res. Lett.*, 42, doi:10.1002/2015GL064955.

Denton, M. H., et al. (2006), Geomagnetic storms driven by ICME- and CIR-dominated solar wind, *J. Geophys. Res.*, 111, A07S07, doi:10.1029/2005JA011436.

Dessler, A. J., and R. Karplus (1961), Some effects of diamagnetic ring currents on Van Allen radiation, *J. Geophys. Res.*, 66, 2289.

Elkington, S. R., M. K. Hudson, and A. A. Chan (1999), Acceleration of relativistic electrons via drift resonant interactions with toroidal-mode Pc-5 ULF oscillations, *Geophys. Res. Lett.*, 26, 3273.

Erlandson, R. E. and A. J. Ukhorskiy, (2001). Observations of electro- magnetic ion cyclotron waves during geomagnetic storms: wave occurrence and pitch angle scattering. *Journal of Geophysical Research* 106, 3883–3895.

Evensen, G. (1994), Sequential data assimilation with a nonlinear quasi-geostrophic model using Monte Carlo methods to forecast error statistics, *J. Geophys. Res.*, 99(C5), 10,143–10,162.

Evensen, G. (2003), The ensemble Kalman filter: Theoretical formulation and practical implementation, *Ocean Dyn.*, 53, 343–367, doi:10.1007/s10236-003-0036-9.

Falthammar, C.-G. (1965), Effects of time-dependent electric fields on geomagnetically trapped radiation, *J. Geophys. Res.*, 70(11), 2503.

Feldman, W., Aiello, W., Drake, D., and M. Herrin (1985), The bdd II: An Improved Electron Dosimeter for the Global Positioning System, LANL Technical Report, LA-10453-MS.

Fennell, J. F., S. G. Claudepierre, J. B. Blake, T. P. O'Brien, J. H. Clemmons, D. N. Baker, H. E. Spence, and G. D. Reeves (2015), Van Allen Probes show the inner radiation zone contains no MeV electrons: ECT/MagEIS data, *Geophys. Res. Lett.*, DOI: 10.1002/2014GL062874.

Friedel, R., Bourdarie, S., and T. E. Cayton (2005), Intercalibration of magnetopsheric energetic electron data, *Space Weather*, 3, S09B04, doi:10.1029/ 2005SW00153.

Gerhardt, D. and S. Palo (2010), Passive Magnetic Attitude Control for CubeSat Spacecraft, *24th Proceedings of the AIAA/USU Conference on Small Satellites*, Frank J. Redd Student Scholarship Competition, SSC10-VIII-5.

Gerhardt, D., S. Palo, Q. Schiller, L. Blum, X. Li, and R. Kohnert (2014), The Colorado Student Space Weather Experiment (CSSWE) on-orbit performance, *Journal of Small Satellites*, Vol. 03, No. 01, pp. 265-281.

Glassmeier, K.-H., and M. Stellmacher, Concerning the local time asym- metry of Pc5 wave power at the ground and field line resonance widths, *J. Geophys. Res.*, 105, 18,847, 2000.

Goldstein, J., S. De Pascuale, C. Kletzing, W. Kurth, K. J. Genestreti, R. M. Skoug,

B. A. Larsen, L. M. Kistler, C. Mouikis, and H. Spence (2014), Simulation of Van Allen Probes plasmapause encounters, *J. Geophys. Res*. Space Physics, 119, 7464–7484, doi:10.1002/2014JA020252.

Gonzalez, W. D., et al. (1999), Interplanetary origin of geomagnetic storms, *Space Sci. Rev.*, **88**, 529–562.

Godinez, H. C., and J. Koller, (2012), Localized Adaptive Inflation in Ensemble Data Assimilation for a Radiaiton Belt Model, *Space Weather*, doi:10.1029/2012SW000800.

Green, J. C., and M. G. Kivelson (2004), Relativistic electrons in the outer radiation belt: Differentiating between acceleration mechanisms, *J. Geophys. Res*., 109 (A3), A03213, doi:10.1029/2003JA010153.

Green, J. C. (2006), Using electron phase space density signatures to identify the electromagnetic waves responsible for accelerating relativistic electrons in Earth's magnetosphere, *Geophys. Monograph Series*, 169, doi:10.1029/169GM15.

Hartley, D. P., M. H. Denton, and J. V. Rodriguez (2014), Electron number density, temperature, and energy density at GEO and links to the solar wind: A simple predictive capability, *J. Geophys. Res. Space Physics*, 119, 4556–4571, doi:10.1002/2014JA019779.

Hilmer, R., G. Ginet, and T. Cayton (2000), Enhancement of equatorial energetic electron fluxes near L = 4.2 as a result of high speed solar wind streams, *J. Geophys. Res.*, 105, 23,311–23,322.

Horne, R. B., G. V. H. Wheeler, and C. K. St. Alleyne (2000), Proton and electron heating by radially propagating fast magnetosonic waves, *J. Geophys. Res.*, 105, 27,597–27,610.

Horne, R. B., R. M. Thorne, S. A. Glauert, J. M. Albert, N. P. Meredith, and R. R. Anderson (2005), Timescale for radiation belt electron acceleration by whistler mode chorus waves, *J. Geophys. Res.*, 110, A03225, doi:10.1029/2004JA010811.

Horne, R. B., R. M. Thorne, S. A. Glauert, N. P. Meredith, D. Pokhotelov, and O. Santolik (2007), Electron acceleration in the Van Allen radiation belts by fast magnetosonic waves, *Geophys. Res. Lett.*, 34, L17107, doi:10.1029/2007GL030267.

Horne, R. B., and R. M. Thorne (1998), Potential waves for relativistic electron scattering and stochastic acceleration during magnetic storms, *Geophys. Res. Lett.*, 25(15), 3011–3014, doi:10.1029/98GL01002.

Hwang, J., et al. (2004), A case study to determine the relationship of relativistic electron events to substorm injections and ULF power, *Geophys. Res. Lett.*, 31, L23801.

Ingraham, J. C., et al. (2001), Substorm injection of relativistic electrons to geosynchronous orbit during the great magnetic storm of March 24, 1991, *J. Geophys. Res.*, 106, 25,759–25,776, doi:10.1029/2000JA000458.

Jazwinski, A. (1970), *Stochastic processes and filtering theory*, Academic Press.

Jaynes, A. N., X. Li, Q. Schiller, L. W. Blum, W. Tu, D. L. Turner, B. Ni, J. Bortnik, D. N. Baker, S. G. Kanekal, J. B. Blake, and J. Wygant (2014), Evolution of relativistic outer belt electrons during an extended quiescent period, *Journal of Geophysical Research*, 119.

Jaynes, A. N., et al., Source and seed populations for relativistic electrons: their roles in radiation belt changes, submitted to *J. Geophys. Res.*.

Kalman, R. E. (1960), A new approach to linear filtering and prediction problems, *Trans. ASME, Ser. D: J. Basic Eng.*, 82, 35-45.

Kalnay, E. (2003), *Atmospheric Modeling, Data Assimilation and Predictability*, Cambridge University Press.

Kappenman, J. G. (2001), "An Introduction to Power Grid Impacts and Vulnerabilities from Space Weather," Space Storms and Space Weather Hazards, edited by I. A. Daglis, Kluwer Academic, Dordrecht, Netherlands, pp. 335–361.

Kellerman, A. C., Y. Y. Shprits, and D. L. Turner (2013), A Geosynchronous Radiation- belt Electron Empirical Prediction (GREEP) model, *Space Weather*, 11, 463–475, doi:10.1002/swe.20074.

Kellerman, A. C., Y. Y. Shprits, D. Kondrashov, D. Subbotin, R. A. Makarevich, E. Donovan, and T. Nagai (2014), Three-dimensional data assimilation and reanalysis of radia- tion belt electrons: Observations of a four-zone structure using five space- craft and the VERB code, *J. Geophys. Res. Space Physics,* 119, 8764–8783, doi:10.1002/2014JA020171.

Kim, H.-J. and A. A. Chan (1997). Fully adiabatic changes in storm time relativistic electron fluxes, *J. Geophys. Res.* 102, 22107–22116.

Kim, H.-J., et al. (2006), Origin of geosynchronous relativistic electron events, *J. Geophys. Res.,* 111, A03208, doi:10.1029/2005JA011469.

Kivelson, M. G., and C. T. Russell (Eds.) (1995), Introduction to Space Physics, Cambridge Univ. Press, New York.

Kletzing, C. A. et al. (2013), The electric and magnetic field instrument suite and integrated science (EMFISIS) on RBSP, *Space Sci. Rev.,* 179:127-181, doi: 10.1007/s11214-013-9993-6.

Koller, J., Y. Chen, G. D. Reeves, R. Friedel, T. E. Cayton, and J. A. Vrugt (2007), Identifying the radiation belt source region by data assimilation, *J. Geophys. Res.*, 112, A06,244, doi:10.1029/2006JA012196.

Koller, J. and S. K. Morley (2010), Magnetopause Shadowing Effects for Radiation Belt Models During High-Speed Solar Wind Streams, SM13A-1787 poster presented at 2010 Fall Meeting, AGU, San Francisco, Calif., 13-17 Dec.

Kondrashov, D., Y. Shprits, M. Ghil, and R. Thorne (2007), A Kalman filter technique to estimate relativistic electron lifetimes in the outer radiation belt, *J. Geophys. Res., 112*, A10227.

Kondrashov, D., M. Ghil, and Y. Shprits (2011), Lognormal Kalman filter for assimilating phase space density data in the radiation belts, *Space Weather*, 9, S11006, doi:10.1029/2011SW000726.

Lainiotis, D. G. (1971), Optimal adaptive estimation: Structure and parameter adaptation, *IEEE Trans. Autom. Control*, AC-16(2), 160–170.

Leo, W. R. (1987), Techniques for Nuclear and Particle Physics Experiments, Springer-Verlag, New York.

Li, W., Y. Y. Shprits, and R. M. Thorne (2007), Dynamic evolution of energetic outer zone electrons due to wave-particle interactions during storms, *J. Geophys. Res.*, 112, A10220, doi:10.1029/2007JA012368.

Li, W., R. M. Thorne, V. Angelopoulos, J. Bortnik, C. M. Cully, B. Ni, O. LeContel, A. Roux, U. Auster, and W. Magnes (2009), Global distribution of whistler-mode chorus waves observed on the THEMIS spacecraft, *Geophys. Res. Lett.*, 36, L09104, doi:10.1029/2009GL037595.

Li, W. et al. (2013), Constructing the global distribution of chorus wave intensity using measurements of electrons by the POES satellites and waves by the

Van Allen Probes, *Geophys. Res. Lett.*, 40, 4526-4532, DOI: 10.1002/grl.50920.

Li, X., D. N. Baker, M. Temerin, T. E. Cayton, G. D. Reeves, R. A. Christiansen, J. B. Blake, M. D. Looper, R. Nakamura, and S. G. Kanekal (1997), Multi-satellite observations of the outer zone electron variation during the November 3 – 4, 1993, magnetic storm, *J. Geophys. Res.*, 102, 14, 123.

Li, X., and M. A. Temerin (2001), The electron radiation belt, *Space Sci. Rev.*, 95, 569.

Li, X., et al. (2001), SAMPEX long term observations of MeV electrons, *Geophys. Res. Lett.*, 28, 3827.

Li, X., et al. (2003), Energetic particle injections in the inner magnetosphere as a response to an interplanetary shock, *J. Atmos. Sol. Terr. Phys.*, 65(2), 233–244, doi:10.1016/S1364- 6826(02)00286-9.

Li, X., S. Palo, and R. Kohnert (2011), Small space weather research mission designed fully by students, *Space Weather*, *9*, doi:10.1029/2011sw000668

Li, X., S. Palo, R. Kohnert, L. Blum, D. Gerhardt, Q. Schiller, and S. Califf (2013a), Small mission accomplished by students – big impact on space weather research, *Space Weather*, *11*, doi: 10.1002/swe.20025.

Li, X., S. Palo, R. Kohnert, D. Gerhardt, L. Blum, Q. Schiller, D. Turner, W. Tu, N. Sheiko, and C. S. Cooper (2013b), Colorado student space weather experiment: Differential flux measurements of energetic particles in a highly inclined low Earth orbit, in Dynamics of the Earth's Radiation Belts and Inner Magnetosphere, Geophys. Monogr. Ser., vol. 199, edited by D. Summers, I. R. Mann, D. N. Baker, and M. Schulz, pp. 385–404, AGU, Washington, D. C., doi:10.1029/2012GM001313.

Li, X., Q. Schiller, L. Blum, S. Califf, H. Zhao, W. Tu, D. Turner, D. Gerhardt, S. Palo, S. Kanekal, D. N. Baker, J. Fennell, J. B. Blake, M. Looper, G. D. Reeves, and H. Spence (2013c), First results from CSSWE: characteristics of relativistic electrons in near earth environment during the October 2012 magnetic storms, *J. Geophys. Res. Space Physics*, 118, doi:10.1002/2013JA019342.

Li, X., R. S. Selesnick, D. N. Baker, A. N. Jaynes, S. G. Kanekal, Q. Schiller, L. Blum, J. Fennell, J. B. Blake (2015), Upper limit on the inner radiation belt MeV electron intensity, *J. Geophys. Res. Space Physics*, 120, doi:10.1002/2014JA020777.

Ljung, L. (1979), Asymptotic behavior of the extended Kalman filter as a parameter estimator for linear systems, *IEEE Trans. Autom. Control*, AC-24(1), 36–50.

Love, D. P., Toomb, D. S., Wilkinson, D. C., and Parkinson, J. B. (2000), "Penetrating electron fluctuations as- sociated with GEO spacecraft anomalies," *IEEE Trans. Plasma Sci.*, Vol. 28, pp. 2075–2084.

Lyons, L. R. and D. J. Williams, *Quantitative aspects of magnetospheric physics*, D. Reidel, Dordrecht-Holland, 1984.

Lyons, L. R. et al. (2005), Solar wind-magnetosphere coupling leading to relativistic electron energization during high-speed streams, *J. Geophys. Res.*, 110, A11202, doi:10.1029/2005JA011254.

Maget, V., S. Bourdarie, D. Boscher, and R. H. W. Friedel (2007), Data assimilation of LANL satellite data into the Salammboˆ electron code over a complete solar cycle by direct insertion, *Space Weather*, 5, S10003, doi:10.1029/2007SW000322.

Mauk, B. H., Fox, N. J., Sibeck, D. G., and Grebowsky, J. M. (2009), "NASA's Radiation Belt Storm Probes (RBSP) Mission," American Geophysical Union Fall Meeting, No. SM21B-03, AGU.

Mauk, B. H., N.J. Fox, S.G. Kanekal, R.L. Kessel, D.G. Sibeck, A. Ukhorskiy (2012), Science objectives and rational for the Radiation Belt Storm Probes Mission, *Space Sci. Rev.*, 179:3-27, doi:10.1007/s11214-012-9908-y.

Meredith, N. P., R. B. Horne, R. H. A. Iles, R. M. Thorne, D. Heynderickx, R. R. Anderson (2002), Outer zone relativistic electron acceleration associated with substorm-enhanced whistler mode chorus, *J. Geophys. Res.*, 107(A7), 1144, doi:10.1029/2001JA900146.

Meredith, N. P., M. Cain, R. B. Horne, R. M. Thorne, D. Summers, and R. R. Anderson (2003a), Evidence for chorus-driven electron acceleration to relativistic energies from a survey of geomagnetically disturbed periods, *J. Geophys. Res.*, 108(A6), 1248, doi:10.1029/2002JA009764.

Meredith, N. P., R. B. Horne, R. M. Thorne, and R. R. Anderson (2003b), Favored regions for chorus-driven electron acceleration to relativistic energies in the Earth's outer radiation belt, *Geophys. Res. Lett.*, 30(16), 1871, doi:10.1029/ 2003GL017698.

Mewaldt, R. A., Cummings, A. C., Cummings, J., Leske, R. A., Selesnick, R. S., Stone, E. C., and von Rosenvinge, T. T. (1994), "Anomalous Cosmic Ray Studies Us- ing the Earth's Field as a Magnetic Rigidity Filter," *Bull. Am. Phys. Soc.*, Vol. 39, 1140.

Mewaldt, R. A., Cohen, C. M. S., Labrador, A. W., Leske, R. A., Mason, G. M., Desai, M. I., Looper, M. D., Mazur, J. E., Selesnick, R. S., and Haggerty, D. K. (2005), "Proton, Helium, and Electron Spectra During the Large Solar

Particle Events of October-November 2003," *Journal of Geophysical Research*, Vol. 110.

Millan, R. M. and D. N. Baker (2012), Acceleration of particles to high energies in Earth's radiation belts, *Space Sci Rev*, 173, 103-131, doi:10.1007/s11214-012-9941-x.

Millan, R. M., et al. (2013), The Balloon Array for RBSP Relativistic Electron Losses (BARREL), *Space Sci. Rev.*, 179:503-530; doi:10.1007/s11214-013-9971-z.

Miyoshi, Y., and R. Kataoka (2008), Flux enhancement of the outer radiation belt electrons after the arrival of stream interaction regions, *J. Geophys. Res.*, 113, A03S09, doi:10.1029/2007JA012506.

Miyoshi, Y. et al. (2013), High-speed solar wind with southward interplanetary magnetic field causes relativistic electron flux enhancement of the outer radiation belt via enhanced condition of whistler waves, *Geophys. Res. Lett.*, 40, doi:10.1002/grl.50916.

Morley, S. K. et al. (2010), Dropouts of the outer electron radiation belt in response to solar wind stream interfaces: global positioning system observations, *Proc. R. Soc. A*, 466, doi: 10.1098/rspa.2010.0078.

Naehr, S. M., and F. R. Toffoletto (2005), Radiation belt data assimilation with an extended Kalman filter, *Space Weather*, 3, S06001, doi:10.1029/2004SW000121.

Nelder, J. A. and R. Mead (1965), A simplex method for function minimization, *Computer J.*, Vol. 7, pp. 308.

Ni, B., Y. Shprits, T. Nagai, R. Thorne, Y. Chen, D. Kondrashov, and H.-J. Kim (2009a), Reanalyses of the radiation belt electron phase space density

using nearly equatorial CRRES and polar-orbiting Akebono satellite observations, *J. Geophys. Res.*, 114, A05208, doi:10.1029/2008JA013933.

Ni, B., Y. Shprits, R. Thorne, R. Friedel, and T. Nagai (2009b), Reanalysis of relativistic radiation belt electron phase space density using multisatellite observations: Sensitivity to empirical magnetic field models, *J. Geophys. Res.*, 114, A12208, doi:10.1029/2009JA014438.

Ni, B., J. Bortnik, R. M. Thorne, Q. Ma, and L. Chen (2013), Resonant scattering and resultant pitch angle evolution of relativistic electrons by plasmaspheric hiss, *J. Geophys. Res. Space Physics*, 118, 7740–7751, doi:10.1002/2013JA019260.

Obara, T., et al. (2000), Main-phase creation of "seed" electrons in the outer radiation belt, *Earth Planets Space*, 52, 41-47.

O'Brien, T. P., and M. B. Moldwin (2003), Empirical plasmapause models from magnetic indices, *Geophys. Res. Lett.*, 30(4), 1152, doi:10.1029/2002GL016007.

O'Brien, T. P., K. R. Lorentzen, I. R. Mann, N. P. Meredith, J. B. Blake, J. F. Fennell, M. D. Looper, D. K. Milling, and R. R. Anderson (2003), Energization of relativistic electrons in the presence of ULF power and MeV microbursts: Evidence for dual ULF and VLF acceleration, *J. Geophys. Res.*, 108(A8), 1329, doi:10.1029/2002JA009784.

O'Brien, T. P., M. D. Looper, and J. B. Blake (2004), Quantification of relativistic electron microburst losses during the GEM storms, *Geophys. Res. Lett.*, 31, L04802, doi:10.1029/ 2003GL018621.

Palo, S., X. Li, D. Gerhardt, D. Turner, R. Kohnert, V. Hoxie and S. Batiste (2010), Conducting Science with a CubeSat: The Colorado Student Space Weather

Experiment, , *24ᵗʰ Proceedings of the AIAA/USU Conference on Small Satellites*, SSC10-XII-8.

Podladchikova, T. V., Y. Y. Shprits, D. Kondrashov, and A. C. Kellerman (2014a), Noise statistics identification for Kalman filtering of the electron radiation belt observations I: Model errors, *J. Geophys. Res. Space Physics*, 119, doi:10.1002/2014JA019897.

Podladchikova, T. V., Y. Y. Shprits, A. C. Kellerman, and D. Kondrashov (2014b), Noise statistics identifica- tion for Kalman filtering of the electron radiation belt observa- tions: 2. Filtration and smoothing, *J. Geophys. Res. Space Physics*, 119, doi:10.1002/2014JA019898.

Press, W. H., B. P. Flannery, S. A. Teukolsky, and W. T. Vetterling (1986), *Numerical Recipes — The Art of Scientific Computing*, 1st ed., Cambridge Univ. Press, New York.

Reeves, G. D. (1998), Relativistic electrons and magnetic storms: 1992–1995, *Geophys. Res. Lett.*, 25(11), 1817–1820.

Reeves, G. D., K. L. McAdams, R. H. W. Friedel, and T. P. O'Brien (2003), Acceleration and loss of relativistic electrons during geomagnetic storms, *Geophys. Res. Lett.*, 30(10), 1529, doi:10.1029/2002GL016513.

Reeves, G. D., Y. Chen, G. S. Cunningham, R. W. H. Friedel, M. G. Henderson, V. K. Jordanova, J. Koller, S. K. Morley, M. F. Thomsen, and S. Zaharia (2012), Dynamic Radiation Environment Assimilation Model: DREAM, *Space Weather*, 10, S03006, doi:10.1029/2011SW000729.

Reeves, G. D., et al. (2013), Electron acceleration in the heart of the Van Allen radiation belts, *Science,* doi:10.1126/science.1237743.

Roederer, J. G. (1970), Dynamics of Geomagnetically Trapped Radiation,

Springer, New York, doi:10.1007/978-3-642-49300-3.

Rossi, B. (1948), Interpretation of cosmic-ray phenomena, *Rev. Mod. Phys.*, **20**(3), 537-583.

Santolık, O., D. A. Gurnett, J. S. Pickett, M. Parrot, and N. Cornilleau- Wehrlin (2005), Central position of the source region of storm-time chorus, *Planet. Space Sci.*, 53, 299–305.

Santolık, O., D. A. Gurnett, J. S. Pickett, J. Chum, and N. Cornilleau-Wehrlin (2009), Oblique propagation of whistler mode waves in the chorus source region, *J. Geophys. Res.*, 114, A00F03, doi:10.1029/2009JA014586.

Schiller, Q. and A. Mahendrakumar (2010), REPTile: a miniaturized detector for a CubeSat mission to measure relativistic particles in near-Earth space, *Proceedings of the AIAA/USU Conference on Small Satellites*, Frank J. Redd Scholarship Competition, SSC10-VIII-1.

Schiller, Q., X. Li, J. Koller, H. Godinez, and D. L. Turner (2012), A parametric study of the source rate for outer radiation belt electrons using a Kalman filter, J. Geophys. Res., 117, A09211, doi:10.1029/2012JA017779.

Schiller, Q. and H. Godinez (2012), Determining source rate parameters of energetic electrons in the outer radiation belt using a Kalman filter, Los Alamos Space Weather Summer School Research Reports, edited by J. Koller, J. R. Terry, and R. D. Gurule, pp. 51-67, LA-   UR 13-23748, Los Alamos, N.M.

Schiller, Q. and H. Godinez (2013), Determining source rate parameters of energetic electrons in the outer radiation belt using a Kalman filter, Los Alamos Space Weather Summer School Research Reports, edited by J. Koller and R. D. Gurule, pp. 79-84, LA-UR 13-29060, Los Alamos, N.M.

Schiller, Q., X. Li, L. Blum, W. Tu, D. L. Turner, and J. B. Blake (2014a), A nonstorm time enhancement of relativistic electrons in the outer radiation belt, *Geophys. Res. Lett.*, *41*, 7–12, doi:10.1002/2013GL058485.

Schiller, Q., D. Gerhardt, L. Blum, X. Li, S. Palo (2014b), Design and scientific return of a miniaturized particle telescope onboard the Colorado Student Space Weather Experiment (CSSWE) CubeSat, 35th IEEE Aerospace , 8.1102.

Schiller, Q. and H. Godinez (2014), Estimating source rate parameters of outer radiation belt electrons using a Kalman filter variant: a progress report, Los Alamos Space Weather Summer School Research Reports, edited by M. Cowee, pp. 127-137, LA-UR 15-20136, Los Alamos, N.M.

Schulz, M., and L. J. Lanzerotti (1974), *Particle Diffusion in the Radiation Belts*, Springer, New York.

Selesnick, R. S. (2006), Source and loss rates of radiation belt relativistic electrons during magnetic storms, *J. Geophys. Res.,* 111, A04210, doi:10.1029/2005JA011473.

Selesnick, R. S., J. B. Blake, and R. A. Mewaldt (2003), Atmospheric losses of radiation belt electrons, *J. Geophys. Res.*, 108(A12), 1468, doi:10.1029/2003JA010160.

Selesnick, R. S., M. D. Looper, and J. M. Albert (2004), Low-altitude dis- tribution of radiation belt electrons, *J. Geophys. Res.*, 109(A11), A11209, doi:10.1029/2004JA010611.

Shi, Y., E. Zesta, and L. R. Lyons (2009), Features of energetic particle radial profiles inferred from geosynchronous responses to solar wind dynamic

pressure enhancements, *Ann. Geophys.*, 27, 851-859, doi:10.5194/angeo-27-851-2009.

Shprits, Y. Y., R. M. Thorne, G. D. Reeves, and R. Friedel (2005), Radial diffusion modeling with empirical lifetimes: Comparison with CRRES observations, *Annales Geophys.*, 23, 1467–1471.

Shprits, Y. Y., R. M. Thorne, R. B. Horne, S. A. Glauert, M. Cartwright, C. T. Russell, D. N. Baker, and S. G. Kanekal (2006a), Acceleration mechanism responsible for the formation of the new radiation belt during the 2003 Halloween solar storm, *Geophys. Res. Lett.*, 33, L05104, doi:10.1029/2005GL024256.

Shprits, Y. Y., W. Li, and R. M. Thorne (2006b), Controlling effect of the pitch angle scattering rates near the edge of the loss cone on electron lifetimes, *J. Geophys. Res.*, 111, A12206, doi:10.1029/2006JA011758.

Shprits, Y. Y., D. Kondrashov, Y. Chen, R. Thorne, M. Ghil, R. Friedel, and G. Reeves (2007), Reanalysis of relativistic radiation belt electron fluxes using CRRES satellite data, a radial diffusion model, and a Kalman filter, *J. Geophys. Res.*, 112, A12, 216, doi: 10.1029/2007JA012579.

Shprits, Y., M. Daae, and B. Ni (2012), Statistical analysis of phase space density buildups and dropouts, *J. Geophys. Res.*, 117, A01219, doi:10.1029/2011JA016939.

Skrobot, G. L. and Coelho, R. (2012), ELaNa Educational Launch of Nanosatellite Providing Routine RideShare Opportunities, SSC12-V-5, *26th AIAA/USU Conference on Small Satellites.*

Slepian, D. (1978), Prolate spheroidal wave functions, Fourier analysis, and uncertainty—V: The discrete case, *Bell System Tech. J.*, 57,1371–1430,

doi:10.1002/j.1538-7305.1978.tb02104.x.

Spence, H. E., et al. (2013), Science Goals and Overview of the Energetic Particle, Composition, and Thermal Plasma (ECT) Suite on NASA's Radiation Belt Storm Probes (RBSP) Mission, *Space Sci. Rev.*, 179:311-336; doi: 10.1007/s11214-013-0007-5.

Stachura, M and E.W. Frew (2011), Cooperative Target Localization with a Communication Aware Unmanned Aircraft System, *AIAA Journal of Guidance, Control, and Dynamics*, 34(5), DOI:10.2514/1.51591.

Su, Z., et al. (2014), Nonstorm time dynamics of electron radiation belts observed by the Van Allen Probes, *Geophys. Res. Lett.*, 41, 229–235, doi:10.1002/2013GL058912.

Subbotin, D. A., and Y. Y. Shprits (2009), Three-dimensional modeling of the radiation belts using the Versatile Electron Radiation Belt (VERB) code, *Space Weather*, 7, S10001, doi:10.1029/2008SW000452.

Sugiura, M., and T. Kamei (1991), Equatorial Dst index 1957- 1986, *IAGA Bulletin*, 40, edited by A. Berthelier and M. Menvielle, ISGI Publ. Off., Saint. Maur-des-Fosses, France, 1991.

Summers, D. et al. (1998), Realtivistic theory of wave-particle resonant diffusion with application to electron acceleration in the magnetosphere, *J. Geophys. Res.*, 103, A9, 20487-20500.

Summers, D., and R. M. Thorne (2003), Relativistic electron pitch angle scattering by electromagnetic ion cyclotron waves during geomagnetic storms, J. Geophys. Res., 108(A4), 1143, doi:10.1029/2002JA009489.

Summers, D., B. Ni, and N. P. Meredith (2007), Timescales for radiation belt electron acceleration and loss due to resonant wave-particle interactions:

2. Evaluation for VLF chorus, ELF hiss, and electromagnetic ion cyclotron waves, *J. Geophys. Res.,* 112, A04207, doi:10.1029/2006JA011993.

Tapley, B. D., B. E. Schutz, G. H. Born (2004), *Statistical Orbit Determination,* Elsevier Academic Press.

Temerin, M., and X. Li (2002), A new model for the prediction of Dst on the basis of the solar wind, *J. Geophys. Res.,* 107(A12), 1472, doi:10.1029/2001JA007532.

Temerin, M., and X. Li (2006), Dst model for 1995–2002, *J. Geophys. Res.,* 111, A04221, doi:10.1029/2005JA011257.

Temerin, M., and X. Li (2015), The Dst index underestimates the solar cycle variation of geomagnetic activity, *J. Geophys. Res. Space Physics*, 120, doi:10.1002/2015JA021467.

Thomson, D. J. (1982), Spectrum estimation and harmonic analysis, *Proc. IEEE,* 70, 1055–1096, doi:10.1109/PROC.1982.12433.

Thorne, R. M., and C. F. Kennel (1971), Relativistic electron precipitation during magnetic storm main phase, *J. Geophys. Res.*, 76, 4446–4453.

Thorne, R. M., T. P. O'Brien, Y. Y. Shprits, D. Summers, and R. B. Horne (2005), Timescale for MeV electron microburst loss during geomagnetic storms, *J. Geophys. Res.*, 110, A09202, doi:10.1029/2004JA010882.

Thorne, R. M., R. B. Horne, et al. (2005), The Influence of Wave-Particle Interactions on Relativistic Electron Dynamics During Storms, *Inner Magnetosphere Interactions: New Perspectives From Imaging. Geophysical Monograph*, 159, 101.

Thorne, R. M. et al. (2013), Rapid local acceleration of relativistic radiation-belt electrons by magnetospheric chorus, *Nature* 504, 411-414,

doi:10.1038/nature12889.

Tsyganenko, N. A. (1989), A magnetospheric magnetic field model with awarped tail current sheet, *Planet. Space Sci.*, 37, 5–20, doi:10.1016/0032-0633(89)90066-4.

Tsyganenko, N. A., H. J. Singer, and J. C. Kasper (2003), Storm-time distortion of the inner magnetosphere: How severe can it get?, *J. Geophys. Res.*, 108(A5), 1209, doi:10.1029/Turner, D. L. and X. Li (2008a), Radial gradients of phase space density of the outer radiation belt electrons prior to sudden solar wind pressure enhancements, *Geophys. Res. Lett.*, 35, L18101, doi:10.1029/2008GL034866.

Tsyganenko, N. A., and M. I. Sitnov (2005), Modeling the dynamics of the inner magnetosphere during strong geomagnetic storms, *J. Geophys. Res.*, 110, A03208, doi:10.1029/2004JA010798.

Tu, W., et al. (2010), Quantification of the precipitation loss of radiation belt electrons observed by SAMPEX, *J. Geophys. Res.*, 115, A07210, doi:10.1029/2009JA014949.

Tu, W., et al. (2012), Quantifying radial diffusion coefficients of radiation belt electrons based on global MHD simulation and spacecraft measurements, *J. Geophys. Res.*, 117, A10210, doi:10.1029/2012JA017901.

Tu, W., G. S. Cunningham, Y. Chen, S. K. Morley, G. D. Reeves, J. B. Blake, D. N. Baker, and H. Spence (2014), Event- specific chorus wave and electron seed population models in DREAM3D using the Van Allen Probes, *Geophys. Res. Lett.*, 41, doi:10.1002/2013GL058819.

Turner, D. L., and X. Li (2008b), Quantitative forecast of relativistic electron flux at geosynchronous orbit based on low-energy electron flux, *Space Weather*, 6, S05005, doi:10.1029/2007SW000354.

Turner, D. L., X. Li, G. D. Reeves, and H. J. Singer (2010), On phase space density radial gradients of Earth's outer-belt electrons prior to sudden solar wind pressure enhancements: Results from distinctive events and a superposed epoch analysis, *J. Geophys. Res.*, 115, A01205, doi:10.1029/2009JA014423.

Turner, D. L., X. Li, E. Burin des Roziers, and S. Monk (2011), An improved forecast system for relativistic electrons at geosynchronous orbit, *Space Weather*, 9, S06003, doi:10.1029/2010SW000647.

Turner, D. L., et al. (2012a), Explaining sudden losses of outer radiation belt electrons during geomagnetic storms, *Nature Physics*, 8, 3, pp 208-12 , DOI: 10.1038/nphys2185

Turner, D. L., et al. (2012b), Radial distributions of equatorial phase space density for outer radiation belt electrons, *Geophys. Res. Lett.*, 39, L09101, doi:10.1029/2012GL051722.

Turner, R. (2000), "Solar particle events from a risk management perspective," *IEEE Trans. Plasma Sci.*, Vol. 28, No. 6, pp. 2103–2113.

Vampola, A. L. (1998), "Measuring Energetic Electrons," Measurement Techniques in Space Plasmas: Particles, edited by R. F. Pfaff, J. E. Borovsky, and D. T. Young, Geophysical Monograph, American Geophysical Union, p. 102.

Wygant, J. R. et al. (2013), The electric field and waves instruments on the Radiation Belt Storm Probes mission, *Space Sci. Rev.*, 179:183-220, DOI: 10.1007/s11214-013-0013-7.

Zhao, H. et al., The evolution of ring current ion energy density and energy content during geomagnetic storms based on Van Allen Probes measurements, submitted to *J. Geophys. Res.*.

APPENDIX A1

ACRONYMS

AES – Aerospace Engineering Sciences Department

AIAA – American Institute of Aeronautics and Astronautics

BARREL – Balloon Array for RBSP Relativistic Electron Losses

C&DH – Command and Data Handling

CERN – European Organization for Nuclear Research

CIR – Co-rotating Interaction Region

CME – Coronal Mass Ejection

CPLD – Complex Programmable Logic Device

CSA – Charge Sensitive Amplifier

CSSWE – Colorado Student Space Weather Experiment

CU – University of Colorado

ECT – Energetic Particle, Composition, and Thermal Plasma

ELaNa – Educational Launch of Nanosatellites

EM – Engineering Model

ESA – Electrostatic Analyzer

FM – Flight Model

GEO – Geosynchronous Earth Orbit

GOES – Geostationary Operational Environment Satellite

GPS – Global Positioning System

HSS – High Speed Stream

IMF – Interplanetary Magnetic Field

LANL – Los Alamos National Lab

LASP – Laboratory for Atmospheric and Space Physics

LEO – Low Earth Orbit

MagEIS – Magnetic Electron Ion Spectrometer

MCA – Multichannel analyzer

MEO – Middle Earth Orbit

MMS – Magnetospheric Multiscale

NASA – National Aeronautics and Space Administration

NSF – National Science Foundation

NRO – National Reconnaissance Office

PSC – Phase space coordinates

RBSP – Radiation Belt Storm Probes

REPT – Relativistic Electron-Proton Telescope

REPTile – Relativistic Electron and Proton Telescope integrated little experiment

RF – Radio Frequency

SAA – South Atlantic Anomaly

SAMPEX – Solar Anomalous and Magnetospheric Particle Explorer

SEP – Solar Energetic Particle

SOC – Sciene Operations Center

SST – Solid State Telescope

THEMIS – Time History of Events and Macroscale Interactions during Substorms

TVAC – Thermal Vacuum

ULA – United Launch Alliance

ULF – Ultra Low Frequency

USU – Utah State University

x